Optimizing the power-generation performance of flapping-foil turbines while simplifying their mechanical design with the use of elastic supports

Thèse

Matthieu Boudreau

Doctorat en génie mécanique
Philosophiæ doctor (Ph. D.)

Québec, Canada

© Matthieu Boudreau, 2019

Optimizing the power-generation performance of flapping-foil turbines while simplifying their mechanical design with the use of elastic supports

Thèse

Matthieu Boudreau

Sous la direction de:

Guy Dumas, directeur de recherche
Peter Oshkai, codirecteur de recherche

Résumé

Due à la complexité des mécanismes typiquement requis pour contraindre l'aile d'une turbine à aile oscillante à suivre des mouvements spécifiques, cette thèse étudie la possibilité de bénéficier de mouvements non contraints, dits passifs. En pratique, cela implique que l'aile est attachée à la structure de la turbine à l'aide de supports élastiques indépendants en pilonnement et en tangage, formés de ressorts et d'amortisseurs. Par conséquent, seul un contrôle indirect des mouvements est possible en ajustant adéquatement les paramètres structuraux affectant la dynamique de l'aile, tels que les paramètres d'inertie, d'amortissement et de raideur de l'aile et de ses supports élastiques.

En premier lieu, un prototype ayant des mouvements passifs autant en pilonnement qu'en tangage, et donc étant complètement passif, a été conçu et testé dans un canal à surface libre. Cette première phase du présent travail de recherche a confirmé la faisabilité et le potentiel de ce concept en permettant d'extraire une quantité significative d'énergie de l'écoulement d'eau. Cependant, l'efficacité maximale atteinte est demeurée inférieure à ce qui peut être obtenu en contraignant l'aile à suivre des mouvements précis.

Suite à ces expériences, un algorithme résolvant la dynamique du solide a été implémenté et couplé au logiciel résolvant la dynamique du fluide gouverné par les équations de Navier-Stokes. Des simulations numériques ont été réalisées afin d'analyser plus en détail la dynamique de chacun des deux degrés de liberté de l'aile. Plutôt que de poursuivre notre étude du concept complètement passif immédiatement, un concept de turbine semi-passive caractérisée par un mouvement de tangage passif et un mouvement de pilonnement contraint a été considéré. Des efficacités de l'ordre de 45% ont été atteintes, se comparant ainsi aux meilleures performances rapportées dans la littérature concernant les turbines à ailes oscillantes complètement contraintes. En plus de révéler le fort potentiel de ce concept de turbine semi-passive, cette étude nous a permis de nous concentrer sur certains aspects spécifiques concernant la dynamique d'une aile attachée par des ressorts en tangage. Cette analyse plus détaillée de la physique en jeu a été facilitée par le nombre réduit de paramètres structuraux en jeu par rapport à une turbine pour laquelle le mouvement de pilonnement est lui aussi passif. L'une des découvertes importantes est que le centre de masse doit être situé en aval du point de pivot afin de générer un transfert d'énergie du mouvement de pilonnement vers le mouvement de tangage par l'entremise du couplage inertiel entre les deux degrés de liberté. Ce transfert d'énergie est crucial puisque les mouvements de tangage optimaux nécessitent de l'énergie en moyenne pour être soutenus. De plus, un paramètre

combinant les effets liés au moment d'inertie de l'aile par rapport à son point de pivot et à la raideur en tangage a été proposé. Ce paramètre permet de bien caractériser la dynamique du mouvement de tangage passif de la turbine semi-passive. Il permet aussi de déterminer la raideur requise pour différentes valeurs du moment d'inertie afin de maintenir une performance optimale de la turbine.

Utilisant les connaissances acquises concernant la dynamique des mouvements de tangage passifs, le concept de turbine à aile oscillante complètement passive a été revisité. Les meilleures efficacités obtenues avec la turbine semi-passive ont été égalées et ont même été surpassées puisque qu'une efficacité de 53.8% a été atteinte. Les résultats ont aussi démontré qu'une performance optimale pouvait être maintenue sur de larges plages de valeurs en ce qui concerne la masse en pilonnement ainsi que le moment d'inertie par rapport au point de pivot, pourvu que les raideurs en pilonnement et en tangage soient ajustées correctement.

Abstract

Due to the complexity of the mechanisms typically required when designing a flapping-foil turbine to prescribe specific heave and pitch motions, this thesis investigates the possibility of benefiting from unconstrained motions. In practice, this means that the foil is attached to the turbine structure with independent elastic supports in heave and in pitch, which consist in springs and dampers. Consequently, only an indirect control over the foil motions is possible through an adequate adjustment of the structural parameters affecting the foil dynamics, namely the inertial, damping and stiffness characteristics of the elastically-supported foil. Such motions are referred to as passive motions.

As a first step, a turbine prototype with passive heave and pitch motions, thus being fully-passive, has been designed and tested in a water channel. This first phase of the present research work has confirmed the feasibility and the potential of this concept to extract a significant amount of energy from a fluid flow. However, the maximum efficiency that has been obtained is smaller than what can be achieved when prescribing specific foil motions.

Following these experiments, a solid solver has been implemented and coupled with a Navier-Stokes fluid solver. Numerical simulations have been carried out to analyze the dynamics of both degrees of freedom in more details. Instead of immediately pursuing our study of the fully-passive flapping-foil turbine, a semi-passive concept, with a passive pitch motion and a prescribed heave motion, has been considered. Efficiencies of the order of 45% have been achieved, hence competing with the best performance reported in the literature for flapping-foil turbines with prescribed motions. In addition to revealing the great potential of this semi-passive turbine concept, this study has allowed us to focus on some specific aspects of the dynamics of passive pitch motions. This more detailed analysis of the physics at play has been facilitated by the reduced number of structural parameters affecting the foil dynamics compared to a turbine for which the foil is also elastically-supported in heave. One of the main findings is that the center of mass must be positioned downstream of the pitch axis in order to generate a net transfer of energy from the heave motion to the pitch motion via the inertial coupling between the two degrees of freedom. This energy transfer is crucial because optimal pitch motions require energy on average to be sustained. Moreover, a parameter combining the effects of the moment of inertia of the foil about the pitch axis and the pitch stiffness has been proposed. This parameter effectively characterizes the pitch dynamics of the semi-passive turbine. It also allows properly scaling the pitch stiffness when different moments of inertia are considered with the objective of maintaining

an optimal turbine performance.

Having improved our knowledge about the dynamics of passive pitch motions, the fully-passive flapping-foil turbine concept has been revisited. The best efficiencies obtained with the semi-passive concept have been matched, and even exceeded since an efficiency of 53.8% has been reached. The results have also demonstrated that an optimal performance can be maintained over large ranges of values regarding the heaving mass and the moment of inertia when the heave and pitch stiffness coefficients are adjusted adequately.

Contents

List of Tables

List of Figures

À la curiosité et à tous ceux qui
l'éveillent et la propagent.
Merci Jacques et Hélène!

One day I will find the right words,
and they will be simple.

Jack Kerouac

Remerciements

Avis au lecteur:

1. Certains passages de ce qui suit pourraient paraître inusités à un lecteur non averti. Pour remédier à cette situation, je l'invite à apprendre à me connaître davantage.

2. Contrairement aux restaurants asiatiques offrant la possibilité de choisir une version neutre, épicée ou très épicée (ou même parfois littéralement immangeable), ces remerciements ne viennent malheureusement que sous un seul format. La perception de mon niveau de gratitude peut varier d'un lecteur à l'autre. De plus, il est parfois difficile de bien transmettre des émotions par écrit. Quoique dans mon cas, la différence est peut-être moins importante puisque mon air neutre n'ajoute pas nécessairement grand chose de plus à l'oral. Ainsi, j'invite le lecteur à augmenter le niveau de gratitude qu'il perçoit d'un ou deux crans afin de bien traduire mes sentiments.

Ceux qui me connaissent savent que je ne raffole pas des protocoles. Il me paraît donc des plus étranges de remercier machinalement par écrit des gens que je côtoie régulièrement et qui ne liront peut-être jamais ces mots. Je préfère donc vous présenter quelqu'un. Cette personne, c'est la petite voix créatrice qui m'a accompagné tout au long du parcours qui a mené à cette thèse. Appelons-la Béatrice, tiens.

Mais avant de la laisser parler, je dois tout de même la remercier, la remercier d'exister tout simplement. Chacun possède la sienne. Lorsqu'une idée nous vient à l'esprit sans qu'on puisse trop savoir comment elle est arrivée là, ce sont nos voix créatrices qui nous parlent. Heureusement, leur souffle est continu. Suite à l'expiration de l'idée précédente, vient l'inspiration de la suivante. Toutefois, leur débit est très variable et on pense souvent à tort que l'on doit se dépêcher de tout agripper au passage. Mais les débits importants emportent nécessairement quelques débris avec eux. Le défi consiste à ne pas se laisser amadouer et à reconnaître une mauvaise idée comme telle plutôt que de s'efforcer de la justifier. Quoiqu'il en soit, je remercie toutes les mauvaises idées qui sont passées au cours des dernières années puisqu'elles en ont fait naître de bien meilleures. J'espère seulement qu'aucune de ces mauvaises idées n'ait été assez astucieuse pour se camoufler parmi les bonnes et se mériter une place dans cette thèse. Si c'est le cas, je la félicite.

Bon, je divague. Revenons à Béatrice. Comme ses congénères, elle est une personne bien étrange, discrète quand on l'interpelle directement et bavarde lorsqu'on n'y porte plus attention. Elle était d'ailleurs particulièrement loquace lors des balades en vélo que je faisais entre mon appartement et l'université.

Heureusement, il existe des techniques pour la disposer à parler lorsqu'on désire l'entendre. L'une des plus efficace est de la laisser s'amuser avec ses semblables. J'ai été grandement choyé à ce niveau et je tiens à remercier tous mes collègues et amis du Laboratoire de Mécanique des Fluides Numérique (LMFN) pour tout le temps où ils ont laissé à leurs propres voix créatrices interagir avec Béatrice. Je ne pourrai malheureusement pas tous les nommer, mais je pense particulièrement à Christian, Étienne, Guillaume, Jean-Christophe, Kevin, Marine, Mathieu, Maxime, Olivier, Philippe, Rémi, Sébastien, Thierry et Thomas. Vous êtes en très grande partie responsable du fait que je me sois autant plu au LMFN et que j'y suis resté aussi longtemps.

La volubilité de Béatrice dépend grandement de son bien-être. Mes amis et ma famille nous ont offert de nombreux moments de distraction et de bonheur à elle et moi qui nous ont permis de préserver notre santé mentale, du moins selon nous, ou plutôt selon moi (on s'entend là, je suis au courant que Béatrice fait partie de moi). Malgré tout, je trouve qu'on fait un bon duo, tout comme Maxime et le pain naan, Sophie et les poubelles, euh je veux dire la cannelle, oui oui la cannelle, Guillaume et les chats, Félix et les dessins, Sébastien et son mannequin, Olivier et les jeux de mots, Kevin et ce qui reste de son auto ou Jacques et les manteaux.

Je tiens aussi à remercier tous les excellents professeurs que j'ai eu la chance de côtoyer et qui ont façonné la personnalité de Béatrice. Un merci particulier à Yvan Maciel qui a d'ailleurs accepté de réviser cette thèse. Par sa présence et son écoute, il est bien plus qu'un excellent professeur pour ses élèves et je sais que je m'exprime aussi en leurs noms en le remerciant chaleureusement. Merci aussi à Peter et à son groupe à Victoria, en particulier Dylan et Mostafa, qui ont offert un nouveau terrain de jeu et des échanges enrichissants à Béatrice.

Béatrice est d'autant plus productive lorsqu'on lui laisse toute la liberté d'agir comme bon lui semble, sans contrainte. En ce sens, elle a grandement bénéficié du support financier de plusieurs organismes au cours de mon doctorat, soit le Conseil de Recherches en Sciences Naturelles et en Génie du Canada (CRSNG), la Tyler Lewis Clean Energy Foundation et les bourses de leadership et développement durable de l'Université Laval. Ces appuis ont entre autres permis d'éviter que du stress ne lui vole du temps d'antenne.

Évidemment, merci à l'architecte du LMFN, Guy, ainsi qu'à sa voix créatrice dont je ne connais pas le nom. Merci d'avoir accueilli Béatrice au sein de ton laboratoire et d'avoir su créer et entretenir ce milieu propice à son épanouissement, ainsi que celui de bien d'autres voix créatrices avant elle, avec elle et certainement après elle. Tes talents de pédagogue et ta rigueur ont permis à Béatrice et moi de faire bien du chemin depuis que tu nous as inculqué ta passion pour le monde de la mécanique des fluides et nous sommes fiers de faire partie de cette famille. J'ai aussi beaucoup apprécier ta proximité

et tous les échanges “non scientifiques” que nous avons eus, entres autres autour d’une bière lors d’un 5 à 7, en conférence ou lors de notre séjour à Victoria.

Enfin, un merci bien spécial à mes parents, les meilleurs au monde sans aucun doute. Même si je ne suis pas le seul à le penser, la différence c’est que moi j’ai raison. Si la longueur des remerciements à leur égard devait être proportionnel à ma gratitude envers eux, j’aurais mal aux mains.

Foreword

This thesis is composed of four papers for which I am the first author. Their content appear as published but their format is adjusted to comply with the format of the thesis. The papers are preceded by an overall description of the problematic, a literature review, a presentation of the objectives and the outlines of the four papers including their main contributions. An overall conclusion and recommendations for possible future research avenues follow. The publication status of each paper and the role of each contributor are given below.

Paper I

Boudreau, Matthieu, Dumas, Guy, Rahimpour, Mostafa and Oshkai Peter. **Experimental investigation of the energy extraction by a fully-passive flapping-foil hydrokinetic turbine prototype**. *Journal of Fluids and Structures*, 82:446–472, 2018.

Submitted on March 8th 2018

Accepted on July 31st 2018

Available online on September 24th 2018 (https://doi.org/10.1016/j.jfluidstructs.2018.07.014)

I entirely wrote Paper I and the manuscript was revised by the three co-authors. The second and and the fourth authors, Guy Dumas and Peter Oshkai, respectively are my thesis director and co-director. I also supervised the design and assembly of the prototype, conducted all the experiments with the assistance of the third author, Mostafa Rahimpour, and analyzed the results.

Paper II

Boudreau, Matthieu, Gunther, Kevin and Dumas, Guy. **Investigation of the energy-extraction regime of a novel semi-passive flapping-foil turbine concept with a prescribed heave motion and a passive pitch motion**. *Journal of Fluids and Structures*, 84:368–390, 2019.

Submitted on July 27th 2018

Accepted on November 16th 2018

Available online on December 2nd 2018 (https://doi.org/10.1016/j.jfluidstructs.2018.11.014)

Paper III

Boudreau, Matthieu, Gunther, Kevin and Dumas, Guy. **Free-pitching flapping-foil turbines with an imposed sinusoidal heave motion**. Submitted to *Journal of Fluids and Structures*, 2019.

I entirely wrote Papers II and III and the manuscripts were revised by the two co-authors. I developed the methodology myself and carried out the numerical simulations and the analysis of the results with the help of the second author, Kevin Gunther, an undergraduate research assistant.

Paper IV

Boudreau, Matthieu, Picard-Deland, Maxime and Dumas, Guy. **A parametric study and optimization of the fully-passive flapping-foil turbine at high Reynolds number**. Submitted to *Renewable Energy*, 2019.

I entirely wrote Paper IV and the manuscript was revised by the two co-authors. I led the parametric study that has been carried out with the assistance of Maxime Picard-Deland, a research assistant, who wrote a preliminary report on some of the results presented in this paper. I carried out the rest of the simulations and performed the final analysis of the results.

Introduction

Conventional sources of energy relying on fossil fuels are finite and are the cause of many serious environmental threats. Developing new sources of clean and renewable energy is therefore crucial in a sustainable development perspective. Among the different possibilities, the energy extraction from river or tidal currents by hydrokinetic turbines is rapidly drawing more and more attention nowadays. This technology possesses several important advantages over wind turbines. First, the higher density of water compared to air results in a higher energy density, hence resulting in smaller apparatus for the same power output. Moreover, both the direction and the strength of river and tidal currents are more predictable and more constant than wind, which greatly facilitates the electrical grid management. Also, the electricity generated by hydrokinetic turbines could be produced where it is consumed since large urban areas are often located near an important river or the ocean. This would minimize the infrastructure needed for the energy transport and the losses associated to it. It would also not compete with other uses of the land. However, this innovative renewable energy source remains almost unexploited at the moment despite all these pros.

The recent developments in the field of hydrokinetic energy harvesting has drawn a renewed interest for cross-flow turbines, especially in the context of shallow waters due to the rectangular area swept by their blades (M. S. Güney and K. Kaygusuz, 2010; Kinsey et al., 2011; Young et al., 2014). This type of turbine includes the well-known vertical-axis turbine (Paraschivoiu, 2002; Gosselin et al., 2016; Boudreau and Dumas, 2017a) and the flapping-foil turbine (Xiao and Zhu, 2014; Young et al., 2014), to which this thesis is devoted. The flapping-foil turbine, also known as the oscillating-foil turbine, consists in a blade undergoing combined heave (translational) and pitch (rotational) motions, as shown in Fig. 0.1. The energy extraction potential of this turbine technology has already been demonstrated in the past with efficiencies of the same order as those obtained with the more established horizontal-axis and vertical-axis turbines (Xiao and Zhu, 2014; Young et al., 2014).

In order to achieve this level of performance, the heave and pitch motions are generally constrained in a way that allows one to prescribe specific motions. However, this control over the motions comes at the cost of a complex mechanical design, which raises a few issues. Indeed, the more components there are in the mechanical assembly required to couple and constrain both degrees of freedom, the higher is the risk of failure of the device and the more costly it becomes. Moreover, the friction between all the moving components can result in considerable energy losses. For example, 25% of the

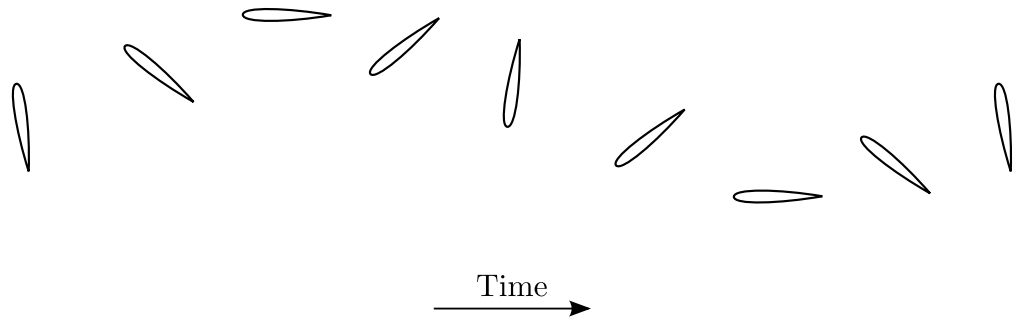

Figure 0.1: Typical foil motions of a flapping-foil turbine as a function of time with the fluid flowing from left to right.

energy extracted from the flow by the flapping-foil turbine prototype tested by Kinsey et al. (2011) was lost due to friction before being converted into electricity. A fundamental change therefore appears unavoidable to fully benefit from the promising potential of this turbine technology.

One possible alternative is to make use of unconstrained motions, either in pitch, in heave or for both degrees of freedom. This is achieved by elastically supporting the turbine blade with springs and dampers. Consequently, the heave and pitch motions cannot be prescribed and rather result from the interaction between the turbine blade, its elastic supports and the flow. This is what we refer to as passive motions. The only way to indirectly control such motions is by adequately adjusting the structural parameters that play a role in the turbine blade dynamics. The challenge of designing a flapping-foil turbine with passive motions therefore consists in finding a set of structural parameters that results in suitable motions to maximize the energy extraction from the flow.

Chapter 1

Background

1.1 Constrained and/or passive motions

In order to avoid any confusion regarding the use of constrained or passive motions for flapping-foil turbines, it is convenient to decompose the heave and pitch motions into 5 different motion parameters, namely the shape and amplitude of the heave motion, the shape and amplitude of the pitch motion, the frequency of the heave motion, the frequency of the pitch motion and the phase lag between the heave and the pitch motions.

When all five motion parameters are constrained, we obtain what we refer to as a fully-constrained turbine. Typically, a slider-crank linkage is used to convert the reciprocating heave motion to a rotating motion in order to use a typical electric generator to produce electricity. The electric generator is usually connected to the heave motion because it is responsible for most of the energy extraction from the flow (Kinsey and Dumas, 2008, 2014; Zhu, 2011). The use of a slider-crank linkage has the consequence of constraining the shape and amplitude of the heave motion, but not its frequency. A constant frequency can be obtained by using a controller with the electric generator. The shape and amplitude of the pitch motion, its frequency and the phase lag between the heave and the pitch motions can be constrained by making use of a motor and a controller for this degree of freedom. This corresponds to a two-degree-of-freedom (2-DOF) fully-constrained flapping-foil turbine (e.g. Kim et al. (2017)). Alternatively, mechanical linkages can be used to couple the heave and the pitch motions together in order to obtain a specific relation between them. In other words, the pitch angle becomes a function of the heave position, thereby constraining all five motion parameters and resulting in a one-degree-of-freedom (1-DOF) fully-constrained flapping-foil turbine (e.g. McKinney and DeLaurier (1981); Kinsey et al. (2011); Xu et al. (2017)). The slider-crank and coupling mechanisms are designed to obtain specific motion shapes in heave and in pitch, which generally correspond to sinusoidal motions.

A fully-passive flapping-foil turbine is obtained when the five motion parameters describing the heave and pitch motions are left free. This means that no slider-crank linkage, no coupling mechanism, no controller and no motor in pitch are used. Instead, the foil is elastically-supported with springs

and/or dampers while still being restricted to move in heave and in pitch only. The consequence of not constraining the five motion parameters is that specific heave and pitch motions cannot be prescribed. Indeed, the designer of a fully-passive turbine only has an indirect control over the motions by adjusting the structural parameters playing a role in the turbine dynamics, as mentioned above. It is worth mentioning that a linear electric generator must be used to produce electricity with this turbine concept since the heave motion is not converted to a rotating motion. For example, such a linear electric generator is used by *Vortex Hydro Energy, Inc.* to generate electricity from the vortex-induced vibrations of cylinders (Vortex Hydro Energy).

In addition to these two limit cases, several other design options arise when constraining or not each of the five motion parameters. These turbine concepts are referred to as semi-passive flapping-foil turbines. A few of the different possibilities have already been proposed and studied in the literature, and they will be briefly presented in Sec. 1.4.

1.2 Turbine dynamics

1.2.1 Fully-constrained flapping-foil turbine

In order to better understand the different dynamics experienced by the fully-constrained and fully-passive flapping-foil turbine concepts, it is useful to analyze their respective equations of motion. General equations of motion for the 1-DOF fully-constrained concept are given below:

$$F_y = m_h \ddot{h} + S\left(\ddot{\theta}\cos\theta - \dot{\theta}^2 \sin\theta\right) + D_h \dot{h} + F_{\text{gen}} + F_{\text{link}} \,, \tag{1.1}$$

$$M = I_\theta \,\ddot{\theta} + S\ddot{h}\cos(\theta) + D_\theta \,\dot{\theta} + M_{\text{link}} \,, \tag{1.2}$$

where the superscript $(\cdot)$ denotes a time derivative and the definitions of the variables appearing in these equations are listed here:

- F_y: hydrodynamic force component in the heave direction;
- M: hydrodynamic moment about the pitch axis;
- h: heave position (vertical position of the pitch axis);
- θ: pitch angle;
- m_h: mass of all the components undergoing the heave motion;
- I_θ: moment of inertia about the pitch axis;
- S: static moment;
- D_h: heave damping coefficient;
- D_θ: pitch damping coefficient;
- F_{gen}: force component in the heave direction stemming from the electric generator;
- F_{link}: force component in the heave direction stemming from the rigid links coupling both degrees of freedom together;
- M_{link}: moment about the pitch axis stemming from the rigid links coupling both degrees of freedom together;

The static moment (S) corresponds to the product of the mass of all the components undergoing the pitch motion (m_θ) with the distance between the center of mass (in pitch) and the pitch axis (x_θ):

$$S = m_\theta x_\theta \ . \tag{1.3}$$

It is therefore equal to zero when the pitch axis, positioned at a distance x_p downstream of the leading edge, coincides with the center of mass. x_θ is defined positive when the center of mass is located downstream of the pitch axis, as shown in Fig. 1.1.

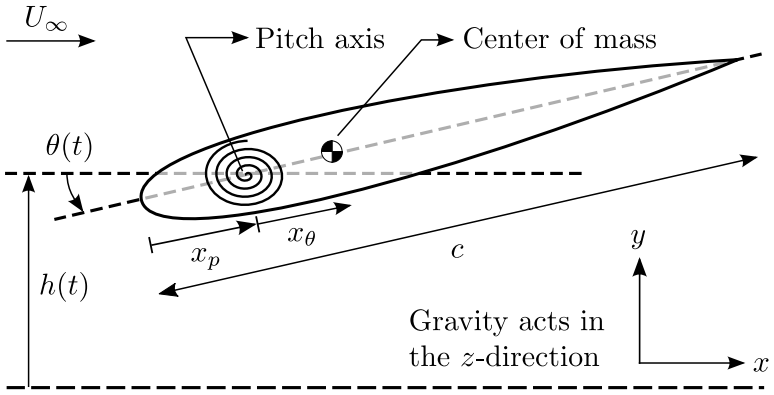

Figure 1.1: Schematic of the flapping-foil illustrating the pitch axis and center of mass locations.

The heave and pitch damping coefficients (D_h et D_θ) stand for the presence of undesired friction in a real turbine setup. Lastly, the gravitational acceleration does not appear in the equations of motion because it is considered to act in a direction aligned with the pitch axis (z-direction in Fig. 1.1).

When designing a fully-constrained flapping-foil turbine, the objective is to prescribe specific functions of time for the heave and pitch motions. This is achieved by properly designing the rigid links that couple the heave and pitch degrees of freedom, in order to enforce a particular relation between the pitch angle and the heave position, and by controlling the resistive force of the electric generator (F_{gen}) in real time. In other words, F_{gen} must be controlled so that the solutions of Eqs. 1.1 and 1.2 correspond to the desired prescribed motions. Generally, sinusoidal motions are prescribed:

$$h = H_0 \sin(2\pi f t) \ , \tag{1.4}$$

$$\theta = \Theta_0 \sin(2\pi f t - \phi) \ , \tag{1.5}$$

where H_0 and Θ_0 are the heave and pitch amplitudes, f is the frequency of the motions, t is time and ϕ is the phase lag between the heave and pitch motions. When conducting numerical simulations, the prescribed motions are usually directly imposed without solving the equations of motion (e.g. Kinsey and Dumas (2008, 2014)), thus assuming that the electric generator would be properly controlled.

Eqs. 1.1 and 1.2 are useful to understand how the power is transferred from the flow to an electric generator. The amount of power available at the generator is obtained by multiplying Eq. 1.1 with the

heave velocity ($\dot{h}$). All the term appearing in the resulting equation are placed on the left hand side of the equation, except the one involving F_{gen}, in addition to being normalized to obtain:

$$\langle C_{P_h} \rangle + \langle C_{P_{m_h}} \rangle + \langle C_{P_{S,h}} \rangle + \langle C_{P_{D_h}} \rangle + \langle C_{P_{\text{link},h}} \rangle = \langle C_{P_{\text{gen}}} \rangle \, , \tag{1.6}$$

where the angle brackets indicate that the values are cycle-averaged. The same is done with Eq. 1.2 after multiplying it with the pitch velocity ($\dot{\theta}$):

$$\langle C_{P_\theta} \rangle + \langle C_{P_{I_\theta}} \rangle + \langle C_{P_{S,\theta}} \rangle + \langle C_{P_{D_\theta}} \rangle + \langle C_{P_{\text{link},\theta}} \rangle = 0 \, . \tag{1.7}$$

The different power coefficients appearing in Eqs. 1.6 and 1.7 are defined as:

$$\langle C_{P_h} \rangle = \frac{1}{T} \int_{t_i}^{t_i+T} \left(\frac{F_y \dot{h}}{0.5 \rho U_\infty^3 b c} \right) dt \, , \tag{1.8}$$

$$\langle C_{P_{m_h}} \rangle = \frac{1}{T} \int_{t_i}^{t_i+T} \left(\frac{-m_h \ddot{h} \dot{h}}{0.5 \rho U_\infty^3 b c} \right) dt \, , \tag{1.9}$$

$$\langle C_{P_{S,h}} \rangle = \frac{1}{T} \int_{t_i}^{t_i+T} \left(\frac{-S \dot{h} \left(\ddot{\theta} \cos\theta - \dot{\theta}^2 \sin\theta \right)}{0.5 \rho U_\infty^3 b c} \right) dt \, , \tag{1.10}$$

$$\langle C_{P_{D_h}} \rangle = \frac{1}{T} \int_{t_i}^{t_i+T} \left(\frac{-D_h \dot{h}^2}{0.5 \rho U_\infty^3 b c} \right) dt \, , \tag{1.11}$$

$$\langle C_{P_{\text{link},h}} \rangle = \frac{1}{T} \int_{t_i}^{t_i+T} \left(\frac{F_{\text{link}} \dot{h}}{0.5 \rho U_\infty^3 b c} \right) dt \, , \tag{1.12}$$

$$\langle C_{P_{\text{gen}}} \rangle = \frac{1}{T} \int_{t_i}^{t_i+T} \left(\frac{F_{\text{gen}} \dot{h}}{0.5 \rho U_\infty^3 b c} \right) dt \, , \tag{1.13}$$

$$\langle C_{P_\theta} \rangle = \frac{1}{T} \int_{t_i}^{t_i+T} \left(\frac{M \dot{\theta}}{0.5 \rho U_\infty^3 b c} \right) dt \, , \tag{1.14}$$

$$\langle C_{P_{I_\theta}} \rangle = \frac{1}{T} \int_{t_i}^{t_i+T} \left(\frac{-I_\theta \ddot{\theta} \dot{\theta}}{0.5 \rho U_\infty^3 b c} \right) dt \, , \tag{1.15}$$

$$\langle C_{P_{S,\theta}} \rangle = \frac{1}{T} \int_{t_i}^{t_i+T} \left(\frac{-S \ddot{h} \dot{\theta} \cos(\theta)}{0.5 \rho U_\infty^3 b c} \right) dt \, , \tag{1.16}$$

$$\langle C_{P_{D_\theta}} \rangle = \frac{1}{T} \int_{t_i}^{t_i+T} \left(\frac{-D_\theta \dot{\theta}^2}{0.5 \rho U_\infty^3 b c} \right) dt \, , \tag{1.17}$$

$$\langle C_{P_{\text{link},\theta}} \rangle = \frac{1}{T} \int_{t_i}^{t_i+T} \left(\frac{M_{\text{link}}\, \dot{\theta}}{0.5\, \rho\, U_\infty^3\, b\, c} \right) dt \ , \tag{1.18}$$

where t_i is the time at which a given foil oscillation starts, T is the period of this oscillation ($T = 1/f$), ρ is the fluid density, U_∞ is the freestream velocity, b is the blade span length and c is the chord length. Note that unless otherwise indicated, the term power coefficient refers to a cycle-averaged value.

$\langle C_{P_{\text{gen}}} \rangle$ is the power coefficient available at the electric generator and therefore measures the power extraction performance of the turbine. The power transfers occurring between the foil and the flow for each degree of freedom are computed with $\langle C_{P_h} \rangle$ and $\langle C_{P_\theta} \rangle$, which are respectively referred to as the heave and pitch power coefficients. They are defined positive when the power is transferred from the flow to the foil and negative when the motions require some power on average to be maintained. $\langle C_{P_{m_h}} \rangle$ and $\langle C_{P_{l_\theta}} \rangle$ correspond to power transfers occurring between the foil motions and different forms of potential energy. $\langle C_{P_{D_h}} \rangle$ and $\langle C_{P_{D_\theta}} \rangle$ represent power losses, that would be dissipated as heat, associated to the presence of viscous friction in heave and in pitch. They are thus necessarily negative. Note that other forms of friction such as Coulomb friction (dry friction) could also be present on a real turbine, but they have been omitted in Eqs. 1.1 and 1.2 for the sake of simplicity. $\langle C_{P_{S,h}} \rangle$ and $\langle C_{P_{S,\theta}} \rangle$ correspond to the power transfers occurring between the heave motion and the pitch motion through the inertial coupling terms in Eqs. 1.1 and 1.2, namely the terms involving the static moment. $\langle C_{P_{\text{link},h}} \rangle$ and $\langle C_{P_{\text{link},\theta}} \rangle$ are similar to $\langle C_{P_{S,h}} \rangle$ and $\langle C_{P_{S,\theta}} \rangle$ since they also represent power transfers occurring between both degrees of freedom, but through the rigid mechanical links coupling both degrees of freedom instead of the inertial coupling terms. These four power coefficients are defined positive when they correspond to a power input in their respective equation and negative for a power output. For example, when $\langle C_{P_{S,h}} \rangle$ is negative but $\langle C_{P_{S,\theta}} \rangle$ is positive, some power is transferred from the heave motion to the pitch motion on average during one cycle[1]. Note that $\langle C_{P_{S,h}} \rangle$ and $\langle C_{P_{S,\theta}} \rangle$ are equal to zero when the center of mass coincides with the pitch axis (see Eq. 1.3 and Fig. 1.1).

Typically, the prescribed motions of a fully-constrained flapping-foil turbine are periodic. As a result, $\langle C_{P_{m_h}} \rangle$ and $\langle C_{P_{l_\theta}} \rangle$ vanish in Eqs. 1.1 and 1.2 because these terms are conservative (Veilleux, 2014). Moreover, the pairs $\langle C_{P_{S,h}} \rangle$ and $\langle C_{P_{S,\theta}} \rangle$ as well as $\langle C_{P_{\text{link},h}} \rangle$ and $\langle C_{P_{\text{link},\theta}} \rangle$ are equal but opposite when the motions are periodic (Veilleux, 2014):

$$\langle C_{P_{S,h}} \rangle = -\langle C_{P_{S,\theta}} \rangle \ , \tag{1.19}$$

$$\langle C_{P_{\text{link},h}} \rangle = -\langle C_{P_{\text{link},\theta}} \rangle \ . \tag{1.20}$$

Eqs. 1.6 and 1.7 can thus be combined to obtain:

$$\langle C_{P_h} \rangle + \langle C_{P_\theta} \rangle + \langle C_{P_{D_h}} \rangle + \langle C_{P_{D_\theta}} \rangle = \langle C_{P_{\text{gen}}} \rangle \ . \tag{1.21}$$

This equation states that, on average, the power available at the electric generator is equal to the sum of the power extracted from the flow through the heave and pitch motions minus the power losses due to friction.

[1] Note that these definitions are slightly different than those presented in the paper of Veilleux and Dumas (2017) due to a different sign convention used for θ.

The efficiency is also commonly used to evaluate the performance of a flapping-foil turbine. It is defined as:

$$\eta = \frac{\langle C_{P_{\text{gen}}} \rangle \, c}{d} \, , \tag{1.22}$$

where d is the overall extent of the foil motion, or, in other words, the distance between the maximum and minimum positions reached by any point on the foil surface in the heave direction during one complete foil oscillation. The efficiency defined by Eq. 1.22 is a measure of the ratio between the power available for the electric generator of a turbine and the power available in the flow passing through the turbine swept area. The power available for the turbine corresponds to the kinetic energy flux passing through the area swept by the foil, i.e., the product of the overall extent of the foil motion (d) with the blade span length (b). The efficiency defined by Eq. 1.22 can therefore be referred to as a "water-to-generator" efficiency. A "water-to-wire" efficiency could be determined by also taking into account the efficiency of the power conversion into electricity performed by the electric generator.

It is also useful to define an efficiency based on the power extracted from the flow that does not take into account the losses due to friction:

$$\eta_{\text{hydro}} = \frac{\left(\langle C_{P_h} \rangle + \langle C_{P_\theta} \rangle \right) c}{d} \, , \tag{1.23}$$

which is referred to as the hydrodynamic efficiency by some authors (e.g. Kinsey et al. (2011)). The corresponding hydrodynamic power coefficient is defined as:

$$\langle C_{P_{\text{hydro}}} \rangle = \langle C_{P_h} \rangle + \langle C_{P_\theta} \rangle \, , \tag{1.24}$$

These two metrics allow comparing the hydrodynamic performances of turbines with different mechanical designs, and thus different amount of friction, therefore remaining more general. For this reason, the hydrodynamic efficiency is often preferred to the efficiency defined by Eq. 1.22 when numerical simulations are conducted. It is worth mentioning that care should be taken when comparing the efficiencies reported by different studies since different definitions are used in the literature. For example, some authors normalize the power extracted with twice the heave amplitude ($2H_0$) instead of the overall extent of the foil motion (d).

1.2.2 Fully-passive flapping-foil turbine

In the case of the fully-passive flapping-foil turbine concept, no rigid links are used to couple the heave and pitch degrees of freedom together. However, the foil can be attached to the turbine structure with independent springs in heave and in pitch. Therefore, the general equations of motion of the fully-passive flapping-foil turbine concept are:

$$F_y = m_h \ddot{h} + S\left(\ddot{\theta}\cos\theta - \dot{\theta}^2 \sin\theta\right) + D_h \dot{h} + k_h h + F_{\text{gen}} \, , \tag{1.25}$$

$$M = I_\theta \, \ddot{\theta} + S\ddot{h}\cos(\theta) + D_\theta \, \dot{\theta} + k_\theta \, \theta \, , \tag{1.26}$$

where k_h is the heave stiffness coefficient and k_θ is the pitch stiffness coefficient. The derivation of the fully-passive flapping-foil equations of motion is presented in the master thesis of Veilleux (2014). Note however that the signs of the inertial coupling terms are different in his thesis because of a different sign convention used for θ.

Since no controller is used with the electric generator, F_{gen} cannot be controlled in real time to obtain specific solutions of Eqs. 1.25 and 1.26 and thus to prescribe the foil motions. Actually, the uncontrolled electric generator connected to the heave motion is often modeled as a linear (viscous) damper (Abiru and Yoshitake, 2011; Boudreau et al., 2018; Deng et al., 2015; Griffith et al., 2016; Iverson, 2018; Peng and Zhu, 2009; Teng et al., 2016; Veilleux and Dumas, 2017; Wang et al., 2017; Zhu, 2012). In that case, F_{gen} is idealized as:

$$F_{\text{gen}} = D_h \dot{h} \,, \tag{1.27}$$

and Eq. 1.25 thus becomes

$$F_y = m_h \ddot{h} + S\left(\ddot{\theta}\cos\theta - \dot{\theta}^2 \sin\theta\right) + D_h \dot{h} + k_h h \,, \tag{1.28}$$

where D_h is now the sum of two different contributions:

$$D_h = D_{h,\text{e}} + D_{h,\text{v}} \,, \tag{1.29}$$

the desired energy sink ($D_{h,\text{e}}$), which corresponds to the energy that could be converted into electricity by an electric generator, and the undesired viscous friction ($D_{h,\text{v}}$).

Unlike the fully-constrained flapping-foil turbine concept, the only control over the foil motions allowed by the fully-passive concept is through the values of the different governing structural parameters. Indeed, the heave and pitch motions result from the interaction of the foil with its elastic supports and the flow. In other words, they are the solutions of Eqs. 1.26 and 1.28. These passive motions can have different shapes that differ from pure sinusoids. In that context, the heave amplitude (H_0), the pitch amplitude (Θ_0) and the phase lag between the heave and the pitch motions (ϕ) are respectively defined as:

$$H_0 = \frac{h_{\max} - h_{\min}}{2} \,, \tag{1.30}$$

$$\Theta_0 = \frac{\theta_{\max} - \theta_{\min}}{2} \,, \tag{1.31}$$

$$\phi = \frac{360}{T}\left(t_{\theta_{\max}} - t_{h_{\max}}\right) \quad \text{[degrees]} \,, \tag{1.32}$$

where $h_{\max}$, $h_{\min}$, $\theta_{\max}$ and $\theta_{\min}$ are the maximum and minimum heave and pitch positions reached during a given foil oscillation and $t_{\theta_{\max}}$ and $t_{h_{\max}}$ are the instants at which the maximum pitch and heave positions are reached during this specific foil oscillation. The motions are also characterized by their frequency, which is the same in heave and in pitch for cases that are suitable for a turbine application. This will be discussed in more details in Paper III.

Using the same procedure described above, equations for the power coefficients can be obtained from Eqs. 1.25 and 1.26:

$$\langle C_{P_h} \rangle + \langle C_{P_{m_h}} \rangle + \langle C_{P_{S,h}} \rangle + \langle C_{P_{D_h}} \rangle + \langle C_{P_{k_h}} \rangle = \langle C_{P_{\text{gen}}} \rangle \,, \tag{1.33}$$

$$\langle C_{P_\theta} \rangle + \langle C_{P_{I_\theta}} \rangle + \langle C_{P_{S,\theta}} \rangle + \langle C_{P_{D_\theta}} \rangle + \langle C_{P_{k_\theta}} \rangle \rangle = 0 \,, \tag{1.34}$$

where:

$$\langle C_{Pk_h} \rangle = \frac{1}{T} \int_{t_i}^{t_i+T} \left(\frac{-k_h \, h \, \dot{h}}{0.5 \, \rho \, U_\infty^3 \, b \, c} \right) dt \,, \tag{1.35}$$

$$\langle C_{Pk_\theta} \rangle = \frac{1}{T} \int_{t_i}^{t_i+T} \left(\frac{-k_\theta \, \theta \, \dot{\theta}}{0.5 \, \rho \, U_\infty^3 \, b \, c} \right) dt \,. \tag{1.36}$$

As will be shown in this thesis, periodic motions can still be obtained with a fully-passive flapping-foil turbine even though they are not prescribed. When this is the case, Eq. 1.19 holds true and the terms $\langle C_{Pk_h} \rangle$ and $\langle C_{Pk_\theta} \rangle$ vanish like $\langle C_{P_{m_h}} \rangle$ and $\langle C_{P_{I_\theta}} \rangle$ because they are also conservative. As a result, the power coefficient at the generator is still given by Eq. 1.21. When the electric generator is modeled as a linear damper, it becomes:

$$\langle C_{P_h} \rangle + \langle C_{P_\theta} \rangle + \langle C_{P_{D_{h,\text{v}}}} \rangle + \langle C_{P_{D_\theta}} \rangle = \langle C_{P_{\text{gen}}} \rangle \,, \tag{1.37}$$

with:

$$\langle C_{P_{\text{gen}}} \rangle = \langle C_{P_{D_{h,\text{e}}}} \rangle \,, \tag{1.38}$$

and:

$$\langle C_{P_{D_{h,\text{e}}}} \rangle = \frac{1}{T} \int_{t_i}^{t_i+T} \left(\frac{-D_{h,\text{e}} \, \dot{h}^2}{0.5 \, \rho \, U_\infty^3 \, b \, c} \right) dt \,, \tag{1.39}$$

$$\langle C_{P_{D_{h,\text{v}}}} \rangle = \frac{1}{T} \int_{t_i}^{t_i+T} \left(\frac{-D_{h,\text{v}} \, \dot{h}^2}{0.5 \, \rho \, U_\infty^3 \, b \, c} \right) dt \,. \tag{1.40}$$

Eq. 1.23 can still be used to compute the hydrodynamic efficiency in the case of a fully-passive flapping-foil turbine. However, while the friction does not affect the prescribed motions of a fully-constrained flapping-foil turbine because the resistive force of the electric generator (F_{gen}) can be controlled accordingly, it does affect the motions of a fully-passive turbine, hence also affecting the values of $\langle C_{P_h} \rangle$ and $\langle C_{P_\theta} \rangle$. Consequently, Eq. 1.23 does not maintain the same level of generality for different mechanical designs of fully-passive turbines. Moreover, the difference between the efficiencies defined by Eqs. 1.22 and 1.23 is not only related to the presence of undesired friction when the motions are not periodic. Because of that, the efficiency defined by Eq. 1.22 is more often used in the literature to characterize the power extraction performance of fully-passive turbines than the hydrodynamic efficiency. Unless otherwise indicated, the efficiency defined by 1.22 is used in this thesis.

1.3 Dimensionless form of the governing equations

The fluid dynamics pertaining to the study of hydrokinetic turbines is governed by the incompressible Navier-Stokes equations (see e.g. Panton (2013)):

$$\nabla \cdot u = 0 \,, \tag{1.41}$$

$$\frac{\partial u}{\partial t} + u \cdot \nabla u = -\frac{1}{\rho}\nabla p + \frac{1}{\nu}\nabla^2 u \,, \tag{1.42}$$

where u is the velocity vector, ρ is the fluid density, p is the pressure and ν is the kinematic viscosity of the fluid.

Using appropriate reference scales for length (L_{ref}), velocity (U_{ref}), time (t_{ref}) and pressure (p_{ref}):

$$L_{\text{ref}} = c \,, \tag{1.43}$$

$$U_{\text{ref}} = U_\infty \,, \tag{1.44}$$

$$t_{\text{ref}} = L_{\text{ref}}/U_{\text{ref}} = c/U_\infty \,, \tag{1.45}$$

$$p_{\text{ref}} = \rho\, U_\infty^2 \,, \tag{1.46}$$

where c is the chord length and U_∞ is the freestream velocity, Eqs. 1.41 and 1.42 can be written in dimensionless form:

$$\nabla \cdot u^* = 0 \,, \tag{1.47}$$

$$\frac{\partial u^*}{\partial t^*} + u^* \cdot \nabla^* u^* = -\nabla^* p^* + \frac{1}{\text{Re}}\nabla^{*2} u^* \,. \tag{1.48}$$

The superscript $*$ indicates a dimensionless variable (e.g. $t^* = t/t_{\text{ref}}$) and Re is the Reynolds number:

$$Re = \frac{U_\infty c}{\nu} \,. \tag{1.49}$$

Considering also the following reference scales for the hydrodynamic force component in the heave direction ($F_{y\,\text{ref}}$) and the hydrodynamic moment about the pitch axis (M_{ref}):

$$\theta_{\text{ref}} = 1 \,, \tag{1.50}$$

$$F_{y\,\text{ref}} = \frac{1}{2}\rho\, U_\infty^2\, b\, c \,, \tag{1.51}$$

$$M_{\text{ref}} = \frac{1}{2}\rho\, U_\infty^2\, b\, c^2 \,, \tag{1.52}$$

where b is the span length, the equations of motion of the fully-passive turbine can also be written in a dimensionless form:

$$C_{F_y}/2 \;=\; m_h^*\,\ddot{h}^* \;+\; S^*\left(\ddot{\theta}^*\cos\theta - \dot{\theta}^{*2}\sin\theta\right) + D_h^*\,\dot{h}^* \;+\; k_h^*\,h^* \,, \tag{1.53}$$

$$C_M/2 \;=\; I_\theta^*\,\ddot{\theta}^* \;+\; S^*\ddot{h}^*\cos\theta \;+\; D_\theta^*\,\dot{\theta}^* \;+\; k_\theta^*\,\theta \,, \tag{1.54}$$

where:

$$C_{F_y} = \frac{F_y}{0.5\,\rho\,U_\infty^2\,b\,c}\ ,\quad C_M = \frac{M}{0.5\,\rho\,U_\infty^2\,b\,c^2}\ ,\quad m_h^* = \frac{m_h}{\rho\,b\,c^2}\ ,\quad I_\theta^* = \frac{I_\theta}{\rho\,b\,c^4}\ ,\quad S^* = \frac{S}{\rho\,b\,c^3}\ ,$$

$$D_h^* = \frac{D_h}{\rho\,U_\infty\,b\,c}\ ,\quad D_\theta^* = \frac{D_\theta}{\rho\,U_\infty\,b\,c^3}\ ,\quad k_h^* = \frac{k_h}{\rho\,U_\infty^2\,b}\ ,\quad k_\theta^* = \frac{k_\theta}{\rho\,U_\infty^2\,b\,c^2}\ ,$$

$$h^* = \frac{h}{c}\ ,\quad \dot{h}^* = \frac{\dot{h}}{U_\infty}\ ,\quad \ddot{h}^* = \frac{\ddot{h}\,c}{U_\infty^2}\ ,\quad \dot{\theta}^* = \frac{\dot{\theta}\,c}{U_\infty}\ ,\quad \ddot{\theta}^* = \frac{\ddot{\theta}\,c^2}{U_\infty^2}\ .$$

The same reference scales are also used to normalize the heave amplitude:

$$H_0^* = \frac{H_0}{c}\ , \tag{1.55}$$

and the frequency of the motion to obtain what we refer to as the reduced frequency:

$$f^* = \frac{f\,c}{U_\infty}\ . \tag{1.56}$$

Note that the pitch amplitude defined according to Eq. 1.31 is already dimensionless since a reference scale of one is used for θ (see Eq. 1.50).

This normalization is the same as the one used by Veilleux and Dumas (2017) and is analogous to that used by Onoue et al. (2015) and by Shiels et al. (2001) for their respective study of an elastically-supported pitching flat plate and a cylinder undergoing vortex-induced vibrations (VIV). Unlike other traditional normalizations relying on the concept of natural frequency for the reference time scale, the current normalization remains valid for any value of the inertial and stiffness properties characterizing the elastically-supported foil, including zero.

1.4 Literature review

1.4.1 Proposed turbine concepts

The fully-constrained flapping-foil turbine was first investigated experimentally by McKinney and DeLaurier (1981). Several other studies on a similar device have followed covering various aspects of the technology such as the 3D effects (Kinsey and Dumas, 2012b; Deng et al., 2014; Kim et al., 2017), the blockage effects (Gauthier et al., 2016), the impact of using non-sinusoidal motions (Deng et al., 2014), multiple-foil configurations (Kinsey et al., 2011; Kinsey and Dumas, 2012a), the relation between the wake instability and the energy-extraction performance (Zhu, 2011) and the vorticity dynamics in the wake (Boudreau and Dumas, 2017b). The interested reader is referred to the comprehensive review papers on the flapping-foil turbine concept conducted by Young et al. (2014) and by Xiao and Zhu (2014) for more information. According to these reviews, high hydrodynamic efficiencies (see Eq. 1.23) exceeding 40% are usually obtained for reduced frequencies ranging between 0.10 and 0.25, with large pitch amplitudes ($\approx 70-95°$), a heave amplitude of about one chord length and a phase lag of about 90° between the heave and the pitch motions when the pitch axis is located at the

third-chord point ($x_p/c = 1/3$). This phase lag between the heave and the pitch motions is a critical parameter because it is responsible for the timing between the hydrodynamic force component acting on the foil in the heave direction and the heave velocity. A suitable phase lag results in maximum forces and velocities occurring at the same time, thereby maximizing the energy extraction from the flow.

In addition to the fully-constrained flapping-foil turbine concept, there are several different designs of flapping-foil turbines making use of passive motions that have been considered in the literature. Young et al. (2013) investigated the possibility of linking both the pitch and the heave motions to a flywheel, which is itself connected to a linear damper that models the energy extraction. Consequently, the shapes and amplitudes of the heave and pitch motions and the phase lag between them are constrained, but the frequency is not. Nonetheless, the frequency is necessarily the same for both motions. This turbine concept resulted in interesting efficiencies reaching 30%. However, such a device is not much simpler than a fully-constrained turbine since both a coupling mechanism between the heave and the pitch motions and a slider-crank mechanism converting the reciprocating heave motion into a rotational motion are still needed. Nevertheless, no controller is used and a simple energy-conversion device could be used since no energy input is required throughout the foil oscillations. In the case of a fully-constrained turbine, the electric generator usually has to act as an actuator during a fraction of the foil oscillations. Young et al. (2013) referred to their concept as a fully-passive turbine but this definition differs from the definition proposed in this thesis. Indeed, we define a fully-passive turbine as a turbine for which the shapes, the amplitude and the frequencies of both motions as well as the phase lag between them are all unconstrained.

The most studied flapping-foil turbine configuration making use of passive motions involves fewer constraints. It consists in an elastically-mounted blade in heave with a prescribed pitch motion (Shimizu et al., 2008; Zhu et al., 2009; Zhu and Peng, 2009; Abiru and Yoshitake, 2011, 2012; Huxham et al., 2012; Wu et al., 2014; Deng et al., 2015; Sitorus et al., 2015; Wu et al., 2015; Teng et al., 2016; Derakhshandeh et al., 2016; Griffith et al., 2016; Zhan et al., 2017; Chen et al., 2018). In other words, the shape, the amplitude and the frequency of the pitch motion of such a turbine are constrained while the heave motion characteristics as well as the phase lag between both motions are free. Obviously, the amount of power extracted from the flow must necessarily overcome the power required to drive the prescribed pitch motion if the turbine is to generate electricity. Efficiencies of the order of 30% and 20% have respectively been obtained from two-dimensional (2D) numerical simulations (Deng et al., 2015; Teng et al., 2016) and experiments (Abiru and Yoshitake, 2011, 2012; Huxham et al., 2012) for this semi-passive turbine. Although this concept is simpler than the fully-constrained flapping-foil turbine because no coupling mechanism is required between the heave and the pitch motion, it needs a motor in pitch along with a control system to adequately prescribe this motion. As pointed out by Zhu (2012), this therefore results in a more complex device than the fully-passive alternative.

Peng and Zhu (2009) were the first to consider a fully-passive flapping-foil turbine. Through 2D numerical simulations using a Navier-Stokes solver, they studied the dynamics of a foil attached to a

torsional spring in pitch and a linear damper in heave and assumed that the mass and inertia of the foil were negligible. The resulting equations of motion are therefore greatly simplified compared to the more general ones presented in this thesis (see Eqs. 1.25 and 1.26). For a given freestream flow, they observed four different responses of the foil depending on the values of the structural parameters characterizing the foil and its supports. Among these four responses, only one is suitable for a stable energy extraction. It is characterized by periodic heave and pitch motions of large amplitudes, which leads to efficiencies reaching 20% and power coefficients at the generator of about 0.3. The other observed responses are either irregular, thus negatively affecting the predictability and the controllability of the energy extraction, or damped, meaning that the foil remains steady at its equilibrium position and does not extract any energy from the flow. Peng and Zhu (2009) also showed that the interesting periodic responses are insensitive to the initial conditions unlike the irregular ones. As pointed out by the authors, this suggests that an accurate prediction of the foil dynamics is crucial since even small variations of the structural parameter values, from those characterizing an efficient turbine, could lead to potentially hazardous irregular motions or to a significant reduction of the amount of energy extracted.

Zhu (2012) used the same methodology than Peng and Zhu (2009), except that he also considered the presence of shear in the freestream flow and a spring in heave to prevent the continuous transverse shifting of the foil mean position in heave. He found that the presence of shear does not significantly affect the best fully-passive turbine performance, but it results in the creation of two new types of irregular motions. More importantly, it affects the size of the region covered by the interesting large-amplitude periodic motions in the parametric space. Indeed, this region is significantly broadened when a small shear rate is present in the oncoming flow compared to a uniform oncoming flow. However, this interesting region almost disappears as the shear rate is further increased. This suggests that one should carefully choose the sites where fully-passive flapping-foil turbines will be deployed.

Veilleux (2014); Veilleux and Dumas (2017) and Wang et al. (2017) studied a more general version of the fully-passive flapping-foil turbine than Peng and Zhu (2009) and Zhu (2012) by considering springs and dampers for both degrees of freedom even though the energy is only extracted from the heave motion. The general equations of motion solved by Veilleux (2014); Veilleux and Dumas (2017) actually correspond to Eqs. 1.25 and 1.26, except for a different sign convention used for θ. The power dissipated through the damper connected to the pitch motion is considered to be lost as heat and thus does not contribute to the electricity generation. In the works of Veilleux (2014) and Veilleux and Dumas (2017), the position of the pitch axis was fixed at the third-chord point ($x_p/c = 1/3$). The effects of varying the seven remaining dimensionless structural parameters (m_h^*, I_θ^*, S^*, D_h^*, D_θ^*, k_h^* and k_θ^*) were investigated. As in the works of Peng and Zhu (2009) and Zhu (2012), Veilleux (2014) and Veilleux and Dumas (2017) observed different responses of the foil including periodic motions with large amplitudes. Following a brief optimization process, they obtained an efficiency of 29.1% and a power coefficient at the generator of 0.935. The corresponding hydrodynamic efficiency and power coefficient at the generator are respectively equal to 33.6% and 1.079. They pointed out that

an adequate timing between the pitch and the heave motions is crucial for this turbine technology, as in the case of the fully-constrained flapping-foil turbine concept (Xiao and Zhu, 2014; Young et al., 2014). The difference is that the phase lag between the heave and the pitch motions cannot be enforced in the case of the fully-passive flapping-foil turbine concept, but rather results from the fluid-structure interaction.

1.4.2 Prototypes

A turbine prototype mounted on a pontoon boat was tested by Kinsey et al. (2011) and the maximum hydrodynamic efficiency they obtained was estimated as being equal to about 40% for a dual-hydrofoil turbine in tandem configuration. While this work confirmed the great potential of the fully-constrained flapping-foil turbine technology, it also revealed the great complexity of the mechanisms needed to link both oscillatory motions and to convert them to a rotating motion for the electric generator. The hydrodynamic efficiency estimation was obtained by subtracting the estimated mechanical losses in the system up to the gearbox where the torque measurements were made. These losses were found to correspond to at least 25% of the average power extracted. A second generation prototype was designed by the same research group with the aim of reducing these mechanical losses but it did not reach the expectations (Kinsey, 2015). As mentioned in the introduction, the complexity of the mechanism linking both degrees of freedom to the generator is one of the main drawback of the fully-constrained version of the flapping-foil turbine.

A few semi-passive flapping-foil turbine prototypes, with a passive heave motion and a prescribed pitch motion, have been built and tested. Abiru and Yoshitake (2011, 2012) designed such a turbine with an eddy-current brake, which acts as a linear damper, to model the presence of an electric generator. The damping coefficient could be varied by shifting the position of three pairs of neodymium magnets with respect to a copper plate sliding between them without making contact. They tested their turbine prototype in a water channel and reported an efficiency reaching 22% at a Reynolds number of about 90 000. Using similar facilities and at the same Reynolds number, Sitorus et al. (2015) tested a semi-passive turbine with a pitch axis perpendicular to the gravitational acceleration so that the buoyancy of the blade had an effect on its dynamics. They used a non-sinusoidal pitch motion and an unidirectional gearbox to convert the reciprocating heave motion into a one-direction rotational motion. The presence of the generator was simulated by applying a constant resistive torque, thus corresponding to a nonlinear damping coefficient. Unfortunately, they obtained very modest efficiencies below 4%.

Huxham et al. (2012) tested a semi-passive flapping-foil turbine with a prescribed pitch motion and a passive angular heave motion since the blade was attached to a lever arm. They obtained an efficiency of 23.8% during their tests in a water tunnel at a Reynolds number of 45 000. The first ever flapping-foil turbine developed by the industry was also a semi-passive turbine with a prescribed pitch motion and a similar angular heave motion. This full-scale prototype called *Stingray* was developed by the company Engineering Business Ltd. and was expected to produce 150 kW (Stingray, 2002). However,

it did not reach the expectations. This failure was later attributed to the fact that they had based their design on a quasi-steady approach to estimate the hydrodynamic force, which led them to use small pitch amplitudes (Xiao and Zhu, 2014; Young et al., 2014).

Lastly, fully-passive flapping-foil prototypes have also been built and tested by a few different research groups, but these works did not focus on the energy extraction performance of the device (e.g. Amandolese et al. (2013); Dimitriadis and Li (2009); Pigolotti et al. (2017); Poirel and Mendes (2014); Šidlof et al. (2016)).

1.4.3 Dynamic stall and leading-edge vortices

The lift of a static foil is known to increase with the angle of attack (α) until a critical angle is reached, above which it suddenly decreases due to the separation of the boundary layers near the leading edge of the foil (Anderson, 1991). This phenomenon is known as stall. For a thin symmetric foil profile, the moment about the quarter-chord point is around zero when the angle of attack is below its critical value, but it becomes negative for larger angles of attack. The occurrence of stall also results in a sudden increase of the drag.

When the flow is unsteady in the foil reference frame, either due to a motion of the foil or to variations of the upstream flow, the relation between the forces and moment acting on the foil and the angle of attack can significantly differ from the steady behavior. In particular, the foil can temporarily reach much higher lift coefficients at large angles of attack before utimately stalling. This phenomenon is known as dynamic stall. Qualitative representation of typical evolutions of the lift, drag and moment coefficient as functions of the angle of attack are shown in Fig. 1.2 for a pitching foil. First, it shows that the lift exceeds its maximum static value at angles of attack beyond the static stall angle. This is due to a delay in the boundary layers separation and the suction associated to a vortex formed near the leading edge of the foil (Corke and Thomas, 2015). This leading-edge vortex (LEV), is also responsible for the large negative moment coefficient observed. Moreover, Fig. 1.2 shows that the unsteadiness results in a significant hysteresis for the force and moment coefficients, which in turn leads to a negative aerodynamic damping. In other words, this means that a net amount of energy is transferred from the flow to the foil when it undergoes a cyclic pitch motion. Under such conditions, a self-sustained pitch motion can therefore occur. Similar phenomena are observed for a foil undergoing a cyclic heave motion or a combined pitch-heave motion. It is worth noting that the above discussion only presents a general overview of the effects of unsteadiness. Dynamic stall is a complex phenomenon that depends on several parameters, including the frequency and the amplitude of the foil motion as well as the characteristics of the freestream flow. More detailed information on this matter is provided in the works of Corke and Thomas (2015), McCroskey (1981, 1982) and Lee and Gerontakos (2004).

Dynamic stall and the associated formation of leading-edge vortices (LEVs) is known to play a crucial role regarding the performance of fully-constrained flapping-foil turbines (Kinsey and Dumas,

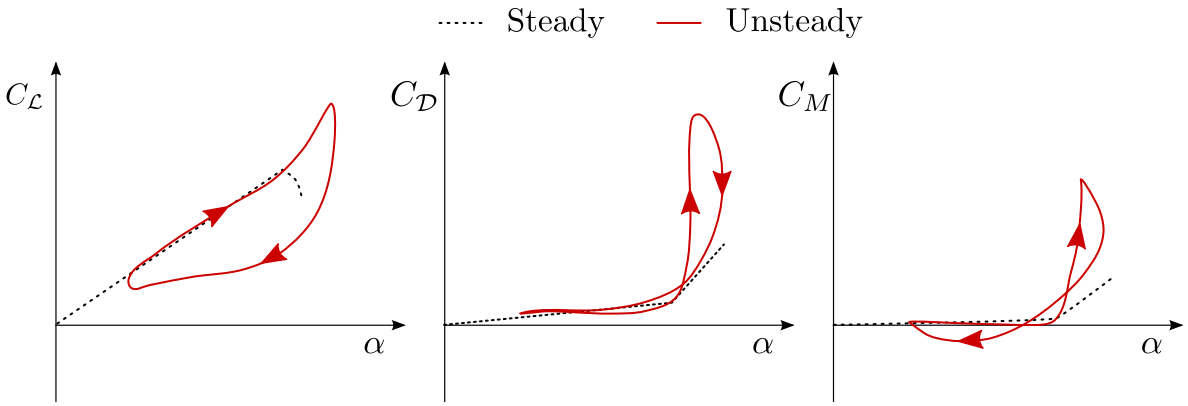

Figure 1.2: Qualitative representation of typical evolutions of the lift, drag and moment coefficient about the quarter-chord point as functions of the angle of attack for a steady foil and a pitching foil. The sign convention illustrated in Fig. 1.1 is used so that the angle of attack and the moment coefficient are positive in the counterclockwise direction. This figure is inspired from the work of Corke and Thomas (2015).

2008; Young et al., 2014). For example, the comprehensive parametric study carried out by Kinsey and Dumas (2008) showed that the enhanced force in the heave direction resulting from the LEVs positively contribute to the power extraction from the flow when the timing between its formation and the foil motions is adequate. The best hydrodynamic efficiencies (see Eq. 1.23) they achieved, with a maximum of 34%, have been obtained with LEVs. This work was carried out at a low Reynolds number of the order of 1 000, as for the majority of the studies devoted to the flapping-foil turbine in the literature (Young et al., 2014). Such a low Reynolds number is not representative of the operation of a full-scale turbine. Since dynamic stall and the formation of LEVs are both related to the robustness of the boundary layers, these phenomena are sensitive to the Reynolds number.

Kinsey and Dumas (2014) performed a parametric study similar to their previous one (Kinsey and Dumas, 2008), but at a much larger Reynolds number of 500 000, which is of the same order as the one characterizing the operation of the fully-constrained turbine prototype tested by the same research group (Kinsey et al., 2011). They found that the efficiency is maximized when no LEVs are formed, unlike what they had previously observed at a Reynolds number of 1 000 (Kinsey and Dumas, 2008). In fact, the maximum efficiency obtained at a Reynolds number of 500 000 is 43% without LEVs and around 35% with LEVs. Note that the absence of LEVs does not mean that the unsteadiness of the flow in the foil reference frame is not important since angles of attack of the order of 30°, largely above the static stall angle, are still reached for the optimal cases with no LEVs.

Understanding the effects of LEVs in the case of flapping-foil turbines with passive motions is far from trivial and much remains unknown in that regard. They are expected to play an even more important role in those cases than for fully-constrained flapping-foil turbines because of the coupling between the foil motions and the hydrodynamic force and moment. This coupling is not present for fully-constrained turbines because the resistive force of the electric generator (F_{gen}) can be adjusted

to maintain the same desired heave and pitch motions even when the presence of LEVs affects the hydrodynamic force and moment.

Studies conducted on a semi-passive flapping-foil with a passive heave motion, operating at a Reynolds number of 1 000, have confirmed the crucial role of the LEVs regarding the foil dynamics (Zhu and Peng, 2009; Deng et al., 2015). Zhu and Peng (2009) found that LEVs can both positively or negatively contribute to the overall power-extraction performance of the turbine depending on the timing between the formation of the LEVs and the foil motions. Like Kinsey and Dumas (2008), they observed that the increase of the hydrodynamic force component in the heave direction stemming from the suction associated to the presence of a LEV can result in a larger amount of power extracted from the flow when this increase is well synchronized with the heave velocity. Zhu and Peng (2009) also showed that the LEVs can generate a moment about the pitch axis in the same direction as the pitch velocity when the pitch velocity is maximum, hence positively contributing to the power extraction. However, this contribution remains small compared to that related to the heave motion.

If the positive contribution to the power extraction stemming from the LEVs observed by Kinsey and Dumas (2008) and Zhu and Peng (2009) is such that the pitch motion does not require power on average during one complete cycle ($\langle C_{P_\theta} \rangle > 0$), we can expect that a passive self-sustained pitch motion is feasible. This is indeed what Veilleux and Dumas (2017) observed with their optimal fully-passive turbine case. Wang et al. (2017) and Peng and Zhu (2009) also demonstrated the importance of the LEVs for fully-passive turbines, but these two studies were conducted at low Reynolds numbers, namely 400 and 1 000 respectively. In comparison, the study of Veilleux and Dumas (2017) was carried out at a Reynolds number of 500 000. The hydrodynamic efficiency of the optimal operating point obtained by Veilleux and Dumas (2017), namely 33.6%, is of the same order as the best efficiency obtained by Kinsey and Dumas (2014) for a fully-constrained flapping-foil turbine operating at the same Reynolds number and with LEVs ($\approx 35\%$). Based on the results of Kinsey and Dumas (2014) regarding fully-constrained cases without LEVs, higher efficiencies could potentially be obtained with passive motions if such a turbine could also operate without LEVs.

1.4.4 Inertial effects

When the prescribed heave and pitch motions are periodic, which is usually the case, the metrics computed from cycle-averages, such as the efficiency and the various cycle-averaged power coefficients, are independent of the mass and the moment of inertia of the turbine blade because the corresponding terms in the equations of motion in heave and in pitch (see Eqs. 1.1 and 1.2) are conservative. However, the instantaneous values of the different terms appearing in these equations of motion, including the instantaneous resistive force of the electric generator (F_{gen}), are affected by these two inertial parameters. This means that in order to maintain the same desired prescribed motions for different masses and moments of inertia, the resistive force of the electric generator (F_{gen}) must be adjusted accordingly.

Such a control is not possible with passive motions and they are therefore expected to be affected by variations of the mass and moment of inertia. Yet, only a few studies on flapping-foil turbines with passive motions have investigated these effects. Actually, a few studies even neglected these inertial effects by considering a massless foil for a semi-passive flapping-foil turbine with a passive heave motion and a prescribed pitch motion (e.g. Zhu et al. (2009) and Zhu and Peng (2009)) or a fully-passive flapping-foil turbine (e.g. Peng and Zhu (2009) and Zhu (2012)).

The influence of the mass of the foil has been assessed by Deng et al. (2015) for a semi-passive flapping-foil turbine with an elastically-supported foil in heave with a damper, modeling an electric generator, but no spring. The pitch motion was prescribed and the turbine operated at a Reynolds number of 1 000. Deng et al. (2015) varied the ratio between the density of the foil and the fluid density from 0.125 to 100, while keeping the damping coefficient constant. It translates into dimensionless heaving masses[2] (m_h^*) ranging from about 0.01 to 10. The efficiency was found to decrease linearly from the smallest mass tested to $m_h^* \approx 4$, followed by a more gradual decrease for larger mass values. They attributed this behavior to a continuous decrease of the phase lag between the heave and the pitch motions (ϕ) as m_h^* is increased. However, the power coefficient was found to be less sensitive to variations of the heaving mass, as long as m_h^* remains below 1, because the increase of overall extent of the foil motion is compensating for the efficiency decrease.

Zhu (2012) investigated the effects of the mass and the moment of inertia for a fully-passive flapping-foil turbine at the same Reynolds number of 1 000. He tested two different values of the ratio between the density of the foil and the fluid density, corresponding to $m_h^* \approx 0.1$ and $m_h^* \approx 1$. Three different idealized cases were tested for the moment of inertia by considering that the mass is concentrated at the pitch axis, at the mid-chord point or at the leading edge. Zhu (2012) observed an increase of the efficiency with an increase of the moment of inertia. He attributed this result to a decrease of the oscillation frequency and an increase of the pitch amplitude. However, he did not present the equations of motion that were solved for the foil having nonzero mass and moment of inertia. More specifically, he did not mentioned if gravity was acting in the direction of the motions or not and if the inertial coupling terms, which arise when the pitch axis and the center of mass does not coincide, were considered.

The mass and the moment of inertia have also been varied by Veilleux and Dumas (2017) when optimizing a fully-passive flapping-foil turbine at a Reynolds number of 500 000. However, these variations remained small and were accompanied with variations of all the other governing structural parameters, thereby making it difficult to discriminate the effects of these two inertial parameters from the effects of the other structural parameters. Veilleux (2014) presented a more systemic study of the inertial effects in his master thesis by varying each parameter independently around their optimal case characterized by $m_h^* = 3.036$ and $I_\theta^* = 0.095$. When increasing m_h^* from about 2 to 6, they found that the heave amplitude is continuously increasing with the heaving mass while the pitch

[2]For a NACA0015 profile, the dimensionless heaving mass (m_h^*) per unit span length is approximately equal to the ratio between the density of the foil and the fluid density divided by 9.7.

amplitude is less affected. The efficiency rather decreases when the dimensionless heaving mass is either increased or decreased from the value characterizing the optimal case. The same trend has also been observed for the frequency of the motions. Unfortunately, Veilleux (2014) did not present the effects of varying the heaving mass on the phase lag between the heave and the pitch motions (ϕ). Regarding the dimensionless moment of inertia (I_θ^*), he found that the efficiency, the heave and pitch amplitudes and the frequency were all varying by less than 2% when I_θ^* is varied between 0.065 and 0.13. Veilleux (2014) and Veilleux and Dumas (2017) used an explicit fluid-structure coupling algorithm (weak coupling), which prevented them from investigating cases with very low mass and moment of inertia values.

1.4.5 Pitch axis and center of mass locations

The effects of varying the position of the pitch axis (x_p/c) was investigated by Davids (1999) for a fully-constrained flapping-foil turbine using an unsteady panel code. He found that the timing between the hydrodynamic force and the foil motions is strongly affected by this parameter. Consequently, the optimal phase lag between the heave and the pitch motions varies with x_p/c. It is above 90° when the pitch axis is located upstream of the third-chord point ($x_p/c < 1/3$) and below 90° when it is located downstream of the third-chord point ($x_p/c > 1/3$). However, Davids (1999) restricted his study to operating points with small effective angles of attack ($< 10°$) because of the limitations related to the use of a potential flow solver.

Kinsey and Dumas (2008) conducted numerical simulations, using a Navier-Stokes solver, of a fully-constrained flapping-foil turbine operating at a Reynolds number of 1 100 with three different pitch axis locations, namely the quarter-chord, the third-chord and the mid-chord points. By doing so, they confirmed that the timing between the hydrodynamic force and the foil motions is also affected by a variation of x_p/c when larger effective angles of attack are reached. Based on their results, they decided to position the pitch axis at the third-chord point for the rest of their work and for their following study conducted at a Reynolds number of 500 000 (Kinsey and Dumas, 2014).

The majority of the studies conducted on flapping-foil turbines making use of passive motions used a pitch axis located at the third-chord point (e.g. Chen et al. (2018); Deng et al. (2015); Teng et al. (2016); Veilleux and Dumas (2017); Wu et al. (2015)) or the quarter-chord point (e.g. Huxham et al. (2012); Sitorus et al. (2015)). Only a very few of them considered more than one position of the pitch axis.

Zhu and Peng (2009) tested different positions of the pitch axis, ranging from the leading edge to the trailing edge, for a semi-passive flapping-foil turbine with a foil that was elastically-supported in heave with a damper only (no spring) and a prescribed pitch motion. They found that the power coefficient at the generator and the efficiency are maximized when the pitch axis is located between $x_p/c = 0.3$ and $x_p/c = 0.4$, hence corroborating the choice of $x_p/c = 1/3$ used in most studies. They attributed this result to the fact that the power required to drive the pitch motion is minimal with these

positions of the pitch axis.

In the case of a fully-passive flapping-foil turbine, the same authors showed that the pitch axis location plays an important role regarding the foil stability (Peng and Zhu, 2009). As already mentioned in Sec. 1.4.1, they observed four completely different types of response. They found that the transition between the different responses depends on the position of the pitch axis and the pitch stiffness coefficient. For a given pitch stiffness coefficient and as the position of the pitch axis is shifted from the leading edge toward the trailing edge, the foil response is switching from a regime characterized by damped motions (the foil remaining steady at its equilibrium position), periodic motions leading to a significant energy extraction from the flow and two different types of irregular motions. Moreover, the transition between these different responses is shifted toward the trailing edge as the pitch stiffness coefficient is increased.

Unlike the results of Peng and Zhu (2009), Zhu and Peng (2009) and Zhu (2012), which were obtained with a massless foil, Wang et al. (2017) considered a fully-passive flapping-foil turbine with a foil having a nonzero mass operating at a Reynolds number of 400. They also observed different responses of the foil by varying the pitch axis location, with a fixed position of the center of mass. They obtained an optimal performance with $x_p/c = 0.35$. However, the general equations of motion of the fully-passive flapping-foil turbine concept (see Eqs. 1.25 and 1.26) show that the important parameter regarding the center of mass is its distance from the pitch axis (x_θ), not its position itself, since x_θ appears in the definition of the static moment (see Eq. 1.3). Consequently, Wang et al. (2017) were also varying the value of the static moment when testing different positions of the pitch axis. In fact, both the pitch axis location and the static moment are known to be important parameters regarding the stability of a flapping foil (Dowell, 2004; Fung, 2008). For example, two well-known aeroelastic instabilities, namely divergence and coupled-mode flutter, can respectively arise when the pitch axis is located downstream of the point of application of the hydrodynamic force and when the center of mass is located downstream of the pitch axis ($S > 0$). The interested reader is referred to the books of Fung (2008) and Dowell (2004) for more information on this subject.

Lastly, Veilleux (2014) investigated the importance of the static moment for a fixed pitch axis location ($x_p/c = 1/3$) using a previously obtained optimal case as a baseline. For this specific case, he found that it is best to keep the static moment close to zero to maximize the energy extraction.

1.4.6 Other types of aeroelastic energy harvesters

Semi-passive and fully-passive flapping-foil turbines are not the only possible aeroelastic energy harvesters. Other simple concepts have been proposed in the literature. The interested reader is referred to the review of Abdelkefi (2016) on this subject. For example, electricity can be generated when a piezoelectric material is connected to a flapping flag. However, the amount of power generated with such an apparatus is limited. It is therefore intended to be used for powering small electronic devices rather than providing electricity to an electrical grid.

Another popular concept is to connect an elastically-supported cylinder undergoing vortex-induced vibrations (VIVs) to an electric generator (e.g. Bernitsas et al. (2008)). While this one-degree-of-freedom (1-DOF) device is simpler than a 2-DOF fully-passive flapping-foil turbine, it is not as efficient. In fact, the maximum efficiency achieved with an idealized two-dimensional cylinder undergoing VIVs is of the order of 10% (Barrero-Gil et al., 2012; Paré-Lambert and Olivier, 2018)[3] compared to maximum reported efficiency of about 30% for the fully-passive flapping-foil turbine concept (Veilleux and Dumas, 2017). A fully-passive flapping-foil turbine can therefore either be seen as a simplified flapping-foil turbine or an elaborate aeroeslastic energy harvester.

1.4.7 The use of passive motions with flapping foils for propulsion

The idea of using a flapping-foil with passive motions has also been considered for propulsion purposes. A flapping-foil can achieve higher propulsive efficiencies than a foil undergoing a pure heave or a pure pitch motion (Mackowski and Williamson, 2017). However, actuating both degrees of freedom require mechanisms having the same level of complexity than those required to prescribe the motions of a fully-constrained flapping-foil turbine. A possible alternative is to use a semi-passive flapping-foil by actuating only one degree of freedom and elastically-supporting the other. Both the passive heave (Mackowski and Williamson, 2017) and the passive pitch (Thaweewat et al., 2018) versions have been tested. While Mackowski and Williamson (2017) reported a significant increase of the propulsive efficiency for a foil actuated in heave with a passive pitch motion compared to a pure heave motion, the efficiency remained far below the maximum efficiency that can be obtained when actuating both degrees of freedom.

Note that in order to generate thrust, a motor needs to provide power to the actuated degree of freedom. Consequently, it is impossible to generate thrust with a fully-passive flapping-foil since there is no way to provide power to the foil with this concept.

1.5 Objectives

Although the best hydrodynamic efficiencies reported for the fully-passive flapping-foil turbine concept ($\approx 30\%$) are smaller than those reported for the fully-constrained concept ($\approx 40\%$), the increased mechanical simplicity of the fully-passive device could justify its selection over the fully-constrained technology. However, several questions regarding the use of passive motions remain unanswered.

Flapping-foil turbines with passive motions operating at large Reynolds numbers have almost not been investigated so far, as pointed out by Zhu (2012) and Xiao and Zhu (2014). In fact, only Veilleux (2014); Veilleux and Dumas (2017) considered a Reynolds number above 100 000.

[3] This efficiency value is obtained using the definition presented in the work of Paré-Lambert and Olivier (2018) based on the overall transverse extent reached by any point on the surface of the cylinder. It is therefore consistent with the definition used in the present thesis.

Furthermore, there is a lack of experimental work on turbines with passive motions in the literature, especially regarding passive pitch motions. The efficiencies of the order of 30% reported for the fully-passive turbine have been obtained from numerical simulations in idealized conditions, i.e., often neglecting friction and considering a two-dimensional foil (infinite span). Moreover, it might be challenging to design a fully-passive turbine for which all the structural parameters match those characterizing the best reported numerical cases, while still remaining simple in terms of the mechanical design and being able to withstand the forces at play.

The parametric space characterizing the fully-passive turbine is vast and only a few regions have been explored. For instance, most of the studies conducted on semi-passive and fully-passive flapping-foil turbines have either considered a pitch axis coinciding with the center of mass (Abiru and Yoshitake, 2011, 2012; Deng et al., 2015; Griffith et al., 2016; Shimizu et al., 2008; Teng et al., 2016; Wu et al., 2014, 2015; Zhan et al., 2017), thereby not involving any inertial coupling between the heave and pitch degrees of freedom ($S = 0$), or even massless foils (Peng and Zhu, 2009; Zhu et al., 2009; Zhu and Peng, 2009; Zhu, 2012).

Besides, some flapping-foil turbine concepts have not even been considered yet. This is the case, for example, of a flapping-foil turbine with a prescribed heave motion and a passive pitch motion. Part of the interest in such a device lies in the fact that the electric generator is expected to be connected to the heave motion because most of the energy extracted by flapping-foil turbines comes from the heave motion (Kinsey and Dumas, 2008, 2014; Zhu, 2011). Consequently, the heave motion can be constrained while no pitch controller, no pitch actuator and no coupling mechanism between the heave and pitch degrees of freedom are required. This turbine concept is therefore simpler in terms of the mechanical design than the other already proposed semi-passive turbine alternative, with a passive heave motion and a prescribed pitch motion.

In addition to the practical interest in such a semi-passive turbine, it also provides a convenient way to improve our fundamental knowledge of the dynamics of passive pitch motions because the number of structural parameters affecting this turbine dynamics is reduced compared to the dynamics of the fully-passive flapping-foil turbine concept. This should therefore facilitate the process of finding optimal operating points.

Following these observations, the main objective of the present thesis can be summarized by the following question:

What is the power generation potential of flapping-foil turbines with passive motions and under which conditions an optimal performance can be achieved with such devices?

More specifically, the current study aims at:

1. Proving the feasibility and testing the power generation performance of the fully-passive concept experimentally;

2. Investigating the potential of the semi-passive turbine concept with a passive pitch motion;

3. Improving our understanding of the dynamics of passive pitch motions;

4. Using this new knowledge to optimize flapping-foil turbines with passive motions.

Note that the optimization of the design of the turbine structure as well as the circuitry required to convert the energy extracted from the flow into electricity is out of the scope of the current thesis, but should be considered in future studies.

1.6 Outline

This section outlines the content of the four papers forming the present thesis. The context and the main conclusions of each paper are repeated here even if they are already presented in the papers in order to better highlight the direction and coherence of the thesis. Note that the full papers are presented to ensure that they can be read individually without needing to read the whole thesis. I therefore apologize for the redundancy of some sections, especially regarding the introductions, the numerical methodology and the definitions of the performance metrics.

1.6.1 Paper I:

Experimental investigation of the energy extraction by a fully-passive flapping-foil hydrokinetic turbine prototype

Context and objective

A few research groups have already revealed the potential of the fully-passive flapping-foil turbine concept (Peng and Zhu, 2009; Zhu, 2012; Veilleux and Dumas, 2017; Wang et al., 2017) with maximum reported efficiencies of the order of 30%. However, their conclusions were only based on two-dimensional numerical simulations. Although some experiments have also been performed with fully-passive flapping foils (Amandolese et al., 2013; Pigolotti et al., 2017), the main focus of these studies were not directed toward power generation. The main objective of this paper therefore consists in designing, testing and evaluating the performance of a fully-passive flapping-foil turbine prototype.

Main conclusions

The experimental campaign has confirmed the feasibility and the potential of the fully-passive flapping-foil turbine concept. After releasing the blade in the water channel, a permanent response characterized by large heave and pitch amplitudes and nearly sinusoidal motions is quickly reached, namely after completing only about three foil oscillations. The periodicity and robustness of the motions are notable and a maximum efficiency of 31% has been achieved. The sensitivity of the turbine performance to seven structural and inflow parameters has been assessed, thereby revealing some valuable information for the design of fully-passive turbines.

The mechanism driving the fully-passive foil of this prototype is a divergence instability (Dowell, 2004; Fung, 2008). It is responsible for the rapid growth of the heave and pitch amplitudes following the release of the blade, which are limited by the occurrence of deep dynamic stall and the formation and ejection of strong leading-edge vortices (LEVs) for all the cases considered during the experimental campaign.

Other remarks

More information regarding the eddy-current brake, the calibration of the load cell used to calibrate the springs as well as the estimation of the uncertainties is provided in Appendix A.

The dimensionless equations of motion governing the fully-passive flapping-foil turbine prototype presented in this paper are slightly different than Eqs. 1.53 and 1.54 because Coulomb friction is considered.

The x-axis is reversed in Fig. 2.1 compared to Fig. 1.1 in order to be consistent with the photos and videos of the turbine prototype accompanying Paper I.

1.6.2 Paper II:

Investigation of the energy-extraction regime of a novel semi-passive flapping-foil turbine concept with a prescribed heave motion and a passive pitch motion

Context and objective

Although the results of the experiments presented in Paper I have confirmed that a fully-passive flapping-foil can extract a significant amount of power from the flow, the best performance obtained is still far from what can be achieved when constraining the foil motions to follow specific motions. For example, Kinsey and Dumas (2014) reported a maximum efficiency of 43.3% for a two-dimensional fully-constrained turbine operating at a Reynolds number of 500 000. They showed that the best efficiencies are achieved when the foil motions are such that no LEVs are formed, unlike what is generally accepted in the literature. Since the best efficiencies reported in Paper I as well as by Veilleux and Dumas (2017) were all obtained with strong LEVs, one may reasonably ask oneself if the performance of the fully-passive flapping-foil turbine concept could be improved by avoiding the formation and ejection of LEVs. The task of finding a set of structural parameters that would result in motions of the foil satisfying this is however not so simple, partly due to the large number of parameters influencing the foil dynamics.

A convenient way to reduce the number of parameters involved is to constrain one degree of freedom while leaving the other free. Since the heave motion is responsible for most, if not all, of the energy extracted from the flow, it is judicious to connect the electric generator to this degree of freedom and to constrain it with the use of a controller. In addition to facilitating the study of the passive pitch dynamics of a flapping-foil, it results in an innovative turbine concept which had never been considered so far. The objectives of this second paper are therefore to investigate the potential of this

new flapping-foil turbine concept as well as to increase our knowledge of the dynamics of passive pitch motions.

Main conclusions

The results showed that it is possible to avoid deep dynamic stall and the formation of LEVs with passive pitch motions. Under such conditions, a maximum efficiency of 45.4% was reached, thereby competing with the fully-constrained turbine concept in terms of performance, but with a simpler device. One of the keys to achieve this is to have the center of mass positioned downstream of the pitch axis, which is itself located at the quarter-chord point ($x_p/c = 0.25$). The reason is that the passive pitch motion requires energy on average to be sustained ($\overline{C_{P_\theta}} < 0$) in order to undergo the types of motions that maximize the turbine performance. In the case of a fully-constrained turbine, this energy is either transferred from the heave motion to the pitch motion through rigid links that mechanically couple both degrees of freedom together or via a motor in pitch. An alternative way of transferring energy to the pitch motion is needed when this degree of freedom is unconstrained (passive). This can be achieved with the inertial coupling between the heave and pitch degrees of freedom that arises when the static moment is not zero, i.e., when the center of mass does not coincide with the pitch axis. A positive static moment is required for the energy to be transferred from the heave motion to the pitch motion.

1.6.3 Paper III:

Free-pitching flapping-foil turbines with an imposed sinusoidal heave motion

Context and objective

Paper II demonstrated that the performance of a flapping-foil turbine with a passive pitch motion can match the best performance reported in the literature for fully-constrained turbines. It also proved the importance of the static moment to achieve this. However, this good performance was only obtained for a few precise sets of structural parameters and the influence of some important parameters were not investigated. More specifically, the position of the pitch axis and the moment of inertia were not varied and the pitch stiffness coefficient was set so that pitch natural frequency was matching the frequency of the prescribed heave motion for all the cases considered.

When designing and building such a semi-passive flapping-foil turbine, it may be challenging to match a specific set of structural parameters known to provide good results while also ensuring that it can withstand the forces at play and remains as simple and cheap as possible. This is especially true regarding the moment of inertia and the static moment. With that in mind, the objective of this third paper is to investigate how the findings of Paper II can be generalized. In other words, we look for the required ingredients to maintain an optimal performance for different sets of structural parameters and over a broad range of values.

Main conclusions

The moment of inertia and the pitch stiffness coefficient can be collapsed into a single effective parameter, which we refer to as the effective pitch stiffness, λ_θ^*:

$$\lambda_\theta^* = k_\theta^* - (2\pi f_\theta^*)^2 I_\theta^* \,. \tag{1.57}$$

because the passive pitch motion is nearly sinusoidal and its frequency is synchronized with the frequency of the prescribed heave motion for the cases achieving a positive efficiency. Actually, the pitch motion approaches a pure sinusoid as I_θ^* increases. This reduces the number of parameters affecting the foil dynamics and allows properly scaling the pitch stiffness coefficient for turbine designs with different moments of inertia. Indeed, the efficiency is essentially unaffected by variations of I_θ^* spanning two orders of magnitude when k_θ^* is adjusted accordingly. However, the efficiency decreases as I_θ^* approaches zero even when k_θ^* is properly scaled. This is because the pitch motion departs from a sinusoid under such circumstances, thereby violating the condition that leads to the derivation of the effective pitch stiffness λ_θ^*.

The results of this paper also show that an optimal turbine performance, with efficiencies exceeding 40%, can be obtained with different positions of the pitch axis, ranging from the leading edge to the three-quarter-chord point. The key is to maintain similar motions of the foil surface across the various pitch axis locations considered since this is what matters regarding the fluid dynamics. Recalling that the heave motion is the transverse motion of the pitch axis (y direction in Fig. 1.1), this implies that the phase lag between the heave and the pitch motion must vary with x_p/c. As the dynamics of the elastically-supported foil depends on the motion of the pitch axis along with the hydrodynamic force and moment acting at this point, the values of the structural parameters must vary with x_p/c in order to maintain specific motions of the foil surface. More specifically, the static moment value required when $x_p/c = 0.75$ is around zero and it increases as the pitch axis is shifted toward the leading edge. Regarding λ_θ^*, its optimal value is around zero when $x_p/c = 0.25$, below zero when $x_p/c < 0.25$ and above zero when $x_p/c > 0.25$. This implies that the frequency of the prescribed heave motion must be close to the pitch natural frequency when $x_p/c = 0.25$, larger than the pitch natural frequency when $x_p/c < 0.25$ and smaller than the pitch natural frequency when $x_p/c > 0.25$.

Other remarks

Additional results and discussions about the work presented in Paper III are given in Appendix B.

1.6.4 Paper IV:

A parametric study and optimization of the fully-passive flapping-foil turbine at high Reynolds number

Context and objective

With the newly gained knowledge from the results presented in Papers II and III, the fully-passive flapping-foil turbine concept is revisited in Paper IV in an attempt to match the performance obtained with the semi-passive concept analyzed in the previous two papers, but with an even simpler device. To that end, cases which are not subject to the divergence instability, but rather to the coupled-mode flutter instability, are considered. The idea of benefiting from the coupled-mode flutter instability as the driving mechanism for passive heave and pitch motions is corroborated by the results of Papers II and III, which have shown that a positive static moment is required to achieve high efficiencies when the pitch axis is upstream of the three-quarter-chord point. A positive static moment is indeed a required condition to trigger the classical coupled-mode flutter instability.

Besides looking for an optimal performance, the objective of this fourth paper is also to test the applicability of the inertial-stiffness scaling proposed in Paper III to characterize the heave and pitch dynamics of a fully-passive flapping-foil. Furthermore, the effect of having a nonzero pitch damping is investigated.

Main conclusions

The results prove that the fully-passive turbine concept can be as efficient as the best fully-constrained turbines reported in the literature. Actually, the maximum efficiency obtained in this work is 53.8%, which is even higher than the maximum efficiency of 43.3% reported by Kinsey and Dumas (2014) for a fully-constrained turbine.

For all the cases considered in this work, the foil oscillates at the same frequency in heave and in pitch, and it essentially follows the pitch natural frequency ($f^*_{n,\theta}$):

$$f^*_{n,\theta} = \frac{1}{2\pi}\sqrt{\frac{k^*_\theta}{I^*_\theta}}\,. \tag{1.58}$$

Since the passive heave motions are nearly sinusoidal, the heave dynamics can be effectively characterized with a parameter combining the heaving mass and the heave stiffness coefficient together, which is not the heave natural frequency. This effective parameter is analogous to the parameter λ^*_θ proposed in Paper III to characterize the pitch dynamics of the semi-passive turbine concept. We refer to it as λ^*_h:

$$\lambda^*_h = k^*_h - (2\pi f^*_h)^2 m^*_h\,. \tag{1.59}$$

However, λ^*_θ is inappropriate to characterize the pitch dynamics of the fully-passive flapping-foil even though the passive pitch motions are also nearly sinusoidal. The reason is that the frequency of the foil motions is altered when I^*_θ and k^*_θ are varied, unlike what is observed for the semi-passive turbine

concept. The other terms appearing in the equation of motion in pitch, namely the moment coefficient and the inertial coupling term, are thus affected by variations of I_θ^* and k_θ^*. As a result, the pitch dynamics of the fully-passive turbine is characterized by the pitch natural frequency instead of the parameter λ_θ^*. An optimal energy-extraction performance can be maintained over large ranges of values for m_h^* and I_θ^*, as long as k_h^* and k_θ^* are properly scaled to keep λ_h^* and $f_{n,\theta}^*$ constant.

The heave and pitch amplitudes as well as the efficiency considerably decrease when considering a nonzero pitch damping coefficient (D_θ^*). Beyond a critical value of D_θ^*, the motions are even completely damped and the foil returns to its equilibrium position no matter if large perturbations are used as the initial conditions. Nevertheless, the level of pitch damping present on a real turbine setup is expected to be small enough to avoid a significant decrease of the turbine performance.

Chapter 2

Paper I:
Experimental investigation of the energy extraction by a fully-passive flapping-foil hydrokinetic turbine prototype

2.1 Résumé

Des expériences ont été menées dans le but d'évaluer la performance d'une hydrolienne à aile oscillante complètement passive, pour laquelle les mouvements auto-induits et auto-maintenus de l'aile sont le résultat de l'interaction entre ses supports élastique (des ressorts et des amortisseurs) et l'écoulement. Des études numériques antérieures ont démontré qu'une telle hydrolienne peut extraire une quantité considérable d'énergie de l'écoulement tout en offrant la possibilité de simplifier les mécanismes complexes qui sont généralement requis pour contraindre et coupler les mouvements de tangage et de pilonnement dans le cas d'une hydrolienne à aile oscillante complètement contrainte conventionnelle. Suite à ces résultats prometteurs, un prototype a été conçu et testé dans un canal à un nombre de Reynolds basé sur la corde de 21 000. Des mouvements périodiques de grandes amplitudes ont été observés et ont mené à une efficacité et un coefficient de puissance atteignant respectivement 31% et 0.86. La sensibilité de la dynamique de la turbine à sept différents paramètres caractérisant la structure et l'écoulement a été évaluée expérimentalement autour d'un cas de référence performant. Les résultats ont révélé que la turbine maintient une bonne performance sur une large plage de paramètres.

2.2 Abstract

Experiments were conducted to assess the performance of a fully-passive flapping-foil hydrokinetic turbine for which the self-induced and self-sustained blade motions are resulting from the interaction

between the blade's elastic supports (springs and dampers) and the flow field. Previous numerical studies have shown that such a turbine can extract a substantial amount of energy from the flow while offering the possibility to simplify the complex mechanical apparatus generally needed to constrain and couple the blade pitching and heaving motions in the case of the conventional fully-constrained flapping-foil turbine. Based on these promising numerical investigations, a prototype was designed and tested in a water channel at a chord Reynolds number of 21 000. Robust and periodic motions of large amplitudes were observed leading to an energy harvesting efficiency reaching 31% and a power coefficient of 0.86. The sensitivity of the turbine dynamics to seven different structural and inflow parameters was evaluated experimentally around a baseline case achieving a high level of performance. It was found that the turbine maintains a good performance over a large range of parameters.

2.3 Introduction

The flapping-foil turbine concept is one of the various innovative and promising sources of clean and renewable energy that have received an increased attention during the last decade (Young et al., 2014; Xiao and Zhu, 2014). It consists in one or multiple blades undergoing both pitching (rotational) and heaving (translational) motions with a swept area that is perpendicular to the flow. Although it would also be possible for these turbines to extract energy from the wind, they have mostly been developed as hydrokinetic turbines, which extract energy from rivers or tidal currents. The flapping-foil turbine concept has proven to be competitive with the horizontal-axis and vertical-axis turbine technologies, with efficiencies exceeding 40% (Kinsey et al., 2011; Kinsey and Dumas, 2012, 2014; Young et al., 2014; Xiao and Zhu, 2014).

In order to reach such a good level of performance, the designers have, in the past, mechanically coupled and constrained the two motions through complex mechanisms, hence making the turbine a single-degree-of-freedom (1-DOF) device (McKinney and DeLaurier, 1981; Kinsey et al., 2011; Xu et al., 2017). This approach allows prescribing the amplitudes and the frequencies of the heaving and pitching motions as well as the phase lag between them. However, several issues can arise from this complexity. First, a significant amount of energy can be lost before being converted into electricity. For example, Kinsey et al. (2011) reported that 25% of the power extracted from the flow by their fully-constrained flapping-foil turbine was lost before reaching the electric generator due to the friction between the different moving components forming the coupling mechanism. Moreover, complex mechanical assemblies are usually prone to a higher risk of failure in addition to being more expensive.

Instead of optimizing the coupling mechanism, a more fundamental change has been proposed: the mechanism can simply be removed! One possible way to achieve this is to use an independent actuator for the pitching motion (Kim et al., 2017), making the concept a two-degree-of-freedom (2-DOF) turbine. Let us recall here that efficient flapping-foil turbines usually require only a small amount of energy to drive the pitching motion on a cycle-averaged basis, while the heaving motion accounts for the net energy extraction (Kinsey and Dumas, 2008, 2014; Zhu, 2011). Such a 2-DOF turbine

does not necessitate rigid mechanical links to couple the heaving and the pitching motions, but needs a dedicated actuator for the pitching motion, controllers for both degrees of freedom and an electric generator connected to the heaving motion. Moreover, the electric generator of such a turbine may need to act as an actuator at some instants during the turbine blade cycle in order to prescribe the desired heaving motion. Therefore, this motion-constrained strategy still results in a relatively complex apparatus.

Several authors proposed a simplification to the aforementioned 2-DOF version of the flapping-foil turbine by considering a free or passive heaving motion (Abiru and Yoshitake, 2011, 2012; Deng et al., 2015; Derakhshandeh et al., 2016; Griffith et al., 2016; Huxham et al., 2012; Shimizu et al., 2008; Sitorus et al., 2015; Teng et al., 2016; Wu et al., 2014, 2015; Zhan et al., 2017; Zhu et al., 2009; Zhu and Peng, 2009). More specifically, this scenario involves a blade that is elastically supported in heave instead of being connected to the turbine structure with rigid links. One consequence of this simplification is that the heaving motion cannot be prescribed, but rather solely relies on the interaction between the elastically-supported foil and the flow. The heaving motion is thus self-induced and self-sustained. Two-dimensional (2D) numerical studies (Deng et al., 2015; Teng et al., 2016) and experimental works (Abiru and Yoshitake, 2011, 2012; Huxham et al., 2012) reported efficiencies exceeding 30% and 20%, respectively. This "semi-passive" turbine concept does not need a controller in heave and a simpler form of energy-extracting device (generator) can be used. Indeed, since the heaving motion is free, the energy-conversion device never has to act as an actuator. It corresponds in this case to an energy sink throughout the turbine blade cycle. This device could still be an electric generator in order to convert the energy extracted from the flow into electricity, but other possibilities also arise, such as using the flapping-foil turbine concept as a reciprocating pump (Farthing, 2013). However, both an actuator and a controller are still needed to prescribe the pitching motion.

A further simplification, for which both degrees of freedom are decoupled and elastically supported, was first proposed by Peng and Zhu (2009). This is referred to as a fully-passive flapping-foil turbine. For a given flow, they observed four different types of responses depending on the structural parameters characterizing the elastically-supported foil. Among them, only one was suitable for a stable and efficient energy extraction. This response was characterized by periodic pitching and heaving motions with large amplitudes and it led to an efficiency of 20% and a power coefficient of about 0.3. The other responses were either irregular, thereby negatively affecting the predictability and the controllability of the energy extraction, or the foil remained stationary at its equilibrium position and did not extract any energy from the flow. Zhu (2012) demonstrated that the presence of shear in the inflow could lead to new undesired types of responses and, more importantly, could restrict the parameter range for which useful large-amplitude periodic motions are observed. Wang et al. (2017) later found that this parameter range is also affected by the pitch axis location and that a pitch axis located at 0.35 chord length from the leading edge was optimal in their case.

The above-cited studies performed by Peng and Zhu (2009), Zhu (2012) and Wang et al. (2017) have all been conducted in the laminar regime ($\mathrm{Re} = 1\,000$ and $\mathrm{Re} = 400$). Veilleux and Dumas (2017)

carried out 2D numerical simulations at a much larger Reynolds number of 500 000 using the Spalart-Allmaras URANS turbulence model (Spalart and Allmaras, 1994), which is more representative of the operation of full-scale turbines. As in the works of Peng and Zhu (2009) and Zhu (2012), Veilleux and Dumas (2017) observed different responses of the foil, including large-amplitude periodic motions. Following an optimization process, they obtained a turbine efficiency reaching 29.1% and a power coefficient of 0.935. Furthermore, they pointed out that an adequate synchronization between the pitching and heaving motions is crucial for an optimal energy extraction by fully-passive flapping-foil turbines, as is also the case for their fully-constrained counterparts (Xiao and Zhu, 2014; Young et al., 2014).

While the aforementioned studies reported good results from 2D numerical simulations, the same level of performance has yet to be observed experimentally with a fully-passive flapping-foil turbine prototype. Similar devices have been studied previously but these works did not focus on the energy extraction performance (Amandolese et al., 2013; Pigolotti et al., 2017). Such a prototype has therefore been designed for the present work and has been tested in a water channel with the objective of proving the feasibility and confirming the potential of the fully-passive flapping-foil turbine concept. The current study also evaluates the sensitivity of the turbine performance to the variation of several governing parameters. The fully-passive concept, the experimental setup and the measurement methodology are described in Section 2.4, while the analysis of a baseline case and the results of a parametric study are presented in Section 2.5.

2.4 Methodology

2.4.1 The fully-passive flapping-foil turbine concept

The fully-passive flapping-foil turbine concept considered in this study is similar to the one described in the work of Veilleux and Dumas (2017). As shown in Fig. 2.1, it consists in a rigid blade elastically supported by springs in heave and in pitch as well as by a damper in heave. This damper models the energy sink that would result, for example, from the energy conversion into electricity by an electric generator. The blade is free to pitch ($\theta(t)$) about a pitch axis located at a distance x_p from the leading edge and to heave ($h(t)$) in the y-direction. The motions are restricted to these two degrees of freedom (DOF) and gravity acts in the span direction, or z-direction, hence playing no role in the blade dynamics. Unlike the turbine analyzed by Veilleux and Dumas (2017), no pitch damper is explicitly used in the current study. However, due to the inherent presence of friction in a real experimental setup, some undesired viscous pitch damping ($D_{\theta,\mathrm{v}}$) is inevitably present and must be considered in addition to some viscous heave damping ($D_{h,\mathrm{v}}$) as well as some Coulomb friction (dry friction) both in heave ($F_{y\,\mathrm{Coulomb}}$) and in pitch (M_{Coulomb}). As a result, the total linear heave damping coefficient (D_h) is the sum of the desired energy sink ($D_{h,\mathrm{e}}$), corresponding to the energy that could be converted into electricity, and the viscous damping stemming from the additional undesired friction in heave ($D_{h,\mathrm{v}}$):

$$D_h = D_{h,\mathrm{e}} + D_{h,\mathrm{v}} \,, \tag{2.1}$$

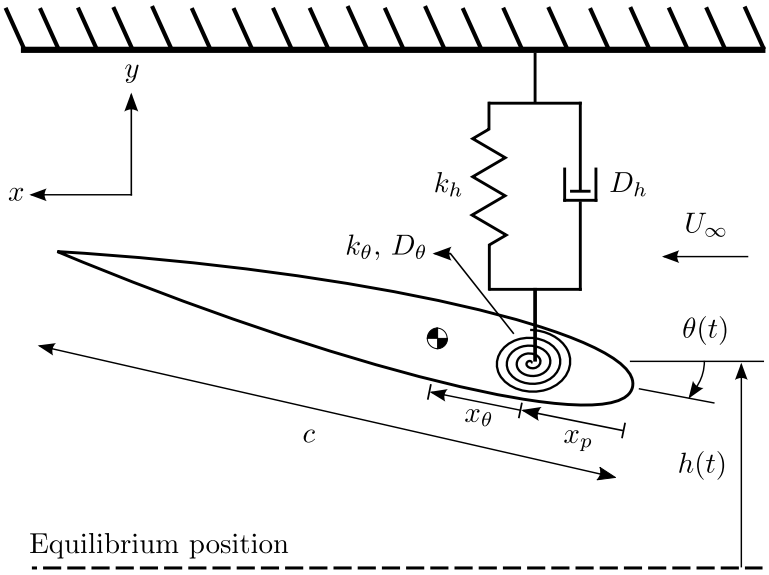

Figure 2.1: Outline of the fully-passive flapping-foil turbine concept.

while the total linear pitch damping coefficient (D_θ) simply corresponds to the undesired viscous damping in pitch:

$$D_\theta = D_{\theta,\mathrm{v}} \, . \tag{2.2}$$

Because of the presence of Coulomb friction in the experimental setup and the use of a different sign convention for θ, the equations of motion are slightly different than those presented by Veilleux and Dumas (2017). They are given here in their dimensionless form:

$$C_{F_y}/2 \;=\; m_h^* \ddot{h}^* \;+\; S^* \left(\ddot{\theta}^* \cos\theta - {\dot{\theta}^*}^2 \sin\theta \right) + D_h^* \dot{h}^* \;+\; k_h^* h^* \;+\; C_{F_{y\,\mathrm{Coulomb}}}/2 \, , \tag{2.3}$$

$$C_M/2 \;=\; I_\theta^* \, \ddot{\theta}^* \;+\; S^* \ddot{h}^* \cos\theta \;+\; D_\theta^* \, \dot{\theta}^* \;+\; k_\theta^* \, \theta + C_{M_{\,\mathrm{Coulomb}}}/2 \, , \tag{2.4}$$

where the superscript $(\cdot)$ denotes differentiation with respect to time and:

$$C_{F_y} = \frac{F_y}{0.5\,\rho\,U_\infty^2\,b\,c} \;, \qquad C_M = \frac{M}{0.5\,\rho\,U_\infty^2\,b\,c^2} \, , \qquad C_{F_{y\,\mathrm{Coulomb}}} = \frac{F_{y\,\mathrm{Coulomb}}}{0.5\,\rho\,U_\infty^2\,b\,c} \;,$$

$$C_{M_{\,\mathrm{Coulomb}}} = \frac{M_{\,\mathrm{Coulomb}}}{0.5\,\rho\,U_\infty^2\,b\,c^2} \, , \qquad m_h^* = \frac{m_h}{\rho\,b\,c^2} \;, \qquad I_\theta^* = \frac{I_\theta}{\rho\,b\,c^4} \;, \qquad S^* = \frac{S}{\rho\,b\,c^3} \, ,$$

$$D_h^* = \frac{D_h}{\rho\,U_\infty\,b\,c} \;, \qquad D_\theta^* = \frac{D_\theta}{\rho\,U_\infty\,b\,c^3} \, , \qquad k_h^* = \frac{k_h}{\rho\,U_\infty^2\,b} \;, \qquad k_\theta^* = \frac{k_\theta}{\rho\,U_\infty^2\,b\,c^2} \, ,$$

$$h^* = \frac{h}{c} \;, \qquad \dot{h}^* = \frac{\dot{h}}{U_\infty} \;, \qquad \ddot{h}^* = \frac{\ddot{h}\,c}{U_\infty^2} \, , \qquad \dot{\theta}^* = \frac{\dot{\theta}\,c}{U_\infty} \;, \qquad \ddot{\theta}^* = \frac{\ddot{\theta}\,c^2}{U_\infty^2} \, .$$

The definitions of all the parameters involved in the equations of motion as well as those shown in Fig. 2.1 are provided in Table 2.1. Details about the derivation of the dimensionless equations can be found in the work of Veilleux (2014).

Table 2.1: List of the parameters involved in the equations of motion.

Symbol	Units	Definition
b	[m]	Blade span length
c	[m]	Chord length
ρ	[Kg/m^3]	Water density
U_∞	[m/s]	Freestream velocity
h	[m]	Heave position of the pitch axis (upward positive in Fig. 2.1)
θ	[rad]	Pitch angle (clockwise positive in Fig. 2.1)
t	[s]	Time
x_p	[m]	Distance between the leading edge and the pitch axis
x_θ	[m]	Distance between the pitch axis and the center of mass (defined positive when the pitch axis is upstream of the center of mass)
F_y	[N]	Hydrodynamic force component in the heave (y) direction
M	[N·m]	Hydrodynamic moment about the pitch axis
$F_{y\,\mathrm{Coulomb}}$	[N]	Coulomb friction force component in the heave (y) direction
$M_{\,\mathrm{Coulomb}}$	[N·m]	Coulomb friction moment about the pitch axis
m_h	[Kg]	Mass of all the components undergoing the heaving motion
I_θ	[Kg·m^2]	Moment of inertia about the pitch axis
S	[Kg·m]	Static moment (mass only undergoing the pitching motion times x_θ)
D_h	[N·s/m]	Total linear heave damping coefficient
$D_{h,\mathrm{e}}$	[N·s/m]	Linear heave damping coefficient of the eddy-current brake (desired energy sink)
$D_{h,\mathrm{v}}$	[N·s/m]	Linear heave damping coefficient of the heave bearings
D_θ	[N·m·s/rad]	Linear pitch damping coefficient of the pitch bearings
k_h	[N/m]	Heave stiffness coefficient
k_θ	[N·m/rad]	Pitch stiffness coefficient

The two nonlinear equations of motion (Eqs. 2.3 and 2.4) are coupled both via the coupling between the hydrodynamic force and moment and the inertial coupling terms, i.e., the terms involving the static moment S^*[1]. However, the inertial coupling terms only play a role when the static moment is not zero, i.e., when the center of mass does not coincide with the pitch axis. It is worth recalling that there are

[1]This parameter was referred to as the static imbalance in the work of Veilleux (2014); Veilleux and Dumas (2017).

no mechanical links between the heaving and the pitching motions that could enforce a particular relation between these two degrees of freedom. In other words, the motion shapes, the amplitudes, the frequencies and the phase lag between the heaving and the pitching motions are not imposed.

For a given flow, there are 9 structural parameters playing a role in the turbine dynamics explicitly appearing in Eqs. 2.3 and 2.4, namely:

$$C_{F_{y\,\mathrm{Coulomb}}}, \qquad C_{M_{\mathrm{Coulomb}}}, \qquad m_h^*, \qquad I_\theta^*, \qquad S^*, \qquad D_h^*, \qquad D_\theta^*, \qquad k_h^* \quad \text{and} \quad k_\theta^*,$$

in addition to the position of the pitch axis (x_p/c) for a total of 10 governing structural parameters. The challenge of designing a fully-passive flapping-foil turbine therefore consists in finding adequate values for these 10 parameters that result in useful motions in terms of energy extraction, i.e., periodic motions of large amplitudes, with a single frequency for both degrees of freedom and an appropriate phase lag between the heaving motion and the pitching motion.

2.4.2 Experimental setup

The experiments were carried out in the water channel of the Fluid Mechanics Laboratory at the University of Victoria, BC, Canada. Its test section has a cross section of 0.45 m by 0.45 m and a length of 2.5 m. The fully-passive flapping-foil turbine prototype is composed of non-moving components, components only undergoing the heaving motion and components undergoing both the heaving and the pitching motions, indicated by different colors in Fig. 2.2. These different components can also be observed in Fig. 2.3, which shows the blade at two different positions during a given test in the water channel.

A carriage is mounted on linear guided roller bearings, thereby allowing it to move in the heave (transverse) direction. The top end of the blade is attached to a shaft, which is itself free to rotate while moving with the heaving carriage. The turbine blade is straight, its cross section corresponds to a symmetric NACA0015 profile with a 50 mm chord length and the pitch axis is located at the third-chord point ($x_p/c = 1/3$). In order to minimize the tip losses, end plates are placed at both ends of the blade. Moreover, the distance between the free extremity of the blade and the channel floor was set to a very small gap of 5 mm, which corresponds to a tenth of the blade chord length. The blade span length (b) is 0.38 m and the water level was set to 0.42 m at rest. As a result, the blade is completely submerged during the tests, while all the other components are located above water, except for the end plates and a fraction of the shaft holding the blade. This can be seen in Fig. 2.4.

The fully-passive flapping-foil turbine prototype presented in this work was designed based on the optimal case reported by Veilleux and Dumas (2017). However, several aspects differ from their optimal 2D numerical case due to practical design limitations, especially regarding the Reynolds number, the static moment, the presence of Coulomb friction, the three-dimensionality of the flow, the blockage and the presence of a free surface. Besides, the prototype allows us to independently vary the three inertial properties, namely the heaving mass (m_h), the moment of inertia about the pitch axis (I_θ) and the

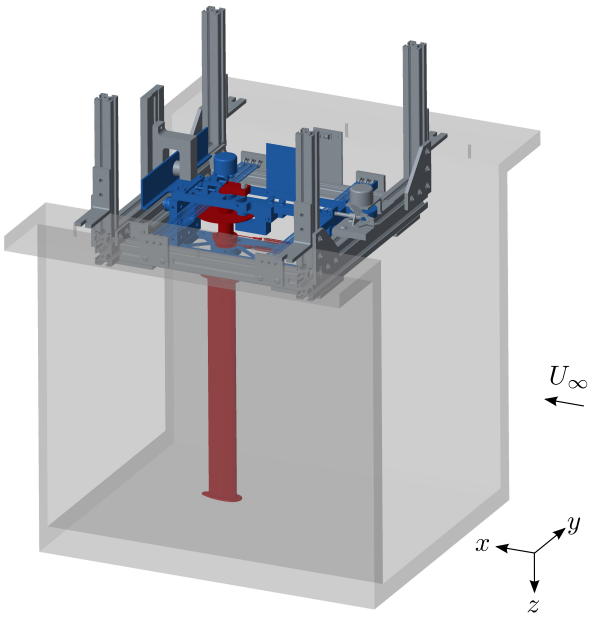

Figure 2.2: 3D model of the turbine prototype showing the non-moving components in gray, the components only undergoing the heaving motion in blue and the components undergoing both the heaving and the pitching motions in red. (For interpretation of the references to color in this figure legend, the reader is referred to the web version of this article.)

static moment (S), as well as the heave damping ($D_{h,\mathrm{e}}$) and the heave and pitch stiffness coefficients (k_h and k_θ). More information about how these variations can be achieved is given in Appendix 2.A.

2.4.3 Measurement protocols

For each test, the blade is initially held in place at its equilibrium position, namely the middle of the channel in heave ($h/c = 0$) with the blade chord line being aligned with the inflow velocity ($\theta = 0$). The water velocity is then set to a desired value before suddenly releasing the blade. The blade positions in heave and in pitch are recorded at a sampling frequency of 83.3 Hz and during 120 seconds, which roughly corresponds to 100 oscillations of the blade, with two rotary encoders generating 10 000 pulses per revolution. The digital signals provided by each encoder are converted into analog signals (0-5 V) using a 14-bit digital-to-analog converter (DAC), and these analog signals are sampled with a NI USB-6218 data-acquisition board connected to a laptop.

In order to convert the reciprocating heaving motion into a rotational motion that can be measured by the heave encoder, a timing belt pulley is fixed to the shaft of the heave encoder and is in contact with a timing belt glued to an aluminum plate undergoing the heaving motion, as shown in Fig. 2.5. Note that the blade velocity components in heave and in pitch are computed using second-order central-difference schemes.

The inflow velocity (U_∞) is measured using Particle Image Velocimetry (PIV) on a vertical plane

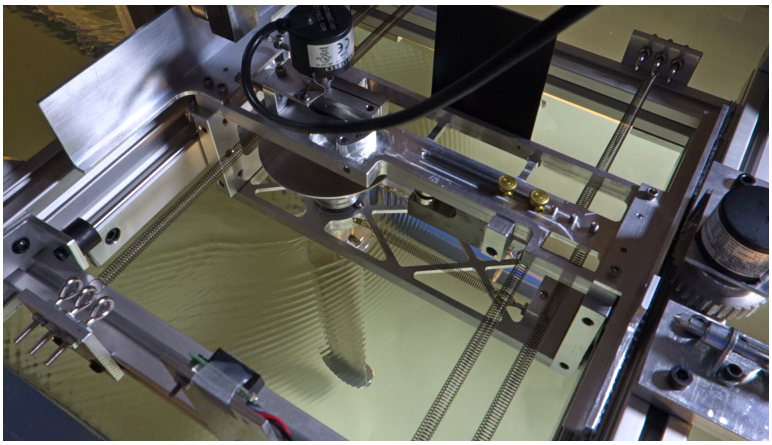

(a) $h/c = 0$ and $\theta = 0°$ (equilibrium position).

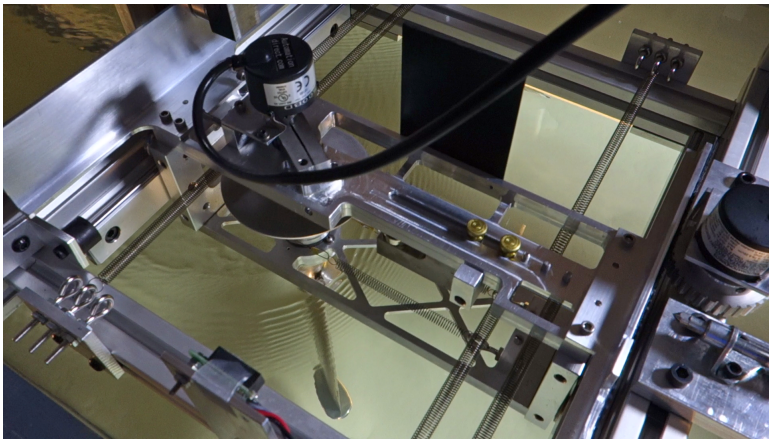

(b) $h/c \neq 0$ and $\theta \neq 0°$.

Figure 2.3: Top view of the fully-passive flapping-foil turbine prototype with the blade at two different positions during a given test in the water channel. The water is flowing from the bottom right corner of the figure toward the top left corner, which is perpendicular to the heaving motion. A video showing such a top view of the baseline case presented in Section 2.5.1 is available in the supplementary material provided with the online version of this paper.

(xz) located 13 chord lengths upstream of the pitch axis and covering 0.8c in the streamwise (x) direction and 4.2c in the spanwise (z) direction. The PIV measurements are carried out with a sampling frequency of 100 Hz during 16 seconds, which roughly corresponds to between 15 and 20 blade cycles. The turbulent intensity of the inlet flow based on the streamwise velocity fluctuations is below 1% and the uniformity of the inflow has been verified by computing the standard deviations of the velocity profiles in the spanwise (z) and transverse (y) directions, which are around 0.1% in both directions.

Since the friction in the pitch and heave bearings can change over time due to their slight wear, it was estimated at the start and at the end of every series of experiments conducted in the channel. A range of values is therefore given to characterize the different friction contributions for a specific test. The methodology that has been used to estimate these friction contributions is presented in

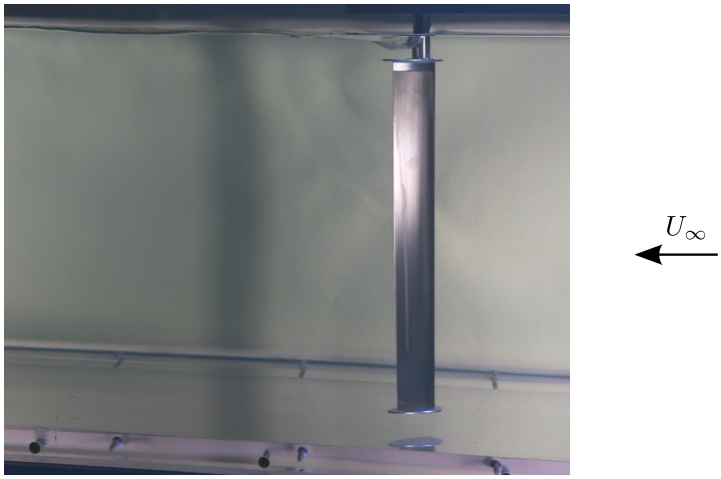

Figure 2.4: Side view showing the submerged turbine components, namely the blade, the end plates and a fraction of the shaft holding the blade. The water is flowing from right to left. A video showing such a side view of the baseline case presented in Section 2.5.1 is available in the supplementary material provided with the online version of this paper.

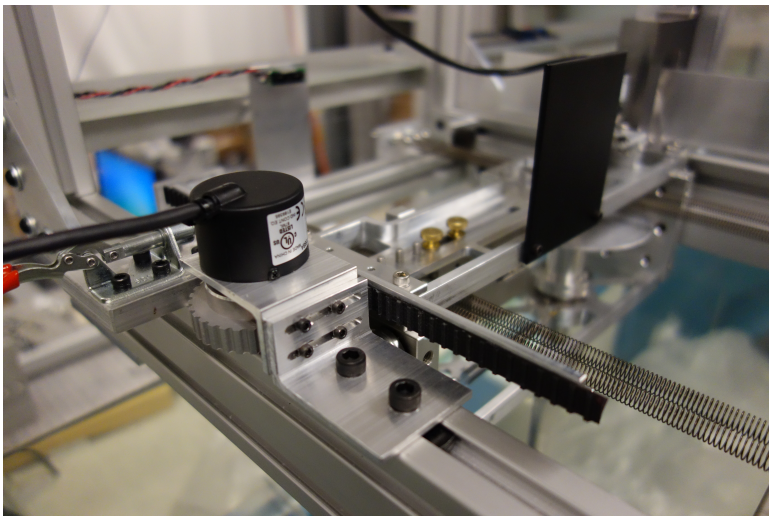

Figure 2.5: Timing belt used to convert the reciprocating heaving motion into a rotational motion for the heave encoder.

Appendix 2.B.4.

The ambient temperature as well as the temperature of the aluminum sliding plate of the eddy-current brake are measured with a standard mercury thermometer and an infrared thermometer (Fluke 65), respectively. The ambient temperature during a given test is used to determine the water properties, namely its density and its dynamic viscosity, by interpolating the tabulated data available in the book of Munson (2013). Regarding the temperature of the eddy-current brake's sliding plate, it is used to correct the values of the heave damping coefficient of the eddy-current brake, as described in Appendix 2.B.4.

2.4.4 Performance metrics

The motions of the different cases considered are compared in terms of the reduced frequency (f^*), the phase lag between the heaving motion and the pitching motion (ϕ) and the amplitudes in heave (H_0^*) and in pitch (Θ_0). These metrics are defined as:

$$f_j^* = \frac{f_j\, c}{U_\infty}\,, \tag{2.5}$$

$$\phi_j = \frac{360}{T_j}\left(t_{\theta_{\max\, j}} - t_{h_{\max\, j}}\right) \quad \text{[degrees]}\,, \tag{2.6}$$

$$H_{0\,j}^* = \frac{h_{\max\, j} - h_{\min\, j}}{2c}\,, \tag{2.7}$$

$$\Theta_{0\,j} = \frac{\theta_{\max\, j} - \theta_{\min\, j}}{2}\,, \tag{2.8}$$

where the subscript j stands for the j^{th} turbine blade oscillation, f is the frequency of the motions, which is always the same for both degrees of freedom for all the cases reported in this study, T is the oscillation period ($T = 1/f$), $h_{\max}$, $h_{\min}$, $\theta_{\max}$ and $\theta_{\min}$ are the extreme heave and pitch positions reached during a given turbine blade oscillation, and $t_{\theta_{\max}}$ and $t_{h_{\max}}$ are the instants at which these extreme positions are reached. Note that the value of ϕ obtained from Eq. 2.6 is given in degrees.

Two other metrics characterizing the energy extraction, namely the efficiency (η_{e}) and the power coefficient in heave ($\overline{C_{P_{h,\text{e}}}}$), both based on the cycle-averaged power dissipated in the eddy-current brake which models the energy extraction, are also used to compare the different cases that have been tested. They are defined as:

$$\eta_{\text{e}\,j} = \frac{\overline{P_{h,\text{e}\,j}}}{\frac{1}{2}\rho\, U_\infty^3\, b\, d_j}\,, \tag{2.9}$$

where:

$$\overline{P_{h,\text{e}\,j}} = \frac{1}{T_j}\int_t^{t+T_j}\left(D_{h,\text{e}}\,\dot{h}^2\right)\,dt\,, \tag{2.10}$$

and:

$$\overline{C_{P_{h,\text{e}\,j}}} = \eta_{\text{e}\,j}\,\frac{d_j}{c}. \tag{2.11}$$

with b being the blade span length and d_j being the overall transverse extent of the blade motion during the j^{th} turbine blade cycle (Kinsey and Dumas, 2008). In other words, d_j corresponds to the distance between the highest and the lowest points reached by any point on the blade surface during the j^{th} cycle.

Note that these definitions of the efficiency and the power coefficient must not be confused with the definitions that are typically used for fully-constrained turbines (Kinsey and Dumas, 2014). Indeed,

the efficiency and the power coefficient that are usually reported for fully-constrained turbine technology are based on the energy transferred from the flow to the turbine blade and do not take into account the power transmission efficiency. With the present experimental setup, it is not possible to directly compute the power transferred from the flow to the blade since the forces acting on the blade are not measured. The power dissipated in the heave damper that is used to compute η_e and $\overline{C_{P_{h,\mathrm{e}}}}$ is necessarily smaller than the total power extracted from the flow because a fraction is inevitably lost due the undesired friction in the moving components.

Lastly, all the results presented in the following sections have been obtained by computing average values from 90 turbine blade cycles. For example:

$$f^* = \frac{1}{90}\sum_{j=1}^{90} f_j^* \,. \tag{2.12}$$

2.5 Results

2.5.1 Baseline case

Following a preliminary series of tests, a case achieving a high efficiency has been selected as the baseline case and is presented in this section. The parameters describing this baseline case as well as some metrics characterizing its performance are given in Table 2.2, while time evolutions of the pitch and heave positions are presented in Fig. 2.6. Moreover, two videos of this case are available in the supplementary material provided with the online version of this paper.

Table 2.2: Baseline case description and performance.

Parameter	Value	Performance metric	Averaged value
Re	21 000	f^*	0.133 ± 0.001
m_h^*	3.36 ± 0.05	ϕ	$99° \pm 3°$
I_θ^*	0.091 ± 0.001	H_0^*	0.891 ± 0.002
S^*	0.040 ± 0.001	Θ_0^*	$85.0° \pm 0.9°$
$D_{h,\mathrm{e}}^*$	1.23 ± 0.03	η_e	$26.8\% \pm 0.7\%$
k_h^*	1.91 ± 0.03	$\overline{C_{P_{h,\mathrm{e}}}}$	0.68 ± 0.02
k_θ^*	0		
$D_{h,\mathrm{v}}^*$	$[0.047 - 0.074] \pm 0.008$		
D_θ^*	$[0.003 - 0.005] \pm 0.003$		
$C_{F_{y\,\mathrm{Coulomb}}}$	$[0.07 - 0.07] \pm 0.04$		
$C_{M_{\mathrm{Coulomb}}}$	$[0.015 - 0.021] \pm 0.005$		

It is worth recalling again that the amplitudes, the frequency and the phase lag between the heaving and the pitching motions are not constrained, but rather result from the structural and hydrodynamic

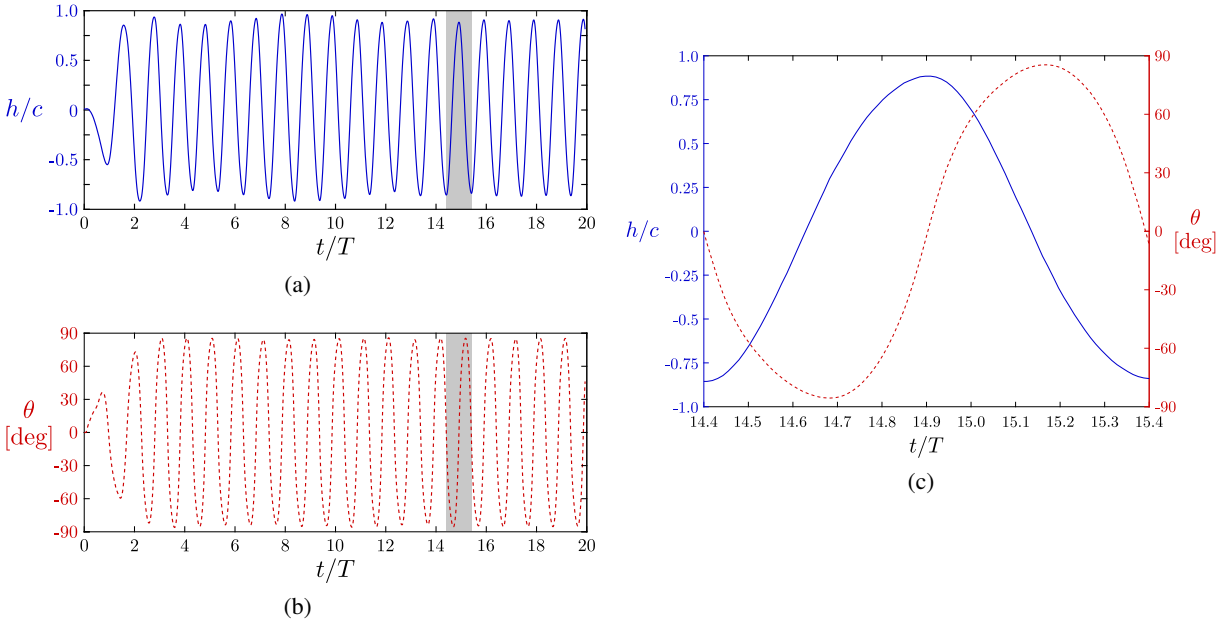

Figure 2.6: Heave (a) and pitch (b) positions over time for the baseline case (see Table 2.2), shown in solid blue and in dashed red respectively, with the blade released from its equilibrium position at $t/T = 0$, where t is the dimensional time and T is the dimensional oscillation period of the blade averaged over 90 oscillations. A zoom of the shaded area in (a) and (b), which approximately corresponds to one turbine blade oscillation, is shown in (c). The zoom area starts at an instant for which the pitch angle is zero and the heave position is close to a minimum.

parameters characterizing a specific case. It is therefore impressive to notice that the kinematics of the baseline case turn out to be very similar to the motions leading to the best performance achieved with fully-constrained turbines. Indeed, previous studies devoted to the fully-constrained turbine concept have shown that high efficiencies are usually observed when the turbine blade undergoes large-amplitude motions in heave (on the order of one chord length) and in pitch ($\approx 80°$), at a reduced frequency between 0.10 and 0.20 approximately and with a phase lag close to 90° (Kinsey and Dumas, 2014; Young et al., 2014; Xiao and Zhu, 2014).

Following the 2D numerical works of Veilleux and Dumas (2017) and Wang et al. (2017), who respectively obtained efficiencies of 29.1% and 32% and power coefficients of 0.935 and 0.95, the current experimental work further demonstrates that such performance can be obtained despite the presence of some "real-life" effects such as the viscous and Coulomb friction contributions stemming from the bearings, the tip losses, the drag of the submerged fraction of the shaft holding the blade and the presence of a free surface. It is also interesting to note that since the undesired viscous damping in the heave bearings is about 5% of the eddy-current brake damping for the baseline case (see Table 2.2), the efficiency and the power coefficient would be both 5% larger if this undesired damping contribution was zero. An even larger increase would be expected if the viscous damping in pitch as well as the Coulomb friction in heave and in pitch could also be eliminated.

The regularity and the periodicity of the motions, once a permanent regime is reached, are notable. A quantitative measure of this periodicity is given in Table 2.3 by providing the standard deviations of the different performance metrics presented in Table 2.2. Considering that the ultimate objective of this study is to develop a simple and reliable energy extraction device, this makes the baseline case even more suitable for a turbine application.

Table 2.3: Averaged values and standard deviations of the performance metrics characterizing the baseline case computed from 90 blade cycles.

Performance metric	Averaged value	Standard deviation
f^*	0.133	0.014
ϕ	99°	3°
H_0^*	0.891	0.017
Θ_0^*	85.0°	0.5°
η_e	26.8%	0.6%
$\overline{C_{P_{h,e}}}$	0.68	0.02

It is interesting to note that the blade pitches passively even if $k_\theta^* = 0$ for the baseline case. By analyzing the relative contributions of each term appearing in the governing equations of motion (Eqs. 2.3 and 2.4), Veilleux and Dumas (2017) found that the dominant term responsible for limiting the pitch amplitude and reversing the pitch velocity for their optimal case was the hydrodynamic moment about the pitch axis for which a large peak was observed every half cycle. The contribution of the pitch spring stiffness, although not zero in their case, was negligible. Veilleux and Dumas (2017) have highlighted the fact that the large moment peak was related to the generation of a strong leading-edge vortex following the deep stall of the blade. It was also responsible for a non-sinusoidal pitching motion with smaller pitch velocities observed when the blade is approaching an extremum in pitch than when the blade departs from an extremum.

Unfortunately, the experimental setup used for the current study does not allow measuring the hydrodynamic forces and moment acting on the blade, hence preventing us from performing a similar analysis. However, PIV measurements have been carried out and a series of instantaneous vorticity fields around the blade are presented in Fig. 2.7. This figure shows that the blade is subject to deep stall and that a large leading-edge vortex is shed every half cycle in the case of the baseline operating point, as for the optimal case of Veilleux and Dumas (2017). Furthermore, a similar non-sinusoidal pitching motion has been obtained in the current study, as shown in Fig. 2.6c. Considering that the flow fields and the time evolutions of the pitch angle are very similar in both studies and that the contribution of the pitch spring is close or equal to zero in both cases, the hydrodynamic moment is most likely responsible for limiting the pitch amplitude and reversing the pitch velocity for the baseline case of the current study, as it was for the optimal case found by Veilleux and Dumas (2017).

Even if the moment about the pitch axis cannot be directly measured, all the terms on the right hand side of Eq. 2.4 can be computed, which allows estimating the moment coefficient by summing all of them. The evolution of the terms appearing in Eq. 2.4 are shown in Fig. 2.8 over the same time span as in Fig. 2.6c, which approximately corresponds to one complete blade cycle starting when the pitch angle is zero and the heave position is close to a minimum. The results show that the inertia term ($I^*_\theta \ddot{\theta}^*$) is much larger than all the other terms appearing on the right hand side of Eq. 2.4. This confirms the hypothesis that the pitching motion of the baseline case essentially results from the balance between the moment generated by the fluid flow and the inertia term. By observing Figs. 2.6c, 2.7 and 2.8, one can notice that the large leading-edge vortex that is generated as the blade stalls results in a large positive moment peak when $\theta < 0$ (see the instants $t/T = 0.4$ in Fig. 2.7 and $t/T \approx 14.8$ in Fig. 2.8), which in turn results in a large positive pitch acceleration that limits the pitch amplitude. Once the leading-edge vortex is shed beyond the trailing edge, the moment quickly becomes negative (see the instants $t/T = 0.5$ in Fig. 2.7 and $t/T \approx 14.9$ in Fig. 2.8). A similar behavior was observed by Veilleux and Dumas (2017) and is described in more details in their work. Note that the results presented in Fig. 2.8 are a bit noisy because they involve the computation of the heave and pitch accelerations from the position measurements. In order to limit the uncertainty of the results presented in this figure, the sampling rate was reduced to half its nominal value of 83.3 Hz, used for the rest of the current study, to 41.7 Hz. This results in an uncertainty of the inertia term corresponding to 5% of its peak value.

A static instability, known as divergence, can occur when the restoring moment stemming from the pitch springs is not large enough to counteract the hydrodynamic moment (Dowell, 2004). More precisely, the theory predicts that the critical dimensionless pitch spring stiffness coefficient ($k^*_{\theta\,\mathrm{crit}}$) is given by:

$$k^*_{\theta\,\mathrm{crit}} = \frac{\pi e}{c}\,, \tag{2.13}$$

where e is the distance between the point of application of the fluid force and the pitch axis and it is defined positive when the point of application of the fluid force is located upstream of the pitch axis. The blade is unstable when $k^*_\theta < k^*_{\theta\,\mathrm{crit}}$, which means that this instability can only occur if the pitch axis is located downstream of the point at which the fluid force acts.

Based on the linear unsteady theory (Dowell, 2004; Fung, 2008) and considering a thin symmetric foil, the fluid force is expected to act around the quarter-chord point. Since the pitch axis is located further downstream, at the third-chord point, and because $k^*_\theta = 0$, the baseline case of the current study is expected to be subject to the divergence instability. The fact that the blade starts to pitch even when it is being held in place in the heave direction supports this inference. Indeed, this pitching motion would not occur if the present turbine was rather driven by the coupled-mode flutter instability, which is a coupled-mode instability that requires both degrees of freedom to be active in order to arise. Moreover, the motions of the current turbine are always damped when using pitch springs with too large stiffness coefficients, as shown in Section 2.5.2, which again suggests that the divergence instability is the driving mechanism of this fully-passive flapping-foil prototype. The occurrence of

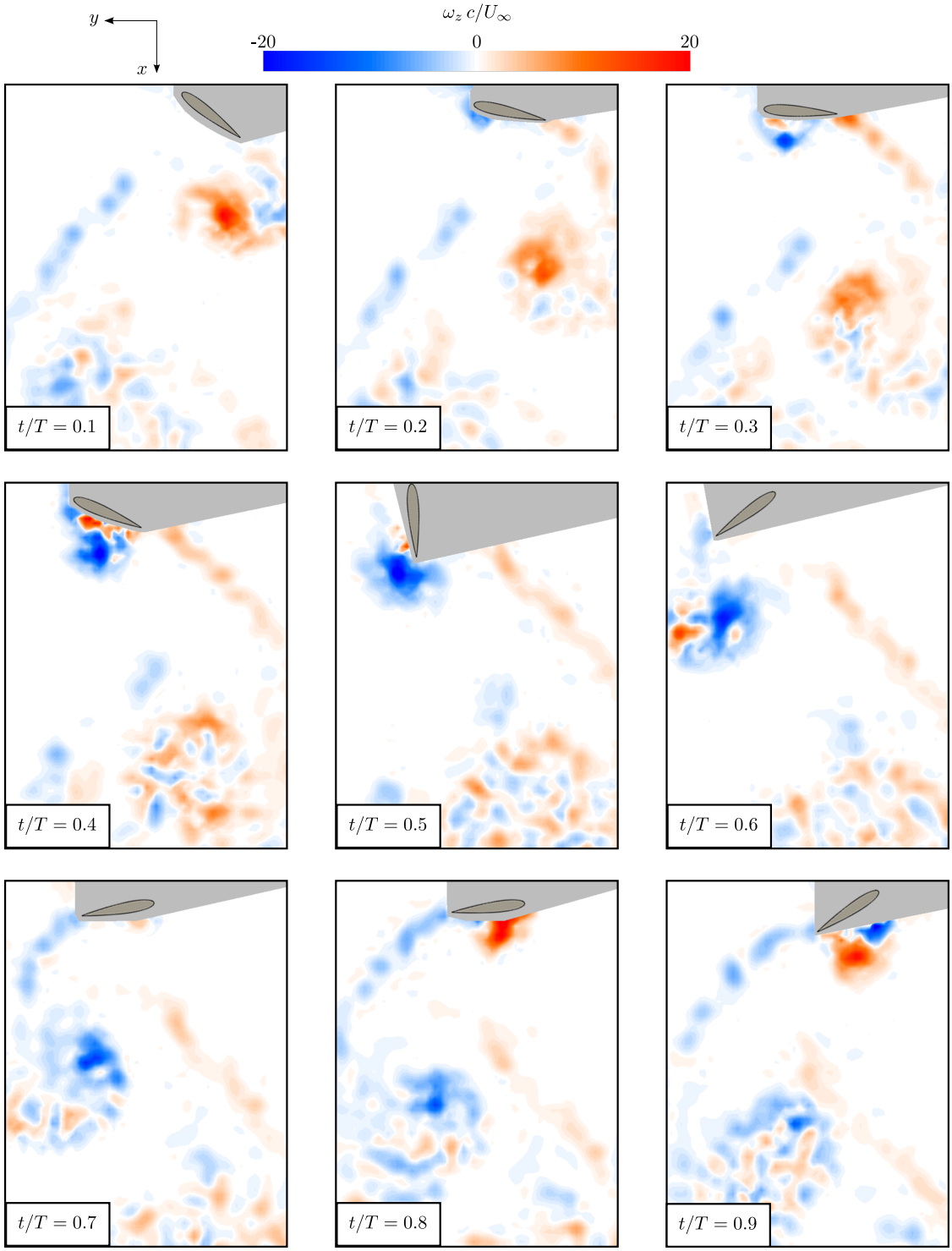

Figure 2.7: Snapshots of the normalized spanwise vorticity field measured by PIV at different instants during one representative blade cycle of the baseline case. The start of the cycle ($t/T = 0$) is defined as an instant for which the pitch angle is zero and the heave position is close to a minimum. As a result, the time $t/T = 0$ in this figure is similar to the time $t/T = 14.4$ in Figs. 2.6 and 2.8.

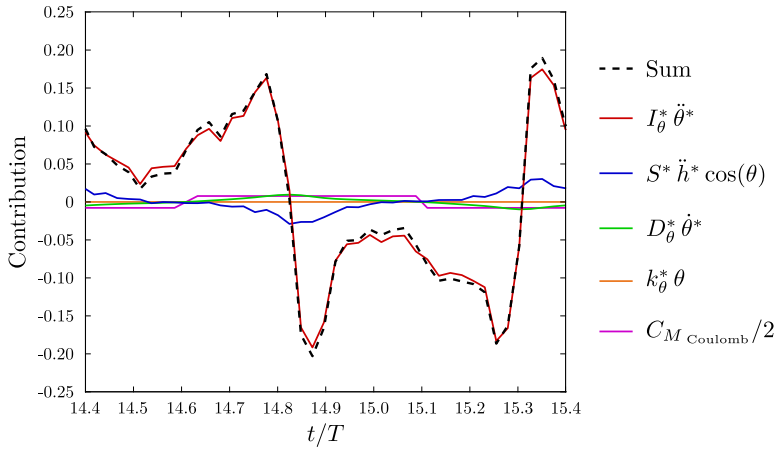

Figure 2.8: Time evolutions of the terms on the right hand side of Eq. 2.4 for the baseline case over the same time span as in Fig. 2.6c, i.e., approximately one turbine cycle. The sum of all the terms (dashed black line) estimates $C_M/2$.

this static instability can also explain why the transient period following the release of the blade is so short, as observed in Figs. 2.6a and 2.6b. About only two oscillation periods ($t/T \approx 2$) are required before the turbine reaches a permanent regime characterized by stable limit-cycle oscillations (LCO) of large amplitudes. It is important to note that the theory leading to the divergence instability threshold, given by Eq. 2.13, relies on the assumption of small displacements and a quasi-static approximation. According to this theory, nothing limits the growth of the pitch amplitude when the blade is unstable. This theory is therefore useful to explain why the pitching motion is initiated, which in turn drives the heaving motion, but it does not apply when large amplitudes are reached in heave and in pitch because the nonlinearities of the flow become important.

By releasing the turbine blade from different initial pitch angles, it has been found that the permanent response of the baseline case is not affected by variations of the initial conditions. Moreover, tests consisting of temporary increasing or decreasing the flow velocity above or below its nominal value were conducted while the blade was oscillating in the water. The turbine response was always returning to the same permanent regime following these perturbations. These observations corroborate the findings of Peng and Zhu (2009), Amandolese et al. (2013) and Wang et al. (2017) for large-amplitude and periodic limit-cycle oscillations. These studies also showed that, for other types of responses, an oscillating blade could be significantly sensitive to the initial conditions and could be subject to hysteresis, but this has not been observed during the current study.

2.5.2 Sensitivity of the turbine performance to the governing structural parameters

In this section, the impact of various structural parameters affecting the turbine blade dynamics is analyzed. The effects of each structural parameter are investigated individually by keeping all the other structural parameters constant with their baseline value (see Table 2.2).

Unless otherwise specified, all the tests presented in this section were conducted with an inflow velocity of 0.38 m/s, which corresponds to a Reynolds number of 21 000 based on the chord length. Moreover, all the cases that are presented are similar to the baseline case in terms of the low sensitivity to the initial conditions and to perturbations, the regularity of the permanent response and the shortness of the initial transient period.

In the figures presented in the following sections, empty markers are used to identify the baseline case and to discriminate it from the other cases (filled markers). For the sake of clarity, the uncertainties are not shown in the figures, but they are available in the supplementary material provided with the online version of this paper.

In order to evaluate the repeatability of the results, some experiments have been carried out twice for a given set of structural parameters. More specifically, the same set of parameters was tested before and after each series of experiments. The values obtained from these tests are included in Figs. 2.9, 2.11, 2.13, 2.14 and 2.15. This explains why two markers can be observed for one specific value of the structural parameter considered. The baseline parameter values were used to conduct these repeatability tests except when studying the effects of k_θ^* and U_∞, for which $k_\theta^* = 0.068$ and $U_\infty = 0.35$ m/s were respectively used instead.

Heave stiffness

Fig. 2.9 shows the impact of the dimensionless heave stiffness (k_h^*) on various performance metrics. All the other structural parameters are kept constant except for the heaving mass (m_h^*), which slightly varies between the various cases because of the different number of heave springs used for each of them, as indicated in the legend of Fig. 2.9.

The maximum efficiency, reduced frequency and pitch amplitude, namely 28.9%, 0.139 and 87.8°, are all observed at the same operating point: $k_h^* = 2.54$. While the efficiency and the power coefficient follow the same trend, the largest power coefficient, with a value of 0.74, is obtained for a slightly smaller dimensionless heave stiffness ($k_h^* = 1.91$). This can be explained by the fact that the heave amplitude is larger with $k_h^* = 1.91$ than with $k_h^* = 2.54$, hence allowing for more energy extraction. However, the efficiency decreases from $k_h^* = 2.54$ to $k_h^* = 1.91$ because the kinetic energy flux passing through the turbine extraction plane increases even more than the power extracted.

Another noteworthy observation is that large amplitude motions with a significant energy extraction are even observed with no spring in heave and no spring in pitch (zero stiffness). The adequate synchronization between the pitching and the heaving motions leading to a good performance for this case, although not optimal, is therefore mainly due to the hydrodynamic force and moment acting on the turbine blade. This has indeed been shown by Veilleux (2014) who analyzed in more details a similar case with no spring in heave and no spring in pitch.

Furthermore, it is found that the pitch and heave amplitudes, the efficiency and the power coefficient

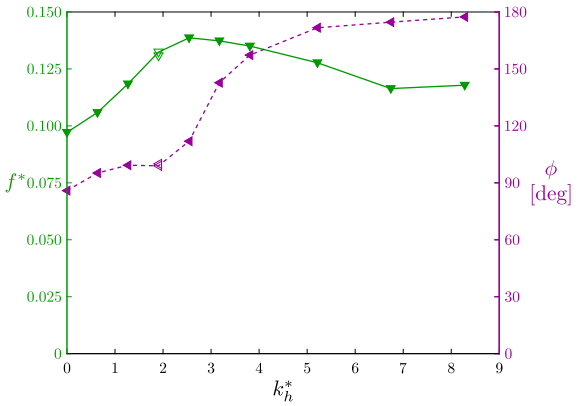

(a) Reduced frequency (solid green) and phase lag between the heaving and the pitching motions (dashed purple)

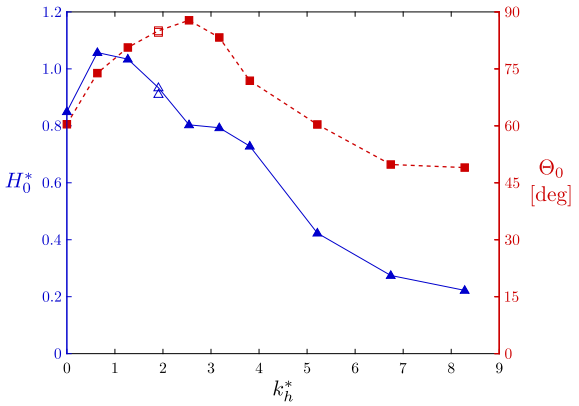

(b) Heave amplitude (solid blue) and pitching amplitude (dashed red)

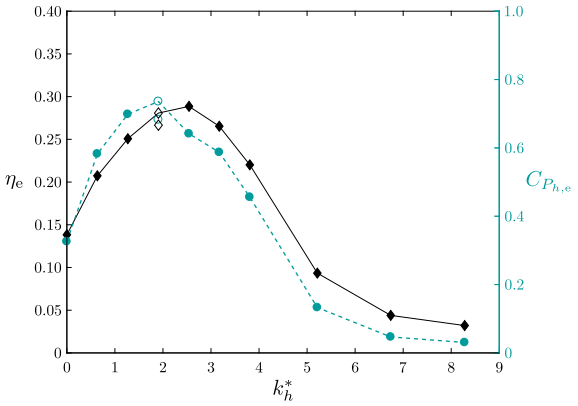

(c) Efficiency (solid black) and power coefficient (dashed turquoise)

Figure 2.9: Various performance metrics as functions of the dimensionless heave stiffness (k_h^*). Empty markers are used to identify the baseline case and the uncertainties are provided in the supplementary material along with the tabulated data used to produce this figure. $m_h^* = [3.34 - 3.38]$; $I_\theta^* = 0.091$; $S^* = 0.040$; $D_{h,\mathrm{e}}^* = 1.21$; $k_\theta^* = 0$; $D_{h,\mathrm{v}}^* = [0.047 - 0.074]$; $D_\theta^* = [0.003 - 0.005]$; $C_{F_{y\,\mathrm{Coulomb}}} = [0.07 - 0.07]$; $C_{M_{\,\mathrm{Coulomb}}} = [0.015 - 0.021]$.

all quickly drop when k_h^* exceeds approximately 3. This drop is related to the sudden transition from a phase lag around 90° between the heaving motion and the pitching motion to a phase lag close to 180°. Indeed, it is known that a phase lag of 90° is close to optimal when the pitch axis is located at the third-chord point (Xiao and Zhu, 2014) because the largest force acting on the blade in the heave direction and the largest heave velocity occur approximately at the same time in this case. Conversely, the force component in the heave direction is completely out of phase with the heave velocity when the phase lag is 180°.

While the phase lag between the heaving and the pitching motions is considerably altered as the dimensionless heave stiffness is increased, the reduced frequency is not affected as much. Moreover, the reduced frequency is neither directly correlated with the heave natural frequency ($f_{n,h}^* = \sqrt{k_h^*/m_h^*}/2\pi$),

as shown in Fig. 2.10, nor with the pitch natural frequency ($f^*_{n,\theta} = \sqrt{k^*_\theta / I^*_\theta}/2\pi$) since no pitch springs are used for all the cases presented in Figs. 2.9 and 2.10, resulting in $f^*_{n,\theta} = 0$. This suggests that the reduced frequency is related to another time scale associated to the fluid flow around the turbine blade. However, the heave natural frequency remains relevant since it is found that the point of maximum efficiency and maximum pitch amplitude are obtained when the reduced frequency and the heave natural frequency coincide, which occurs when $k^*_h = 2.54$. Furthermore, Fig. 2.10 shows that the reduced frequency increases with the heave natural frequency until they coincide and then decreases as the heave natural frequency further increases. It is also worthwhile to mention that the abrupt transition of the phase lag from 90° to 180° occurs when the heave natural frequency becomes larger than the reduced frequency.

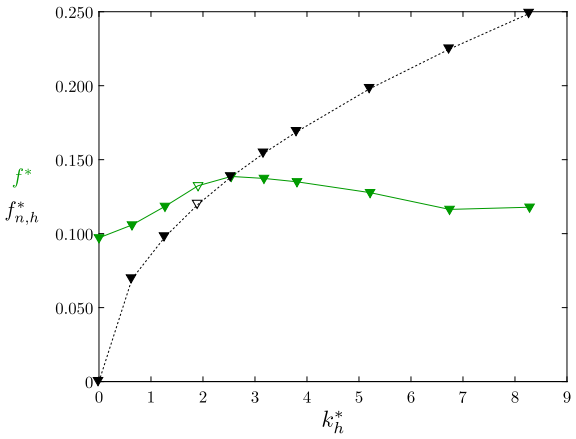

Figure 2.10: Comparison of the reduced frequency (f^* in solid green) and the reduced heave natural frequency ($f^*_{n,h}$ in dashed black) as a function of the dimensionless heave stiffness (k^*_h). Empty markers are used to identify the baseline case.

Heaving mass

The effect of the dimensionless heaving mass is presented in Fig. 2.11. Due to the experimental setup limitations, it is not possible to vary the dimensionless heaving mass to the same extent than the dimensionless heave stiffness. It is therefore normal to observe smaller variations for the different performance metrics in Fig. 2.11 than what is observed in Fig. 2.9.

It is found that increasing the dimensionless heaving mass by 45% from the minimum value tested only results in a variation of 2.5% (absolute) in terms of the efficiency (see Fig. 2.11c). This means that the manufacturer of a similar fully-passive flapping-foil turbine would have some useful freedom regarding this structural parameter, which should greatly facilitate the design process. Regarding the power coefficient, it is even less affected than the efficiency by variations of the heaving mass, as was also observed by Deng et al. (2015) in the case of a flapping-foil turbine with a prescribed pitching motion and an elastically-supported heaving motion.

The good performances reported here over the entire range of dimensionless heaving masses that have

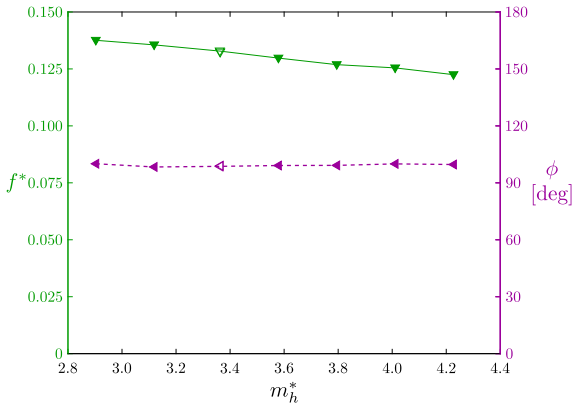

(a) Reduced frequency (solid green) and phase lag between the heaving and the pitching motions (dashed purple)

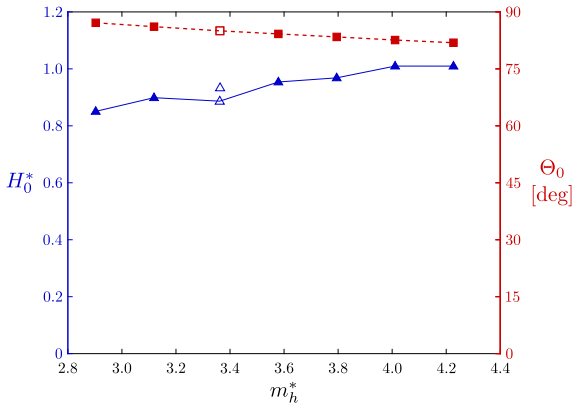

(b) Heave amplitude (solid blue) and pitching amplitude (dashed red)

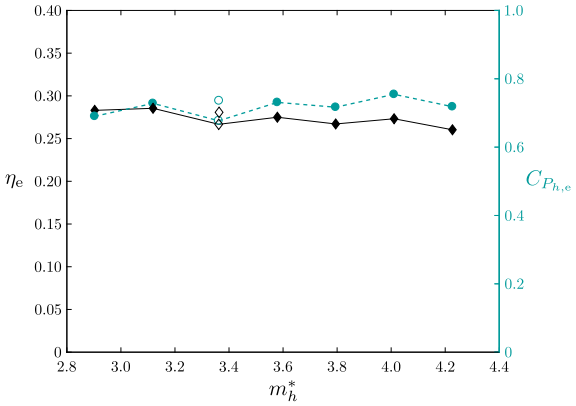

(c) Efficiency (solid black) and power coefficient (dashed turquoise)

Figure 2.11: Various performance metrics as functions of the dimensionless heaving mass (m_h^*). Empty markers are used to identify the baseline case and the uncertainties are provided in the supplementary material along with the tabulated data used to produce this figure. $I_\theta^* = 0.091$; $S^* = 0.040$; $D_{h,\mathrm{e}}^* = 1.21$; $k_h^* = 1.91$; $k_\theta^* = 0$; $D_{h,\mathrm{v}}^* = [0.047 - 0.074]$; $D_\theta^* = [0.003 - 0.005]$; $C_{F_{y\,\mathrm{Coulomb}}} = [0.07 - 0.07]$; $C_{M_{\mathrm{Coulomb}}} = [0.015 - 0.021]$.

been tested is related to the fact that the phase lag between the heaving and the pitching motions remains close to the optimal value of 90°. In the previous section, it was shown that the phase lag was shifting toward 180° as the heave natural frequency was exceeding the reduced frequency. Figure 2.12 shows that the heave natural frequency remains below the reduced frequency when varying the dimensionless heaving mass. It is expected that the heave natural frequency would exceed the reduced frequency with smaller dimensionless heaving mass and that the phase lag would then tend toward 180°, as is observed when increasing the dimensionless heave stiffness (see Figs. 2.9a and 2.10). As mentioned earlier, it is unfortunately not possible to test smaller values of dimensionless heaving mass with the current experimental setup.

It can be observed in Figs. 2.9 and 2.11 that the dimensionless heave stiffness and the dimensionless

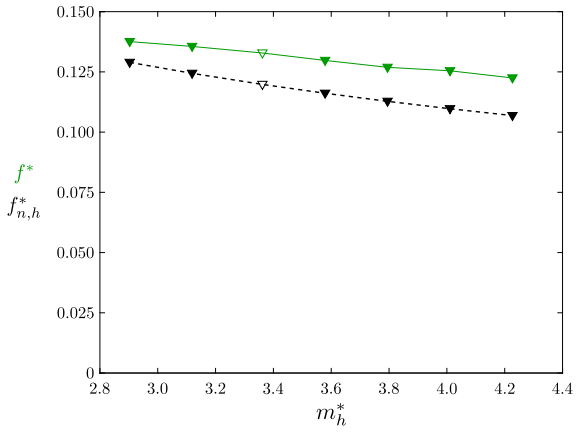

Figure 2.12: Comparison of the reduced frequency (f^* in solid green) and the reduced heave natural frequency ($f^*_{n,h}$ in dashed black) as a function of the dimensionless heaving mass (m^*_h). Empty markers are used to identify the baseline case.

heaving mass have opposite effects on the motions around the baseline case. Indeed, Fig. 2.9 shows that, around the baseline dimensionless heave stiffness coefficient ($k^*_h = 1.91$), the reduced frequency and the pitch amplitude increase while the heave amplitude decreases as the dimensionless heave stiffness is increased. The opposite behavior is observed in Fig. 2.11 for increasing values of the dimensionless heaving mass. This is because the heaving motion is very close to a sine wave for all the cases presented in Figs. 2.9 and 2.11. Consequently, the heave acceleration is also resembling a sine wave, but in antiphase with the heave position. In other words, the inertia term ($m^*_h \ddot{h}^*$) and the stiffness term ($k^*_h h^*$), appearing in Eq. 2.3, have similar shapes as functions of time, but with opposite signs.

Heave damping

For the sake of conciseness, the term dimensionless heave damping is used in this section to refer to the dimensionless heave damping stemming only from the eddy-current brake ($D^*_{h,e}$). The viscous damping contribution coming from the bearings is therefore not included in the analysis. The reader is referred to 2.B.4 for more details about the evaluation of the heave damping. Let us recall that the energy dissipated in the eddy-current brake represents the energy extracted from the flow that could be converted into electricity by an electric generator.

Fig. 2.13 presents the various performance metrics considered as functions of the dimensionless heave damping. It is found that increasing the dimensionless heave damping does not significantly affect the reduced frequency and the phase lag between the heaving and the pitching motions, but it results in a considerable decrease of the heave amplitude, and, to a lesser extent, of the pitch amplitude. In spite of these amplitude decreases, Fig. 2.13c shows that the efficiency remains relatively constant over the range of dimensionless heave damping coefficients that have been tested. However, because of this constant efficiency and the decreasing amplitudes, the power coefficient decreases when increasing

the damping. These observations are very relevant in practice as they suggest that varying the dimensionless heave damping allows controlling the turbine blade amplitudes in heave and in pitch without affecting the efficiency too much. This could be especially useful when such turbines are deployed in an environment restricted in space or if several turbines are positioned in close proximity.

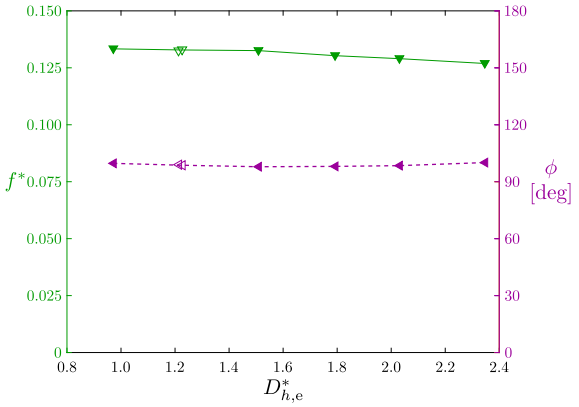

(a) Reduced frequency (solid green) and phase lag between the heaving and the pitching motions (dashed purple)

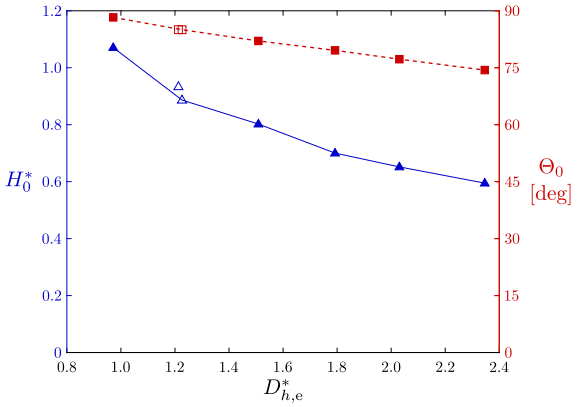

(b) Heave amplitude (solid blue) and pitching amplitude (dashed red)

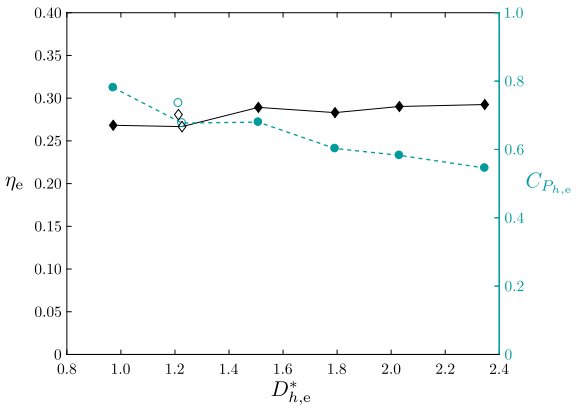

(c) Efficiency (solid black) and power coefficient (dashed turquoise)

Figure 2.13: Various performance metrics as functions of the dimensionless eddy-current brake damping in heave ($D^*_{h,e}$). Empty markers are used to identify the baseline case and the uncertainties are provided in the supplementary material along with the tabulated data used to produce this figure. $m^*_h = 3.36$; $I^*_\theta = 0.091$; $S^* = 0.040$; $k^*_h = 1.91$; $k^*_\theta = 0$; $D^*_{h,v} = [0.047 - 0.074]$; $D^*_\theta = [0.003 - 0.005]$; $C_{F_{y\,\text{Coulomb}}} = [0.07 - 0.07]$; $C_{M_{\text{Coulomb}}} = [0.015 - 0.021]$.

Pitch stiffness

A very different behavior is observed when increasing the dimensionless pitch stiffness. Indeed, Fig. 2.14 shows that the motions are completely damped when $k^*_\theta = 0.154$ or $k^*_\theta = 0.236$. For these two cases, the blade is always returning to its equilibrium position, both in heave and in pitch, even if large heave positions and pitch angles are used as the initial condition. As mentioned in Sec. 2.5.1,

this supports the hypothesis that the blade is subject to the divergence instability, which only occurs when the dimensionless pitch stiffness coefficient is below a given threshold (see Eq. 2.13).

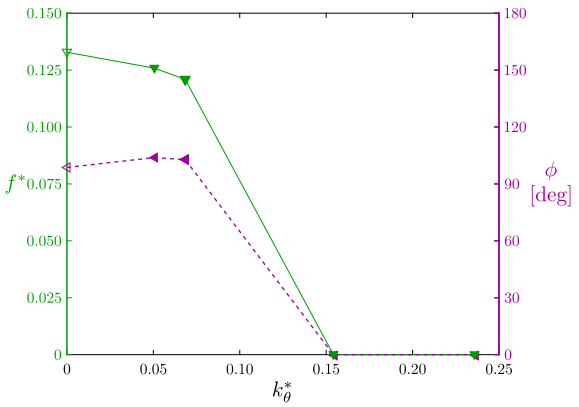

(a) Reduced frequency (solid green) and phase lag between the heaving and the pitching motions (dashed purple)

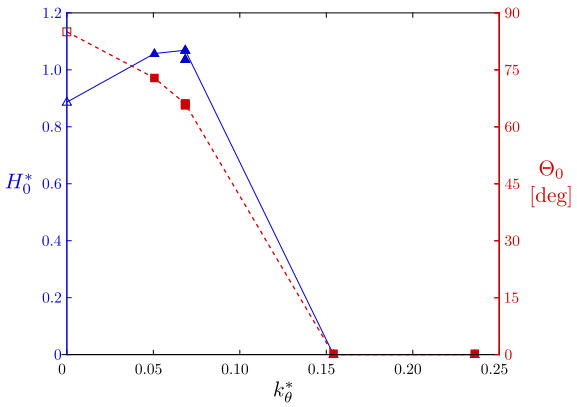

(b) Heave amplitude (solid blue) and pitching amplitude (dashed red)

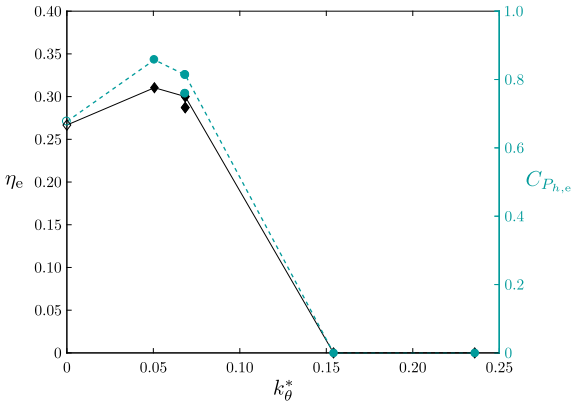

(c) Efficiency (solid black) and power coefficient (dashed turquoise)

Figure 2.14: Various performance metrics as functions of the dimensionless pitch stiffness (k_θ^*). Empty markers are used to identify the baseline case and the uncertainties are provided in the supplementary material along with the tabulated data used to produce this figure. $m_h^* = 3.36$; $I_\theta^* = 0.091$; $S^* = 0.040$; $D_{h,\mathrm{e}}^* = 1.21$; $k_h^* = 1.91$; $D_{h,\mathrm{v}}^* = [0.069 - 0.070]$; $D_\theta^* = [0.002 - 0.002]$; $C_{F_{y\,\mathrm{Coulomb}}} = [0.04 - 0.06]$; $C_{M_{\mathrm{Coulomb}}} = [0.02 - 0.02]$.

Fig. 2.14 also shows that both the efficiency and the power coefficient could increase for non-zero dimensionless pitch stiffness compared to the baseline case, for which the dimensionless pitch stiffness is zero (no pitch springs). Indeed, the maximum efficiency and power coefficient values that have been observed throughout this experimental campaign, namely 31.0% and 0.86, have been obtained with $k_\theta^* = 0.051$. This is the operation point at which the reduced frequency and the pitch natural frequency are the closest to each other, with a difference of about 5% between them. Once again, this good performance is related to the fact that the phase lag between the heaving and the pitching motions is close to the optimal value of 90°. It is worth mentioning that this high efficiency is obtained even if the pitch amplitude considerably decreases when using non-zero dimensionless pitch stiffness

coefficients.

Lastly, it is found that the reduced frequency does not follow the trend of the pitch natural frequency, as it decreases for increasing pitch stiffness coefficients. This suggests once again that the reduced frequency of the passive motions is related to a time scale of the fluid flow around the blade, as mentioned in Section 2.5.2.

Moment of inertia and static moment

The turbine prototype used for the current study allows testing only two different values of the moment of inertia (I_θ) and three different values of the static moment (S). Moreover, with the current turbine design, it is not possible to modify these parameters without slightly affecting the heaving mass, as described in 2.A.2. Indeed, the heaving mass is increased by 4% compared to the baseline case when I_θ or S are varied. Nevertheless, all the tests conducted to assess the effects of the static moment are characterized with this same increased mass value.

The performance metrics of the different cases that have been tested are given in Tables 2.4 and 2.5. One can notice that the variations of both the moment of inertia and the static moment do not significantly affect the turbine permanent response. In the case of the dimensionless static moment, it is found that a larger value results in slightly smaller pitch amplitudes, efficiencies and power coefficients. In future works, it would be useful to extend the range covered by these two parameters to better evaluate their full impact.

Table 2.4: Various performance metrics as functions of the dimensionless moment of inertia about the pitch axis (I_θ^*). The uncertainties are provided in the supplementary material. $S^* = 0.040$; $D_{h,\mathrm{e}}^* = 1.21$; $k_h^* = 1.91$; $k_\theta^* = 0$; $D_{h,\mathrm{v}}^* = [0.047 - 0.074]$; $D_\theta^* = [0.003 - 0.005]$; $C_{F_y\,\mathrm{Coulomb}} = [0.07 - 0.07]$; $C_{M\,\mathrm{Coulomb}} = [0.015 - 0.021]$.

I_θ^*	m_h^*	f^*	ϕ [deg]	H_0^*	Θ_0^*	η_e	$\overline{C_{P_{h,\mathrm{e}}}}$
0.091	$m_h^* = 3.36$	0.131	100	0.911	84.6	26.7%	0.68
0.117	$m_h^* = 3.50$	0.131	97	0.908	87.3	26.5%	0.68

Table 2.5: Various performance metrics as functions of the dimensionless static moment (S^*). The uncertainties are provided in the supplementary material. $m_h^* = 3.50$; $I_\theta^* = 0.117$; $D_{h,\mathrm{e}}^* = 1.21$; $k_h^* = 1.91$; $k_\theta^* = 0$; $D_{h,\mathrm{v}}^* = [0.047 - 0.074]$; $D_\theta^* = [0.003 - 0.005]$; $C_{F_y\,\mathrm{Coulomb}} = [0.07 - 0.07]$; $C_{M\,\mathrm{Coulomb}} = [0.015 - 0.021]$.

S^*	f^*	ϕ [deg]	H_0^*	Θ_0^*	η_e	$\overline{C_{P_{h,\mathrm{e}}}}$
0.023	0.128	99	0.935	86.8	27.3%	0.70
0.040	0.131	97	0.908	87.3	26.5%	0.68
0.056	0.132	95	0.864	87.8	25.1%	0.63

2.5.3 Effect of the inflow velocity on the turbine performance

So far, the effects of varying different dimensionless structural parameters have been presented. These different cases correspond to different designs of the fully-passive flapping-foil concept. In this section, we turn our attention to the effects of varying the inflow velocity (U_∞) for a given set of dimensional structural parameters. Consequently, some dimensionless structural parameters do not remain constant since they vary with U_∞ (see their definitions in Section 2.4.1). Fig. 2.15 therefore provides some information about the response of a specific turbine design, with fixed structural parameters, to different inflow velocities.

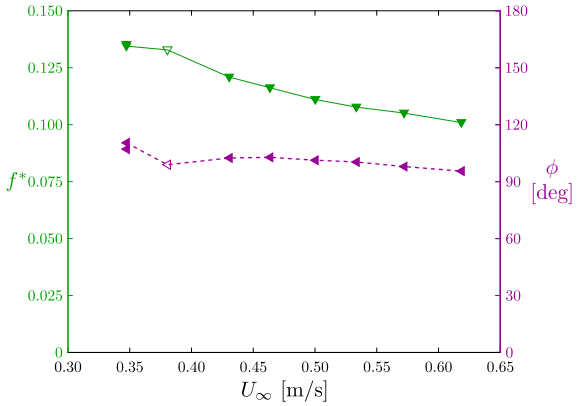

(a) Reduced frequency (solid green) and phase lag between the heaving and the pitching motions (dashed purple)

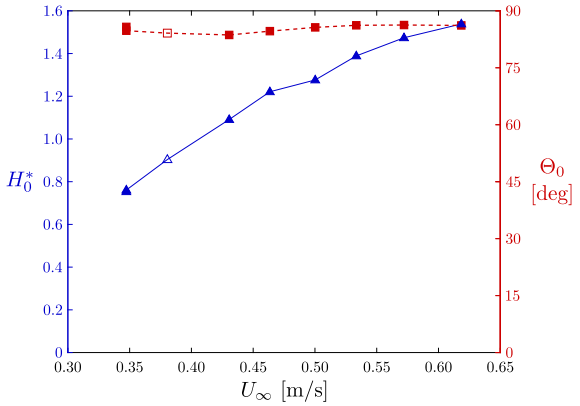

(b) Heave amplitude (solid blue) and pitching amplitude (dashed red)

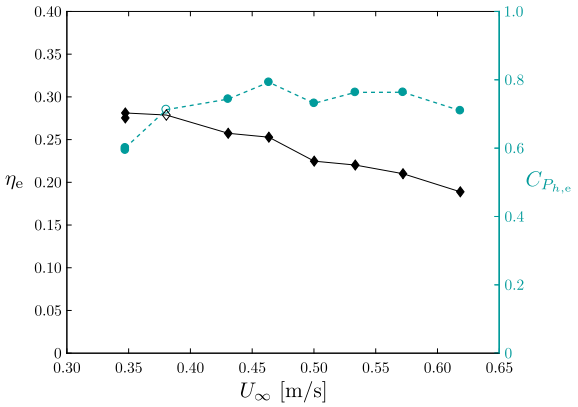

(c) Efficiency (solid black) and power coefficient (dashed turquoise)

Figure 2.15: Various performance metrics as functions of the inflow velocity (U_∞). Empty markers are used to identify the baseline case and the uncertainties are provided in the supplementary material along with the tabulated data used to produce this figure. $m_h^* = 3.36$; $I_\theta^* = 0.091$; $S^* = 0.040$; $D_{h,\mathrm{e}}^* = 1.21$; $k_h^* = 1.91$; $k_\theta^* = 0$; $D_{h,\mathrm{v}}^* = [0.063 - 0.072]$; $D_\theta^* = [0.003 - 0.007]$; $C_{F_{y\,\mathrm{Coulomb}}} = [0.04 - 0.05]$; $C_{M_{\mathrm{Coulomb}}} = [0.01 - 0.01]$; $\mathrm{Re} = 21\,000$ at $U_\infty = 0.38$ m/s (baseline case).

It is found that the phase lag is not significantly altered when the inflow velocity varies from approximately 0.35 m/s to 0.62 m/s. As a result, large efficiencies and power coefficients are still obtained

for all the inflow velocities that have been tested. Even though the efficiency decreases slightly when increasing the inflow velocity, the power coefficient remains relatively constant because of the considerable increase of the heave amplitude. This is a significant finding as this means that the power output that could be converted into electricity by this specific turbine design would not be much affected by the velocity perturbations that could occur in the river or the tidal current in which this turbine would be deployed.

2.6 Conclusion

A fully-passive flapping-foil turbine prototype has been successfully designed and tested in a water channel. This innovative concept may lead to significant simplifications of some previously tested flapping-foil turbine designs, which should yield cheaper and more reliable devices. Large-amplitude periodic motions have been observed and these self-induced and self-sustained motions have led to a very good performance in terms of the efficiency and the power coefficient, which have respectively reached 31.0% and 0.86. The present experimental demonstration therefore confirms the feasibility and the great potential of the fully-passive concept.

Seven structural and inflow parameters have been independently varied around a baseline case. Good performances have been achieved over a large range of parameter values, which is important in practice since this gives some flexibility to the designer of such turbines. Periodic motions of large amplitudes leading to a high efficiency have even been observed with no pitch spring and no heave spring. The phase lag between the heaving and the pitching motions has been found to be a critical factor and it appears to be related to the ratio between the reduced frequency of the turbine blade motions and the heave natural frequency. Moreover, the current results have shown that no sustained motions could be obtained when the dimensionless pitch stiffness coefficient is larger than $k_\theta^* = 0.154$. This is because the divergence instability is believed to be the driving mechanism of the current fully-passive flapping-foil turbine prototype. Consequently, the position of the pitch axis is expected to play a significant role as it is a crucial parameter for the divergence instability (Dowell, 2004; Fung, 2008). This particular aspect should be investigated in future studies along with the effects of the tip losses.

Acknowledgments

Financial support from the Natural Sciences and Engineering Research Council of Canada (NSERC Discovery Grant/RGPIN/121819-2013 and CGS-D scholarship), the Tyler Lewis Clean Energy Research Foundation (2016 TLCERF grant) and the Leadership and Sustainable Development Scholarship Program of Université Laval is gratefully acknowledged by the authors. The authors also wish to thank Marc-André Plourde Campagna, Sylvain Ménard, Yves Jean and Thierry Villeneuve for their help regarding the design and fabrication of the turbine prototype.

Appendix

2.A Structural parameters

2.A.1 Elastic supports

The heaving carriage is attached to the fixed structure of the turbine with extension springs. Two different sets of extension springs can be used and the number of springs attached to the carriage can also be varied from zero spring to a maximum of 6 pairs of springs (12 springs; see Fig. 2.3 where 3 pairs of springs can be seen). In pitch, the number of springs that can be used is limited to either zero or two, but springs with four different stiffness coefficients have been tested. Note that the desired torsional stiffness is obtained through the use of extension springs with one of their end fixed to the carriage and the other end attached to a cable which is fastened to the shaft holding the blade, thereby undergoing the pitching motion, as shown in Fig. 2.A.1. Both the heave springs and the pitch springs can be seen in Fig. 2.3.

As mentioned earlier, a linear damper is used as an energy sink in heave. It consists of a thin aluminum sliding plate which is undergoing the heaving motion and passing, without making contact, between two magnets yoked together with 1020 carbon steel to form an eddy-current brake. This eddy-current brake is shown in Fig. 2.A.2 and a schematic is presented in Fig. 2.A.3. This damper is similar in principle to the one that has been used by Abiru and Yoshitake (2011, 2012) for their flapping-foil turbine with a prescribed pitching motion and a passive heaving motion or by Pigolotti et al. (2017) for their fully-passive flapping-plate setup.

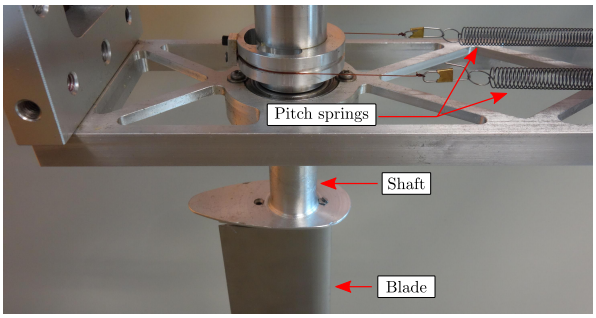

Figure 2.A.1: Pitch springs attached to the shaft holding the turbine blade.

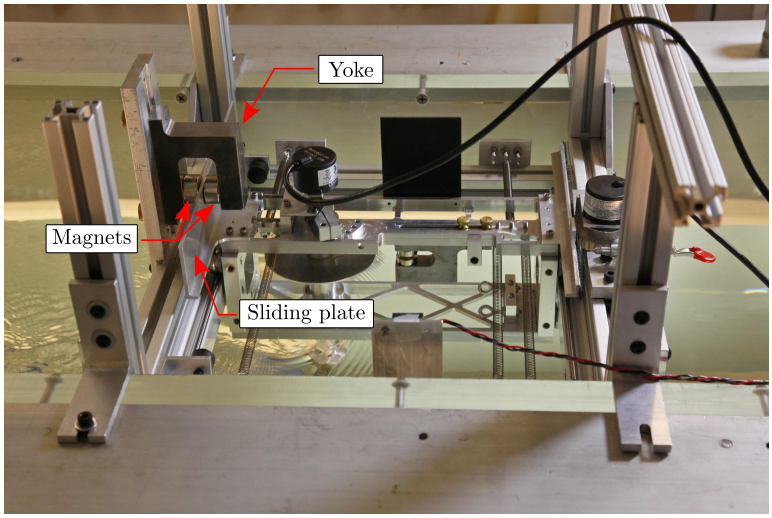

Figure 2.A.2: Eddy-current brake used as the heave damper which provides the desired energy sink.

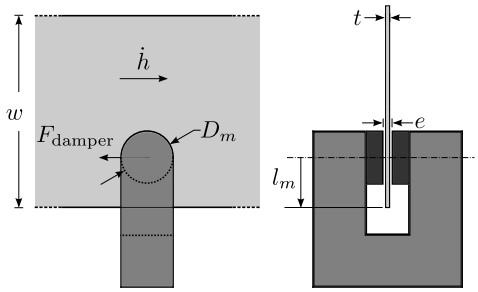

Figure 2.A.3: Schematic of the eddy-current brake. The aluminum sliding plate, the yoke and the magnets are identified with the color varying from the lighter gray to the darker one.

In theory, the resistive force (F_{damper}) acting on the sliding plate of an eddy-current brake is given by (Wouterse, 1991):

$$F_{\text{damper}} = \left(\frac{\pi D_m^2 t B_0^2 K}{4 \rho_e} \right) \dot{h} \,, \tag{2.14}$$

where ρ_e is the electrical resistivity of the sliding plate material, namely aluminum, D_m is the magnet diameter, t is the sliding plate thickness, B_0 is the magnetic field in the middle of the gap (e) between the magnets when the plate is not moving, $\dot{h}$ is the heave velocity and K is a constant given by:

$$K = \frac{1}{2} \left[1 - \frac{\pi^2 D_m}{24 w} \right] \,, \tag{2.15}$$

with w being the width of the plate. The theoretical heave damping coefficient of the eddy-current brake ($D_{h,\text{e theory}}$) is then simply obtained by dividing the resistive force with the heave velocity:

$$D_{h,\text{e theory}} = \frac{\pi D_m^2 t B_0^2 K}{4 \rho_e} \,. \tag{2.16}$$

Table 2.A.1: Design of the heave damper

Parameter	Value
D_m	1 in
e	1/8 in
Magnet thickness	1/2 in
Magnet material	Neodymium (N48)
w	50 mm
t	1/8 in
Plate material	Aluminum

The various parameters characterizing the heave damper are given in Table 2.A.1.

In order to modify the heave damping coefficient, the distance between the center of the magnets and the edge of the sliding plate (see l_m in Fig. 2.A.3) can be varied by moving the yoke so that the magnets can be shifted toward the edge of the sliding plate, thereby reducing the magnetic field passing through the plate and, at the same time, the heave damping coefficient of the eddy-current brake (see Eq. 2.16). A value of $l_m = 0$ corresponds to the center of the magnets being aligned with the edge of the aluminum sliding plate, which is close to what is observed in Fig. 2.A.2.

According to the theory (Gosline et al., 2006), the relation between the heave velocity and the resistive force generated by the eddy-current damper is linear if the heave velocity remains below a critical value. With 1/8 inch aluminum plates, this critical velocity is around 19 m/s and is well above the maximum velocity reached with the prototype during the tests conducted in the water channel.

It is important to note that the theory presented above has only been used to design the damper. The actual heave damping coefficient of the prototype has been determined following a calibration process described in 2.B.4.

2.A.2 Inertial properties

The turbine has been designed to be as light as possible while being able to withstand the forces at play and to limit the deflection of the blade. To increase the heaving mass, some steel bars simply have to be added and fixed to the carriage undergoing the heaving motion. The moment of inertia and the static moment can also be altered by adding components specifically designed for that purpose, which are shown in black in Fig. 2.A.4. Care has been taken so that the modifications of the moment of inertia and the static moment can be made independently. The moment of inertia can be increased by 28.6% with a variation of the static moment of less than 0.2% (left configuration in Fig. 2.A.4). Then, from this increased moment of inertia value, the static moment can be reduced by 42.5% (middle configuration) or increased by 40% (right configuration) without affecting the moment of inertia.

However, for all these cases, the heaving mass is increased by 4% since the components in black in Fig. 2.A.4 need to be added to the setup.

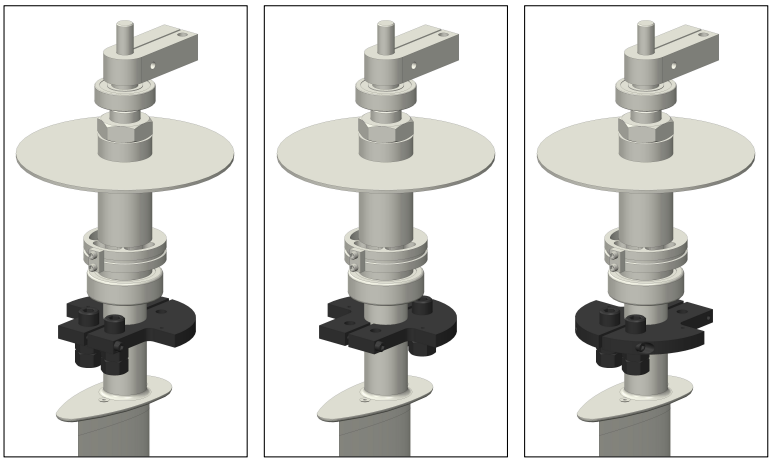

Figure 2.A.4: Components undergoing the pitching motion.The light gray components are always present while the black components are added to the setup when one wants to increase the moment of inertia or to modify the static moment. Increased I_θ + same S (left); Increased I_θ + reduced S (middle); Increased I_θ + increased S (right).

2.B Calibrations

2.B.1 Heave and pitch positions

The heave position is determined from the output voltage of the heave encoder using the following linear relation:

$$h = A_h \cdot (E_h - E_{h_i}) + h_i \ , \tag{2.17}$$

where A_h is the slope of the relation between the heave position (h) and the output voltage (E_h), and h_i and E_{h_i} respectively correspond to the initial heave position and the initial output voltage of the heave encoder.

The equation giving the pitch angle is analogous to Eq. 2.17:

$$\theta = A_\theta \cdot (E_\theta - E_{\theta_i}) + \theta_i \ , \tag{2.18}$$

where A_θ is the calibration constant relating the output voltage of the pitch encoder (E_θ) to a pitch angle (θ), and θ_i and E_{θ_i} correspond to the initial pitch angle and the initial output voltage of the pitch encoder, respectively.

In order to determine the value of the calibration constant A_h in Eq. 2.17, the heaving carriage has been attached to the tool of a machining center (computer numerical control (CNC) milling machine), which allowed us to prescribe two different known heave positions (± 0.09 m) with great accuracy.

The value of A_h has then been obtained using the relation:

$$A_h = \frac{\left(\overline{h_2 - h_1}\right)}{\left(\overline{E_{h_2} - E_{h_1}}\right)} \, , \tag{2.19}$$

where E_h is the output voltage of the heave encoder and the subscripts 1 and 2 correspond to the two prescribed heave positions so that $\left(\overline{h_2 - h_1}\right) = 0.18$ m. The average voltage difference $\left(\overline{E_{h_2} - E_{h_1}}\right)$ has been computed from a total of 100 measurements and is equal to 3.3667 V. The resulting value of A_h is therefore:

$$A_h = 0.05346 \text{ m/V} \, . \tag{2.20}$$

The value of A_θ in Eq. 2.18 has been evaluated using a similar method with the following relation:

$$A_\theta = \frac{\left(\overline{\theta_2 - \theta_1}\right)}{\left(\overline{E_{\theta_2} - E_{\theta_1}}\right)} \, . \tag{2.21}$$

The blade has been successively held at 0° and 30° pitch angles so that $\left(\overline{\theta_2 - \theta_1}\right) = 30°$. This process has been repeated 100 times in order to obtain an accurate estimation of $\left(\overline{E_{\theta_2} - E_{\theta_1}}\right)$, which is 0.2543 V. The resulting value of A_θ is then found to be equal to:

$$A_\theta = 118 \text{ degrees/V} \, . \tag{2.22}$$

Finally, note that the digital-to-analog converter has been set so that its resolution is the same as that of the encoders. In other words, one state of the 14-bit DAC corresponds to one pulse of the encoders.

2.B.2 Springs

A machining center has also been used to determine the stiffness of the different springs. One end of the springs was fixed to the machining center's mill table while the other end was attached to a load cell fastened to the machining center's moving tool. By prescribing different vertical positions of the tool and performing a linear regression analysis, the relation between the force measured with the load cell and the spring elongation could be found:

$$F = k\Delta + F_0 \, , \tag{2.23}$$

where k is the spring stiffness, Δ is the spring elongation, i.e., the distance between the position of the moving end of the spring (extended) and its initial position (not extended), F_0 is the tension force in the spring when the moving end is at its initial position and F is the tension force in the spring for a given elongation. An example of the relation between the force in a spring and its elongation is shown in Fig. 2.B.1. It confirms the linear behavior of the springs.

Since several heave springs could be used in parallel to attach the carriage undergoing the heaving motion to the structure of the turbine, the resultant heave stiffness (k_h) in N/m is given by:

$$k_h = \sum_{i=1}^{N_h} k_i \, , \tag{2.24}$$

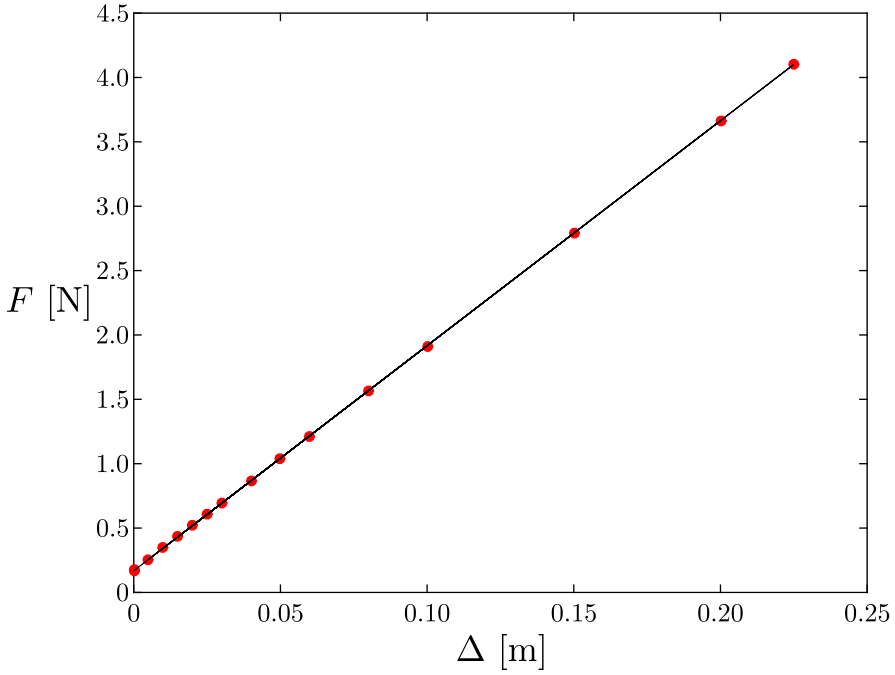

Figure 2.B.1: Measurements of the force (F) as a function of the elongation (Δ) for a given spring (red dots) along with the linear regression curve.

where N_h is the number of heave springs used for a given case and k_i is the stiffness of the i^{th} heave spring.

Regarding the resultant pitch stiffness in N.m/rad, it is given by:

$$k_\theta = (k_1 + k_2)\,\frac{D^2}{4}\,, \tag{2.25}$$

where k_1 and k_2 are the stiffness coefficients of the two extension springs used in pitch and D is the diameter of the groove in the component around which the cable linking both pitch springs is rotating, as seen in Fig. 2.A.1.

Lastly, it is worth mentioning that some springs have been calibrated both before and after the experimental campaign in order to confirm that their stiffness coefficients remained constant over time.

2.B.3 Mass, moment of inertia and static moment

Free vibration tests have been performed independently in heave and in pitch (with the other degree of freedom fixed in place) at a sampling frequency of 5000 Hz to determine the mass undergoing the heaving motion (m_h) and the moment of inertia (I_θ). These tests have been conducted in ambient air so that the fluid forces are negligible compared to the friction in the bearings. The blade, the end plate and the screws needed to fasten them together and to fix them to the shaft undergoing the pitching motion were not in place during the free vibration tests in heave. As a result, only a fraction of the total heaving mass has been evaluated using this method. The remaining mass fraction has been

determined by weighing the other components individually and summing their masses. The reason for not simply weighing all the components undergoing the heaving motion is that using free vibration tests is a simple and straightforward method allowing us to evaluate the equivalent mass stemming from the rotation of some components such as the linear guided roller bearings and that of the heave springs which are not moving as rigid bodies with the carriage since one of their end is attached to the fixed turbine structure.

The fraction of the heaving mass ($m_{h\,\text{free}}$) present during the free vibration tests has been determined using the following relation:

$$m_{h\,\text{free}} = k_h / \omega_{n,h\,\text{free}}^2 \,, \tag{2.26}$$

where k_h is the heave stiffness, which is known following the calibration described in 2.B.2, and $\omega_{n,h\,\text{free}}$ is the heave natural frequency of the components present during the free vibration tests. However, as there was some viscous friction in heave even if the heave damper was not present during these tests due to presence of the linear guided roller bearings, the carriage did not exactly oscillate at its natural frequency ($\omega_{n,h\,\text{free}}$), but rather at its damped natural frequency ($\omega_{d,h\,\text{free}}$):

$$\omega_{n,h\,\text{free}} = \frac{\omega_{d,h\,\text{free}}}{\sqrt{1-\zeta_h^2}} \,, \tag{2.27}$$

where ζ_h is the damping ratio in heave, whose evaluation is described in the next subsection. The heaving mass of the components involved in the free vibration tests has therefore been computed using the equation:

$$m_{h\,\text{free}} = \frac{k_h\, T_{h\,\text{free}}^2 \left(1-\zeta_h^2\right)}{4\pi^2} \,, \tag{2.28}$$

where $T_{h\,\text{free}}$ is the oscillation period ($T_{h\,\text{free}} = 2\pi/\omega_{d,h\,\text{free}}$).

The same procedure has been used to determine the moment of inertia (I_θ), resulting in the equation:

$$I_\theta = \frac{k_\theta\, T_\theta^2 \left(1-\zeta_\theta^2\right)}{4\pi^2} \,, \tag{2.29}$$

Note that, unlike the heaving mass, all the components undergoing the pitching motion were in place during the free vibration tests as the individual contribution of a single component to the total moment of inertia cannot be easily estimated. The average period evaluated from 15 to 120 complete oscillations, recorded during a few free vibration tests, have been used to evaluate the period of oscillation $T_{h\,\text{free}}$, while 20 to 40 oscillations have been used for T_θ.

Determining the static moment using free vibration tests would have involved the computation of the pitch and heave accelerations which would therefore have been much less accurate than the computation of the heaving mass and the moment of inertia. Consequently, the static moment has rather been determined using a 3D computer model produced with a computer-aided design (CAD) software to localize the center of mass of each components undergoing the pitching motion. Knowing the volume of these components from the CAD and their mass using a weighing scale, their density could be computed and set in the computer model. The position of the center of mass could then be accurately

evaluated from the CAD software. In order to validate this procedure, the moment of inertia has been computed from the CAD and compared to the value obtained from the free vibration tests. The difference between the values obtained from both methods is below 1% for all the different moment of inertia values.

The static moment of each component undergoing the pitching motion has been found by multiplying their mass with the distance between their center of mass and the pitch axis (x_θ) (see Fig. 2.1 and Table 2.1 for the sign convention). The total static moment is then simply given by:

$$S = \sum_{i=1}^{N_\theta} (m_i x_{\theta,i}) \ , \tag{2.30}$$

where N_θ is the number of components involved in the pitching motion and m_i is the mass of the i$^{\text{th}}$ component undergoing the pitching motion.

2.B.4 Linear damping and Coulomb friction

The friction in heave and in pitch is considered to be a sum of linear (viscous) and Coulomb contributions. A simplified model of the Coulomb friction is considered for which the friction force ($f_{y\,\text{Coulomb}}$) and moment ($m_{\,\text{Coulomb}}$) are constant and acting in the opposite directions than the heave and pitch velocities:

$$F_{y\,\text{Coulomb}} = -f_{y\,\text{Coulomb}}\ \text{sign}(\dot{h}) \ , \tag{2.31}$$

$$M_{\,\text{Coulomb}} = -m_{\,\text{Coulomb}}\ \text{sign}(\dot{\theta}) \ . \tag{2.32}$$

Using this assumption and following the procedure described in the work of Feeny and Liang (1996), the linear damping and Coulomb friction contributions of a given degree of freedom can be evaluated from a single free vibration test with the other degree of freedom being held in place, as has been done to evaluate the mass and the moment of inertia (see 2.B.3).

To determine the linear damping contribution, the parameter β has first been determined using:

$$\beta = -\frac{1}{\pi} \ln\left(-\frac{(X_{i+1} - X_{i-1})}{(X_i - X_{i-2})} \right) \ , \tag{2.33}$$

where X_i is the i^{th} peak value in heave or in pitch of a free vibration test. This parameter is then used to compute the damping ratio (ζ) of a given degree of freedom:

$$\zeta = \frac{\beta}{\sqrt{1+\beta^2}} \ , \tag{2.34}$$

from which the linear damping coefficients in heave (D_h) and in pitch (D_θ) can be evaluated:

$$D_h = 2\,\zeta_h \sqrt{k_h\, m_h} \ , \tag{2.35}$$

$$D_\theta = 2\,\zeta_\theta \sqrt{k_\theta\, I_\theta} \ . \tag{2.36}$$

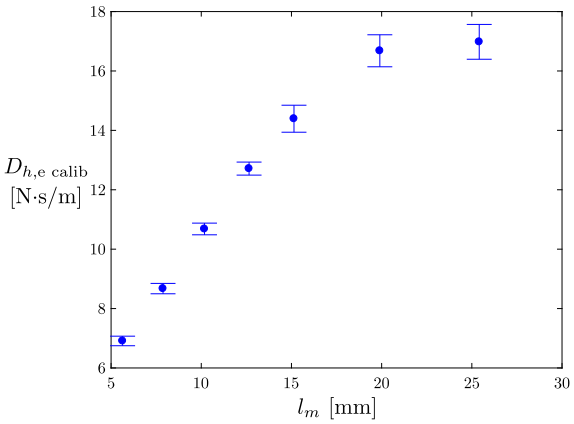

Figure 2.B.2: Contribution of the eddy-current brake to the heave damping coefficient ($D_{h,\mathrm{e}}$) as a function of the distance between the center of the magnets and the edge of the sliding plate (l_m). Note that l_m is zero when the center of the magnets is aligned with the edge of the sliding plate and is positive when the magnets are shifted toward the center of the sliding plate (see Fig. 2.A.3).

Note that this method allows computing the total linear damping (D_h) and therefore includes both the contribution of the eddy-current brake ($D_{h,\mathrm{e}}$) and the friction in the heave bearings ($D_{h,\mathrm{v}}$). The value of $D_{h,\mathrm{v}}$ can be easily determined as it is equal to D_h when the eddy-current brake is removed from the setup. As a result, the value of $D_{h,\mathrm{e}}$ can be evaluated for different positions of the magnets (l_m) by performing successive free vibration tests, including a case without the eddy-current brake:

$$D_{h,\mathrm{e\ calib}} = D_{h\ \mathrm{calib}} - D_{h,\mathrm{v\ calib}}\ , \tag{2.37}$$

and the results are presented in Fig. 2.B.2.

The different positions of the magnets tested during the calibration of the eddy-current brake have been chosen to match those used during the tests conducted in the water channel. Nevertheless, the positions of the magnets were not exactly the same and a linear interpolation has been performed to obtain a more accurate value of the eddy-current brake damping during the tests in the channel for a given position of the magnets (l_m). Moreover, one can notice from the theory (see Eq. 2.16) that the eddy-current brake damping varies with temperature since the magnets' magnetic field (B_0) and the electrical resistivity of aluminum (ρ_e) are temperature dependent. The eddy-current brake damping therefore needs to be corrected to take into account the temperature difference (ΔT) of the aluminum sliding plate between the time at which a given test is conducted and the time at which the calibration has been carried out. The eddy-current brake damping coefficient value for a given test is therefore given by:

$$D_{h,\mathrm{e}} = \frac{\left(1+\alpha_{B_0}\Delta T\right)^2}{\left(1+\alpha_{\rho_e}\Delta T\right)} D_{h,\mathrm{e\ calib}}\ , \tag{2.38}$$

with:

$$\Delta T = T - T_{\mathrm{calib}}\ , \tag{2.39}$$

where T is the temperature of the aluminum sliding plate during a given test, T_{calib} is its temperature during the calibration process (25.5 °C), $D_{h,\text{e calib}}$ is the linearly interpolated eddy-current brake damping coefficient evaluated during the calibration for a given position of the magnets, α_{B_0} is the temperature coefficient of the magnetic field given by (Pyrhonen et al., 2014):

$$\alpha_{B_0} = -0.0012\ {}^{\circ}C^{-1}\ , \tag{2.40}$$

and α_{ρ_e} is the temperature coefficient of the electrical resistivity, which has a value of (Haynes, 2015):

$$\alpha_{\rho_e} = 0.0044\ {}^{\circ}C^{-1}\ , \tag{2.41}$$

around 24.85°C.

Note that the variations of the ambient temperature during the experimental campaign, which took place over several weeks, have resulted in a maximum difference between the ambient temperature during a test and the ambient temperature during the calibration of approximately 4 °C, which corresponds to a variation of the damping coefficient by less than 3%.

Since most of the energy extracted from the flow is dissipated as heat in the aluminum sliding plate of the eddy-current brake, an increase of the aluminum sliding plate temperature during a single test would not have been surprising. However, the plate temperature has been measured with an infrared thermometer at the beginning and at the end of every test conducted in the channel, each lasting 2 minutes, and the temperature difference was always equal or below 0.2 °C. Consequently, the eddy-current brake damping can be considered to be constant during a given test since its variation due to the temperature differences occurring during a single test is below 0.1%, which is smaller than the damping coefficient uncertainty.

Regarding the Coulomb friction contributions, the constant friction force and moment (See Eqs. 2.31 and 2.32) are given by:

$$f_{y\,\text{Coulomb}} = C_h\, k_h\ , \tag{2.42}$$

$$m_{\,\text{Coulomb}} = C_\theta\, k_\theta\ , \tag{2.43}$$

where C_h and C_θ are Coulomb friction parameters that are evaluated using the following equation with the corresponding variables in heave and in pitch:

$$C = \frac{\left[(X_{i+1} - X_i) + \mathrm{e}^{-\beta\,\pi}\,(X_i - X_{i-1})\right]}{2\left(1 + \mathrm{e}^{-\beta\,\pi}\right)}\ , \tag{2.44}$$

These formulations eliminate the bias that would arise from nonzero equilibrium positions in heave and in pitch since subtractions of successive positive and negative peak values are used in Eqs. 2.33 and 2.44. Moreover, these two equations have been generalized to consider all the peak values from each free vibration tests instead of just two pairs of successive peaks. Lastly, the aerodynamic drag of the turbine components located above the water has been found to be negligible compared to the friction in the bearings, even when considering the largest velocities that have been reached during the whole experimental campaign.

2.C Validation of the calibrations

In order to validate the parameter values determined from the calibrations, the equations of motion (Eqs. 2.3 and 2.4) have been solved numerically with second-order schemes and the results have been compared with free vibration tests carried out with the experimental setup. These tests have been conducted in ambient air and without the blade. Consequently, the numerical solver did not need to solve the Navier-Stokes equations because the aerodynamic drag (in the air) of the remaining moving components is negligible compared to the other contributions in the equations of motion. First, the results from one-degree-of-freedom free vibration tests in heave and in pitch are presented in Figs. 2.C.1 and 2.C.2.

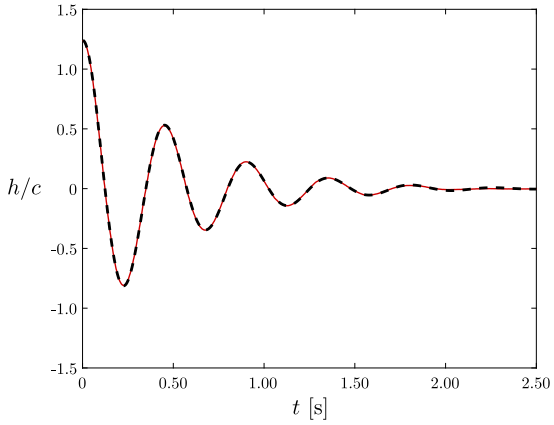

Figure 2.C.1: Comparison between the experimental data (solid red line) and the numerical solution (dashed black line) of a free vibration test in heave with the blade being held at $\theta = 0°$. $m_h = 2.54$ kg; $D_h = 9.4$ N.s/m; $k_h = 503.4$ N/m; $f_{y\,\text{Coulomb}} = 0.1$ N.

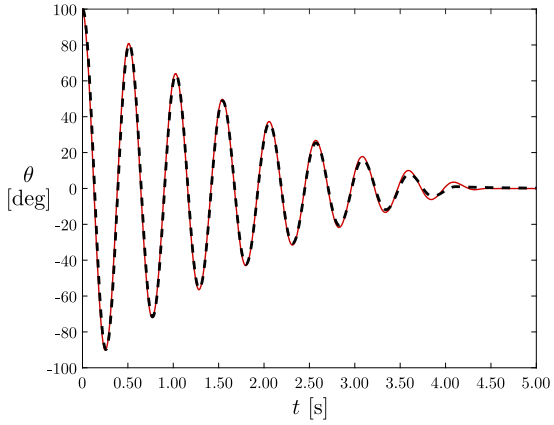

Figure 2.C.2: Comparison between the experimental data (solid red line) and the numerical solution (dashed black line) of a free vibration test in pitch with the blade being held at $h/c = 0$. $I_\theta = 2.23 \times 10^{-4}$ Kg.m^2; $D_\theta = 1.28 \times 10^{-4}$ N.m.s/rad; $k_\theta = 0.0333$ N.m/rad; $m_{\,\text{Coulomb}} = 9 \times 10^{-4}$ N.m.

As the frequencies of the experimental signals agree well with those of the numerical solutions, one can conclude that the evaluation of the heaving mass (m_h), the heave stiffness (k_h), the moment of

inertia (I_θ) and the pitch stiffness (k_θ) are accurate. Furthermore, the fact that the amplitudes also agree well with each other validate that the estimations of the linear damping and Coulomb friction contributions are also correct. This leaves the evaluation of the static moment which could not be confirmed with a 1-DOF free vibration test since this parameter couples the heaving and the pitching motions. A 2-DOF free vibration in the air has therefore been carried out and the results are presented in Fig. 2.C.3. Once again, a good match between the experimental results and the numerical simulation is observed for both degrees of freedom, hence confirming that all the structural parameters have been correctly evaluated.

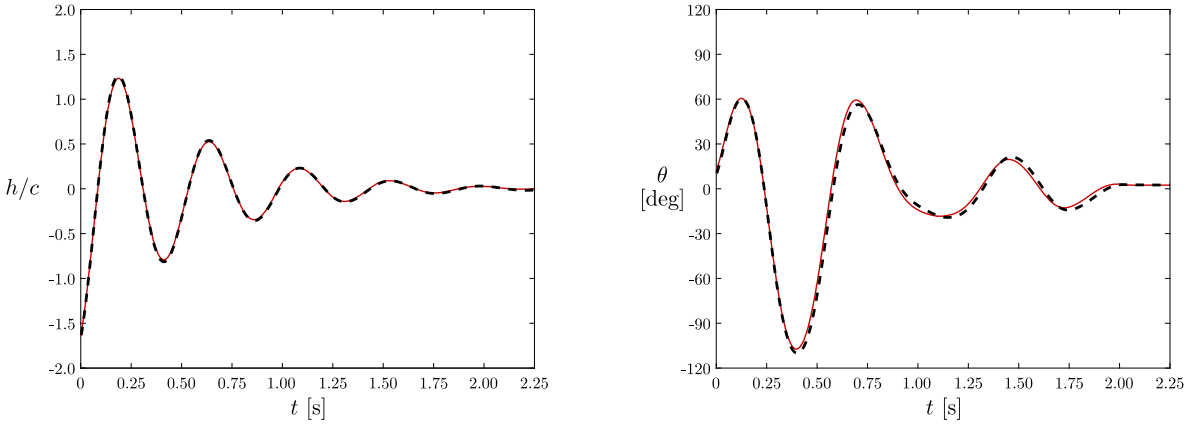

(a) Heave (b) Pitch

Figure 2.C.3: Comparison between the experimental data (solid red lines) and the numerical solution (dashed black lines) of a free vibration test involving both degrees of freedom. $m_h = 2.54$ kg, $I_\theta = 1.01 \times 10^{-4}$ Kg.m^2, $S = -0.00131$ kg.m; $D_h = 9.4$ N.s/m; $k_h = 503.4$ N/m; $k_\theta = 0.0097$ N.m/rad; $D_\theta = 3.8 \times 10^{-5}$ N.m.s/rad; $f_{y\,\text{Coulomb}} = 0.1$ N; $m_{\,\text{Coulomb}} = 9 \times 10^{-4}$ N.m.

Bibliography

Abiru, Hisanori and Yoshitake, Akira. Study on a Flapping Wing Hydroelectric Power Generation System. *Journal of Environment and Engineering*, 6(1):178–186, 2011.

Abiru, Hisanori and Yoshitake, Akira. Experimental Study on a Cascade Flapping Wing Hydroelectric Power Generator. *Journal of Energy and Power Engineering*, 6(9):1429–1436, 2012.

Amandolese, X., Michelin, S., and Choquel, M. Low speed flutter and limit cycle oscillations of a two-degree-of-freedom flat plate in a wind tunnel. *Journal of Fluids and Structures*, 43:244–255, 2013.

Deng, Jian, Teng, Lubao, Pan, Dingyi, and Shao, Xueming. Inertial effects of the semi-passive flapping foil on its energy extraction efficiency. *Physics of Fluids*, 27(5):053103 (17 pp.) –, 2015.

Derakhshandeh, J.F., Arjomandi, M., Dally, B., and Cazzolato, B. Flow-induced vibration of an elastically mounted airfoil under the influence of the wake of a circular cylinder. *Experimental Thermal and Fluid Science*, 74:58 – 72, 2016.

Dowell, E. H. *A Modern Course in Aeroelasticity Fourh Revised and Enlarged Edition*. Kluwer Academic Publishers, Dordrecht, The Netherlands, 4$^{\text{th}}$ edition, 2004.

Farthing, S. P. Binary flutter as an oscillating windmill — scaling & linear analysis. *Wind Engineering*, 37(5):483–499, 2013.

Feeny, B.F. and Liang, J.W. A decrement method for the simultaneous estimation of coulomb and viscous friction. *Journal of Sound and Vibration*, 195(1):149 – 154, 1996.

Fung, Y.C. *An Introduction to the Theory of Aeroelasticity*. Dover Publications, Mineola, New York, USA, 2008.

Gosline, Andrew H., Campion, Gianni, and Hayward, Vincent. On the Use of Eddy Current Brakes as Tunable, Fast Turn-On Viscous Dampers For Haptic Rendering. In *Proc. Eurohaptics 2006*, pages 229–234, 2006.

Griffith, Martin D., Jacono, David Lo, Sheridan, John, and Leontini, Justin S. Passive heaving of elliptical cylinders with active pitching – from cylinders towards flapping foils. *Journal of Fluids and Structures*, 67:124 – 141, 2016.

Haynes, W.M. *CRC Handbook of Chemistry and Physics*. CRC Press, Boca Raton, FL, USA, 96$^{\text{th}}$ edition, 2015.

Huxham, G. H., Cochard, S., and Patterson, J. Experimental Parametric Investigation of an Oscillating Hydrofoil Tidal Stream Energy Converter. In *Proceedings of the 18th Australasian Fluid Mechanics Conference*, Launceston, Australia, 2012.

Kim, Daegyoum, Strom, Benjamin, Mandre, Shreyas, and Breuer, Kenneth. Energy harvesting performance and flow structure of an oscillating hydrofoil with finite span. *Journal of Fluids and Structures*, 70:314 – 326, 2017.

Kinsey, Thomas and Dumas, Guy. Parametric Study of an Oscillating Airfoil in a Power-Extraction Regime. *AIAA Journal*, 46(6):1318–1330, 2008.

Kinsey, Thomas and Dumas, Guy. Computational Fluid Dynamics Analysis of a Hydrokinetic Turbine Based on Oscillating Hydrofoils. *Journal of Fluids Engineering*, 134(2):021104 (16 pp.) –, 2012.

Kinsey, Thomas and Dumas, Guy. Optimal Operating Parameters for an Oscillating Foil Turbine at Reynolds Number 500,000. *AIAA Journal*, 52(9):1885–1895, 2014.

Kinsey, Thomas, Dumas, Guy, Lalande, G., Ruel, J., Mehut, A., Viarouge, P., Lemay, J., and Jean, Y. Prototype testing of a hydrokinetic turbine based on oscillating hydrofoils. *Renewable Energy*, 36 (6):1710 – 1718, 2011.

McKinney, William and DeLaurier, James. Wingmill: An Oscillating-Wing Windmill. *Journal of Energy*, 5(2):109–115, 1981.

Munson, Bruce Roy. *Fundamentals of fluid mechanics*. John Wiley & Sons, Hoboken, NJ, USA, 7th edition, 2013.

Peng, Zhangli and Zhu, Qiang. Energy harvesting through flow-induced oscillations of a foil. *Physics of Fluids*, 21(12):174–191, 2009.

Pigolotti, Luca, Mannini, Claudio, Bartoli, Gianni, and Thiele, Klaus. Critical and post-critical behaviour of two-degree-of-freedom flutter-based generators. *Journal of Sound and Vibration*, 404: 116 – 140, 2017.

Pyrhonen, Juha, Jokinen, Tapani, and Hrabovcová, Valeria. *Design of rotating electrical machines*. Wiley, Chichester, West Sussex, United Kingdom, 2nd edition, 2014.

Shimizu, Eriko, Isogai, Koji, and Obayashi, Shigeru. Multiobjective Design Study of a Flapping Wing Power Generator. *Journal of Fluids Engineering*, 130(2):021104 (8 pp.) –, 2008.

Sitorus, Patar Ebenezer, Le, Tuyen Quang, Ko, Jin Hwan, Truong, Tri Quang, and Park, Hoon Cheol. Design, implementation, and power estimation of a lab-scale flapping-type turbine. *Journal of Marine Science and Technology*, 2015.

Spalart, Philippe. R. and Allmaras, Steven R. A One-Equation Turbulence Model for Aerodynamic Flows. *Recherche Aérospatiale*, (1):5–21, 1994.

Teng, Lubao, Deng, Jian, Pan, Dingyi, and Shao, Xueming. Effects of non-sinusoidal pitching motion on energy extraction performance of a semi-active flapping foil. *Renewable Energy*, 85:810 – 818, 2016.

Veilleux, Jean-Christophe. Optimization of a Fully-Passive Flapping-Airfoil Turbine. Master's thesis, Université Laval, Québec, Qc, Canada, 2014.

Veilleux, Jean-Christophe and Dumas, Guy. Numerical optimization of a fully-passive flapping-airfoil turbine. *Journal of Fluids and Structures*, 70:102 – 130, 2017.

Wang, Zhuo, Du, Lin, Zhao, Jisheng, and Sun, Xiaofeng. Structural response and energy extraction of a fully passive flapping foil. *Journal of Fluids and Structures*, 72:96 – 113, 2017.

Wouterse, J.H. Critical torque and speed of eddy current brake with widely separated soft iron poles. *Electric Power Applications, IEE Proceedings B*, 138(4):153–158, 1991.

Wu, J., Qiu, Y. L., Shu, C., and Zhao, N. Pitching-motion-activated flapping foil near solid walls for power extraction: A numerical investigation. *Physics of Fluids*, 26(8):083601, 2014.

Wu, J., Chen, Y. L., and Zhao, N. Role of induced vortex interaction in a semi-active flapping foil based energy harvester. *Physics of Fluids*, 27(9):093601, 2015.

Xiao, Qing and Zhu, Qiang. A review on flow energy harvesters based on flapping foils. *Journal of Fluids and Structures*, 46:174–191, 2014.

Xu, G.D., Xu, W.H., and Dai, J. Numerical and experimental study of a flapping foil generator. *Applied Ocean Research*, 63:242 – 250, 2017.

Young, John, Lai, Joseph C. S., and Platzer, Max F. A review of progress and challenges in flapping foil power generation. *Progress in Aerospace Sciences*, 67:2–28, 2014.

Zhan, Jiapu, Xu, Bing, Wu, Jie, and Wu, Jing. Power extraction performance of a semi-activated flapping foil in gusty flow. *Journal of Bionic Engineering*, 14(1):99 – 110, 2017.

Zhu, Qiang. Optimal frequency for flow energy harvesting of a flapping foil. *Journal of Fluid Mechanics*, 675:495–517, 5 2011.

Zhu, Qiang. Energy harvesting by a purely passive flapping foil from shear flows. *Journal of Fluids and Structures*, 34:157–169, 2012.

Zhu, Qiang and Peng, Zhangli. Mode coupling and flow energy harvesting by a flapping foil. *Physics of Fluids*, 21(3):033601 (10 pp.) –, 2009.

Zhu, Qiang, Haase, Max, and Wu, Chin H. Modeling the capacity of a novel flow-energy harvester. *Applied Mathematical Modelling*, 33(5):2207–2217, 2009.

Chapter 3

Paper II:

Investigation of the energy-extraction regime of a novel semi-passive flapping-foil turbine concept with a prescribed heaving motion and a passive pitching motion

3.1 Résumé

Due à la complexité inhérente aux mécanismes requis pour imposer les mouvements de pilonnement et de tangage des turbines à aile oscillante optimales, plusieurs groupes de recherche se sont tournés vers l'utilisation de mouvements non contraints. L'amplitude, la phase et la fréquence de tels mouvements passifs dépendent de l'interaction de l'aile avec l'écoulement et ses supports élastiques, soit des ressorts et des amortisseurs. Plus spécifiquement, ce travail propose un concept novateur de turbine à aile oscillante semi-passive pour laquelle le mouvement de pilonnement est contraint alors que le mouvement de tangage est passif. Des simulations numériques en deux dimensions ont été réalisées à un nombre de Reynolds de 3.9×10^6 basé sur la corde avec un point de pivot situé au quart de corde de l'aile. Une étude paramétrique a été menée en variant la valeur du moment statique, un paramètre impliquant la distance entre les positions du centre de masse et du point de pivot, et la fréquence du mouvement imposé en pilonnement. Plusieurs types de réponse ont été observés incluant une réponse correspondant à un régime d'extraction d'énergie caractérisé par des mouvements périodiques de grandes amplitudes avec un déphasage entre les mouvements de pilonnement et de tangage se situant entre 90° et 105°. Une efficacité maximale de 45.4% a été atteinte, confirmant ainsi le grand potentiel de ce concept de turbine. Ce travail démontre qu'une telle performance est obtenue lorsque le centre de masse de l'aile est situé en aval du point de pivot et lorsque qu'aucun tourbillon

de bord d'attaque n'est généré.

3.2 Abstract

Due to the inherent complexity of the mechanisms needed to prescribe the heaving and the pitching motions of optimal flapping-foil turbines, several research groups are now investigating the potential of using unconstrained motions. The amplitude, the phase and the frequency of such passive motions are resulting from the interaction of the foil with the flow and its elastic supports, namely springs and dampers. More specifically, this work proposes an innovative semi-passive flapping-foil turbine concept with a prescribed sinusoidal heaving motion and a passive pitching motion. Two-dimensional numerical simulations have been carried out at a Reynolds number of 3.9×10^6 based on the chord length with a foil having its pitch axis located at the quarter-chord point. A parametric study has been conducted by varying the value of the static moment, which involves the distance between the center of mass and the pitch axis, and the frequency of the prescribed heaving motion. Different responses of the foil have been observed and one of them corresponds to an energy-extraction regime that is characterized by periodic limit-cycle oscillations of large amplitudes with a phase lag between the heaving and the pitching motions ranging between 90° and 105°. A maximum efficiency of 45.4% has been reached, hence confirming the great potential of this turbine concept. This works shows that such good performance is achieved when the center of mass of the foil is located downstream of the pitch axis and when no leading-edge vortices are formed.

3.3 Introduction

3.3.1 Context

By constraining a foil to undergo combined heave (translational) and pitch (rotational) motions with adequate kinematics, it is possible to extract a significant amount of energy from a fluid flow (Young et al., 2014; Xiao and Zhu, 2014). This concept is known as the flapping-foil turbine and it has primarily been developed with the objective of using it as a hydrokinetic turbine to extract energy from rivers or tidal currents. Efficiencies exceeding 40% have been obtained when prescribing appropriate heave and pitch motions (Kinsey and Dumas, 2014), which results in what we refer to as a fully-constrained flapping-foil turbine. However, prescribing these motions presents several challenges regarding the design of such a device. Indeed, the mechanisms that are used to achieve the desired foil motions are complex, which can affect the costs and the reliability of the apparatus. Furthermore, the complexity of these mechanisms can also result in significant power losses due to the friction occurring in the large number of moving components involved, as reported by Kinsey et al. (2011).

An alternative consisting in a device for which only the pitch motion is prescribed has been proposed (Abiru and Yoshitake, 2011, 2012; Chen et al., 2018; Deng et al., 2015; Derakhshandeh et al., 2016; Griffith et al., 2016; Huxham et al., 2012; Shimizu et al., 2008; Sitorus et al., 2015; Teng et al.,

2016; Wu et al., 2014, 2015; Zhan et al., 2017; Zhu et al., 2009; Zhu and Peng, 2009). The heave motion is then said to be passive as the foil is elastically supported with springs and dampers for this degree of freedom instead of being connected to the turbine structure with rigid links. As a result, the heave motion cannot be prescribed and rather results from the interaction of the pitching foil with its elastic supports and the flow. The use of this simplified turbine concept, known in the literature as the semi-passive flapping-foil turbine, allows getting rid of the complex coupling mechanisms linking both degrees of freedom that are needed in the case of the fully-constrained concept. Efficiencies exceeding 30% were reported by Deng et al. (2015) and Teng et al. (2016), who carried out 2D unconfined numerical simulations, while Abiru and Yoshitake (2011, 2012) and Huxham et al. (2012) conducted experiments in water channels and measured efficiencies reaching 20%. Griffith et al. (2016) evaluated the energy-extraction potential of a device for which the foil was replaced by different elliptical cylinders having an aspect ratio ranging from 1 (circular cylinder) to 6. They showed that the amount of energy extracted is increasing as the aspect ratio of the elliptical cylinder is increased, hence suggesting that a foil geometry is optimal for this type of turbine and that turbines solely relying on the vortex-induced vibration phenomenon are less efficient. While this semi-passive flapping-foil turbine concept is simpler than its fully-constrained counterpart, it still requires an actuator and a controller in pitch in addition to an electric generator in heave, the latter being usually modeled as a viscous damper.

A simpler device for which both degrees of freedom are independent and elastically supported has also been proposed and is known as the fully-passive flapping-foil turbine concept (Peng and Zhu, 2009; Veilleux and Dumas, 2017; Zhu, 2012; Wang et al., 2017; Boudreau et al., 2018). Again, no coupling mechanism is needed with such a device but, unlike the semi-passive concept presented above, no actuator and no controller are required in pitch. A few numerical studies showed that different types of response can be observed by varying the values of the structural parameters governing the turbine dynamics and the flow characteristics (Peng and Zhu, 2009; Veilleux and Dumas, 2017; Wang et al., 2017). Among these different responses, only one is appropriate in an energy extraction perspective and it is characterized by large amplitudes and periodic heave and pitch motions. This regular response was also observed experimentally by Boudreau et al. (2018) using a fully-passive turbine prototype in a water channel. The sensitivity of the turbine performance to seven different parameters affecting the turbine dynamics was evaluated and a maximum efficiency of 31% was reported by the authors. While this performance has confirmed the potential of the fully-passive turbine concept, it does not match the best performance reported for the fully-constrained flapping-foil turbine yet.

The studies conducted on the fully-passive flapping-foil turbine have demonstrated that it is possible to achieve a good level of performance with a passive pitch motion. Since most of the energy extracted by flapping-foil turbines comes from the heave motion (Kinsey and Dumas, 2008, 2014; Zhu, 2011), it is logical to connect an electric generator to this degree of freedom, thereby allowing one to constrain this motion. Following this idea, the current work proposes a novel semi-passive flapping-foil turbine concept for which the heave motion is prescribed and the pitch motion is passive. This results in a

simpler device than the other semi-passive turbine version described above since no actuator and no controller are required in pitch. The objective of this study consists in evaluating the potential of this innovative flapping-foil turbine concept compared to the other turbine designs that have already been proposed. Moreover, this work aims at developing a fundamental understanding of the dynamics of passive pitch motions, which is not only relevant for the semi-passive flapping-foil turbine proposed in this work, but also for the fully-passive flapping-foil turbine concept. This is achieved by varying the static moment, which is a structural parameter involving the distance between the center of mass and the pitch axis that has not received a lot of attention in the literature so far. Indeed, most of the studies conducted on semi-passive and fully-passive flapping-foil turbines either considered a pitch axis coinciding with the center of mass (Abiru and Yoshitake, 2011, 2012; Deng et al., 2015; Griffith et al., 2016; Shimizu et al., 2008; Teng et al., 2016; Wu et al., 2014, 2015; Zhan et al., 2017) or massless foils (Peng and Zhu, 2009; Zhu et al., 2009; Zhu and Peng, 2009; Zhu, 2012). Moreover, the present work is performed at a large Reynolds number of 3.9×10^6 representative of full-scale turbines, unlike most of the previous studies on flapping-foil turbine which rather considered low Reynolds numbers of the order of 1 000 (Young et al., 2014; Xiao and Zhu, 2014).

More information about the use of passive or prescribed motions is given in Sec. 3.3.2. The semi-passive turbine concept considered in this study is described in Sec. 3.4.1. The fluid and solid solvers that are used, their validation and the definition of different performance metrics are presented in Secs. 3.4.2 to 3.4.5. A description of the different types of response that have been observed in this study is then given in Sec. 3.5.1 followed by an analysis of the role of the electric generator for this turbine concept in Sec. 3.5.2.

3.3.2 Additional information regarding the use of passive or prescribed motions

The motions undergone by the foil of a flapping-foil turbine can be characterized with 5 motion parameters, namely the motion shape and amplitude in heave, the motion shape and amplitude in pitch, the heave frequency, the pitch frequency and the phase lag between the heave and the pitch motions. Each of these motion parameters can be left free or constrained depending on the specific design of the flapping-foil turbine.

We refer to as a fully-constrained turbine when all the motion parameters are constrained. This can be achieved by using three components: 1) a slider-crank linkage to convert the reciprocating heave motion to a rotating motion and to connect the foil to an electric generator, hence constraining the motion shape and amplitude in heave; 2) a controller to enforce a constant rotational velocity of the electric generator's rotor, which imposes the frequency of the heave motion; 3) rigid links to mechanically couple both degrees of freedom together, thereby also constraining the motion shape and amplitude and pitch, the frequency of the pitch motion and the phase lag between both degrees of freedom. One example of such a fully-constrained turbine prototype is described in the work of Kinsey et al. (2011).

Another possibility is to leave all the motion parameters free to obtain what we refer to as a fully-passive turbine. This has been done by Peng and Zhu (2009), Veilleux and Dumas (2017), Wang et al. (2017) and Boudreau et al. (2018). Such a turbine concept is obtained when no slider-crank linkage, no coupling mechanism and no controller are used. Nevertheless, springs and dampers can be independently connected to the foil in heave and in pitch to allow an indirect control of the motions. Moreover, such turbine is designed to restrict the motions to the heave and pitch degrees of freedom only.

Several other "semi-passive" alternatives are possible between these two extreme cases by constraining or not each of the five motion parameters describing the flapping-foil motions. The most popular semi-passive concept in the literature involves a passive heave motion and a prescribed pitch motion (Abiru and Yoshitake, 2011, 2012; Chen et al., 2018; Deng et al., 2015; Derakhshandeh et al., 2016; Griffith et al., 2016; Huxham et al., 2012; Shimizu et al., 2008; Sitorus et al., 2015; Teng et al., 2016; Wu et al., 2014, 2015; Zhan et al., 2017; Zhu et al., 2009; Zhu and Peng, 2009). More specifically, an actuator and a controller allow constraining the motion shape and amplitude in pitch in addition to the frequency of this motion while letting all the other motion parameters free because the foil of such a device is elastically supported in heave. Young et al. (2013) have proposed another turbine concept for which a slider-crank linkage and a coupling mechanism are present but no controller is used. As a result, all the motion parameters are constrained except the frequency, which is however constrained to be the same for both degrees of freedom due to the presence of the coupling mechanism. It is worth mentioning that they have used the term fully-passive to describe this turbine concept in their study, but their definition is different from the one proposed in the current work. Indeed, we define a fully-passive turbine as one for which all the motion parameters are free.

As mentioned earlier, a novel semi-passive turbine concept with a prescribed heave motion and a passive pitch motion is proposed in this study. More specifically, this implies that the foil is elastically supported with springs and dampers in pitch and that a slider-crank linkage is required to convert the reciprocating heave motion to a rotating motion, hence constraining the motion shape and amplitude in heave. This slider-crank linkage also connects the foil to an electrical generator, which is controlled to enforce a constant rotational velocity and thus, a constrained frequency for the heave motion. However, no coupling mechanism is used, therefore leaving all the remaining motion parameters, namely the motion shape and amplitude in pitch, the frequency of the pitch motion and the phase lag between the heave and the pitch motions, free. For the sake of conciseness, we use the term semi-passive turbine to refer to this heave-prescribed semi-passive turbine concept in this work. This should not be confused with other semi-passive turbine concepts that have been studied in the literature.

3.4 Methodology

3.4.1 Turbine description

The semi-passive flapping-foil turbine considered in this study, which is shown schematically in Fig. 3.1, consists in a rigid NACA0015 foil that is elastically-supported in pitch (θ) with a prescribed heave motion (h). The pitch motion is entirely governed by the following equation of motion:

$$M = I_\theta\,\ddot{\theta} + S\ddot{h}\cos(\theta) + D_\theta\,\dot{\theta} + k_\theta\,\theta\ , \tag{3.1}$$

where the superscript $(\cdot)$ denotes a time derivative, M is the moment about the pitch axis resulting from the fluid loading, I_θ is the moment of inertia about the pitch axis, S is the static moment, which corresponds to the pitching mass (m_θ) times the distance between the center of mass and the pitch axis (x_θ) (see Fig. 3.1 for the sign convention):

$$S = m_\theta\,x_\theta\ , \tag{3.2}$$

D_θ is the pitch damping coefficient and k_θ is the pitch spring stiffness coefficient (rotational stiffness). Note that the static moment is zero when the pitch axis coincides with the center of mass and that the gravitational acceleration does not appear in the equation of motion because it is considered to act in a direction aligned with the pitch axis (z-direction in Fig. 3.1).

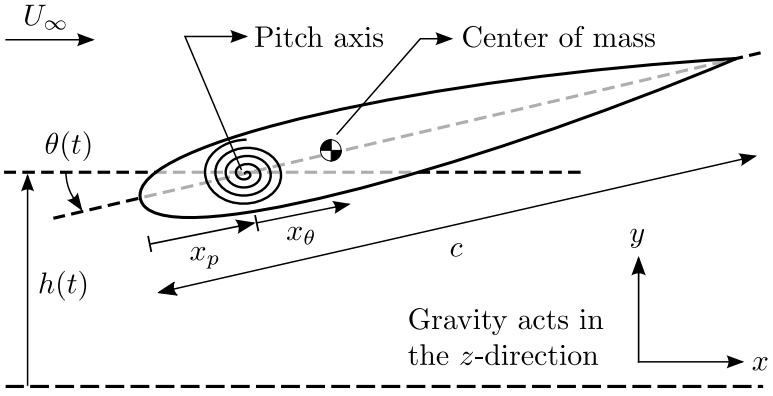

Figure 3.1: Outline of the semi-passive flapping-foil turbine concept with a prescribed heave motion and a passive pitch motion. Note that x_θ is defined positive as shown in the figure, namely with the center of mass being located downstream of the pitch axis.

In its dimensionless form, Eq. 3.1 becomes:

$$C_M/2 = I^*_\theta\,\ddot{\theta}^* + S^*\,\ddot{h}^*\cos(\theta) + D^*_\theta\,\dot{\theta}^* + k^*_\theta\,\theta\ , \tag{3.3}$$

with:

$$C_M = \frac{M}{0.5\,\rho\,U_\infty^2\,b\,c^2}\ ,\quad I^*_\theta = \frac{I_\theta}{\rho\,b\,c^4}\ ,\quad S^* = \frac{S}{\rho\,b\,c^3}\ ,\quad D^*_\theta = \frac{D_\theta}{\rho\,U_\infty\,b\,c^3}\ ,\quad k^*_\theta = \frac{k_\theta}{\rho\,U_\infty^2\,b\,c^2}\ ,$$

$$h^* = \frac{h}{c}\,, \qquad \dot{h}^* = \frac{\dot{h}}{U_\infty}\,, \qquad \ddot{h}^* = \frac{\ddot{h}\,c}{U_\infty^2}\,, \qquad \dot{\theta}^* = \frac{\dot{\theta}\,c}{U_\infty}\,, \qquad \ddot{\theta}^* = \frac{\ddot{\theta}\,c^2}{U_\infty^2}\,,$$

where ρ is the fluid density, U_∞ is the freestream velocity, c is the chord length and b is the span length. Note that forces per unit span are always considered in this work, so that b is taken to be unity ($b = 1$).

The heave motion is prescribed to be a sine wave with an amplitude growing linearly from zero to its nominal value (H_0) over the first three foil oscillations:

$$h = H_0 \min\left(\frac{t}{3T}, 1\right) \sin\left(2\,\pi\,f\,t\right)\,, \tag{3.4}$$

where t is time, f is the frequency of the prescribed heave motion and T is the period of one oscillation or cycle ($T = 1/f$). This linear growth of the heave amplitude at the beginning of the simulations is used in order to avoid imposing a shock in heave velocity or heave acceleration, therefore providing a smooth initial condition.

Throughout the current study, the dimensionless heave amplitude (H_0/c), the dimensionless moment of inertia (I_θ^*), and the dimensionless pitch damping coefficient (D_θ^*) are all kept constant with the values listed in Table 3.1. A heave amplitude of one chord length has been chosen based on the study of the fully-constrained concept conducted by Kinsey and Dumas (2014) and because the best efficiencies reported in the works of Veilleux and Dumas (2017), Wang et al. (2017) and Boudreau et al. (2018) on fully-passive flapping-foil turbines have been obtained with a passive heave motion having an amplitude of that order ($1c$). The dimensionless moment of inertia is set to 2, which is similar to the mass ratio used in the work of Wang et al. (2017) on a fully-passive turbine. An idealized turbine with no friction in pitch is considered. As a result, the pitch damping coefficient is set to zero. This is justified by the fact that the pitch damping should be minimized in practice since it results in undesired losses of energy. As a reference point, the pitch damping coefficient was of the order of $D_\theta^* = 0.005$ for the fully-passive flapping-foil turbine prototype tested by Boudreau et al. (2018). For all the cases considered in this study, the pitch axis is located at the quarter-chord point ($x_p/c = 0.25$) and the dimensionless pitch spring stiffness coefficient (k_θ^*) is set so that the dimensionless pitch natural frequency always matches the reduced frequency of the prescribed heave motion. This results in:

$$k_\theta^* = \left(2\,\pi\,f^*\right)^2 I_\theta^*\,, \tag{3.5}$$

where f^* is given by:

$$f^* = f\,c/U_\infty\,. \tag{3.6}$$

The Reynolds number is fixed at 3.9×10^6, based on the chord length, in order to characterize large-scale turbines (e.g., Cape Sharp Tidal Venture Ltd. (2018)). It also ensures that the boundary layers are turbulent, which allows us to solve them with a turbulence model in fully turbulent mode, as stated in Sec. 3.4.2. The results of the present study are expected to be representative of turbines

operating at different Reynolds numbers provided that they are large enough so that the boundary layers remain turbulent. Moreover, this choice is consistent with previous works conducted on large-scale hydrokinetic turbines (e.g., Boudreau and Dumas (2017); Sitorus and Ko (2019). The values of the dimensionless static moment (S^*) and the reduced frequency of the prescribed heave motion (f^*) are respectively varied between 0 and 0.8 and between 0.10 and 0.30. These ranges have been selected based on preliminary results and previous studies conducted on fully-constrained flapping-foil turbines (Kinsey and Dumas, 2014; Young et al., 2014; Xiao and Zhu, 2014).

Table 3.1: Governing parameter values

Parameter	Value
$\mathrm{Re} = U_\infty c/\nu$	3.9×10^6
x_p/c	0.25
H_0/c	1
I^*_θ	2
D^*_θ	0
k^*_θ	$(2\pi f^*)^2 I^*_\theta$
S^*	0 to 0.8
f^*	0.10 to 0.30

3.4.2 Fluid and solid solvers

The semi-passive turbine concept proposed in this work is analyzed by carrying out two-dimensional incompressible Unsteady Reynolds-Averaged Navier-Stokes (URANS) simulations using the Spalart-Allmaras one-equation turbulence model with rotation correction (Dacles-Mariani et al., 1995, 1999; Spalart and Allmaras, 1994). Kinsey and Dumas (2012) and Veilleux and Dumas (2017) have previously validated the use of this turbulence modeling approach for the study of flapping-foil turbines by comparing their numerical results with experimental data. Siemens' STAR-CCM+® software is used as the fluid solver with second-order numerical schemes and a segregated approach making use of the SIMPLE algorithm for the pressure-velocity coupling (Ferziger and Perić, 2002). The computational domain is the same as the one used in the work of Veilleux and Dumas (2017) and it simply consists in a square of 100 chord lengths by 100 chord lengths with the foil being located at the center. A uniform and constant velocity together with a modified turbulent viscosity ratio of three ($\tilde{\nu}/\nu = 3$) is imposed at the inlet boundary. The modified turbulent viscosity ($\tilde{\nu}$) is the variable of interest in the single equation of the Spalart-Allmaras turbulence model and it is related to the turbulent viscosity (ν_t) through an empirical relation (Spalart et al., 1997). An inlet value of three for the modified turbulent viscosity ratio has been chosen to ensure that the turbulence model is used in its fully turbulent

mode, following the recommendation of Spalart and Rumsey (2007). At the outlet, a pressure of zero is imposed and symmetry conditions are used for the two remaining boundaries. Regarding the initial condition, the velocity and turbulent viscosity ratio values at the inlet along with the pressure value at the outlet are imposed throughout the computational domain.

The overset mesh technique is used to handle the foil motions with two different meshes, one for the background region and one for the foil region. A structured mesh is used near the foil surface with a dimensionless normal wall distance (y^+) of the order of one, a maximum growth factor of 1.2 and approximately 500 nodes around the foil. The background mesh region is composed of hexagonal cells for a total of about 78 614 cells. The time step corresponds to 0.003 convective time units for all the simulations:

$$\frac{\Delta t\, U_\infty}{c} = 0.003\ . \tag{3.7}$$

This results in a number of time steps per foil oscillation ranging between approximately 1 100 and 3 300 depending on the frequency of the prescribed heave motion.

In order to solve Eq. 3.1, it is discretized in time and written as:

$$R_\theta^n = I_\theta\, \ddot{\theta}^n + S\ddot{h}^n \cos(\theta^n) + D_\theta\, \dot{\theta}^n + k_\theta\, \theta^n - M^n\ , \tag{3.8}$$

where:

$$\ddot{\theta}^n = c_1\, \dot{\theta}^n + c_2\, \dot{\theta}^{n-1} + c_3\, \dot{\theta}^{n-2}\ , \tag{3.9}$$

$$\dot{\theta}^n = c_1\, \theta^n + c_2\, \theta^{n-1} + c_3\, \theta^{n-2}\ , \tag{3.10}$$

$$\ddot{h}^n = c_1\, \dot{h}^n + c_2\, \dot{h}^{n-1} + c_3\, \dot{h}^{n-2}\ , \tag{3.11}$$

$$\dot{h}^n = c_1\, h^n + c_2\, h^{n-1} + c_3\, h^{n-2}\ , \tag{3.12}$$

R_θ is the residual of the discretized version of Eq. 3.1, the superscript n denotes the current time step to be solved, while $n-1$ and $n-2$ correspond to the two previous time steps, and c_1, c_2 and c_3 are the constants of the numerical scheme. In the current study, the temporal discretization of the solid solver is chosen to match that of the fluid solver, namely a second-order backward difference scheme. This results in:

$$c_1 = \frac{3}{2\,\Delta t}\ , \qquad c_2 = \frac{-4}{2\,\Delta t}\ , \qquad c_3 = \frac{1}{2\,\Delta t}\ , \tag{3.13}$$

where Δt is the time step.

Considering Eqs. 3.8 to 3.13, the only unknowns on the right hand side of Eq. 3.8 are θ^n and M^n since the heave motion is prescribed. However, these two unknowns are not independent as the hydrodynamic moment (M) is a function of the foil motion and thus of the pitch angle (θ). The objective therefore consists in finding the value of θ^n which minimizes the absolute value of the residual R_θ^n. In other words, the solver has to find the roots of the function on the right hand side of Eq. 3.8 with θ^n as the independent variable. It achieves this task with the secant method. The resulting fluid-solid coupling algorithm is written in pseudocode in Appendix 3.A.

The formulation of the fluid-solid coupling algorithm is implicit since the value of the residual for the current time step (R_θ^n) is a function of both the pitch angle and the hydrodynamic moment at the same time step (θ^n and M^n). Consequently, the pitch angle is determined for a given time step by iterating and updating its value a few times within this specific time step. These iterations are referred to as outer loops in Appendix 3.A and they are indicated with subscripts. For each outer loop, the fluid solver has to perform a few iterations with the updated pitch angle in order to determine the moment (M_i^n) corresponding to the i^{th} outer loop. Fluid iterations are conducted until the difference between the moment coefficient (C_M) values obtained from two successive iterations falls below 10^{-5}. Outer loops are conducted until the difference between the pitch angle values in radians, estimated from the two last outer loops and normalized with $\pi/2$, falls below a given convergence criterion (ε), which is set to 10^{-8}. Three or four outer loops are typically required to reach convergence for the pitch angle. Once this is achieved, some additional fluid iterations are carried out to ensure that the fluid residuals for the pressure, the streamwise and transverse momentums and the turbulent viscosity at least drop by a factor of 10^{-4} for the first three residuals and 5×10^{-4} for the residual of the turbulent viscosity for a given time step. When the pitch angle and the fluid residuals' convergence criteria are all met, the time step is incremented and the process starts over.

3.4.3 Power transfer and performance metrics

In order to evaluate the power extracted by the semi-passive turbine investigated in the current work, it is useful to write a general equation of motion in heave:

$$F_y = m_h \ddot{h} + S\left(\ddot{\theta}\cos\theta - \dot{\theta}^2 \sin\theta\right) + D_h \dot{h} + F_{\text{gen}} \,, \tag{3.14}$$

where F_y is the component of the hydrodynamic force acting on the foil in the heave direction, m_h is the mass of the components undergoing the heave motion, D_h is the heave damping coefficient, which accounts for the possible presence of friction in heave, and F_{gen} corresponds to the force stemming from the presence of an electric generator.

Eq. 3.14 should not be confused with Eq. 3.4. Indeed, Eq. 3.14 is not solved during the simulations since the heave motion is rather prescribed according to Eq. 3.4. Nevertheless, Eq. 3.14 tells us that in order to prescribe a sinusoidal heave motion, the generator must be controlled and might have to act as an actuator during a fraction of the foil oscillations. In other words, on a real turbine setup, F_{gen} would need to be adjusted in real time so that the solution of Eq. 3.14 corresponds to the desired (imposed) heave motion given by Eq. 3.4.

The amount of power available at the generator is obtained by multiplying Eq. 3.14 with the heave velocity ($\dot{h}$). After putting all the terms on the left hand side of this equation, except F_{gen}, normalizing and cycle-averaging the result, one obtains the following relation for the different power coefficients:

$$\langle C_{P_h} \rangle + \langle C_{P_{m_h}} \rangle + \langle C_{P_{S,h}} \rangle + \langle C_{P_{D_h}} \rangle = \langle C_{P_{\text{gen}}} \rangle \,, \tag{3.15}$$

where the angle brackets indicate the cycle-averaging process and $\langle C_{P_{\text{gen}}} \rangle$ is the power coefficient available at the electric generator. Note that unless otherwise indicated, the term power coefficient refers to a cycle-averaged value.

A similar procedure is used for the pitch motion by multiplying Eq. 3.1 with the pitch velocity ($\dot{\theta}$). Again, after putting all the terms on the left hand side of the equation, normalizing and cycle-averaging the result, the following relation is obtained:

$$\langle C_{P_\theta} \rangle + \langle C_{P_{I_\theta}} \rangle + \langle C_{P_{S,\theta}} \rangle + \langle C_{P_{D_\theta}} \rangle + \langle C_{P_{k_\theta}} \rangle = 0 \,. \tag{3.16}$$

The different power coefficients appearing in Eqs. 3.15 and 3.16 are defined as:

$$\langle C_{P_h} \rangle = \frac{1}{T} \int_{t_i}^{t_i+T} \left(\frac{F_y \dot{h}}{0.5 \rho U_\infty^3 b c} \right) dt \,, \tag{3.17}$$

$$\langle C_{P_{m_h}} \rangle = \frac{1}{T} \int_{t_i}^{t_i+T} \left(\frac{-m_h \ddot{h} \dot{h}}{0.5 \rho U_\infty^3 b c} \right) dt \,, \tag{3.18}$$

$$\langle C_{P_{S,h}} \rangle = \frac{1}{T} \int_{t_i}^{t_i+T} \left(\frac{-S \dot{h} \left(\ddot{\theta} \cos\theta - \dot{\theta}^2 \sin\theta \right)}{0.5 \rho U_\infty^3 b c} \right) dt \,, \tag{3.19}$$

$$\langle C_{P_{D_h}} \rangle = \frac{1}{T} \int_{t_i}^{t_i+T} \left(\frac{-D_h \dot{h}^2}{0.5 \rho U_\infty^3 b c} \right) dt \,, \tag{3.20}$$

$$\langle C_{P_{\text{gen}}} \rangle = \frac{1}{T} \int_{t_i}^{t_i+T} \left(\frac{F_{\text{gen}} \dot{h}}{0.5 \rho U_\infty^3 b c} \right) dt \,, \tag{3.21}$$

$$\langle C_{P_\theta} \rangle = \frac{1}{T} \int_{t_i}^{t_i+T} \left(\frac{M \dot{\theta}}{0.5 \rho U_\infty^3 b c} \right) dt \,, \tag{3.22}$$

$$\langle C_{P_{I_\theta}} \rangle = \frac{1}{T} \int_{t_i}^{t_i+T} \left(\frac{-I_\theta \ddot{\theta} \dot{\theta}}{0.5 \rho U_\infty^3 b c} \right) dt \,, \tag{3.23}$$

$$\langle C_{P_{S,\theta}} \rangle = \frac{1}{T} \int_{t_i}^{t_i+T} \left(\frac{-S \ddot{h} \dot{\theta} \cos(\theta)}{0.5 \rho U_\infty^3 b c} \right) dt \,, \tag{3.24}$$

$$\langle C_{P_{D_\theta}} \rangle = \frac{1}{T} \int_{t_i}^{t_i+T} \left(\frac{-D_\theta \dot{\theta}^2}{0.5 \rho U_\infty^3 b c} \right) dt \,, \tag{3.25}$$

$$\langle C_{P_{k_\theta}} \rangle = \frac{1}{T} \int_{t_i}^{t_i+T} \left(\frac{-k_\theta \theta \dot{\theta}}{0.5 \rho U_\infty^3 b c} \right) dt \,, \tag{3.26}$$

where t_i is the time at which a given cycle starts, which is defined as the moment at which $h = 0$ and $\dot{h} > 0$, and T is the period of one cycle ($T = 1/f$). The metrics $\langle C_{P_h} \rangle$ and $\langle C_{P_\theta} \rangle$ are the heave and pitch power coefficients and they measure the power transfers occurring between the foil and the flow. They are positive when the power is transferred from the flow to the foil. Conversely, a negative value for one of these power coefficients means that some power is required to maintain the corresponding motion. $\langle C_{P_{m_h}} \rangle$, $\langle C_{P_{l_\theta}} \rangle$ and $\langle C_{P_{k_\theta}} \rangle$ correspond to power transfers occurring between the foil motions and different forms of potential energy. $\langle C_{P_{D_h}} \rangle$ and $\langle C_{P_{D_\theta}} \rangle$ are necessarily negative and correspond to power losses due to the presence of friction in heave and in pitch. Finally, $\langle C_{P_{S,h}} \rangle$ and $\langle C_{P_{S,\theta}} \rangle$ stand for the power transfers occurring between the heave motion and the pitch motion through the inertial coupling terms in Eqs. 3.1 and 3.14, namely the terms involving the static moment. They are defined positive when they correspond to a power input in their respective equation (Eq. 3.15 or Eq. 3.16) and negative for a power output. For example, when $\langle C_{P_{S,h}} \rangle$ is negative but $\langle C_{P_{S,\theta}} \rangle$ is positive, some power is transferred from the heave motion to the pitch motion on a cycle-averaged basis[1]. They are equal to zero when the center of mass coincides with the pitch axis (see Eq. 3.2 and Fig. 3.1).

Throughout the current investigation, no friction is considered in heave and in pitch. Consequently, $D_h = 0$ and $D_\theta = 0$, and thus $\langle C_{P_{D_h}} \rangle = 0$ and $\langle C_{P_{D_\theta}} \rangle = 0$. Furthermore, when the foil motions are periodic, $\langle C_{P_{m_h}} \rangle$, $\langle C_{P_{l_\theta}} \rangle$ and $\langle C_{P_{k_\theta}} \rangle$ vanish because these terms are conservative (Veilleux, 2014). This is always true in the case of $\langle C_{P_{m_h}} \rangle$ since sinusoidal heave motions are prescribed. Under such conditions, Eqs. 3.15 and 3.16 simplify to:

$$\langle C_{P_h} \rangle + \langle C_{P_{S,h}} \rangle = \langle C_{P_{\text{gen}}} \rangle \,, \tag{3.27}$$

$$\langle C_{P_\theta} \rangle + \langle C_{P_{S,\theta}} \rangle = 0 \,. \tag{3.28}$$

Also, $\langle C_{P_{S,h}} \rangle$ and $\langle C_{P_{S,\theta}} \rangle$ are equal but opposite when the motions are periodic:

$$\langle C_{P_{S,h}} \rangle = -\langle C_{P_{S,\theta}} \rangle \,. \tag{3.29}$$

By combining Eqs. 3.27 to 3.29, one finally obtains:

$$\langle C_{P_{\text{gen}}} \rangle = \langle C_{P_h} \rangle + \langle C_{P_\theta} \rangle \,. \tag{3.30}$$

This last relation means that when the foil motions are periodic and no friction is considered, the power coefficient at the generator is simply equal to the sum of the heave and pitch contributions of the power transferred between the foil and the flow. In other words, all the power extracted from the flow is available at the electric generator. Nevertheless, $\langle C_{P_{\text{gen}}} \rangle$ has been evaluated using Eq. 3.27 throughout this study to include the possibility of non-periodic pitch motions.

The results presented in this work are analyzed in terms of different performance metrics. Indeed, each foil oscillation or cycle can be characterized by its efficiency:

$$\eta = \langle C_{P_{\text{gen}}} \rangle c/d \,, \tag{3.31}$$

[1] Note that these definitions are slightly different than those presented in the paper of Veilleux and Dumas (2017) due to a different sign convention used for θ.

its pitch amplitude:

$$\Theta_0 = \frac{\theta_{\max} - \theta_{\min}}{2} \,, \tag{3.32}$$

and its phase lag between the heave and the pitch motions, here given in degrees:

$$\phi = \frac{360}{T} \left(t_{\theta_{\max}} - t_{h_{\max}} \right) \,, \tag{3.33}$$

where d is the overall extent of the foil motion, i.e., the distance between the maximum and minimum positions reached by any point on the foil surface in the heave direction during this specific cycle, $\theta_{\max}$ and $\theta_{\min}$ are the maximum and minimum pitch angles reached during this same cycle and $t_{\theta_{\max}}$ and $t_{h_{\max}}$ are the instants at which the maximum pitch angle and the maximum heave position are attained. In addition to these metrics, the streamwise and heave force coefficients are defined as:

$$C_{F_x} = \frac{F_x}{0.5\,\rho\,U_\infty^2\,b\,c} \,, \tag{3.34}$$

$$C_{F_y} = \frac{F_y}{0.5\,\rho\,U_\infty^2\,b\,c} \,, \tag{3.35}$$

where F_x and F_y are the streamwise and transverse (heave) components of the hydrodynamic force acting on the foil.

The time-averaged values presented in this work have been determined by starting the averaging process after reaching limit-cycle oscillations (LCO) in order to avoid the transient period at the beginning of the simulations. A sufficient number of cycles have been completed in order to obtain converged values while also making sure that a minimum of 10 cycles has been used. For example, the time-averaged power coefficient at the generator is computed as:

$$\overline{C_{P_{\text{gen}}}} = \frac{1}{N_{\text{end}} - N_{\text{start}} + 1} \sum_{j=N_{\text{start}}}^{N_{\text{end}}} \langle C_{P_{\text{gen}}} \rangle_j \,, \tag{3.36}$$

where the subscript j stands for the j^{th} cycle, N_{start} is the cycle at which the averaging process begins, N_{end} is the total number of completed cycles and $\langle C_{P_{\text{gen}}} \rangle_j$ is the power coefficient at the generator for the j^{th} cycle.

3.4.4 Spatial and temporal resolution levels

In order to validate that the spatial and temporal resolution levels used to conduct the present study are adequate, simulations with two other resolution levels have been carried out. More specifically, both the time step and the spatial resolution of the mesh have been varied by 33%, while keeping a dimensionless normal wall distance (y^+) of the order of one at the foil surface, to obtain a fine resolution case and a coarse resolution case. This results in 42 697, 78 614 and 135 789 cells for the coarse mesh, the baseline mesh and the fine mesh, respectively. The time evolution of the pitch angle as a function of time is presented in Fig. 3.2 for the three resolution levels at an operating point characterized by $f^* = 0.20$ and $S^* = 0.65$. As will be discussed in Section 3.5.1, this operating point

corresponds to the best efficiency point. Fig. 3.2 shows that the differences between the cases with the three resolution levels are negligible since the three curves are almost perfectly superimposed on each other. This therefore confirms that the baseline resolution is adequate.

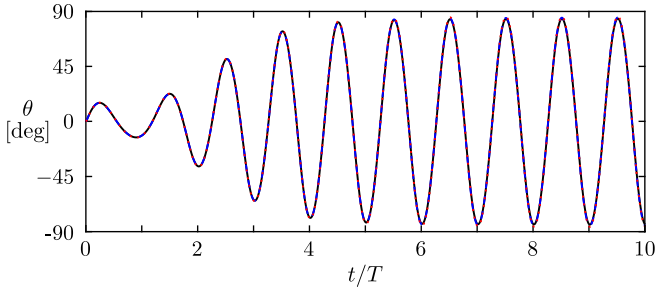

Figure 3.2: Time evolution of the pitch angle as a function of time during the first ten oscillations of an operating point characterized by $f^* = 0.20$ and $S^* = 0.65$ obtained with three different spatial and temporal resolution levels: coarse (dashed blue line), baseline (solid black line) and fine (dotted red line).

In order to make sure that the time step is also adequate for cases with a large reduced frequency, some simulations have been conducted with time steps varying from 0.00225 to 0.01 convective time units for a case with $f^* = 0.30$ and $S^* = 0.5$. The time-averaged pitch amplitude and phase lag values obtained with the different time steps are presented in Table 3.2. The maximum relative differences obtained between the different pitch amplitude and phase lag values are both around 1%. Moreover, the agreement between the time evolutions of the pitch angle obtained with the different time steps is as good as in Fig. 3.2. This confirms that the time step value of 0.003 convective time units that has been chosen to conduct this study is appropriate.

Table 3.2: Time-averaged pitch amplitude and phase lag values obtained with different temporal resolutions and the baseline mesh. These values are obtained from an operating point characterized by $f^* = 0.30$ and $S^* = 0.5$.

Time step ($\Delta t\, U_\infty / c$)	$\overline{\Theta_0}$	$\overline{\phi}$
0.01	85.3°	104.8°
0.006	84.8°	104.3°
0.004	84.8°	104.3°
0.003	84.8°	104.2°
0.00225	85.8°	105.2°

3.4.5 Validation

Some simulations of an elastically-supported cylinder undergoing vortex-induced vibrations (VIV) with various spring stiffness coefficients have been conducted to validate our numerical methodology. The benchmark case that has been chosen to perform this task was studied by Shiels et al. (2001), who used a viscous vortex method as the fluid solver. It consists in a massless cylinder of diameter D with no damping at a Reynolds number of 100. The equation of motion of such an elastically-supported cylinder is given by:

$$F_y = k\,y\,, \tag{3.37}$$

where F_y is the hydrodynamic force component normal to the freestream flow, y is the transverse displacement of the cylinder and k is the spring stiffness coefficient. This benchmark case has been chosen because such applications with large fluid-to-solid density ratios are known to be challenging for fluid-solid coupling algorithms.

As shown in Fig. 3.3, the results obtained with the present methodology are in good agreement with the results of Shiels et al. (2001). This confirms that our approach is not only accurate, but also stable and not limited in terms of the inertial property of the rigid body involved in the fluid-solid interaction problem to be solved.

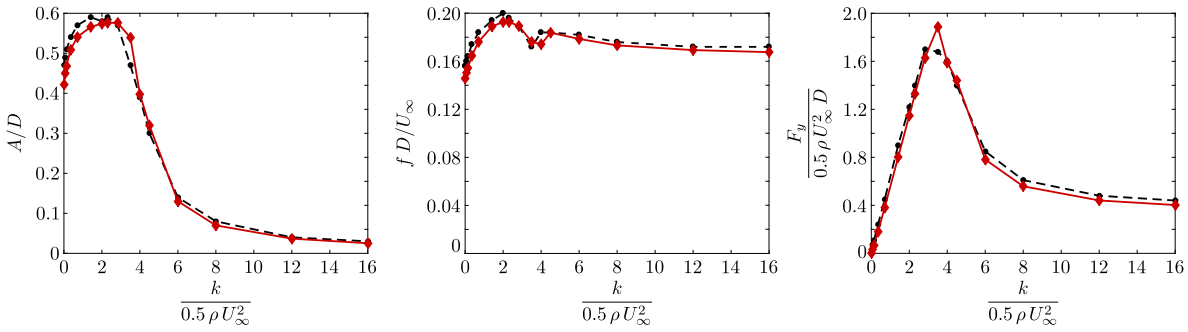

Figure 3.3: Comparison between the benchmark results of Shiels et al. (2001) (dashed black curves) and the results obtained with the present methodology (solid red curves) for a massless cylinder undergoing vortex-induced vibrations. The results are compared in terms of the amplitude of motion (A), the frequency of the motion (f) and the amplitude of the force component acting on the cylinder in the transverse direction (F_y).

Furthermore, our methodology has also been used to simulate the optimal fully-passive flapping-foil turbine case that was obtained by Veilleux and Dumas (2017) with their well-validated fluid-solid solver. The time evolutions of the heave position and the pitch angle obtained with our methodology are compared to their results in Fig. 3.4. It is found that our results agree well with those of Veilleux and Dumas (2017), hence confirming that our numerical methodology is suitable for fluid-solid simulations involving a flapping foil.

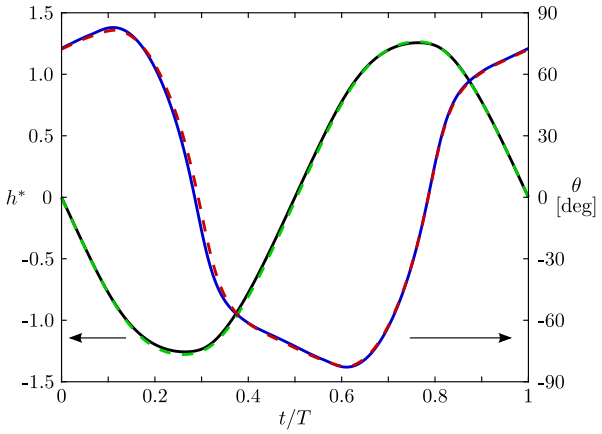

Figure 3.4: Comparison between the motions of a fully-passive flapping-foil turbine over one cycle of period T simulated with our numerical methodology (dashed lines) and as reported by Veilleux and Dumas (2017) (solid lines) for their optimal case. The dimensionless heave position (h^*) is shown in black and green while the pitch angle (θ) is shown in blue and red.

3.5 Results

3.5.1 Classification of the different regimes of motion

As mentioned in Sec. 3.4, the values of the dimensionless static moment (S^*) and the reduced frequency of the prescribed heave motion (f^*) are varied while all the other governing parameters are kept constant. Different responses are observed and they are classified into five different regimes of motion based on their time-averaged efficiency ($\overline{\eta}$), pitch amplitude ($\overline{\Theta_0}$) and phase lag ($\overline{\phi}$) values as well as the regularity of the motions. These regimes are represented with different colors and markers in Fig. 3.1, with each marker corresponding to a different simulated operating point.

Typical time evolutions of the pitch angle for each regime are shown in Fig. 3.2 while the contours of the time-averaged efficiency, the time-averaged pitch amplitude and the time-averaged phase lag between the heave and the pitch motions are respectively presented in Figs. 3.3, 3.4a and 3.4b. The white areas in Fig. 3.3 indicate a negative efficiency. Also, the time-averaged values are not presented for the orange regime because of the irregularity of the response (see Fig. 3.2d). The corresponding regions in these figures are colored in gray. Note that we are not interested in the details of the orange regime since it is not suitable for a turbine application, as will be discussed below.

The green regime contains the operating points characterized by periodic limit-cycle oscillations, and a positive energy extraction from the flow on a time-averaged basis, as seen in Fig. 3.3. This therefore makes it the only regime that is suitable for a turbine application. The motions in the blue regime rather require energy because it corresponds to a propulsion regime. The three other regimes, namely the black, the orange and the red regimes, correspond to neither energy-extraction regimes nor propulsion regimes. Unlike the periodic motions characterizing the green and the blue regimes, the motions characterizing these three other regimes are less regular (see Fig. 3.2) and they result in significant

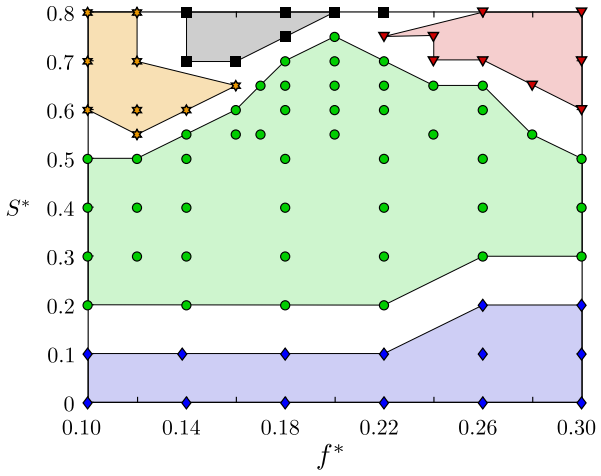

Figure 3.1: Classification of 5 different regimes of motion observed in the parametric space. Each marker corresponds to one simulated operating point.

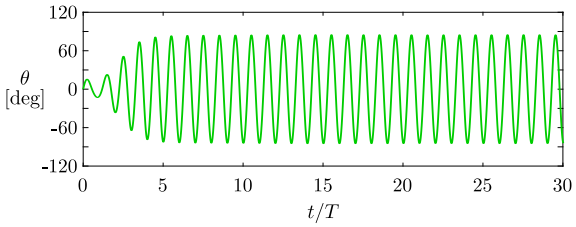

(a) Green regime ($f^* = 0.20$; $S^* = 0.65$).

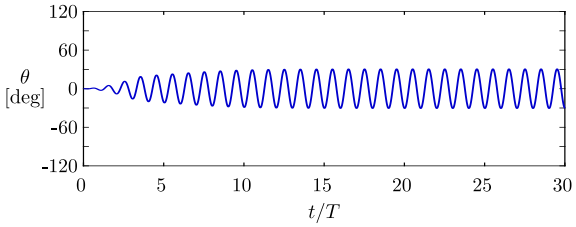

(b) Blue regime ($f^* = 0.26$; $S^* = 0$).

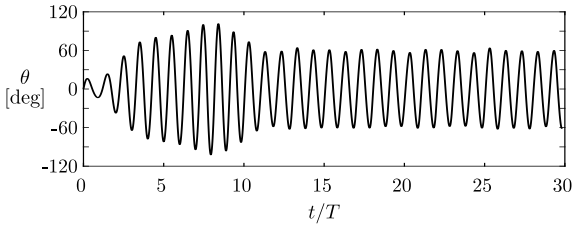

(c) Black regime ($f^* = 0.16$; $S^* = 0.70$).

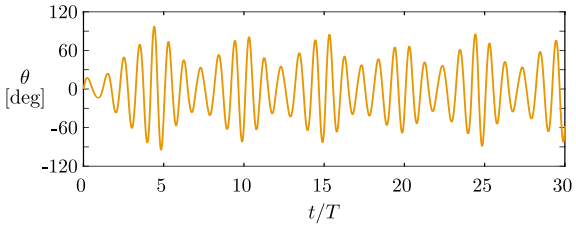

(d) Orange regime ($f^* = 0.10$; $S^* = 0.80$).

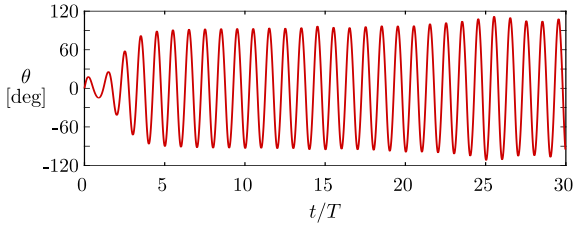

(e) Red regime ($f^* = 0.24$; $S^* = 0.75$).

Figure 3.2: Typical time evolutions of the passive pitch motion as a function of time during the 30 first cycles for each regime of motion. Note that more than 30 cycles have been simulated and that the operating point in the red regime has only reached a permanent response after completing 52 cycles.

variations of the efficiency, the pitch amplitude and the phase lag from cycles to cycles. In fact,

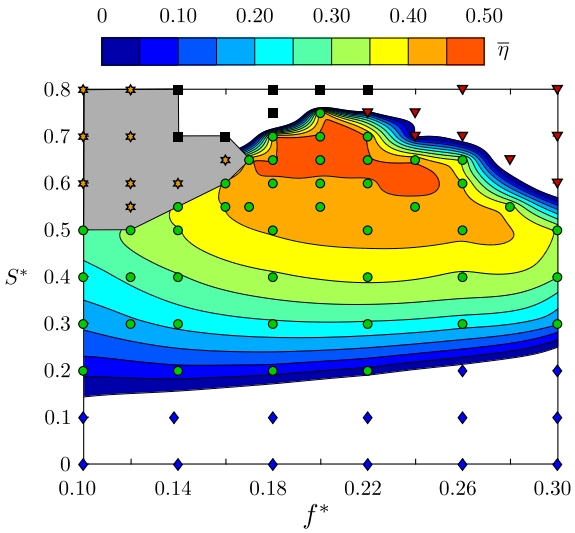

Figure 3.3: Contours of the time-averaged efficiency. A maximum efficiency of 45.4% is obtained when $f^* = 0.20$ and $S^* = 0.65$. The white areas indicate negative values.

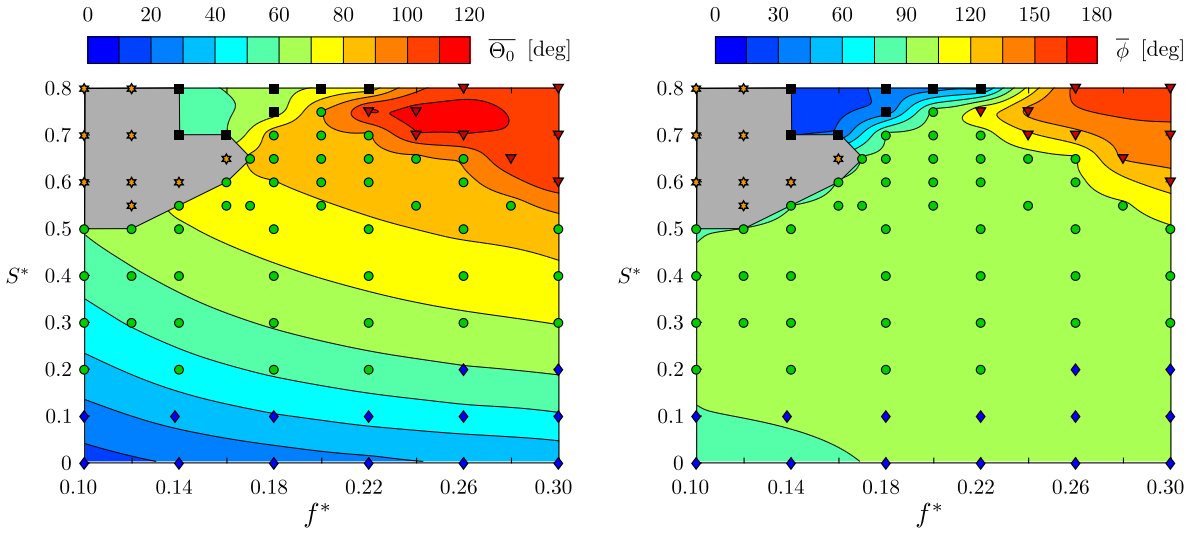

(a) Pitch amplitude.

(b) Phase lag between the heave and the pitch motions.

Figure 3.4: Contours of the time-averaged values of two metrics characterizing the foil motions.

the efficiency of the operating points in these regimes can even alternate between positive and negative values. These large variations of the energy extraction occurring from cycles to cycles prevent these operating points from being potential candidates for a turbine application. Moreover, the time-averaged efficiency of these operating points is negative, except for a few exceptions for which the time-averaged efficiency nevertheless remains small.

As observed in Fig. 3.4b, the different regimes of motion are characterized by time-averaged phase lags ($\overline{\phi}$) around 90°, above 90° and below 90°. When the phase lag is larger than 90°, the leading

edge points outward when the maximum and minimum heave positions are reached. In other words, a negative pitch angle is observed when the maximum heave position is reached, and vice versa. The opposite behavior is observed when the phase lag is smaller than 90°. This is shown schematically in Fig. 3.5 and it can also be observed in Fig. 3.6, which presents the limit-cycle oscillations of typical operating points in three different regimes characterized with different time-averaged phase lag values.

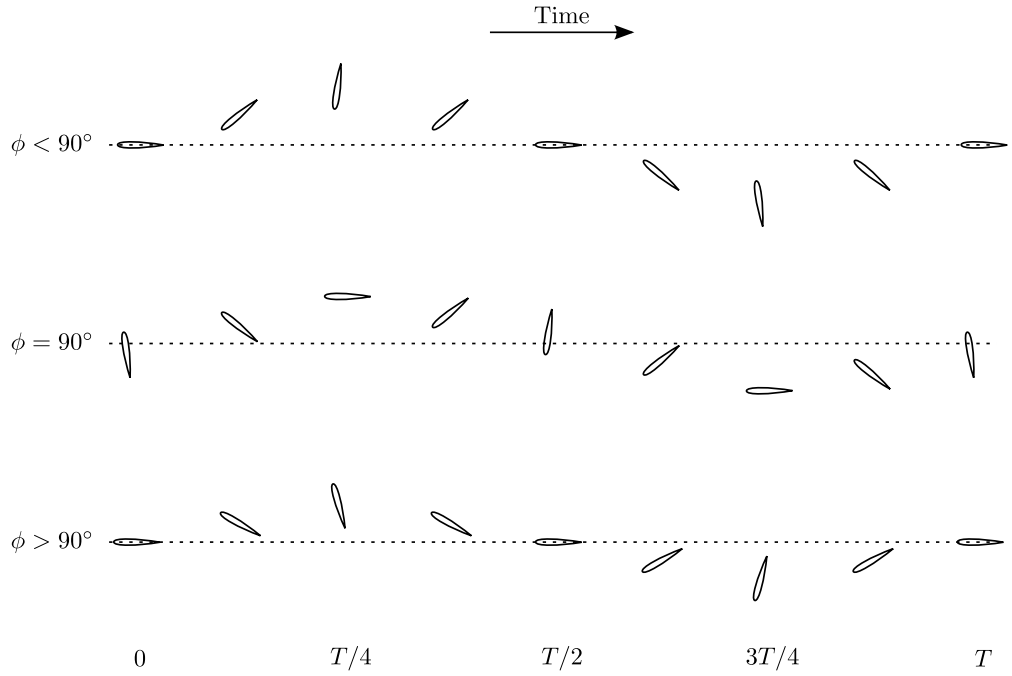

Figure 3.5: Typical foil motions as a function of time for different phase lag values between the heave and the pitch motions. The dashed line indicates the equilibrium position in heave ($h = 0$).

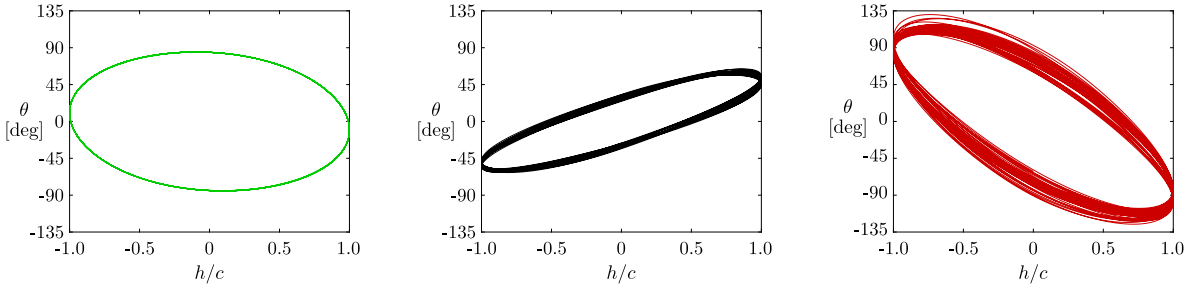

(a) Green regime.
($f^* = 0.20$; $S^* = 0.65$; $\overline{\phi} = 95.4°$)

(b) Black regime.
($f^* = 0.16$; $S^* = 0.70$; $\overline{\phi} = 32.2°$)

(c) Red regime.
($f^* = 0.24$; $S^* = 0.75$; $\overline{\phi} = 140.1°$)

Figure 3.6: Limit-cycle oscillations for three of the five different regimes of motion. The motions follow counterclockwise trajectories.

Even though our main interest in this investigation is directed toward the energy-extraction regime (green regime), the four other regimes are also described in the following sections in order to better highlight the distinctive features of the energy-extraction regime. Lastly, note that for all the operating points considered in this study, the dominant frequency component of the passive pitch motion is

always synchronized with the frequency of the prescribed heave motion. The symbol f^* therefore refers to the frequency of both motions.

Green regime (energy extraction)

As already mentioned, the pitch amplitude is almost constant from cycles to cycles in the green regime (operating points denoted with green dots), except during the initial transient period. It is worth recalling that the pitch motion is not prescribed and it rather solely results from the interaction of the foil with the flow and its elastic supports (see Eq. 3.1). This "well-behaved" pitch motion has therefore been obtained passively.

Fig. 3.4a shows that the pitch amplitude increases with an increase of the dimensionless static moment (S^*) in the green regime. This behavior will be explained further below. Regarding the phase lag between the heave and the pitch motions, it is found to remain relatively close to 90° for all the operating points in this regime. More specifically, it ranges between approximately 90° and 105°. Regarding the efficiency, it increases as S^* increases (see Fig. 3.3) and the largest efficiencies are observed for the operating points with the largest dimensionless static moment values reached in this regime. These best efficiency points are obtained with intermediate prescribed frequencies.

More precisely, a maximum efficiency of 45.4% is achieved when $f^* = 0.20$ and $S^* = 0.65$. This is comparable to the best efficiencies reported for the fully-constrained turbine technology (Kinsey and Dumas, 2014; Xiao and Zhu, 2014), therefore confirming the great potential of this semi-passive turbine concept with a prescribed heave motion and a passive pitch motion. In the parametric study conducted by Kinsey and Dumas (2014) on the fully-constrained turbine, a maximum efficiency of 43.3% was obtained by respectively prescribing the reduced frequency, the pitch amplitude and the phase lag values to 0.18, 80° and 90° to a foil having its pitch axis located at the third-chord point ($x_p/c = 1/3$). In this study, for which $x_p/c = 1/4$, the best operating point has a pitch amplitude of 84.7°, a phase lag of 95.4°, and it has been passively obtained with a prescribed reduced frequency of 0.20.

The efficiency alone is not sufficient to fully characterize the performance of a flapping-foil turbine because it does not allow directly comparing the amount of power extracted by two operating points with different overall extents of the foil motion (d). The time-averaged power coefficient at the generator ($\overline{C_{P_{\text{gen}}}}$) is useful in that respect since it normalizes the power with a common length scale, namely the chord length, instead of the overall extent of the foil motion in heave (d), which varies from an operating point to another. Contours of this metric are presented in Fig. 3.7.

Recalling that the heave amplitude (H_0) is constrained to one chord length for all the cases investigated in this work, the differences between the values of d for the various simulated operating points is solely due to the differences in pitch amplitude. The variations of d therefore remain relatively small between the different operating points in the energy-extraction regime with a minimum value of 2.15, when $f^* = 0.10$ and $S^* = 0.20$, and a maximum value of 2.71, when $f^* = 0.18$ and $S^* = 0.70$. Consequently,

the topology is similar for the contours of the time-averaged efficiency ($\overline{\eta}$) and the time-averaged power coefficient at the generator ($\overline{C_{P_{\text{gen}}}}$). The maximum $\overline{C_{P_{\text{gen}}}}$ of 1.21 is not observed at the maximum efficiency point but rather when $f^* = 0.20$ and $S^* = 0.75$. Nonetheless, this operating point is very close to the maximum efficiency point and the value of $\overline{C_{P_{\text{gen}}}}$ at the maximum efficiency point is very close to the maximum $\overline{C_{P_{\text{gen}}}}$, with a value of 1.19.

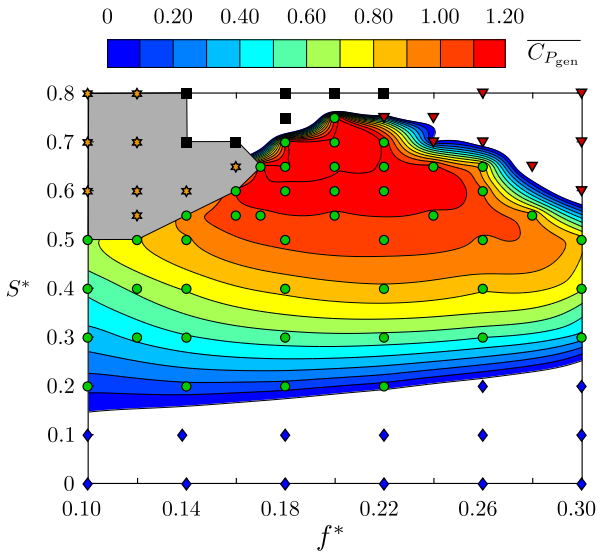

Figure 3.7: Contours of the time-averaged power coefficient available at the generator. The white areas indicate negative values.

One can notice that a positive static moment is required in order to obtain the high efficiencies reported above. This means that the center of mass has to be located downstream of the pitch axis (see Eq. 3.2 and Fig. 3.1). In order to understand why this is needed, it is insightful to analyze the heave and pitch contributions to the time-averaged power coefficient at the generator ($\overline{C_{P_{\text{gen}}}}$), namely $\overline{C_{P_h}}$ and $\overline{C_{P_\theta}}$. As described in Sec. 3.4.3, the power coefficient at the generator is equal to the sum of the heave and pitch contributions when the motions are periodic (see Eq. 3.30), which is the case for all the simulated operating points in the energy-extraction regime. These two contributions are shown in Fig. 3.8.

It is found that the time-averaged pitch power coefficient ($\overline{C_{P_\theta}}$) is negative for all the operating points considered in this study. This indicates that the pitch motion never extracts energy from the flow in the mean but rather provides energy to the flow, hence acting as an energy sink in Eq. 3.16. This in turn means that when an operating point has a positive efficiency, it must come from the heave contribution. Indeed, the time-averaged heave power coefficient ($\overline{C_{P_h}}$) is positive throughout the green regime.

Since D^*_θ has been set to zero and because the motions are periodic in the energy-extraction regime, Eq. 3.16 simplifies to Eq. 3.28. This indicates that the power transfer from the foil pitch motion to the flow ($\overline{C_{P_\theta}}$) can only be balanced by the power transfer from the heave motion to the pitch motion

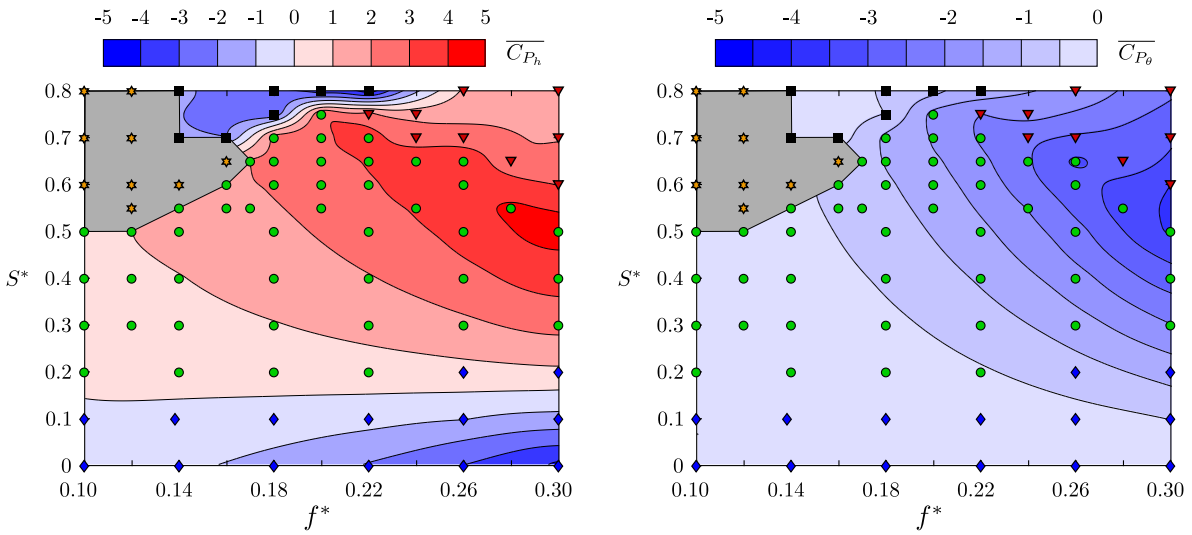

(a) Heave power coefficient.

(b) Pitch power coefficient.

Figure 3.8: Contours of the time-averaged heave and pitch power coefficients.

through the inertial coupling term involving the static moment ($\overline{C_{P_{S,\theta}}}$). In other words, $\overline{C_{P_{S,\theta}}}$ must be positive to balance the negative value of $\overline{C_{P_\theta}}$. Considering the prescribed heave motions and the passive pitch motions that have been obtained in the energy-extraction regime, this can only happen if the static moment is positive, thus implying that the center of mass has to be located downstream of the pitch axis. It is also worth mentioning that Eq. 3.28 implies that when $S^* = 0$, and thus $\overline{C_{P_{S,\theta}}} = 0$ (see Eq. 3.24), $\overline{C_{P_\theta}}$ must also be equal to zero.

$\overline{C_{P_\theta}}$ is also usually negative in the case of fully-constrained flapping-foil turbines with good levels of performance (Campobasso et al., 2013; Kinsey and Dumas, 2014; Kim et al., 2017). With the fully-constrained concept, a power transfer from the foil pitch motion to the flow ($\overline{C_{P_\theta}} < 0$) can either be balanced by the presence of some rigid links that mechanically couple both degrees of freedom together, thereby allowing a transfer of power from the heave motion to the pitch motion to take place, or by the presence of an actuator in pitch, which would provide the necessary power. However, neither of these two possibilities is relevant in the case of the semi-passive turbine concept investigated in this work, thus leaving the static moment contribution as the sole mechanism to achieve a power balance for the pitch motion when $\overline{C_{P_\theta}}$ is negative.

It is still possible to extract energy from the flow with a positive value of $\overline{C_{P_\theta}}$. This is the case, for example, for the optimal operating point reported by Veilleux and Dumas (2017) with a fully-passive flapping-foil turbine having an efficiency of 29.1%. Under such circumstances, no transfer of power from the heave motion to the pitch motion is required. As a result, the dimensionless static moment can be equal to zero or even be negative. In fact, the optimal operating point found by Veilleux and Dumas (2017) had a dimensionless static moment of -0.029. Consequently, some of the power extracted via the pitch motion was transferred from the pitch motion to the heave motion through the inertial

coupling terms, but most of it was dissipated due to the presence of viscous friction in pitch. Veilleux and Dumas (2017) showed that the positive value of $\overline{C_{P_\theta}}$ was attributed to the formation of leading-edge vortices (LEVs) and their interaction with the foil motions. Indeed, the suction associated to the presence of LEVs was found to generate a moment about the pitch axis in the same direction as the pitch velocity, hence positively contributing to $\overline{C_{P_\theta}}$. The same observation was made by Zhu and Peng (2009) for a semi-passive flapping-foil turbine with a passive heave motion and a prescribed pitch motion. Conversely, Kinsey and Dumas (2014) showed that $\overline{C_{P_\theta}}$ was always negative when no LEVs were formed for a fully-constrained flapping-foil turbine undergoing sinusoidal heave and pitch motions. In the literature, the presence of LEVs has been widely recognized as being responsible for an enhanced performance (Young et al., 2014; Xiao and Zhu, 2014). However, most of the studies that led to this conclusion were conducted at low Reynolds numbers of the order of 1 000. At a much larger Reynolds number of 500 000, Kinsey and Dumas (2014) showed that the best efficiencies were rather obtained without LEVs. Indeed, they obtained a maximum efficiency of 43.3% without LEVs and a maximum efficiency of 35.1% with LEVs. This suggests that LEVs should be avoided at large Reynolds numbers to maximize the energy extraction. Negative values of $\overline{C_{P_\theta}}$ are therefore expected, which means that positive values of static moment are required.

In the present work, no leading-edge vortices are observed for any of the operating points in the energy-extraction regime. For example, the time evolution of the vorticity field for the best efficiency point is presented in Fig. 3.9. Moreover, the passive pitch motions are always very similar to sine waves in this regime. The present study therefore demonstrates that it is possible to passively obtain a pitch motion that is very close to the prescribed pitch motion characterizing the best fully-constrained flapping-foil turbine case reported by Kinsey and Dumas (2014) by adequately positioning the center of mass downstream of the pitch axis ($S^* > 0$) in order to provide the power required by the pitch motion ($\overline{C_{P_\theta}} < 0$). It should thus not be surprising to observe that the semi-passive and the fully-constrained flapping-foil turbines can achieve similar efficiencies.

The balance between the power transferred from the heave motion to the pitch motion ($\overline{C_{P_{S,\theta}}}$) and the power transferred to the flow via the foil pitch motion ($\overline{C_{P_\theta}}$) explains why the pitch amplitude increases with the dimensionless static moment (see Fig. 3.4a). Since the pitch motions are always similar to sine waves with relatively large amplitudes, the terms $\dot{\theta}$ and $\dot{\theta}\cos(\theta)$, which respectively appear in the definitions of $\overline{C_{P_\theta}}$ and $\overline{C_{P_{S,\theta}}}$, are both roughly proportional to the pitch amplitude. Considering that the phase lag remains relatively constant throughout the energy-extraction regime, this means that an increase of the dimensionless static moment or the amplitude of the heave acceleration ($\ddot{h}$) has to be balanced by an increase of the amplitude of the moment (M) generated by the fluid flow (see Eqs. 3.22 and 3.24). In this context and for a given prescribed frequency (f^*), and thus a given heave motion, the amplitude of M can only increase if the pitch amplitude increases. Consequently, an increase of S^* results in an increase of $\overline{C_{P_{S,\theta}}}$ and therefore allows for more negative values of $\overline{C_{P_\theta}}$ to occur, which in turn happens when the pitch amplitude increases.

$\overline{C_{P_{S,\theta}}}$ also increases with the reduced frequency (f^*) because $\ddot{h}$ is proportional to the square of the

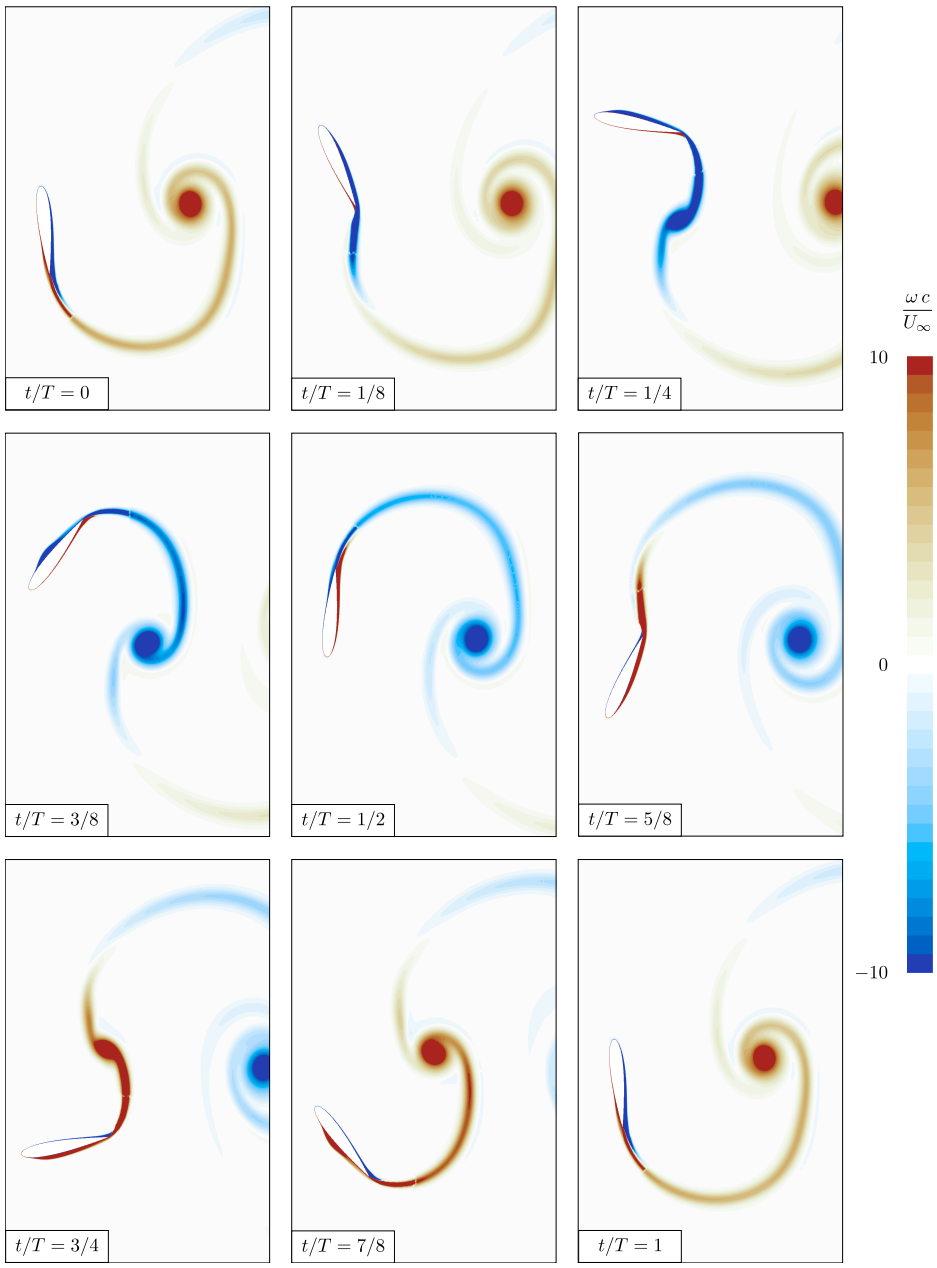

Figure 3.9: Time evolution of the dimensionless vorticity field ($\omega c/U_\infty$) during one cycle of the semi-passive turbine operating at its best efficiency point ($f^* = 0.20$ and $S^* = 0.65$).

frequency. The amplitude of M therefore also has to increase with f^* to respect the balance between $\overline{C_{P_{S,\theta}}}$ and $\overline{C_{P_\theta}}$. Such an increase of the moment with the reduced frequency would occur even if the pitch amplitude would remain constant due to larger pitch and heave velocities in the foil reference frame for larger f^*. Nevertheless, the pitch amplitude is still found to increase with f^*.

The time-averaged heave power coefficient also increases with the reduced frequency, as observed in Fig. 3.8a. The fact that it becomes more positive while $\overline{C_{P_\theta}}$ becomes more negative as the frequency

is increased results in a power coefficient at the generator and an efficiency that are less sensitive to the reduced frequency than $\overline{C_{P_h}}$ and $\overline{C_{P_\theta}}$, as long as we remain in the energy-extraction regime.

Blue regime (propulsion)

The motions in the blue regime (operating points denoted with blue diamonds) are similar to those in the green regime. Indeed, they are periodic (see Fig. 3.2b), no LEVs are formed and the phase lag between the heave and the pitch motions is still around 90°, ranging between 80° and 100°, as observed in Fig. 3.4b. The main difference between these two regimes is the pitch amplitude. More specifically, Fig. 3.4a shows that the pitch amplitude continues to decrease when switching from the green regime to the blue regime as the dimensionless static moment decreases down to zero. The consequence is that the energy-extraction regime switches to a propulsion regime. Indeed, Fig. 3.10 presents the contours of the time-averaged streamwise force coefficient ($\overline{C_{F_x}}$) and shows that all the operating points are characterized by a positive streamwise force coefficient ($\overline{C_{F_x}} > 0$) except for most of the operating points in the blue regime, which rather have a negative streamwise coefficient ($\overline{C_{F_x}} < 0$) or, in other words, a positive thrust coefficient. Consequently, these operating points require energy on a time-averaged basis instead of generating some ($\overline{\eta} < 0$ in Fig. 3.3). The cases with $f^* = 0.26$ and $S^* = 0.20$ and with $f^* = 0.30$ and $S^* = 0.20$ are two exceptions for which the streamwise force coefficient is positive, but the efficiency is negative.

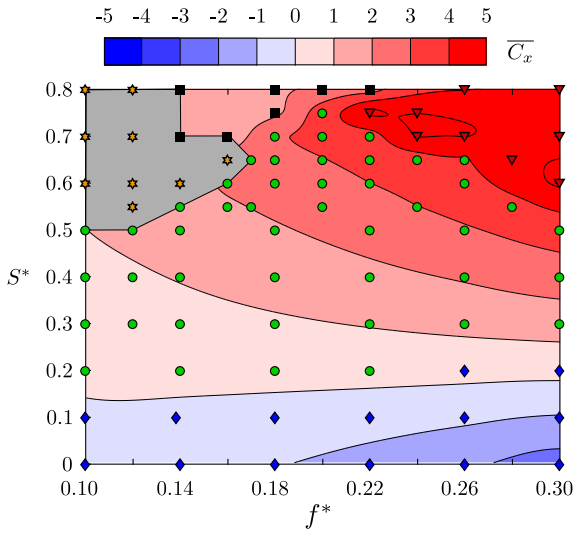

Figure 3.10: Contours of the time-averaged streamwise force coefficient.

Since the motions in the blue regime are periodic like in the green regime, the power coefficient at the generator can still be expressed as the sum of the heave and pitch power coefficients (see Eq. 3.30). As mentioned in the previous section, the time-averaged pitch power coefficient ($\overline{C_{P_\theta}}$) is negative throughout the current parametric study, thereby leaving the time-averaged heave power coefficient ($\overline{C_{P_h}}$) as the sole possible contributor to a positive energy extraction. In fact, it is found that $\overline{C_{P_h}}$ changes sign between the green and the blue regimes. This is attributed to a change of sign of the

heave force resulting from a change of sign of the effective angle of attack as the pitch amplitude decreases below a specific threshold, which depends on the frequency of the motions (Kinsey and Dumas, 2008). For example, time evolutions of the heave power coefficient (C_{P_h}), the dimensionless heave velocity ($\dot{h}^*$) and the heave force coefficient (C_{F_y}) are shown over one cycle for an operating point in the green regime and another one in the blue regime in Fig. 3.11. Note that the heave power coefficient can be expressed as the product of the heave force coefficient with the dimensionless heave velocity. This figure shows that the heave force coefficient is in phase with the dimensionless heave velocity in the green regime (see Fig. 3.11a), while the two are about 180° out of phase in the blue regime (see Fig. 3.11b) due to a change of sign of C_{F_y}. More information on the relation between the pitch amplitude and the transition between an energy-extraction regime and a propulsion regime is given in the works of Xiao and Zhu (2014) and Kinsey and Dumas (2008).

Lastly, it is worth noting that Mackowski and Williamson (2017) used their cyber-physical facility to study a flapping foil with a prescribed pitch motion and a passive heave motion and they obtained their best propulsion performances with the center of mass upstream of the pitch axis, i.e., a negative static moment.

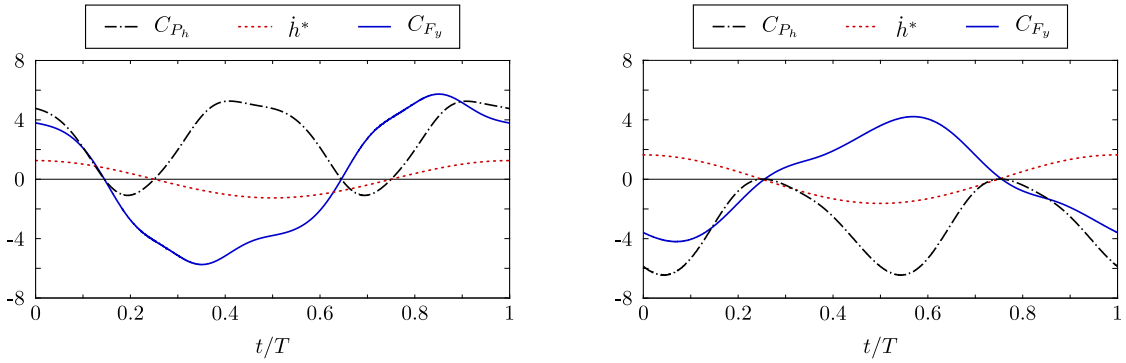

(a) Green regime ($f^* = 0.20$; $S^* = 0.65$).

(b) Blue regime ($f^* = 0.26$; $S^* = 0$).

Figure 3.11: Time evolutions of the heave power coefficient (C_{P_h}), the dimensionless heave velocity ($\dot{h}^*$) and the heave force coefficient (C_{F_y}) over one cycle for an operating point in the green regime and another one in the blue regime. The instant $t/T = 0$ corresponds to a moment at which $h = 0$ and $\dot{h} > 0$.

Black regime

The black regime (operating points denoted with black squares) is significantly different. During the initial transient period, the operating points in this regime behave like those in the green regime. The phase lag is initially around 90° and the pitch amplitude grows from cycles to cycles. For the operating points in the green regime, Fig. 3.12a shows that the moment coefficient generated by the flow about the pitch axis (C_M) is negative and maximum (in absolute value) when the maximum positive pitch velocity is reached, i.e., when the foil is at its maximum (positive) position in heave and $\theta = 0$, considering a phase lag of 90°. The opposite occurs around the minimum (negative) heave position.

Fig. 3.12b shows that this behavior is also observed for the operating points in the black regime at the beginning of the simulations. However, as the pitch amplitude keeps growing, the boundary layers eventually separate near the leading edge and large leading-edge vortices are formed and alter the hydrodynamic moment about the pitch axis, as shown in Fig. 3.13. They are formed before the instant at which the maximum pitch velocity is reached and they have the time to travel past the pitch axis before this specific instant due to the relatively low reduced frequency characterizing the operating points in this regime. As a result, the suction associated to the LEVs generates a positive contribution to the moment about the pitch axis when the pitch velocity is positive and maximum, and vice versa. For instance, the LEV that is observed at the instant $t/T = 5.83$ in Fig. 3.13a generates a negative contribution to the moment about the pitch axis when the pitch velocity is negative, as seen in Fig. 3.13b.

As already mentioned, the same phenomenon was also observed by Veilleux and Dumas (2017) and Zhu and Peng (2009). This modification of the hydrodynamic moment about the pitch axis then alters the phase lag and the pitch amplitude, which both quickly drop to smaller values for the subsequent foil oscillations. Following this series of events, a new limit-cycle oscillation regime is reached, which is characterized by moderate pitch amplitudes, phase lag values below 90° and the formation of LEVs. The occurrence of the boundary layers separation and the associated formation of LEVs are responsible for the slight variations observed for the efficiency, pitch amplitude and phase lag values from cycles to cycles (e.g., see Figs. 3.2c and 3.6b). Lastly, none of the operating points in the black regime extracts energy on a time-averaged basis.

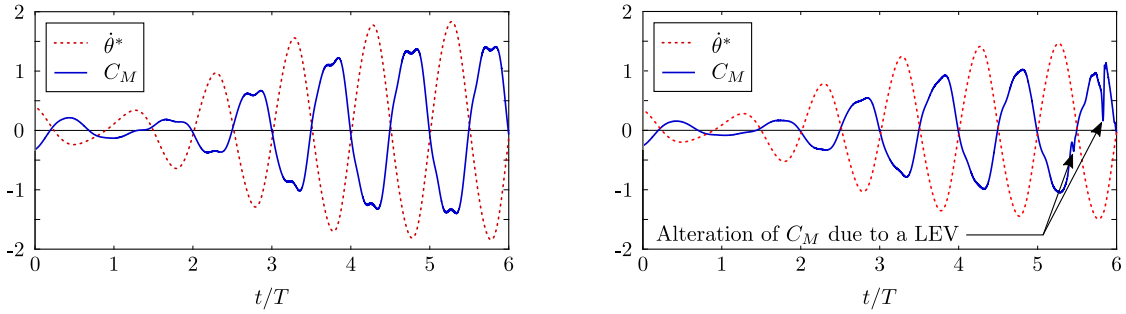

(a) Green regime ($f^* = 0.20$; $S^* = 0.65$).

(b) Black regime ($f^* = 0.16$; $S^* = 0.70$).

Figure 3.12: Time evolutions of the dimensionless pitch velocity ($\dot{\theta}^*$) and the moment coefficient (C_M) over the six first foil oscillations for an operating point in the green regime and another one in the black regime.

Orange regime

Even though the time evolution of the pitch angle appears to be very different in the orange regime (operating points denoted with orange stars) than in the black regime (see Figs. 3.2c and 3.2d), these two regimes are actually very similar. Indeed, the series of events leading to a new limit-cycle oscillation regime that have been described in the previous section also happens in the case of the orange

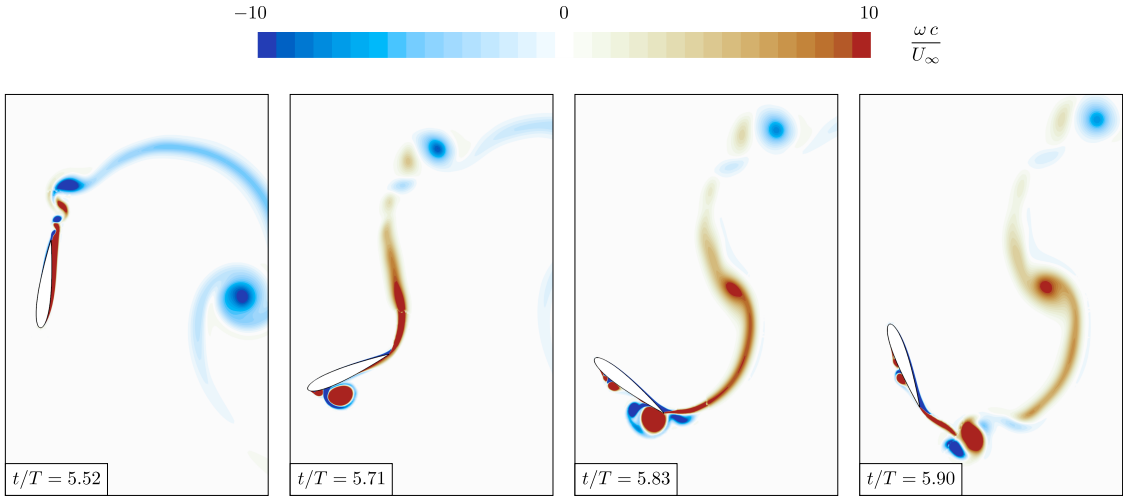

(a) Snapshots of the dimensionless vorticity field ($\omega\, c/U_\infty$) at some specific instants.

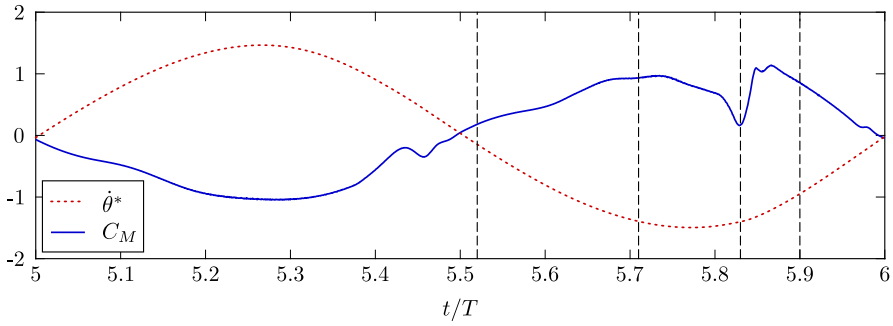

(b) Time evolutions of the dimensionless pitch velocity ($\dot{\theta}^*$) and the moment coefficient (C_M) during the 6$^{\text{th}}$ foil oscillation. The vertical dashed lines indicate the instant at which the different snapshots presented in Fig. 3.13a have been taken.

Figure 3.13: Influence of the formation of LEVs on the moment coefficient for a representative operating point in the black regime ($f^* = 0.16$ and $S^* = 0.70$). The instant $t/T = 0$ corresponds to the beginning of the simulation.

regime. Strong LEVs are formed and affect the moment about the pitch axis, as observed in Fig. 3.13. This results in sudden drops of the pitch amplitude and the phase lag between the heave and the pitch motions. The difference is that the drop in pitch amplitude is so important that the boundary layers eventually reattach. Following that, the foil starts to behave as in the transient period of the green regime again and the pitch amplitude restarts to grow until the boundary layers separate and LEVs are formed once more. This process is repeated endlessly.

Since the operating points in the orange regime alternate between the motion characteristics specific to the green and the black regimes, it is not surprising that the efficiency is found to oscillate between positive and negative values. Indeed, the efficiency can reach values as high as 40% for a few consecutive cycles and then quickly drop to values as low as -90% before becoming positive again. As mentioned earlier, such large variations make this regime inappropriate for a turbine application.

Red regime

The last regime, the red one (operating points denoted with red triangles), is also resulting from the formation of LEVs. The initial transient period is similar to the one in the green regime, like for the black and orange regimes. Again, the growth of the pitch amplitude eventually leads to the separation of the boundary layers near the leading edge and the formation of strong LEVs, which alter the moment generated by the fluid flow about the pitch axis. The first difference is that the formation of LEVs is delayed because the prescribed reduced frequencies are larger in this regime, hence resulting in smaller effective angles of attack for given pitch amplitudes (Kinsey and Dumas, 2014). The larger reduced frequencies also result in faster pitch motions with respect to the speed at which the LEVs travel downstream. Consequently, the LEVs do not have the time to travel past the pitch axis before the maximum pitch velocity is reached, unlike what happens for the black and orange regimes. Instead of generating a positive contribution to the moment about the pitch axis when the pitch velocity is positive and maximum, the LEVs rather result in a negative moment contribution. This strong dependence of the moment coefficient to the time at which the LEVs travel past the pitch axis location as already been pointed out by Young et al. (2013, 2014). The outcome in the case of the operating points in the red regime is that the growth of the pitch amplitude is extended and the phase lag increases and exceeds 90° until a permanent limit-cycle oscillation regime is finally reached. More than 50 complete foil oscillations can be needed before reaching these limit-cycle oscillations, which is much more than for all the other regimes of motion presented in the previous sections. Strong LEVs are still formed during this permanent response, which results in variations of the efficiency, the pitch amplitude and the phase lag from cycles to cycles. Furthermore, the wake is not convected as fast with respect to the foil motions in the red regime than in the black regime due to the fact that the reduced frequencies are larger. The stronger interaction occurring between the flapping foil and its wake in the red regime results in larger variations of the motions from cycles to cycles than in the black regime.

The difference between the black and the red regimes is subtle as it is only related to a different timing between the pitch motion and the formation and convection of LEVs. The operating point characterized with $f^* = 0.22$ and $S^* = 0.80$ has even behaved like the operating points in the red regime during the first 50 cycles before finally switching to a limit-cycle oscillation regime characterizing the black regime.

Lastly, a summary of the characteristics of each regime is given in Table 3.1.

Boundaries between the different regimes of motion

One can notice that some of the best operating points lie on the edge of the energy-extraction regime (see Fig. 3.3). This means that a small change in the operating conditions of these points could lead to a considerable drop in performance. For example, such a consequence could happen if the freestream flow was perturbed, hence affecting the reduced frequency. The reason for this very abrupt drop in performance is due to the sudden nature of separation.

Table 3.1: Summary of the characteristics describing each regime of motion.

Regime	$\overline{\eta}$	$\overline{\Theta_0}$	$\overline{\phi}$
Green	> 0	40° to 90°	90° to 105°
Blue	< 0	15° to 60°	80° to 100°
Black	< 0	55° to 70°	30° to 40°
Orange	Alternate between the green and black regimes		
Red	< 0	105° to 110°	115° to 155°

As mentioned before, no leading-edge vortices (LEVs) are observed in this study for all the operating points in the energy-extraction regime. Conversely, LEVs are formed for all the operating points in the black, the orange and the red regimes. Extra care should therefore be taken when selecting an operating point since the exact position of the boundaries between the green regime and the black, orange and red regimes is expected to be sensitive to the specific characteristics of a given flow. More specifically, every aspect of the flow that can affect the robustness of the boundary layers, such as the Reynolds number and the turbulence level in the freestream flow, for example, is expected to affect the locations of these boundaries. On the other hand, the performances achieved by the operating points in the green regime are not expected to be significantly affected by these aspects.

This sensitivity of the semi-passive turbine performance to the occurrence of separation is more pronounced than in the case of the fully-constrained turbine concept. A decrease of performance has also been reported for such turbines when LEVs are formed, but not a sharp drop (Kinsey and Dumas, 2014). This is because the forces acting on the foil are affected by the LEVs, but not the motions since they are prescribed rather than being passive. In the case of the semi-passive turbine studied in the current work, not only the forces are affected, but also the motions.

3.5.2 Role of the electric generator

It is evident that the operating points requiring energy on a time-averaged basis to sustain the foil motions ($\overline{\eta} < 0$) require the electric generator to act as an actuator. However, the operating points in the energy-extraction regime can also require that the electric generator acts as an actuator at some instants during the foil oscillations. In other words, this means that even though the power coefficient at the generator is positive on a cycle-averaged basis ($\langle C_{P_{\text{gen}}} \rangle > 0$), it can become negative at some instants during one cycle. In order to explain this point, an instantaneous version of Eq. 3.15 is analyzed:

$$C_{P_h} + C_{P_{m_h}} + C_{P_{S,h}} + C_{P_{D_h}} = C_{P_{\text{gen}}} \, . \tag{3.38}$$

If no friction is considered in heave, $D_h = 0$ and thus $C_{P_{D_h}} = 0$. However, $C_{P_{m_h}}$ has to be considered since it only becomes equal to zero on a cycle-averaged basis[2]. The best efficiency point ($f^* = 0.20$ and $S^* = 0.65$) is selected for the analysis and an arbitrary value of 1 is considered for m_h. The resulting values of $C_{P_{m_h}}$ along with the values of the other terms appearing in Eq. 3.38 are shown over one cycle in Fig. 3.14. The term $C_{P_{D_h}}$ is not shown since it is equal to zero and the terms C_{P_h} and $C_{P_{S,h}}$ are combined together.

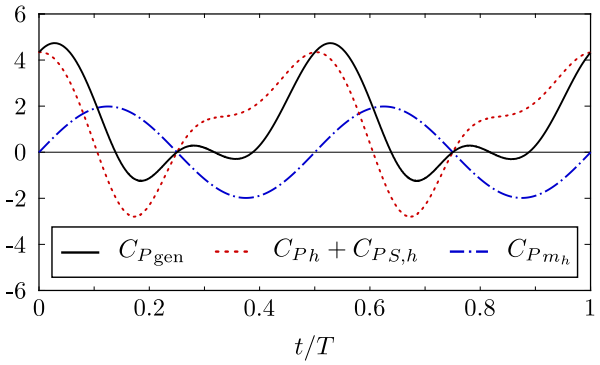

Figure 3.14: Time evolutions of the instantaneous power coefficient at the generator ($C_{P_{\mathrm{gen}}}$) and its contributions (see Eq. 3.38) over one cycle of the best efficiency point ($f^* = 0.20$ and $S^* = 0.65$). No friction is considered in heave ($D_h = 0$) and an arbitrary value of 1 is considered for m_h.

This figure shows that the term $C_{P_{m_h}}$ oscillates between positive and negative values with a cycle-averaged value of zero, as expected. This means that the value of m_h does not affect the cycle-averaged power coefficient at the generator, but it affects its instantaneous value. In order to avoid requiring to use the electric generator as an actuator, $C_{P_{\mathrm{gen}}}$ would need to remain positive throughout the cycle. However, it is found to be negative at different instants when $m_h = 1$. Since this happens both at moments when $C_{P_{m_h}}$ is positive and negative, there is no value of m_h that would allow $C_{P_{\mathrm{gen}}}$ to always remain positive. Nevertheless, this is not problematic because a typical electric generator can act as an actuator. Indeed, fully-constrained flapping-foil turbines also require the electric generator to act as an actuator at some instants during the foil oscillations, such as in the case of the prototype that has been designed and tested by Kinsey et al. (2011).

The semi-passive turbine concept proposed in this study also requires some power to reach the limit-cycle oscillations that characterize the energy-extraction regime. Indeed, the pitch amplitude starts from zero and has to pass through small pitch amplitudes that characterize the propulsion regime (blue regime) before reaching the larger pitch amplitudes characterizing the energy-extraction regime (green regime). This means that the semi-passive turbine concept is not self-starting.

[2]Considering that the heave motion is periodic

3.6 Conclusion

Two-dimensional URANS simulations have been conducted to investigate the potential of a novel semi-passive flapping-foil turbine with a prescribed heave motion and a passive pitch motion. Throughout the parametric study, the Reynolds number has been set to 3.9×10^6 based on the chord length, the pitch axis has been located at the quarter-chord point ($x_p/c = 0.25$), the dimensionless heave amplitude (H_0/c), the dimensionless moment of inertia about the pitch axis (I^*_θ) and the dimensionless pitch damping coefficient (D^*_θ) have been respectively set to 1, 2 and 0, and the dimensionless pitch spring stiffness coefficient (k^*_θ) has been chosen so that the pitch natural frequency matches the frequency of the prescribed heave motion.

By varying the reduced frequency and the dimensionless static moment (S^*), five different regimes of motion have been observed based on the time-averaged efficiency ($\overline{\eta}$), pitch amplitude ($\overline{\Theta_0}$) and phase lag ($\overline{\phi}$) values as well as the regularity of the motions. Among these different responses, one corresponds to an energy-extraction regime and is characterized by periodic limit-cycle oscillations with large pitch amplitudes and no formation of LEVs. It has been shown that the center of mass needs to be located downstream of the pitch axis for such motions to occur in order to balance the power required to sustain the pitch motion with a transfer of power from the heave motion to the pitch motion via the inertial coupling terms in the equations of motion. In practice, this could be achieved with the use of an asymmetric flywheel having the required mass distribution.

A maximum efficiency of 45.4% has been obtained with a pitch amplitude of 84.7° and a phase lag of 95.4° when $f^* = 0.20$ and $S^* = 0.65$. This performance confirms the great potential of the heave-prescribed semi-passive flapping-foil turbine since this efficiency is of the same order as the best efficiencies reported for the fully-constrained flapping-foil turbine concept (Kinsey and Dumas, 2014; Xiao and Zhu, 2014), but it is obtained here with a simpler device in terms of the structural design.

Even though a considerable amount of energy can be extracted from the flow on a time-averaged basis, the electric generator needs to act as an actuator at some instants during the foil oscillations when limit-cycle oscillations are reached as well as to start the device.

Finally, it is worth mentioning that several important structural parameters (see Table 3.1) have not been varied in this first investigation of the semi-passive flapping-foil turbine concept with a prescribed heave motion and a passive pitch motion. Future works are therefore needed in that regard.

Acknowledgments

Financial support from the Natural Sciences and Engineering Research Council of Canada (NSERC Discovery Grant/RGPIN/121819-2013 and CGS-D scholarship), the Tyler Lewis Clean Energy Research Foundation (2016 TLCERF grant) and the Leadership and Sustainable Development Scholarship Program of Université Laval is gratefully acknowledged by the authors. The computations presented in this work have been carried out on the supercomputer Colosse at Université Laval, man-

aged by Calcul Québec and Compute Canada.

Appendix

3.A Fluid-solid coupling algorithm in pseudocode

Beginning of the n^{th} time step

1. Computation of the prescribed heave position, velocity and acceleration at the current time step (h^n, $\dot{h}^n$, $\ddot{h}^n$);

2. Execution of the solid solver for the i^{th} outer loop:

   IF $i = 1$ (first outer loop) **THEN**

   a. Initial guess for the pitch angle at the current time step (θ^n) using the explicit second-order Adams-Bashforth scheme:

$$\theta_1^n = \theta^{n-1} + \frac{\Delta t}{2}\left(3\dot{\theta}^{n-1} - \dot{\theta}^{n-2}\right) ; \tag{3.39}$$

   ELSE IF $i = 2$ (second outer loop) **THEN**

   a. Initial guess for the Jacobian:

$$J_2^n = J^{n-1} ; \tag{3.40}$$

   b. Computation of the new pitch angle:

$$\theta_2^n = \theta_1^n - \frac{{R_\theta}_1^n}{J_2^n} ; \tag{3.41}$$

   ELSE IF $i > 2$ (subsequent outer loops) **THEN**

   a. Computation of the Jacobian:

$$J_i^n = \frac{{R_\theta}_{i-1}^n - {R_\theta}_{i-2}^n}{\theta_{i-1}^n - \theta_{i-2}^n} ; \tag{3.42}$$

   b. Computation of the new pitch angle:

$$\theta_i^n = \theta_{i-1}^n - \frac{{R_\theta}_{i-1}^n}{J_i^n} ; \tag{3.43}$$

END IF

3. Foil rotation according to the updated pitch angle (θ_i^n);

4. Check if the solid convergence criterion is met:
IF $\left(\dfrac{|\theta_i^n - \theta_{i-1}^n|}{\pi/2} < \varepsilon \textbf{ AND } i > 2 \right)$ **THEN**

   a. Execution of the fluid solver: perform fluid iterations until the fluid residuals convergence criteria are met;

   b. Incrementation of the time step and return to step 1.

ELSE THEN

   a. Execution of the fluid solver: perform fluid iterations until the value of the moment with the updated pitch angle (M_i^n) is converged;

   b. Computation of $\dot{\theta}_i^n$ and $\ddot{\theta}_i^n$ using the updated pitch angle θ_i^n with Eqs. 3.9 and 3.10;

   c. Computation of the residual:

$$R_{\theta}{}_i^n = I_\theta \, \ddot{\theta}_i^n + S\ddot{h}^n \cos(\theta_i^n) + D_\theta \, \dot{\theta}_i^n + k_\theta \, \theta_i^n - M_i^n \; ; \tag{3.44}$$

   d. Incrementation of the outer loop and return to step 2.

END IF

Bibliography

Abiru, Hisanori and Yoshitake, Akira. Study on a Flapping Wing Hydroelectric Power Generation System. *Journal of Environment and Engineering*, 6(1):178–186, 2011.

Abiru, Hisanori and Yoshitake, Akira. Experimental Study on a Cascade Flapping Wing Hydroelectric Power Generator. *Journal of Energy and Power Engineering*, 6(9):1429–1436, 2012.

Boudreau, Matthieu and Dumas, Guy. Comparison of the wake recovery of the axial-flow and cross-flow turbine concepts. *Journal of Wind Engineering and Industrial Aerodynamics*, 165:137 – 152, 2017.

Boudreau, Matthieu, Dumas, Guy, Rahimpour, Mostafa, and Oshkai, Peter. Experimental investigation of the energy extraction by a fully-passive flapping-foil hydrokinetic turbine prototype. *Journal of Fluids and Structures*, 82:446 – 472, 2018.

Campobasso, M. Sergio, Piskopakis, Andreas, Drofelnik, Jernej, and Jackson, Adrian. Turbulent navier–stokes analysis of an oscillating wing in a power-extraction regime using the shear stress transport turbulence model. *Computers & Fluids*, 88:136 – 155, 2013.

Cape Sharp Tidal Venture Ltd. http://capesharptidal.com/, 2018. Accessed: 2018-10-09.

Chen, Yongliang, Nan, Jingwen, and Wu, Jie. Wake effect on a semi-active flapping foil based energy harvester by a rotating foil. *Computers & Fluids*, 160:51 – 63, 2018.

Dacles-Mariani, J., Zilliac, G. G., Chow, J. S., and Bradshaw, P. Numerical/Experimental Study of a Wingtip Vortex in the Near Field. *AIAA Journal*, 33(9):1561 – 1568, 1995.

Dacles-Mariani, J., Kwak, D., and Zilliac, G. On numerical errors and turbulence modeling in tip vortex flow prediction. *International Journal for Numerical Methods in Fluids*, 30(1):65 – 82, 1999.

Deng, Jian, Teng, Lubao, Pan, Dingyi, and Shao, Xueming. Inertial effects of the semi-passive flapping foil on its energy extraction efficiency. *Physics of Fluids*, 27(5):053103 (17 pp.) –, 2015.

Derakhshandeh, J.F., Arjomandi, M., Dally, B., and Cazzolato, B. Flow-induced vibration of an elastically mounted airfoil under the influence of the wake of a circular cylinder. *Experimental Thermal and Fluid Science*, 74:58 – 72, 2016.

Ferziger, J.H. and Perić, M. *Computational Methods for Fluid Dynamics*. Springer, third edition, 2002.

Griffith, Martin D., Jacono, David Lo, Sheridan, John, and Leontini, Justin S. Passive heaving of elliptical cylinders with active pitching – from cylinders towards flapping foils. *Journal of Fluids and Structures*, 67:124 – 141, 2016.

Huxham, G. H., Cochard, S., and Patterson, J. Experimental Parametric Investigation of an Oscillating Hydrofoil Tidal Stream Energy Converter. In *Proceedings of the 18th Australasian Fluid Mechanics Conference*, Launceston, Australia, 2012.

Kim, Daegyoum, Strom, Benjamin, Mandre, Shreyas, and Breuer, Kenneth. Energy harvesting performance and flow structure of an oscillating hydrofoil with finite span. *Journal of Fluids and Structures*, 70:314 – 326, 2017.

Kinsey, Thomas and Dumas, Guy. Parametric Study of an Oscillating Airfoil in a Power-Extraction Regime. *AIAA Journal*, 46(6):1318–1330, 2008.

Kinsey, Thomas and Dumas, Guy. Computational Fluid Dynamics Analysis of a Hydrokinetic Turbine Based on Oscillating Hydrofoils. *Journal of Fluids Engineering*, 134(2):021104 (16 pp.) –, 2012.

Kinsey, Thomas and Dumas, Guy. Optimal Operating Parameters for an Oscillating Foil Turbine at Reynolds Number 500,000. *AIAA Journal*, 52(9):1885–1895, 2014.

Kinsey, Thomas, Dumas, Guy, Lalande, G., Ruel, J., Mehut, A., Viarouge, P., Lemay, J., and Jean, Y. Prototype testing of a hydrokinetic turbine based on oscillating hydrofoils. *Renewable Energy*, 36 (6):1710 – 1718, 2011.

Mackowski, A. W. and Williamson, C. H. K. Effect of pivot location and passive heave on propulsion from a pitching airfoil. *Phys. Rev. Fluids*, 2:013101 (24pp.), 2017.

Peng, Zhangli and Zhu, Qiang. Energy harvesting through flow-induced oscillations of a foil. *Physics of Fluids*, 21(12):174–191, 2009.

Shiels, D., Leonard, A., and Roshko, A. Flow-induced vibration of a circular cylinder at limiting structural parameters. *Journal of Fluids and Structures*, 15(1):3 – 21, 2001.

Shimizu, Eriko, Isogai, Koji, and Obayashi, Shigeru. Multiobjective Design Study of a Flapping Wing Power Generator. *Journal of Fluids Engineering*, 130(2):021104 (8 pp.) –, 2008.

Sitorus, Patar Ebenezer and Ko, Jin Hwan. Power extraction performance of three types of flapping hydrofoils at a reynolds number of 1.7e6. *Renewable Energy*, 132:106 – 118, 2019.

Sitorus, Patar Ebenezer, Le, Tuyen Quang, Ko, Jin Hwan, Truong, Tri Quang, and Park, Hoon Cheol. Design, implementation, and power estimation of a lab-scale flapping-type turbine. *Journal of Marine Science and Technology*, 2015.

Spalart, P. R., Jou, W-H., Strelets, M., and Allmaras, S. R. Comments on the Feasibility of LES for Wings, and on a Hybrid RANS/LES Approach. In *Advances in DNS/LES, Proceedings of the First AFOSR International Conference on DNS/LES*, pages 137 – 147, Ruston, Louisiana, USA, 1997.

Spalart, Philippe. R. and Allmaras, Steven R. A One-Equation Turbulence Model for Aerodynamic Flows. *Recherche Aérospatiale*, (1):5–21, 1994.

Spalart, Philippe R. and Rumsey, Christopher L. Effective inflow conditions for turbulence models in aerodynamic calculations. *AIAA Journal*, 45(10):2544 – 2553, 2007.

Teng, Lubao, Deng, Jian, Pan, Dingyi, and Shao, Xueming. Effects of non-sinusoidal pitching motion on energy extraction performance of a semi-active flapping foil. *Renewable Energy*, 85:810 – 818, 2016.

Veilleux, Jean-Christophe. Optimization of a Fully-Passive Flapping-Airfoil Turbine. Master's thesis, Université Laval, Québec, Qc, Canada, 2014.

Veilleux, Jean-Christophe and Dumas, Guy. Numerical optimization of a fully-passive flapping-airfoil turbine. *Journal of Fluids and Structures*, 70:102 – 130, 2017.

Wang, Zhuo, Du, Lin, Zhao, Jisheng, and Sun, Xiaofeng. Structural response and energy extraction of a fully passive flapping foil. *Journal of Fluids and Structures*, 72:96 – 113, 2017.

Wu, J., Qiu, Y. L., Shu, C., and Zhao, N. Pitching-motion-activated flapping foil near solid walls for power extraction: A numerical investigation. *Physics of Fluids*, 26(8):083601, 2014.

Wu, J., Chen, Y. L., and Zhao, N. Role of induced vortex interaction in a semi-active flapping foil based energy harvester. *Physics of Fluids*, 27(9):093601, 2015.

Xiao, Qing and Zhu, Qiang. A review on flow energy harvesters based on flapping foils. *Journal of Fluids and Structures*, 46:174–191, 2014.

Young, John, Ashraf, Muhammad A., Lai, Joseph C. S., and Platzer, Max F. Numerical Simulation of Fully Passive Flapping Foil Power Generation. *AIAA Journal*, 51(11):2727–2739, 2013.

Young, John, Lai, Joseph C. S., and Platzer, Max F. A review of progress and challenges in flapping foil power generation. *Progress in Aerospace Sciences*, 67:2–28, 2014.

Zhan, Jiapu, Xu, Bing, Wu, Jie, and Wu, Jing. Power extraction performance of a semi-activated flapping foil in gusty flow. *Journal of Bionic Engineering*, 14(1):99 – 110, 2017.

Zhu, Qiang. Optimal frequency for flow energy harvesting of a flapping foil. *Journal of Fluid Mechanics*, 675:495–517, 5 2011.

Zhu, Qiang. Energy harvesting by a purely passive flapping foil from shear flows. *Journal of Fluids and Structures*, 34:157–169, 2012.

Zhu, Qiang and Peng, Zhangli. Mode coupling and flow energy harvesting by a flapping foil. *Physics of Fluids*, 21(3):033601 (10 pp.) –, 2009.

Zhu, Qiang, Haase, Max, and Wu, Chin H. Modeling the capacity of a novel flow-energy harvester. *Applied Mathematical Modelling*, 33(5):2207–2217, 2009.

Chapter 4

Paper III:
Free-pitching flapping-foil turbines with an imposed sinusoidal heave motion

4.1 Résumé

Cette étude porte sur la dynamique d'une aile oscillante semi-passive, pour laquelle le mouvement de pilonnement est contraint de suivre un mouvement sinusoïdal tandis que le mouvement de tangage est passif, dans le but d'extraire l'énergie d'un écoulement de fluide auquel elle fait face. Cela implique que le mouvement de pilonnement est contraint mécaniquement alors que des supports élastiques sont utilisés en tangage. Le mouvement de tangage découle donc the l'interaction de l'aile avec l'écoulement et ses supports élastiques, c'est-à-dire des ressorts et des amortisseurs. Des simulations numériques ont été réalisées à un nombre de Reynolds de 3.9×10^6 basé sur la corde. Des efficacités positives et des mouvements de tangage périodiques de grande amplitude sont obtenus lorsque la fréquence du mouvement de tangage se synchronise à celle du mouvement de pilonnement. Les conditions pour lesquelles cela se produit sont examinées. Les résultats de cette étude démontrent qu'une performance optimale, sur le plan de la génération de puissance, peut être maintenue sur une large plage de moments d'inertie et de raideur en tangage, à condition que ces paramètres soient ajustés correctement. Cela peut être réalisé en combinant ces deux paramètres structuraux en un seul paramètre effectif: la raideur effective en tangage. Par ailleurs, quatre positions différentes du point de pivot sont testées, allant du bord d'attaque au trois-quart de corde. En ajustant adéquatement les paramètres structuraux influençant la dynamique de l'aile, des efficacités supérieures à 40% ont été atteintes pour chaque position du point de pivot, avec un maximum de 46% obtenu lorsque le point de pivot est situé au quart de corde. Les résultats de cette étude révèle qu'un déphasage d'environ 90° entre les mouvements de pilonnement et de tangage n'est optimal seulement lorsque le point de pivot est situé au quart de corde. Il doit plutôt être supérieur à 90° lorsque le point de pivot est situé en amont du quart de corde et inférieur à 90° lorsque le point de pivot est plutôt situé en aval de cette

position.

4.2 Abstract

This work investigates the dynamics of a semi-passive flapping-foil with a prescribed sinusoidal heave motion and a passive pitch motion with the objective of extracting energy from an oncoming fluid flow. This implies that the heave motion is mechanically driven while the foil is elastically supported in pitch. The pitch motion therefore results from the interaction of the foil with the flow and its elastic supports, namely springs and dampers. Numerical simulations have been conducted at a Reynolds number of 3.9×10^6 based on the chord length. Positive efficiencies and periodic pitch motions of large amplitude are obtained when the frequency of the pitch motion synchronizes itself to the frequency of the prescribed heave motion. The conditions under which it happens are explored. The results of this study demonstrate that an optimal power-generation performance can be maintained over large variations of the moment of inertia and pitch stiffness, provided that they are properly scaled. This is achieved by combining these two structural parameters into a single effective parameter: the effective pitch stiffness coefficient. Moreover, four different positions of the pitch axis are considered, ranging from the leading edge to the three-quarter-chord point. By adjusting the governing structural parameters adequately, efficiencies exceeding 40% can be achieved with all four positions of the pitch axis, with a maximum of 46.0% obtained when the pitch axis is located at the quarter-chord point. It is found that a phase lag near 90° between the heave and the pitch motions is only optimal with this specific position of the pitch axis. It needs to be larger than 90° when the pitch axis is located upstream of the quarter-chord point and smaller than 90° when it is located downstream of this position.

4.3 Introduction

Typically, the heave (translational) and the pitch (rotational) motions of flapping-foil turbines are constrained to be two pure sinusoids with a specific phase lag between them (McKinney and DeLaurier, 1981; Kinsey and Dumas, 2008; Kinsey et al., 2011; Kinsey and Dumas, 2014; Zhu, 2011; Kim et al., 2017). By adequately selecting the values of the kinematic parameters describing the motions of such a turbine concept, which we refer to as a fully-constrained flapping-foil turbine, a considerable amount of energy can be extracted from an oncoming fluid flow, with efficiencies approaching 45% (Kinsey and Dumas, 2014). More specifically, and according to the comprehensive reviews of this technology performed by Young et al. (2014) and by Xiao and Zhu (2014), an optimal performance is achieved when the reduced frequency of the motions is between 0.10 and 0.25, the heave amplitude is of the order of one chord length, the pitch amplitude is between 70° and 95° and the phase lag between the heave and the pitch motions is around 90°. In addition to these kinematic parameters, Davids (1999) showed that the position of the pitch axis, or pivot point, also plays a crucial role regarding the flapping-foil turbine performance. He found that the optimal phase lag between the heave and the pitch motions depends on the pitch axis location. Kinsey and Dumas (2008) also showed that the

position of the pitch axis significantly affects the timing between the hydrodynamic force component acting on the foil in the heave direction and the heave velocity, which is critical regarding the energy extraction. Young et al. (2013) and Young et al. (2014) pointed out that, when a leading-edge vortex (LEV) is formed, the time evolution of the hydrodynamic moment about the pitch axis is greatly influenced by the time at which the LEV travels past the pitch axis location during the foil oscillation. As a result, the power transfer occurring between the foil and the flow that is attributed to the pitch motion is highly dependent on the pitch axis location.

Design simplicity is a critical factor for maximizing the reliability of turbines while also minimizing their manufacturing and maintenance costs. In this context, the use of passive, or unconstrained, motions has recently started to draw a lot of interest for the design of flapping-foil turbines. This simplification of the turbine design allows getting rid of the complex mechanisms that are typically used to prescribe the heave and the pitch motions of such turbines (McKinney and DeLaurier, 1981; Kinsey et al., 2011; Kim et al., 2017; Xu et al., 2017). Several alternatives, with different degrees of complexity, are possible by constraining or not each of the parameters describing the turbine motions, namely the motion shapes and amplitudes in heave and in pitch, the frequency in heave and in pitch and the phase lag between both degrees of freedom. At one end of the spectrum, all the motion parameters can be constrained, hence leading to what we refer to as a fully-constrained turbine (McKinney and DeLaurier, 1981; Kinsey and Dumas, 2008; Kinsey et al., 2011; Kinsey and Dumas, 2014; Zhu, 2011; Kim et al., 2017; Xu et al., 2017). On the other hand, all the motion parameters can be left free by elastically supporting the foil in heave and in pitch with springs and dampers to obtain a fully-passive flapping-foil turbine (Peng and Zhu, 2009; Zhu, 2012; Veilleux and Dumas, 2017; Wang et al., 2017; Boudreau et al., 2018). While the fully-passive concept is simpler in terms of the structural design than its fully-constrained counterpart, the best efficiencies that have been reported in the literature for this technology remain smaller as they are of the order of 30% (Veilleux and Dumas, 2017; Wang et al., 2017; Boudreau et al., 2018).

Another intermediate option consists in prescribing only one of the two motions while letting the other free. The most popular option is to prescribe the pitch motion and to elastically support the foil in heave (Abiru and Yoshitake, 2011, 2012; Chen et al., 2018; Deng et al., 2015; Derakhshandeh et al., 2016; Griffith et al., 2016; Huxham et al., 2012; Shimizu et al., 2008; Sitorus et al., 2015; Teng et al., 2016; Wu et al., 2014, 2015; Zhan et al., 2017; Zhu et al., 2009; Zhu and Peng, 2009). As for the fully-passive concept, efficiencies of the order of 30% have been reported for this semi-passive concept. Boudreau et al. (2019) proposed the other alternative more recently, with a prescribed heave motion and a passive pitch motion. They reported a maximum efficiency of 45.4%, thereby competing with the best fully-constrained turbines (Kinsey and Dumas, 2014). This performance is reached when the reduced frequency of the prescribed heave motion is set to 0.20, while the pitch amplitude and the phase lag between the heave and the pitch motions, both passively resulting from the interaction of the foil with its elastic supports and the flow, are respectively equal to 84.7° and 95.4°.

When passive motions are considered, the number of governing parameters is typically larger than in

the case of fully-constrained turbines. For example, both Veilleux (2014) and Boudreau et al. (2018) investigated the sensitivity of the fully-passive flapping-foil turbine dynamics to seven different parameters with a fixed pitch axis location. Each of these parameters were varied while all the remaining parameters were kept constant. Among their findings, they showed that the turbine performance is especially sensitive to the heave and pitch stiffness coefficients due to their role in the timing between the heave and the pitch motions.

Peng and Zhu (2009) observed four completely different types of motion when modifying the position of the pitch axis of a similar fully-passive flapping-foil turbine, but with a massless foil that is elastically supported in heave with a damper only (no spring). They found that for a given pitch stiffness and as the position of the pitch axis is shifted from the leading edge toward the trailing edge, the foil response is switching from damped motions (the foil remaining steady at its equilibrium position), periodic motions leading to a net energy extraction from the flow and two different types of irregular motions. The transition between these different responses is shifted toward the trailing edge as the pitch stiffness is increased.

The influence of the mass of the foil was studied by Deng et al. (2015) for a semi-passive flapping-foil turbine with a passive heave motion and a prescribed pitch motion. They varied the ratio between the density of the foil and the fluid density from 0.125 to 100, while keeping the other structural parameters constant. They observed a continuous decrease of the efficiency as the density ratio is increased and attributed this result to a decrease of the phase lag between the heave and the pitch motions.

Unfortunately, it is difficult to draw general conclusions from the literature due to the large number of parameters involved and because the different studies available have been conducted with different flapping-foil turbine designs and around different operating points. Moreover, most of the investigations performed on flapping-foil turbines have been carried out at low Reynolds numbers of the order of 1 000 and with operating points for which the formation of leading-edge vortices (LEVs) plays a important role (Young et al., 2014; Xiao and Zhu, 2014). Conversely, the best efficiencies reported for the fully-constrained flapping-foil turbine concept and the semi-passive flapping-foil turbine concept, with a prescribed heave motion and a passive pitch motion, have both been achieved without LEVs and at a much larger Reynolds numbers, more representative of a full-scale hydrokinetic turbine application (Kinsey and Dumas, 2014; Boudreau et al., 2019). It is therefore legitimate to question the full applicability at large Reynolds numbers of the conclusions drawn from the literature.

Following the study of Boudreau et al. (2019), the present work focuses on the semi-passive turbine concept with a prescribed heave motion and a passive pitch motion operating at a Reynolds number of 3.9×10^6. The objectives are to find what are the required features to achieve an optimal energy extraction from the flow and how an optimal performance can be maintained over a broad range of structural parameter values. For that purpose, we vary some important structural parameters that were kept constant in our previous investigation of the proposed semi-passive turbine concept. More specif-

ically, the effects of the moment of inertia about the pitch axis and the pitch stiffness are investigated. Instead of only evaluating their impact independently, as is often done, we propose a simple effective parameter that combines them in an attempt to reduce the number of governing parameters. Moreover, different pitch axis locations ranging from the leading edge to the three-quarter-chord point are tested. The dynamics of the resulting semi-passive turbine cases are compared to the dynamics of optimal fully-constrained turbine cases. Since only a few studies exist on flapping foils with passive pitch motions, the results of the current study are a valuable addition to our knowledge of the dynamics of such devices.

The description of the semi-passive turbine concept and the numerical methodology are presented in Sec. 4.4. The relevance of combining the moment of inertia and the pitch stiffness into a single effective parameter is analyzed in Secs. 4.5.1 to 4.5.3. The influence of the pitch axis location is then investigated in Sec. 4.5.4, followed by the effect of varying the frequency of the prescribed heave motion in Sec. 4.5.5 and a discussion about some practical considerations in Sec. 4.5.6.

4.4 Methodology

4.4.1 Semi-passive turbine concept

A flapping-foil turbine with a prescribed sinusoidal heave motion (h) and a passive pitch motion (θ), referred to as a semi-passive turbine, is considered in this work. This is achieved by supporting the foil in pitch with elastic supports, i.e., springs and dampers. As a result, the pitch motion is governed by the following equation of motion:

$$M = I_\theta\,\ddot{\theta} + S\,\ddot{h}\cos(\theta) + D_\theta\,\dot{\theta} + k_\theta\,\theta\ , \tag{4.1}$$

where the superscript $(\cdot)$ denotes a time derivative, M is the hydrodynamic moment acting on the foil about the pitch axis, I_θ is the moment of inertia about the pitch axis, S is the static moment, D_θ is the pitch damping coefficient and k_θ is the pitch stiffness coefficient (rotational stiffness). The static moment is given by:

$$S = m_\theta\,x_\theta\ , \tag{4.2}$$

where m_θ is the mass of the components undergoing the pitch motion and x_θ is the distance between the center of mass and the pitch axis. This distance is defined positive when the center of mass is located downstream of the pitch axis, as shown in Fig. 4.1. The foil consists in a rigid NACA0015 profile and its heave motion is prescribed to follow a sinusoidal motion with specific amplitude (H_0) and frequency (f_h):

$$h = H_0\,\min\left(\frac{t}{3\,T_h}, 1\right)\,\sin\left(2\,\pi\,f_h\,t\right)\ , \tag{4.3}$$

where t is time and T_h is the period of one foil oscillation in heave ($T_h = 1/f_h$). A linear growth of the heave amplitude is imposed during the first three foil oscillations in order to provide a smooth initial condition. Note that the heave position (h) corresponds to the position of the pitch axis.

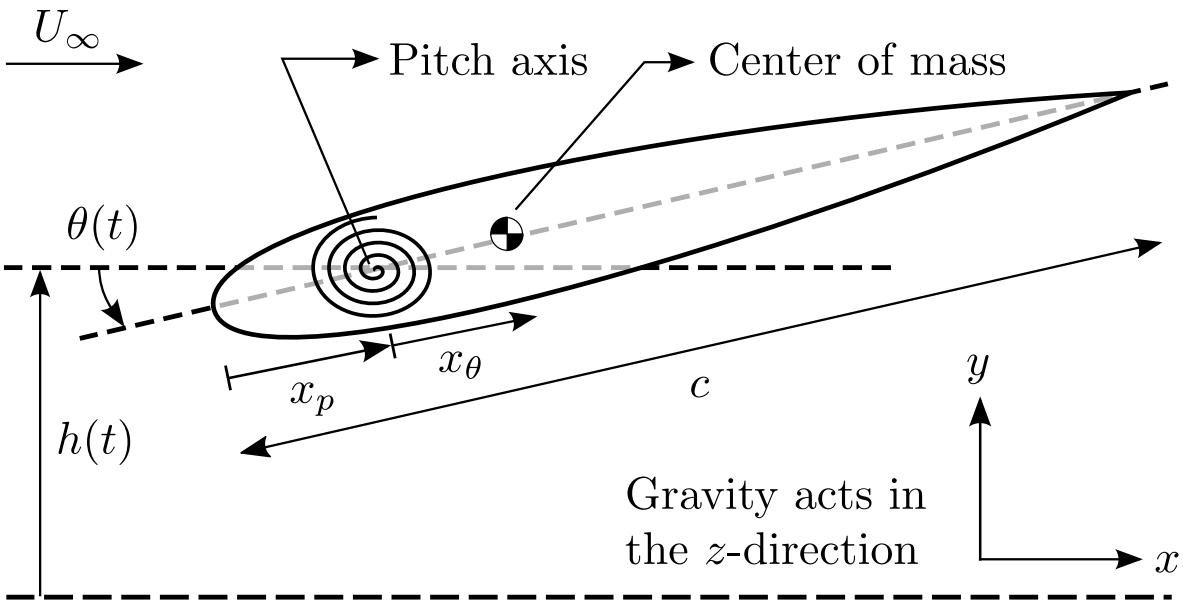

Figure 4.1: Schematic of the semi-passive flapping-foil turbine concept with a prescribed heave motion and a passive pitch motion. Note that the gravitational acceleration acts in the z-direction, hence not affecting the pitch dynamics.

The turbine technology considered in this study differs from another semi-passive turbine concept that has been more commonly studied in the literature and for which the heave motion is passive while the pitch motion is prescribed (Abiru and Yoshitake, 2011, 2012; Chen et al., 2018; Deng et al., 2015; Derakhshandeh et al., 2016; Griffith et al., 2016; Huxham et al., 2012; Shimizu et al., 2008; Sitorus et al., 2015; Teng et al., 2016; Wu et al., 2014, 2015; Zhan et al., 2017; Zhu et al., 2009; Zhu and Peng, 2009). The interest in a semi-passive turbine with a passive pitch motion comes from the fact that no actuator and no controller are needed to drive the pitch motion, hence resulting in a simple device. Furthermore, it is logical to connect the electric generator to the heave motion since most of the energy extracted from the flow by flapping-foil turbines occurs via this degree of freedom (Kinsey and Dumas, 2008, 2014; Zhu, 2011). The addition of a controller allows prescribing the heave motion to follow a desired function of time, namely a sinusoidal motion given by Eq. 4.3 in the present case. More information about the different possibilities of passive motions for flapping-foil turbines is provided in the work of Boudreau et al. (2019).

4.4.2 Dimensionless form of the governing equations

The fluid flow is governed by the incompressible Navier-Stokes equations (see e.g. Panton (2013)):

$$\nabla \cdot u = 0 \,, \tag{4.4}$$

$$\frac{\partial u}{\partial t} + u \cdot \nabla u = -\frac{1}{\rho}\nabla p + \frac{1}{\nu}\nabla^2 u \,, \tag{4.5}$$

where u is the velocity vector, ρ is the fluid density, p is the pressure and ν is the kinematic viscosity of the fluid.

Considering the following reference scales for length (L_{ref}), velocity (U_{ref}), time (t_{ref}) and pressure (p_{ref}):

$$L_{\text{ref}} = c \,, \tag{4.6}$$

$$U_{\text{ref}} = U_{\infty} \,, \tag{4.7}$$

$$t_{\text{ref}} = L_{\text{ref}}/U_{\text{ref}} = c/U_{\infty} \,, \tag{4.8}$$

$$p_{\text{ref}} = \rho\, U_{\infty}^2 \,, \tag{4.9}$$

where c is the chord length and U_{∞} is the freestream velocity, Eqs. 4.4 and 4.5 can be written in dimensionless form:

$$\nabla \cdot u^* = 0 \,, \tag{4.10}$$

$$\frac{\partial u^*}{\partial t^*} + u^* \cdot \nabla^* u^* = -\nabla^* p^* + \frac{1}{\text{Re}} \nabla^{*2} u^* \,, \tag{4.11}$$

with the superscript $*$ indicating a dimensionless operator or variable (e.g., $t^* = t/t_{\text{ref}}$) and Re is the Reynolds number:

$$Re = \frac{U_{\infty}\, c}{\nu} \,, \tag{4.12}$$

which is set to 3.9×10^6, as in our previous investigation of the semi-passive turbine concept (Boudreau et al., 2019).

In addition to the reference length scale (see Eq. 4.6) and time scale (see Eq. 4.8), the following reference scale for the hydrodynamic moment about the pitch axis (M_{ref}) is considered:

$$M_{\text{ref}} = \frac{1}{2} \rho\, U_{\infty}^2\, b\, c^2 \,, \tag{4.13}$$

where b is the span length. This additional reference scale allows deriving the dimensionless form of the equation of motion in pitch (Eq. 4.1):

$$C_M/2 = I_{\theta}^* \ddot{\theta}^* + S^* \ddot{h}^* \cos(\theta) + D_{\theta}^* \dot{\theta}^* + k_{\theta}^* \theta \,, \tag{4.14}$$

where:

$$C_M = \frac{M}{0.5\, \rho\, U_{\infty}^2\, b\, c^2} \,, \tag{4.15}$$

$$I_{\theta}^* = \frac{I_{\theta}}{\rho\, b\, c^4} \,, \tag{4.16}$$

$$S^* = \frac{S}{\rho\, b\, c^3} \,, \tag{4.17}$$

$$D_{\theta}^* = \frac{D_{\theta}}{\rho\, U_{\infty}\, b\, c^3} \,, \tag{4.18}$$

$$k_{\theta}^* = \frac{k_{\theta}}{\rho\, U_{\infty}^2\, b\, c^2} \,, \tag{4.19}$$

and:

$$h^* = \frac{h}{c}\,, \quad \dot{h}^* = \frac{\dot{h}}{U_\infty}\,, \quad \ddot{h}^* = \frac{\ddot{h}\,c}{U_\infty^2}\,, \quad \dot{\theta}^* = \frac{\dot{\theta}\,c}{U_\infty}\,, \quad \ddot{\theta}^* = \frac{\ddot{\theta}\,c^2}{U_\infty^2}\,.$$

Note that the span length is considered to be equal to one ($b = 1$) since forces per unit span are obtained from the two-dimensional (2D) simulations conducted in this study.

The reference scales used to derive the dimensionless form of the equation of motion in pitch lead to the definitions of the dimensionless moment of inertia (I_θ^*), pitch damping coefficient (D_θ^*) and pitch stiffness coefficient (k_θ^*) presented above. These reference scales are the same than those used by Onoue et al. (2015) and by Shiels et al. (2001) for their respective study of an elastically-supported pitching flat plate and a cylinder undergoing vortex-induced vibrations (VIV). As pointed out by these authors, such a normalization is relevant when considering strongly-coupled fluid-structure interactions. Furthermore, it remains valid when the moment of inertia or the pitch stiffness coefficient approaches zero, unlike other traditional normalizations based on the natural frequency for the reference time scale.

Lastly, the dimensionless form of the prescribed heave motion (see Eq. 4.3) is given by:

$$h^* = H_0^* \min\left(\frac{t^*}{3\,T_h^*}, 1\right) \sin\left(2\,\pi\,f_h^*\,t^*\right)\,, \tag{4.20}$$

where $H_0^* = H_0/c$ and f_h^* is the heave reduced frequency:

$$f_h^* = \frac{f_h\,c}{U_\infty}\,. \tag{4.21}$$

4.4.3 Performance metrics

The equation of motion in pitch (Eq. 4.1) can be analyzed from a power balance perspective by putting all the terms on the left hand side of the equation, multiplying each of them by the pitch velocity ($\dot{\theta}$) and then normalizing and cycle-averaging the result to obtain:

$$\langle C_{P_\theta}\rangle + \langle C_{P_{I_\theta}}\rangle + \langle C_{P_{S,\theta}}\rangle + \langle C_{P_{D_\theta}}\rangle + \langle C_{P_{k_\theta}}\rangle = 0\,, \tag{4.22}$$

where the angle brackets denote the cycle-averages. More specifically, these different power coefficients are defined as:

$$\langle C_{P_\theta}\rangle = \frac{1}{T_h}\int_{t_i}^{t_i+T_h}\left(\frac{M\,\dot{\theta}}{0.5\,\rho\,U_\infty^3\,b\,c}\right)dt\,, \tag{4.23}$$

$$\langle C_{P_{I_\theta}}\rangle = \frac{1}{T_h}\int_{t_i}^{t_i+T_h}\left(\frac{-I_\theta\,\ddot{\theta}\,\dot{\theta}}{0.5\,\rho\,U_\infty^3\,b\,c}\right)dt\,, \tag{4.24}$$

$$\langle C_{P_{S,\theta}}\rangle = \frac{1}{T_h}\int_{t_i}^{t_i+T_h}\left(\frac{-S\ddot{h}\,\dot{\theta}\cos(\theta)}{0.5\,\rho\,U_\infty^3\,b\,c}\right)dt\,, \tag{4.25}$$

$$\langle C_{P_{D_\theta}}\rangle = \frac{1}{T_h}\int_{t_i}^{t_i+T_h}\left(\frac{-D_\theta\,\dot{\theta}^2}{0.5\,\rho\,U_\infty^3\,b\,c}\right)dt\,, \tag{4.26}$$

$$\langle C_{P_{k_\theta}} \rangle = \frac{1}{T_h} \int_{t_i}^{t_i+T_h} \left(\frac{-k_\theta \, \theta \, \dot{\theta}}{0.5 \, \rho \, U_\infty^3 \, b \, c} \right) dt \; , \tag{4.27}$$

where t_i is the time at which a given cycle starts. It is defined as the instant at which $h = 0$ and $\dot{h} > 0$. Note that unless otherwise indicated, the term power coefficient refers to a cycle-averaged value throughout the current work.

When an idealized turbine with no friction is considered, D_θ is equal to zero and thus $\langle C_{P_{D_\theta}} \rangle = 0$. Moreover, the power coefficients associated to the inertial and stiffness terms are zero on average during one turbine cycle ($\langle C_{P_{I_\theta}} \rangle = 0$ and $\langle C_{P_{k_\theta}} \rangle = 0$) when the pitch motion is periodic. In this context, Eq. 4.22 simplifies to:

$$\langle C_{P_\theta} \rangle + \langle C_{P_{S,\theta}} \rangle = 0 \; . \tag{4.28}$$

$\langle C_{P_\theta} \rangle$ is the pitch power coefficient and it quantifies the power transfer occurring between the foil's pitch motion and the flow. It is positive when the pitch motion extracts power from the flow. Conversely, it is negative when the pitch motion provides power to the flow, or, in other words, requires power from another source to be sustained. $\langle C_{P_{S,\theta}} \rangle$ is the power coefficient associated to the inertial coupling term in Eq. 4.1. It is associated with the power transfer occurring between the heave and the pitch motions when the static moment is not zero, i.e., when the pitch axis does not coincide with the center of mass. It is positive when the heave motion provides power to the pitch motion.

A similar analysis can be carried out in heave using a general equation of motion for this degree of freedom:

$$F_y = m_h \ddot{h} + S\left(\ddot{\theta}\cos\theta - \dot{\theta}^2 \sin\theta\right) + D_h \dot{h} + F_{\text{gen}} \; , \tag{4.29}$$

where F_y is the component of the hydrodynamic force acting on the foil in the heave direction, m_h is the mass of the components undergoing the heave motion, D_h is the heave damping coefficient and F_{gen} is the force associated to the presence of an electric generator. As for the pitch damping coefficient (D_θ), the heave damping coefficient (D_h) is associated to undesired losses of energy and is considered to be zero in the current study. This means that all the energy extracted from the flow can be transferred to the electric generator.

As mentioned in the work of Boudreau et al. (2019), Eq. 4.29 must not be confused with Eq. 4.3. The heave motion is prescribed according to Eq. 4.3 while Eq. 4.29 is only used to analyze the results once the simulations are completed. However, these two equations are related to each other because one would need to control the value of F_{gen} so that the solution of Eq. 4.29 corresponds to Eq. 4.3 in order to prescribe the heave motion to a specific sinusoidal motion with a real turbine prototype.

Eq. 4.29 can be reformulated by putting all the terms on the left hand side of the equation except F_{gen}, multiplying each of them by the heave velocity ($\dot{h}$) and then normalizing and cycle-averaging the result to obtain:

$$\langle C_{P_h} \rangle + \langle C_{P_{m_h}} \rangle + \langle C_{P_{S,h}} \rangle + \langle C_{P_{D_h}} \rangle = \langle C_{P_{\text{gen}}} \rangle \; , \tag{4.30}$$

where:

$$\langle C_{P_h} \rangle = \frac{1}{T_h} \int_{t_i}^{t_i+T_h} \left(\frac{F_y \dot{h}}{0.5\,\rho\, U_\infty^3\, b\, c} \right) dt \ , \tag{4.31}$$

$$\langle C_{P_{m_h}} \rangle = \frac{1}{T_h} \int_{t_i}^{t_i+T_h} \left(\frac{-m_h \ddot{h} \dot{h}}{0.5\,\rho\, U_\infty^3\, b\, c} \right) dt \ , \tag{4.32}$$

$$\langle C_{P_{S,h}} \rangle = \frac{1}{T_h} \int_{t_i}^{t_i+T_h} \left(\frac{-S \dot{h} \left(\ddot{\theta} \cos\theta - \dot{\theta}^2 \sin\theta \right)}{0.5\,\rho\, U_\infty^3\, b\, c} \right) dt \ , \tag{4.33}$$

$$\langle C_{P_{D_h}} \rangle = \frac{1}{T_h} \int_{t_i}^{t_i+T_h} \left(\frac{-D_h \dot{h}^2}{0.5\,\rho\, U_\infty^3\, b\, c} \right) dt \ , \tag{4.34}$$

$$\langle C_{P_{\text{gen}}} \rangle = \frac{1}{T_h} \int_{t_i}^{t_i+T_h} \left(\frac{F_{\text{gen}} \dot{h}}{0.5\,\rho\, U_\infty^3\, b\, c} \right) dt \ . \tag{4.35}$$

Since the heave damping coefficient (D_h) is considered to be equal to zero, $\langle C_{P_{D_h}} \rangle = 0$. Moreover, $\langle C_{P_{m_h}} \rangle$ is also equal to zero because the prescribed heave motion is periodic. This leaves:

$$\langle C_{P_h} \rangle + \langle C_{P_{S,h}} \rangle = \langle C_{P_{\text{gen}}} \rangle \ . \tag{4.36}$$

$\langle C_{P_h} \rangle$ is the heave power coefficient. It is analogous to $\langle C_{P_\theta} \rangle$ and uses the same sign convention. A positive value of $\langle C_{P_h} \rangle$ stands for a net power extraction from the flow via the heave motion on average during one cycle, while a negative value means that the heave motion provides power to the flow. $\langle C_{P_{S,h}} \rangle$ is similar to $\langle C_{P_{S,\theta}} \rangle$, it is related to the inertial coupling term involving the static moment and is positive when the pitch motion provides power to the heave motion. Lastly, $\langle C_{P_{\text{gen}}} \rangle$ is the power coefficient available at the electric generator and is therefore a measure of the turbine performance.

When the pitch motion is periodic, with the prescribed heave motion always being periodic, $\langle C_{P_{S,h}} \rangle$ and $\langle C_{P_{S,\theta}} \rangle$ are equal but opposite:

$$\langle C_{P_{S,h}} \rangle = -\langle C_{P_{S,\theta}} \rangle \ . \tag{4.37}$$

For example, when $\langle C_{P_{S,h}} \rangle$ is negative but $\langle C_{P_{S,\theta}} \rangle$ is positive, some power is transferred from the heave motion to the pitch motion on average during one cycle.

In the context of periodic motions, Eqs. 4.28, 4.36 and 4.37 can be combined to give:

$$\langle C_{P_{\text{gen}}} \rangle = \langle C_{P_h} \rangle + \langle C_{P_\theta} \rangle \ . \tag{4.38}$$

This last equation states that the cycle-averaged power available at the generator is equal to the net power extracted from the flow when no friction is considered in heave and in pitch and when the motions are periodic. The previous parametric study conducted on the same semi-passive turbine concept (Boudreau et al., 2019) has shown that the operating points with high efficiencies are indeed

characterized by periodic pitch motions. Nevertheless, $\langle C_{P_{\text{gen}}} \rangle$ is evaluated using Eq. 4.36 throughout this study to account for the possibility of non-periodic pitch motions.

In addition to the different power coefficients defined above, it is also useful to evaluate the turbine performance in terms of its efficiency (η), which is given by:

$$\eta = \langle C_{P_{\text{gen}}} \rangle \, c/d \, , \tag{4.39}$$

where d is the overall transverse extent of the foil motion. In other words, it corresponds to the distance between the maximum and minimum positions reached by any point on the foil surface in the heave direction during one foil oscillation.

Two other metrics are also useful to characterize a given cycle, namely the pitch amplitude:

$$\Theta_0 = \frac{\theta_{\text{max}} - \theta_{\text{min}}}{2} \, , \tag{4.40}$$

and the phase lag between the heave and the pitch motions, here given in degrees:

$$\phi = \frac{360}{T_h} \left(t_{\theta_{\text{max}}} - t_{h_{\text{max}}} \right) \quad \text{[degrees]} \, , \tag{4.41}$$

where θ_{max} and θ_{min} are the maximum and minimum pitch angles reached during this specific cycle and $t_{\theta_{\text{max}}}$ and $t_{h_{\text{max}}}$ are the instants at which the maximum pitch angle and heave position are reached.

When time-averaged values are presented in this work, a minimum of 10 cycles is used to compute the averages and a sufficient number of cycles are completed to obtain converged values. The averaging process is only started after reaching limit-cycle oscillations (LCOs), i.e., a permanent response. For example, the time-averaged efficiency is computed as:

$$\overline{\eta} = \frac{1}{N_{\text{end}} - N_{\text{start}} + 1} \sum_{j=N_{\text{start}}}^{N_{\text{end}}} \eta_j \, , \tag{4.42}$$

where the subscript j stands for the j^{th} cycle, N_{start} is the cycle number at which the averaging process begins, N_{end} is the total number of completed cycles for a given simulation and η_j is the efficiency of the j^{th} cycle. Finally, the standard deviation is measured as:

$$\sigma_\eta = \sqrt{\frac{1}{N_{\text{end}} - N_{\text{start}}} \sum_{j=N_{\text{start}}}^{N_{\text{end}}} (\eta_j - \overline{\eta})^2} \, . \tag{4.43}$$

Error bars are used in several figures appearing in the current work to indicate the standard deviation of a specific metric. They are only shown when the standard deviation exceeds 0.01 for $\overline{\eta}$ and 1° for $\overline{\Theta_0}$ and $\overline{\phi}$ for the sake of clarity. The same convention is used throughout this work.

4.4.4 Numerics

The numerical methodology is the same as the approach used by Boudreau et al. (2019). This methodology has been validated by performing comparisons with benchmark cases and by making sure that

the results are independent of the spatial and temporal resolutions levels that are used. The reader is referred to the work of Boudreau et al. (2019) for more information about this validation. The computational fluid dynamics (CFD) simulations are conducted in 2D with the incompressibility assumption using Siemens' STAR-CCM+® software and the rotation-correction version of the one-equation Spalart-Allmaras turbulence model (Dacles-Mariani et al., 1995, 1999; Spalart and Allmaras, 1994). The governing equations are discretized with second-order schemes and the SIMPLE algorithm is used to handle the pressure-velocity coupling (Ferziger and Perić, 2002).

The turbine operates in a square domain of 100 chord lengths by 100 chord lengths with the foil located at the center. Two different meshes are used for the background and the foil regions. The mesh of the foil region is allowed to move with respect to the background mesh using the overset mesh technique. The background mesh is composed of hexagonal cells while a structured mesh composed of rectangular cells is used for the foil region. The cell size at the foil surface results in a dimensionless normal wall distance (y^+) of the order of one and around 500 nodes around the foil. A maximum growth factor of 1.2 is used in the normal direction near the foil surface. The resulting mesh is composed of 78 614 cells. A time step corresponding to 0.003 convective time units is used for all the simulations conducted in this study:

$$\frac{\Delta t \, U_\infty}{c} = 0.003 \, . \tag{4.44}$$

As a result, between approximately 1 100 and 3 300 time steps are simulated per cycle depending on the frequency of the prescribed heave motion.

The inlet boundary condition consists in a uniform and constant velocity with a modified turbulent viscosity ratio of three ($\tilde{\nu}/\nu = 3$), based on the recommendation of Spalart and Rumsey (2007) to use the Spalart-Allmaras model in its fully-turbulent mode. The single equation of the Spalart-Allmaras turbulence model solves for the modified turbulent viscosity ($\tilde{\nu}$), from which the turbulent viscosity (ν_t) is computed using an empirical relation (Spalart et al., 1997). A pressure of zero is imposed at the outlet boundary and a symmetry condition is used for the two lateral boundaries. The values of the velocity and the turbulent viscosity ratio at the inlet boundary along with the value of the pressure at the outlet boundary are used for the initial condition throughout the computational domain. Moreover, the foil is initially located at its equilibrium positions in heave and in pitch ($h^* = 0$ and $\theta = 0$).

An implicit fluid-structure coupling algorithm is used to solve Eq. 4.1 with a second order backward difference scheme for the temporal discretization. Consequently, the pitch angle (θ) and the hydrodynamic moment (M) are updated a few times (typically 3 or 4 times) within a given time step. Updates of these variables are performed until the difference between two successive updates of the pitch angle, in radians and normalized with $\pi/2$, falls below 10^{-8}. When the pitch angle is converged for a given time step, a few more fluid iterations are conducted before incrementing the time step in order to reach the fluid convergence criteria. These convergence criteria are set so that the fluid residuals for the pressure, the streamwise and transverse momentums drop by a factor of 10^{-4} or more during a given time step and the fluid residual for the turbulent viscosity minimally drops by a factor of

5×10^{-4}. A more thorough description of this algorithm is presented in the work of Boudreau et al. (2019).

4.5 Results and discussion

4.5.1 Combining the moment of inertia and the pitch stiffness into a single effective parameter

As mentioned in the introduction, we look for the important characteristics of flapping-foil turbines in the perspective of optimal energy extraction and we aim to maintain an optimal performance across a broad range of structural parameter values. To that end, the effects of varying the moment of inertia about the pitch axis and the pitch stiffness are studied in this section. This investigation is conducted around an efficient operating point reported in our previous work on the semi-passive turbine concept (Boudreau et al., 2019). The characteristics of this initial case are listed in Table 4.1. Unless otherwise indicated, these structural parameter values are used for all the cases considered in Secs. 4.5.1 to 4.5.3.

Table 4.1: Description of the operating point around which the study of the effects of I_θ^* and k_θ^* is conducted.

Parameters	**Values**	**Parameters**	**Values**
Prescribed parameters		*Results*	
x_p/c	0.25	$\overline{\Theta_0}$	74.4°
H_0/c	1	$\overline{\phi}$	94.5°
f_h^*	0.18	$\overline{\eta}$	40.5%
S^*	0.5		
I_θ^*	2		
k_θ^*	2.56		
D_θ^*	0		

First, the pitch stiffness coefficient and the moment of inertia are independently varied while keeping all the other parameters constant. The effects of such variations on the pitch amplitude, the phase lag between the heave and the pitch motions and the efficiency are shown in Fig. 4.1. These results reveal that the semi-passive turbine dynamics is highly sensitive to variations of both k_θ^* and I_θ^*. A maximum efficiency of 46.0%, which exceeds the best efficiency reported by Boudreau et al. (2019), is observed when the dimensionless pitch stiffness coefficient is slightly smaller than that of the initial case, with a value of 2.51. An increase of k_θ^* above this value leads to considerable decreases of all three metrics presented in Figs. 4.1a and 4.1c. In fact, the efficiency almost drops to zero when increasing k_θ^* by

only 10% from the best efficiency point. The drop of efficiency observed when k_θ^* is decreased below 2.51 is even more abrupt. It is due to the fact that the boundary layers separate and that leading-edge vortices (LEVs) are formed and ejected from the foil surface for all the cases tested with $k_\theta^* < 2.51$. As discussed in the work of Boudreau et al. (2019), the formation and ejection of LEVs can significantly alter the semi-passive turbine dynamics. In the present case, it results in sudden increases of both the pitch amplitude and the phase lag between the heave and the pitch motions. Furthermore, the formation of LEVs results in significant cycle-to-cycle variations of the three metrics considered, as shown by the error bars indicating the standard deviation of the corresponding metric. As mentioned in Sec. 4.4.3, error bars are only shown when the standard deviation exceeds 0.01, for $\overline{\eta}$, and 1° for $\overline{\Theta_0}$ and $\overline{\phi}$.

Similar observations are made when varying the moment of inertia while keeping the other structural parameters constant, as seen in Figs. 4.1b and 4.1d, but with opposite trends than when varying the pitch stiffness coefficient. In other words, the effects of increasing k_θ^* is equivalent to decreasing I_θ^*, and vice versa.

While these results reveal the high sensitivity of the semi-passive turbine dynamics to the moment of inertia and the pitch stiffness coefficient, they are not general. Indeed, the values of k_θ^* and I_θ^* leading to the maximum efficiency observed in Fig. 4.1 are specific to this particular set of structural parameters and they do not remain optimal in other situations. Actually, the initial point used to conduct this analysis has been especially selected for its good performance and was obtained from a parametric study in which I_θ^* was set to a value of two. It is therefore not surprising to observe that the turbine performance decreases as the moment of inertia departs from this value when all the other parameters are kept constant. However, similar foil motions and efficiencies can be obtained with considerably different values of I_θ^*, provided that k_θ^* is adjusted accordingly. For example, Fig. 4.2 demonstrates that efficiencies exceeding 40% are obtained with five different values of I_θ^*. Note that the black markers corresponding to the cases with $I_\theta^* = 2$ are the same as those presented in Fig. 4.1c. Note also that for all the cases presented in Figs. 4.1 and 4.2, the foil oscillates in pitch at the same frequency as the frequency of the prescribed heave motion: $f_\theta^* = f_h^* = 0.18$, as indicated in Table 4.1. This aspect is discussed in more details in Sec. 4.5.2.

A decrease of the turbine performance was also observed by Deng et al. (2015) when increasing the mass of the components undergoing the heave motion for a different version of semi-passive flapping-foil turbine, namely a turbine with a passive heave motion and a prescribed pitch motion. Following a parametric study conducted with a ratio between the density of the foil and the fluid density of 1, they selected an efficient case and showed that the efficiency is decreasing when the density ratio is increased up to 100 while all the other parameters are kept constant. Their results therefore showed that the structural parameter values that are optimal when the density ratio is one are not optimal when the density ratio is much larger. However, it does not mean that it is impossible to achieve high efficiencies when the density ratio is of the order of 100.

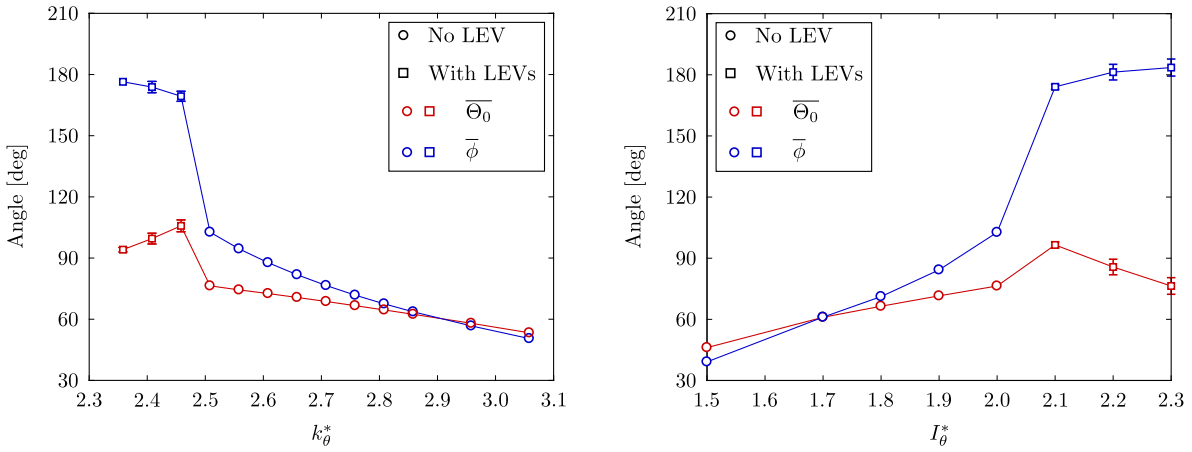

(a) Pitch amplitude and phase lag.

(b) Pitch amplitude and phase lag.

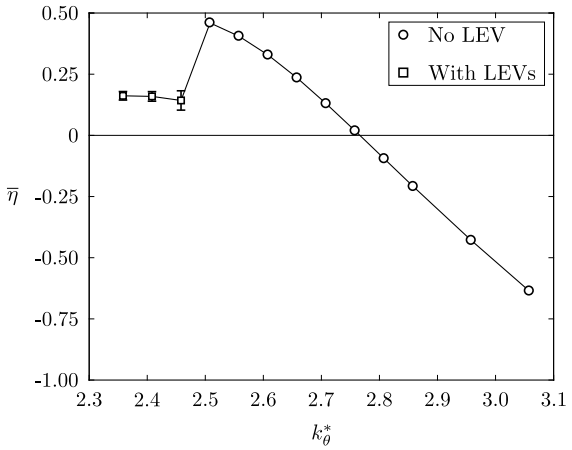

(c) Efficiency.

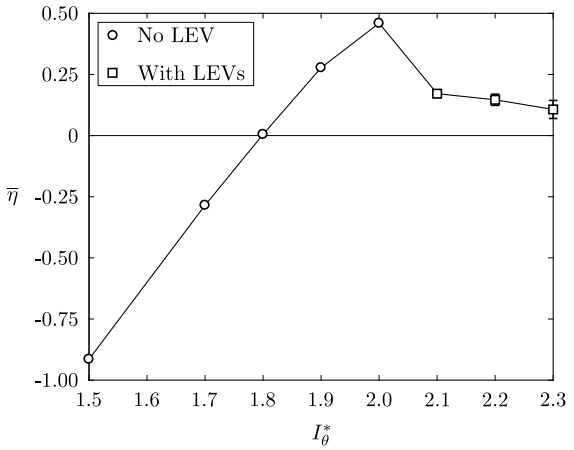

(d) Efficiency.

Figure 4.1: Sensitivity of different metrics to independent variations of the dimensionless pitch stiffness coefficient and moment of inertia. All the other structural parameters are kept constant to the values listed in Table 4.1, except for k_θ^*, which is set to 2.51 when I_θ^* is varied.

The fact that the variations of k_θ^* and I_θ^* have similar but opposite consequences on the passive pitch dynamics and that similar foil motions and efficiencies can be obtained with different values of these two structural parameters suggest that they are closely related. In other words, they are not completely independent from each other. There should therefore exists a relevant parameter combining them.

Following our previous investigation of the semi-passive turbine concept (Boudreau et al., 2019), we know that the passive pitch motions closely follow sinusoidal motions with a single frequency, f_θ^*, for the optimal operating points. Under such conditions, the pitch angle and the pitch acceleration can be roughly approximated as:

$$\theta(t) \approx \Theta_0 \sin\left(2\pi f_\theta^* t^* - \phi\right) , \tag{4.45}$$

$$\ddot{\theta}^*(t) \approx -(2\pi f_\theta^*)^2 \Theta_0 \sin\left(2\pi f_\theta^* t^* - \phi\right) , \tag{4.46}$$

where $t^* = t\,U_\infty/c$. Consequently, the terms involving the moment of inertia and the pitch stiffness

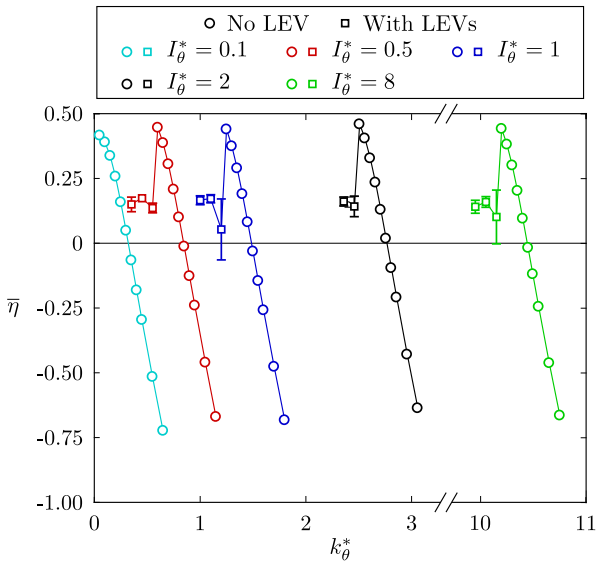

Figure 4.2: Efficiency as a function of k^*_θ for various values of I^*_θ.

coefficient appearing in the equation of motion in pitch can be combined into a single effective parameter, which we refer to as the effective pitch stiffness and we denote it by λ^*_θ:

$$I^*_\theta \, \ddot{\theta}^* + k^*_\theta \, \theta \approx \left(k^*_\theta - (2\pi f^*_\theta)^2 I^*_\theta \right) \theta = \lambda^*_\theta \, \theta \, . \tag{4.47}$$

where:

$$\lambda^*_\theta = k^*_\theta - (2\pi f^*_\theta)^2 I^*_\theta \, . \tag{4.48}$$

This parameter is analogous to the "effective elasticity" used by Shiels et al. (2001) to study the dynamics of an elastically-supported cylinder undergoing vortex-induced vibrations (VIVs). Using the definition of λ^*_θ, Eq. 4.14 can be approximated as:

$$C_M/2 \approx S^* \, \ddot{h}^* \cos(\theta) + D^*_\theta \, \dot{\theta} + \lambda^*_\theta \, \theta \, , \tag{4.49}$$

which is even further simplified when considering an idealized frictionless turbine ($D^*_\theta = 0$):

$$C_M/2 \approx S^* \, \ddot{h}^* \cos(\theta) + \lambda^*_\theta \, \theta \, . \tag{4.50}$$

This last relation suggests that for constant values of heave reduced frequency, heave amplitude and static moment, the dynamics of the passive pitch motion should be almost independent of I^*_θ and k^*_θ, as long as λ^*_θ is kept constant and the pitch motion remains close to a sinusoidal motion with a well-defined single frequency. This statement is confirmed in Fig. 4.3, which presents the pitch amplitude, the phase lag between the heave and the pitch motions and the efficiency as functions of λ^*_θ for different values of I^*_θ. Indeed, this figure shows that the data points presented in Fig. 4.2 essentially collapse to a single curve, even when LEVs are formed (see the square markers), hence confirming the relevance of the parameter λ^*_θ. The maximum efficiencies obtained with the different values of I^*_θ are all obtained around the same value of λ_θ, which is slightly below zero with this specific set of

parameters. However, the data points obtained with the smallest moment of inertia tested ($I_\theta^* = 0.1$) slightly deviate from the other data points. This is because the pitch motion deviates from a pure sinusoidal motion in this case, as will be discussed in more details in Secs. 4.5.2 and 4.5.3.

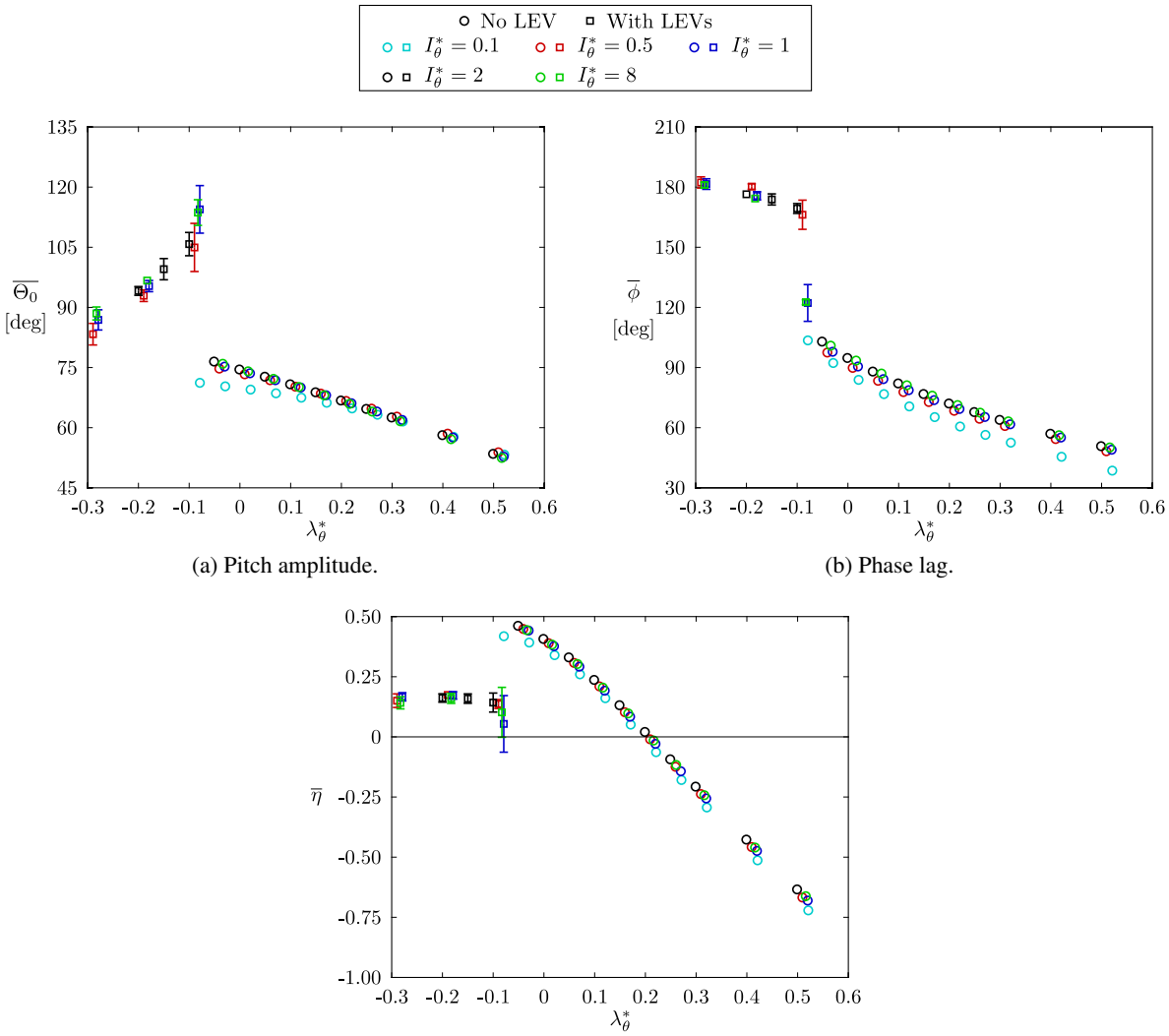

(a) Pitch amplitude.

(b) Phase lag.

(c) Efficiency.

Figure 4.3: Various metrics as functions of the parameter λ_θ^* for various values of I_θ^*.

Instead of characterizing the passive pitch dynamics with the effective pitch stiffness λ_θ, an intuitive choice would have been to use the frequency ratio r, namely the ratio between the frequency of the pitch motion (f_θ^*) and the pitch natural frequency in vacuum ($f_{n,\theta}^*$):

$$r = \frac{f_\theta^*}{f_{n,\theta}^*} \,. \tag{4.51}$$

where:

$$f_{n,\theta}^* = \frac{1}{2\pi}\sqrt{\frac{k_\theta^*}{I_\theta^*}} \,. \tag{4.52}$$

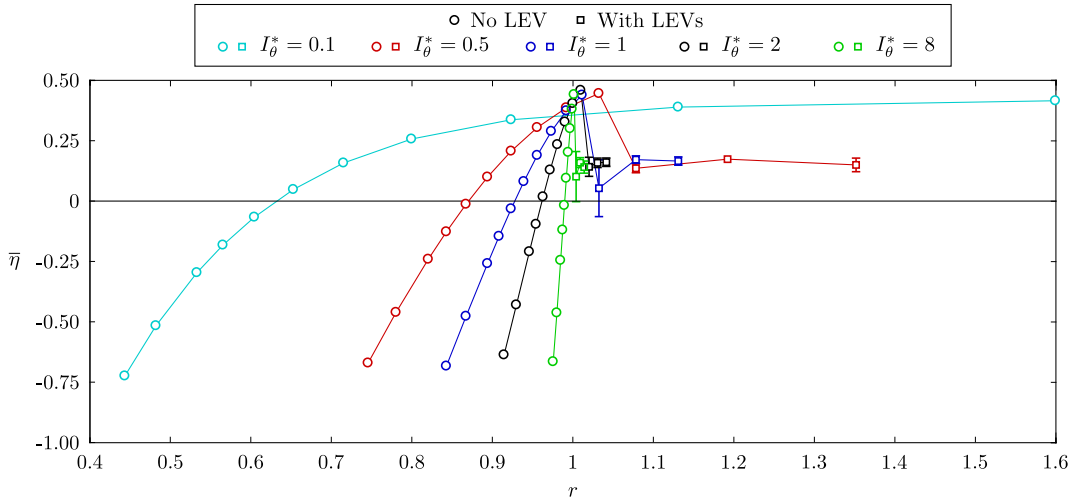

Figure 4.4: Efficiency as a function of the frequency ratio (r) for various values of I^*_θ.

Fig. 4.4 presents the efficiency as a function of the frequency ratio for different values of I^*_θ. Unlike what is observed in Fig. 4.3c, the various curves obtained with different values of I^*_θ do not agree with each other. Moreover, these results show that the maximum efficiency is not always reached at the same frequency ratio. For instance, the optimal frequency ratio is $r = 1.6$, when $I^*_\theta = 0.1$, and it approaches unity, as I^*_θ is increased. The sensitivity of the efficiency to a variation of r also differs for the different values of I^*_θ considered. The sensitivity increases with I^*_θ. This can be explained by the fact that the dynamics of the limit-cycle oscillations in pitch depends on the parameter λ^*_θ. Indeed, λ^*_θ can be expressed as:

$$\lambda^*_\theta = k^*_\theta - (2\pi f^*_\theta)^2 I^*_\theta = 4\pi^2 I^*_\theta \left({f^*_{n,\theta}}^2 - f^{*2}_\theta \right) . \tag{4.53}$$

Consequently, a given variation of ${f^*_{n,\theta}}^2 - f^{*2}_\theta$, and thus of the frequency ratio (r), results in a larger variation of λ^*_θ as I^*_θ increases. All these observations confirm that the pitch dynamics of the turbine permanent response does not directly depend on the frequency ratio, but rather on the effective pitch stiffness λ^*_θ.

4.5.2 Frequency synchronization

For all the cases considered in the previous section, the frequency of the passive pitch motion (f^*_θ) synchronizes itself to the frequency of the prescribed heave motion (f^*_h). However, this does not necessarily happen for any value of the structural parameters governing the pitch dynamics.

When I^*_θ is not equal to zero and D^*_θ is assumed to be zero, Eq. 4.14 can be written in the following form:

$$\frac{C_M}{2I^*_\theta} = \left(\ddot{\theta}^* + (2\pi f^*_{n,\theta})^2 \theta \right) + \frac{S^* \ddot{h}^* \cos(\theta)}{I^*_\theta} . \tag{4.54}$$

When I^*_θ approaches infinity, this equation can be approximated by the following relation:

$$\ddot{\theta}^* + (2\pi f^*_{n,\theta})^2 \theta \approx 0 , \tag{4.55}$$

assuming that S^*, $\ddot{h}^*$ and C_M remain finite. This implies that, when I_θ^* approaches infinity, the pitch motion approaches a pure sinusoidal motion oscillating at the pitch natural frequency ($f_{n,\theta}^*$), regardless of the frequency of the prescribed heave motion (f_h^*). On the other hand, the pitch motion deviates from a pure sinusoid when I_θ^* approaches zero. An example of this behavior is shown in Fig. 4.5. It shows that the differences between the time evolutions of the pitch angle obtained with two significantly different values of I_θ^* is subtle, but the differences between the time evolutions of the pitch accelerations are more evident.

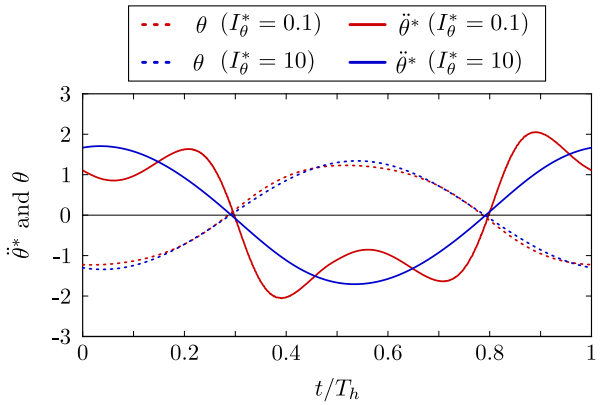

Figure 4.5: Time evolution of the pitch angle (θ) and the dimensionless pitch acceleration ($\ddot{\theta}^*$) over one foil oscillation for two different values of I_θ^* but a constant value of $\lambda_\theta^* = -0.05$. The values of the other structural parameters are given in Table 4.1. Note that θ is given in radians.

Conversely, when $I_\theta^* = 0$, there is no inherent structural time scale in pitch since the pitch natural frequency is undefined. Under this condition, f_θ^* is therefore expected to be dictated by f_h^*, which affects the moment coefficient and the inertial coupling term in Eq. 4.14, no matter the value of k_θ^*.

Fast Fourier Transforms (FFTs) of the pitch angle signals have been carried out in order to obtain the amplitude spectra of the pitch motion and to confirm the above statements. The principal frequency component ($f_{\theta\,1}^*$) is plotted against k_θ^* in Fig. 4.6 for three different values of I_θ^*. The reason for plotting the results against k_θ^* instead of λ_θ^* is discussed below. The shaded gray region indicates the range of λ_θ^* values covered in Fig. 4.3. Only a few representative cases appearing in Fig. 4.3 are reproduced in Fig. 4.6 for the sake of clarity.

Fig. 4.6 confirms that f_θ^* always synchronizes itself to f_h^* when $I_\theta^* = 0$. For nonzero but not infinite values of I_θ^*, this does not always happen. When f_θ^* and f_h^* are not synchronized, the principal frequency component in the amplitude spectrum of the pitch motion rather follows the pitch natural frequency. The region over which f_θ^* synchronizes itself to f_h^*, in terms of the range of k_θ^* values, shrinks as I_θ^* increases. This finding is in agreement with the fact that f_θ^* should approach $f_{n,\theta}^*$ when I_θ^* approaches infinity, as discussed above.

The frequency of the prescribed heave motion, which is set to $f_h^* = 0.18$ for all the cases considered in Fig. 4.6, is always present in the amplitude spectra of the pitch motion, even when the principal

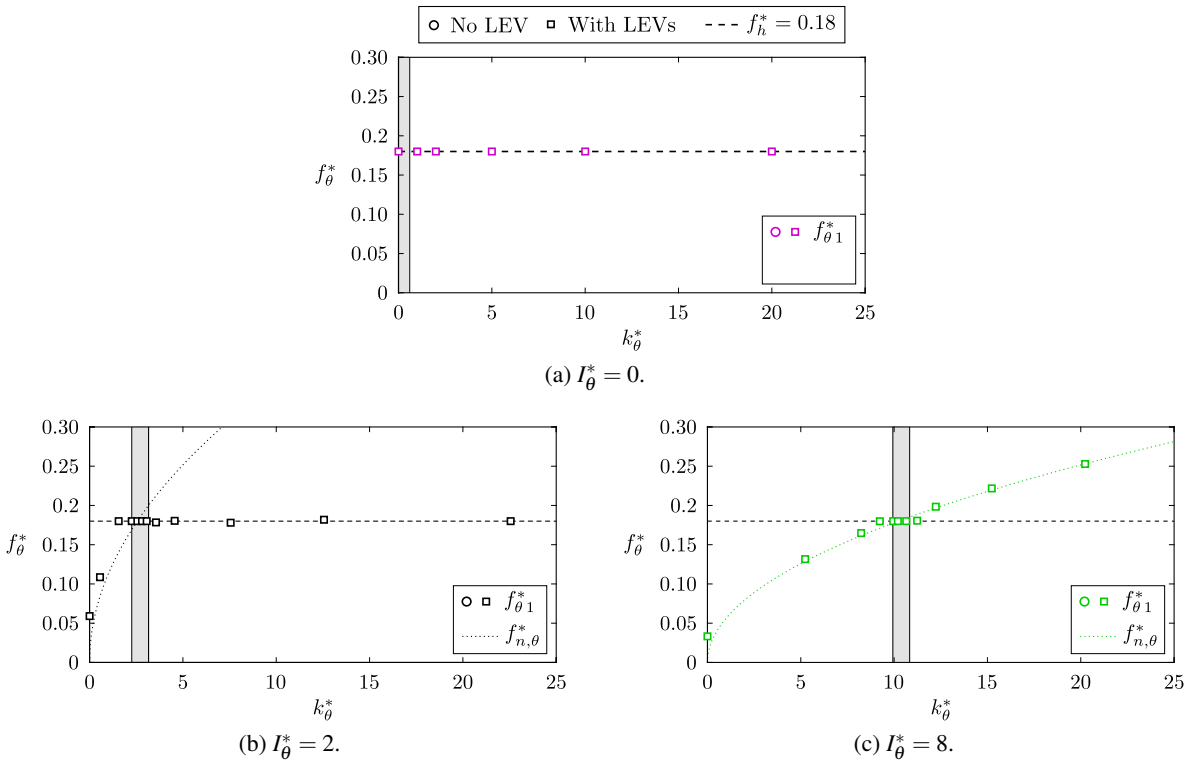

(a) $I_\theta^* = 0$.

(b) $I_\theta^* = 2$.

(c) $I_\theta^* = 8$.

Figure 4.6: Principal frequency component ($f_{\theta\,1}^*$) in the amplitude spectrum of the pitch angle. The values of the other structural parameters are given in Table 4.1.

frequency component is different than 0.18 and rather equal to the pitch natural frequency. This presence of multiple frequencies in the pitch angle signals for the cases located outside of the frequency synchronization region results in significant amplitude modulations. For example, the differences between the pitch motion of three different cases with $I_\theta^* = 8$ are shown in Fig. 4.7. One case is located on the left hand side of the frequency synchronization region in Fig. 4.6c, one case is in the frequency synchronization region and the third one is on the right hand side of this region. This figure also shows that the pitch amplitude is much smaller for the cases located outside the frequency synchronization region. The erratic pitch motions associated to the presence of multiple frequencies and the small pitch amplitudes observed outside the frequency synchronization region are not suitable for a turbine application. Actually, positive efficiencies are only achieved in a narrow range of λ_θ^* values (see Fig. 4.3c) where the passive pitch motion oscillates at a single frequency that is synchronized with the frequency of the prescribed heave motion. For this reason, only cases that fit this description are analyzed in the rest of the present study.

The reason for presenting the results against the parameter k_θ^* instead of λ_θ^* in the current section is that λ_θ^* is not well defined when there is more than one important frequency in the amplitude spectrum of the pitch motion. Moreover, $\lambda_\theta^* = 0$ when the frequency used in its definition corresponds to the pitch natural frequency. As a result, all the cases for which the principal frequency component corresponds to the pitch natural frequency are characterized by the same value of λ_θ^*, even though their dynamics

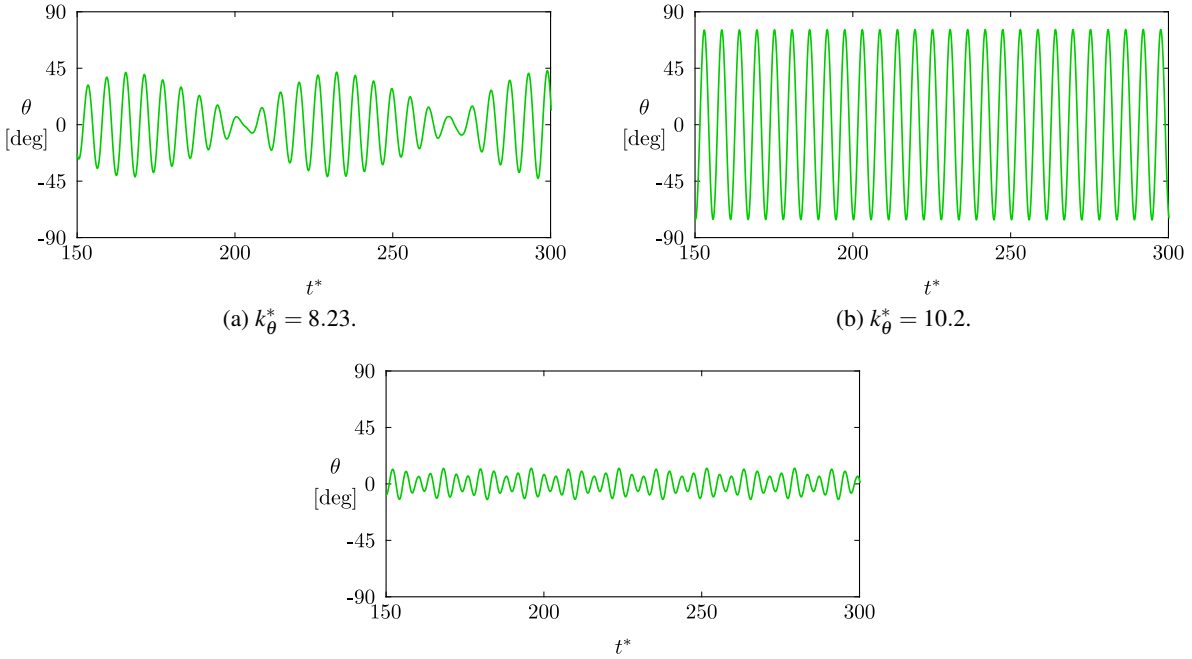

(a) $k_\theta^* = 8.23$. (b) $k_\theta^* = 10.2$.

(c) $k_\theta^* = 20.23$.

Figure 4.7: Time evolution of the pitch motion for three different cases with $I_\theta^* = 8$ (see Fig. 4.6c).

differ. The effective pitch stiffness λ_θ^* is therefore not suitable to characterize such cases.

4.5.3 Scaling I_θ^* and k_θ^*

The results presented in Fig. 4.3 have already shown that the dynamics of the passive pitch motion is essentially independent of the moment of inertia about the pitch axis and the pitch stiffness, provided that I_θ^* is sufficiently large and that the effective pitch stiffness is not altered. Fig. 4.8 better illustrates this point by presenting the variations of $\overline{\Theta_0}$, $\overline{\phi}$ and $\overline{\eta}$ as I_θ^* is increased from 0 to 10 while adjusting k_θ^* in order to maintain λ_θ^* constant at -0.05. Clearly, all three metrics presented in this figure become independent of I_θ^* and k_θ^* once threshold values are exceeded. The threshold value of I_θ^* is around 0.5, in agreement with the results presented in Fig. 4.3. The efficiency only increases by 1.6%, in relative difference, when I_θ^* is increased from 0.5 to 100 (not shown in Fig. 4.8). Note that no LEVs are formed for any of the cases considered in Fig. 4.8 and that the frequency of the pitch motion is always synchronized to the frequency of the prescribed heave motion.

The reason explaining why $\overline{\Theta_0}$, $\overline{\phi}$ and $\overline{\eta}$ vary when I_θ^* and k_θ^* are decreased below the threshold values required to reach the large-inertia asymptote in Fig. 4.8 is that the pitch motion deviates from a pure sinusoidal motion in such circumstances, as already shown in Fig. 4.5. In this context, the approximations of the pitch angle and the pitch acceleration given by Eqs. 4.45 and 4.46 are not accurate. Consequently, the moment of inertia and the pitch stiffness cannot be combined as effectively into a single parameter. In other words, the effective pitch stiffness becomes less relevant.

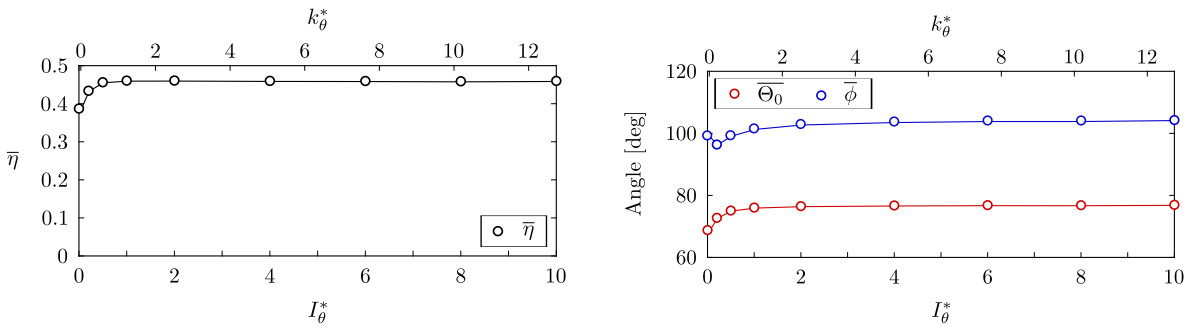

(a) Efficiency.

(b) Pitch amplitude and phase lag.

Figure 4.8: Various metrics as functions of the dimensionless moment of inertia (I_θ^*) and the pitch stiffness coefficient (k_θ^*) with a constant value of $\lambda_\theta^* = -0.05$. The values of all the remaining parameters are equal to the corresponding values listed in Table 4.1.

Lastly, Fig. 4.9 shows that an optimal efficiency is not maintained when varying I_θ^* and adjusting k_θ^* so that the pitch natural frequency remains constant, even though the frequency ratio (r) is maintained at a value very close to unity, namely 1.01. The results are compared to those that have already been presented in Fig. 4.8a, for which λ_θ^* is kept constant at -0.05. Note that the point with $I_\theta^* = 2$ belongs to the two sets of points. These results further demonstrate that the dynamics of optimal pitch motions in terms of energy extraction does not directly depend on the frequency ratio, but rather on λ_θ^*.

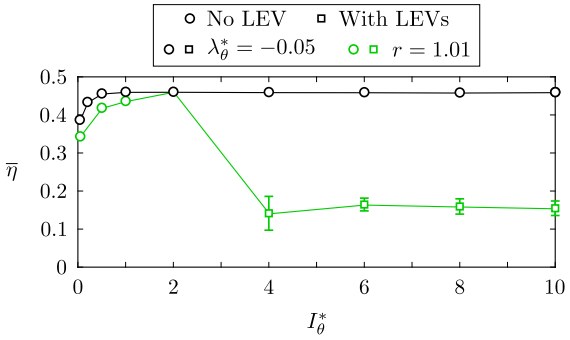

Figure 4.9: Efficiency as a function of I_θ^* for a constant value of $\lambda_\theta^* = -0.05$ (black markers) and for a constant value of $r = 1.01$ (green markers).

4.5.4 Pitch axis location

Having found that the performance of the semi-passive flapping-foil turbine with a passive pitch motion becomes almost independent of I_θ^* and k_θ^* once threshold values are exceeded and when λ_θ^* is kept constant, this section investigates if an optimal performance can also be maintained when the pitch axis is not located at the quarter-chord point ($x_p/c = 0.25$) and if so, how the values of the different governing structural parameters must be adjusted to reach this objective.

Reference fully-constrained turbine cases

Before focusing on the semi-passive turbine dynamics, a few fully-constrained turbine cases with the following prescribed sinusoidal motions are analyzed in this section:

$$h = H_0 \sin(2\pi f t) \ , \tag{4.56}$$

$$\theta = \Theta_0 \sin(2\pi f t - \phi) \ . \tag{4.57}$$

They serve as reference cases to estimate the required values for the structural parameters governing the semi-passive turbine dynamics with different positions of the pitch axis in the next section.

An operating point known to be efficient and well-documented is selected as a starting point (Kinsey and Dumas, 2012, 2014). The different parameters describing the motions and measuring the performance of this operating point are given in Table 4.2. Note that $\overline{C_{P_{\text{gen}}}}$ is equal to the sum of $\overline{C_{P_h}}$ and $\overline{C_{P_\theta}}$ in the case of fully-constrained turbines because the prescribed heave and pitch motions are periodic and an idealized frictionless turbine is considered.

Table 4.2: Reference fully-constrained flapping-foil turbine case with $x_p/c = 0.33$.

Parameters	**Values**	**Parameters**	**Values**
Prescribed parameters		*Results*	
Re	3.9×10^6	$\overline{\eta}$	40.5%
x_p/c	0.33	$\overline{C_{P_h}}$	1.43
H_0/c	1	$\overline{C_{P_\theta}}$	-0.39
Θ_0	75°	$\overline{C_{P_{\text{gen}}}}$	1.04
f^*	0.14		
ϕ	90°		

It is important to realize that the flow dynamics depends on the motion of the foil surface, or, alternatively, the motion of every points on the chord line. If the same motion of the foil surface could be prescribed with different positions of the pitch axis, the fluid would not "feel" the difference and the overall energy transfer between the foil and the flow would therefore remain the same. When simply modifying the position of the pitch axis while keeping all the other kinematic parameters constant, the motion of the foil surface is significantly altered. Indeed, for a given position of the pitch axis, all the points on the chord line undergo different motions. It is therefore normal that the motion of the pitch axis has to be modified when its position is changed in order to maintain the same motion of the chord line as for the efficient reference case.. One way of seeing this difference is to look at the transverse (y or heave direction) motion of specific points on the chord line. For example, Fig. 4.10 presents the motion of the points $x/c = 0.33$ and $x/c = 1$ for a case with the pitch axis located at the third-chord

point ($x_p/c = 0.33$) and another one with the pitch axis located at the trailing edge ($x_p/c = 1$) with the same kinematic parameters in both cases. It shows that the motion of the point $x/c = 1$ with $x_p/c = 1$ (red curve in Fig. 4.10b), matches the motion of the point $x/c = 0.33$ with $x_p/c = 0.33$ (black curve in Fig. 4.10a). However, the motion of the point $x/c = 0.33$ with $x_p/c = 1$ (red curve in Fig. 4.10a) considerably deviates from the motion of the point $x/c = 0.33$ with $x_p/c = 0.33$ (black curve in Fig. 4.10b). The motion of a specific point on the chord line is therefore altered when the position of the pitch axis is varied while the kinematic parameters are kept constant.

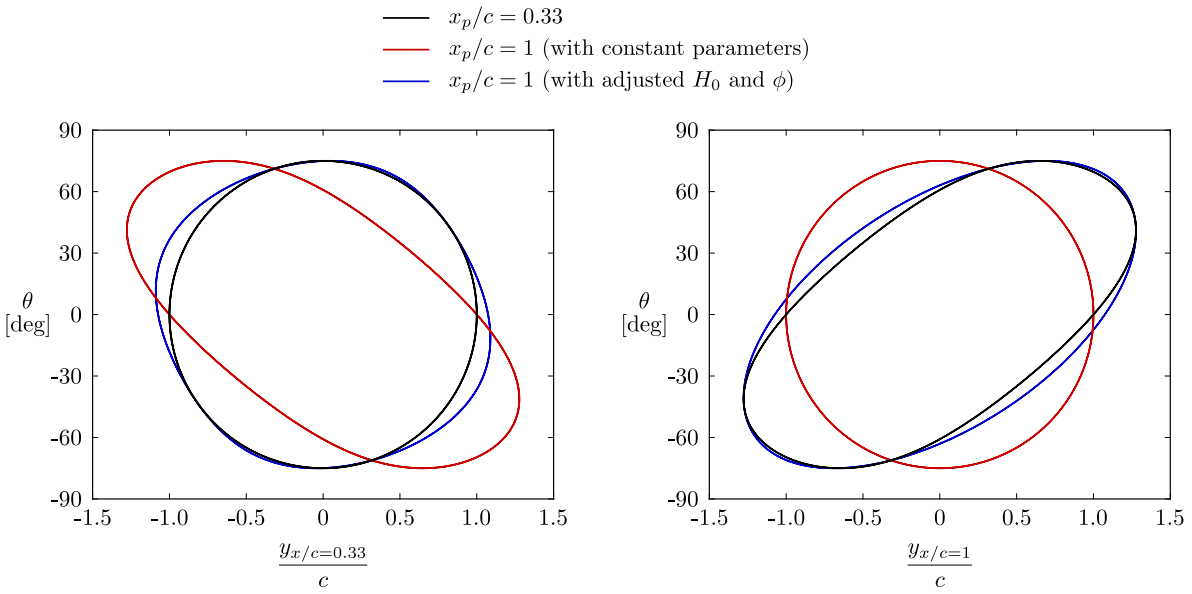

(a) Motion of the point $x/c = 0.33$.

(b) Motion of the point $x/c = 1$.

Figure 4.10: Comparison of the motions of two different points on the chord line as the position of the pitch axis is varied for fully-constrained flapping-foil turbines. The motions follow counterclockwise trajectories.

In order to better reproduce the motion of the foil surface characterizing the efficient case described in Table 4.2, the kinematic parameters must therefore be adjusted when the position of the pitch axis is changed. Since $\phi = 90°$ for this efficient case with $x_p/c = 0.33$, the pitch axis reaches a maximum heave position of one chord length, which corresponds to the heave amplitude, when the pitch angle is equal to zero. However, the trailing edge exceeds this amplitude of one chord length and reaches its maximum transverse position when the pitch angle is not zero, as shown in Fig. 4.10b. This implies that if the pitch axis is instead placed at the trailing edge, the heave amplitude (H_0) and the phase lag between the heave and the pitch motions (ϕ) have to be adjusted in order to maintain a similar motion of the chord line, and thus of the foil surface. The adjusted heave amplitude and phase lag values as functions of the pitch axis location are shown in Fig. 4.11 and the resulting motions of the points $x/c = 0.33$ and $x/c = 1$ when the pitch axis is located at the trailing edge are presented in Fig 4.10. It is observed that, when H_0 and ϕ are adjusted, the transverse motion of the two considered points on the chord line are in much better agreement with the motion of the same points characterizing the case with $x_p/c = 0.33$ than when the kinematic parameters are kept constant. Fig. 4.10 also shows that

when a phase lag of 90° is imposed with $x_p/c = 0.33$, the phase lag between the transverse motion of the trailing edge and the pitch motion is smaller than 90°, that is, the pitch angle has already switched from a negative to a positive value when the maximum transverse position of the trailing edge is reached. As a result, a phase lag below 90° must be imposed when the pitch axis is located at the trailing edge, as indicated in Fig. 4.11, so that the phase lag between the transverse motion of the point $x/c = 0.33$ and the pitch motion remains around 90°. However, it is not possible to impose the exact same motions of the foil surface with different values of x_p/c since the pitch axis is the sole point on the chord line that is restricted to move only in the transverse direction.

The values of $\overline{C_{P_{\text{gen}}}}$, $\overline{C_{P_h}}$ and $\overline{C_{P_\theta}}$, obtained with and without the adjustment of H_0 and ϕ, are shown in Fig. 4.12 for various positions of the pitch axis. The results show that when the kinematic parameters remain constant, the power coefficient at the generator considerably decreases as the position of the pitch axis departs from $x_p/c = 0.33$ and even becomes negative when the pitch axis is located at the trailing edge. Conversely, it remains relatively constant for positions of the pitch axis ranging from the leading to the trailing edge when H_0 ans ϕ are adequately adjusted even though the streamwise motion of the different points on the chord line varies with x_p/c. Note that this also holds true for the efficiency, which is not shown. These results therefore demonstrate that it is possible to maintain an optimal performance over a large range of pitch axis locations. Furthermore, they show that a phase lag of 90° is not a fundamental characteristic of an optimal energy extraction performance although it is often stated as such in the literature. This is because most of the studies on flapping-foil turbines have been conducted with a pitch axis located at the third-chord point (Boudreau et al., 2018; Chen et al., 2018; Deng et al., 2015; Teng et al., 2016; Veilleux and Dumas, 2017; Wu et al., 2015) or the quarter-chord point (Boudreau et al., 2019; Huxham et al., 2012; Sitorus et al., 2015). In fact, a larger phase lag is required when $x_p/c < 0.33$ while a smaller phase lag is needed when $x_p/c > 0.33$, in agreement with the observations of Davids (1999).

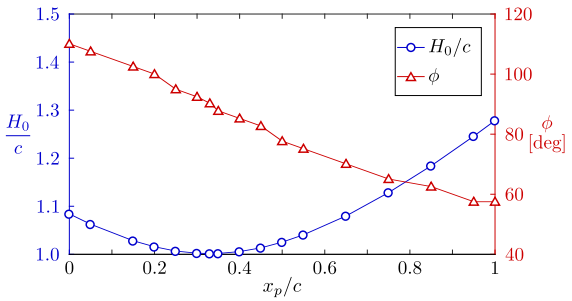

Figure 4.11: Adjustments of the heave amplitude and the phase lag between the heave and pitch motions with a variation of the pitch axis to reproduce the motion of the foil surface characterizing the efficient case described in Table 4.2. The values of the other kinematic parameters all remain equal to the values presented in Table 4.2.

While $\overline{C_{P_{\text{gen}}}}$ is found to remain relatively constant for various positions of the pitch axis when H_0 and ϕ are adjusted accordingly, Fig. 4.12b also shows that the heave and pitch power coefficients ($\overline{C_{P_h}}$ and $\overline{C_{P_\theta}}$) are affected by such variations. As will be discussed further in Sec. 4.5.4, an important

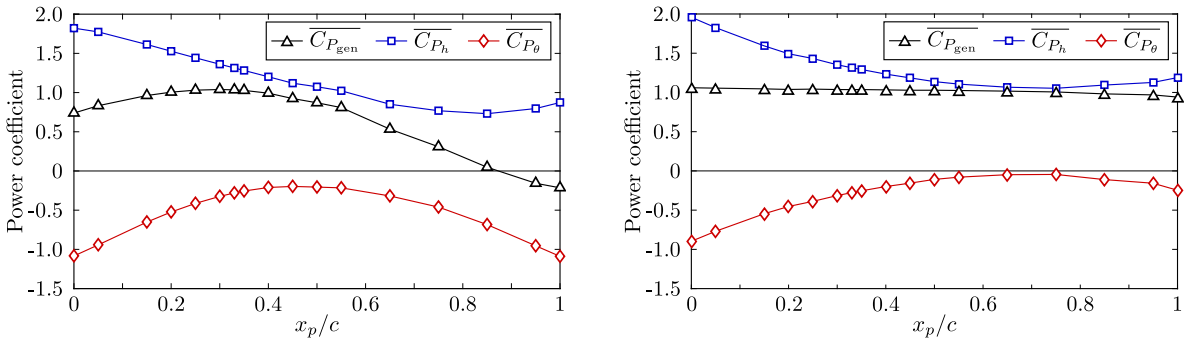

(a) Constant kinematic parameters (see Table 4.2).

(b) Adjusted heave amplitude and phase lag.

Figure 4.12: Different power coefficients as functions of the pitch axis location for a fully-constrained flapping-foil turbine.

observation is that $\overline{C_{P_\theta}}$ increases as the pitch axis is shifted from the leading edge toward the three-quarter-chord point, where it approaches zero. More information about this behavior is provided in Appendix 4.A.

Semi-passive turbine

Following the demonstration that high efficiencies and power coefficients can be maintained over a large range of pitch axis locations with specific prescribed motions, we now try to establish if and how this can be done for a semi-passive flapping-foil turbine with a passive pitch motion. As mentioned in the previous section, the fully-constrained turbine cases are used as reference cases to estimate the values of the structural parameters that are required to passively obtain pitch motions that are similar to the optimal prescribed motions. More specifically, four different fully-constrained cases with different positions of the pitch axis are considered. These reference cases are described in Table 4.3.

Considering that the same heave motions can be prescribed for the reference fully-constrained turbine cases and the semi-passive turbine cases, the forces and moment acting on the foil would be the same for both turbine concepts if the same pitch motions can be obtained passively. Assuming that this is feasible, one can try to determine a set of dimensionless structural parameters (I_θ^*, S^*, D_θ^* and k_θ^*) that satisfies the equation of motion in pitch (Eq. 4.14) with the moment coefficient obtained from a fully-constrained turbine simulation and its prescribed sinusoidal pitch motion. If such a set of parameters exists, it suggests that a passive sinusoidal pitch motion is possible. This "reverse engineering" technique follows the idea of the *Reverse Passive-Airfoil Solver (RPAS)* presented in the work of Veilleux and Dumas (2017).

Since sinusoidal pitch motions are assumed, the approximation of the equation of motion in pitch given by Eq. 4.49 can be used instead of Eq. 4.14 to determine the sets of structural parameters. This leaves three parameters to be determined, namely S^*, D_θ^* and λ_θ^*. Regression analysis using the least-square method have been conducted to determine the values of these three parameters for each pitch

Table 4.3: Reference fully-constrained flapping-foil turbine cases with different pitch axis locations.

Parameters	**Values**			
Prescribed parameters				
x_p/c	0	0.25	0.50	0.75
H_0/c	1.082	1.005	1.024	1.127
Θ_0	75°	75°	75°	75°
f^*	0.14	0.14	0.14	0.14
ϕ	109.8°	94.7°	77.4°	64.8°
Results				
$\overline{\eta}$	40.5%	40.5%	39.9%	39.2%
$\overline{C_{P_h}}$	1.96	1.43	1.14	1.05
$\overline{C_{P_\theta}}$	-0.90	-0.39	-0.11	-0.05
$\overline{C_{P_{\text{gen}}}}$	1.06	1.04	1.03	1.00

axis location considered, namely $x_p/c = 0$, 0.25, 0.50 and 0.75. These sets of parameters are given in Table 4.4.

Table 4.4: Estimation of the structural parameter values required for the different pitch axis locations considered.

Parameters	Values			
x_p/c	0	0.25	0.50	0.75
S^*	1.10	0.50	0.15	0
D_θ^*	0	0	0	0
λ_θ^*	-0.50	0	0.35	0.70

Based on the results of these regression analysis, S^* should be around zero when the pitch axis is located at the three-quarter-chord point and should increase as the pitch axis is shifted toward the leading edge. D_θ^* should always be around zero and λ_θ^* should be around zero when $x_p/c = 0.25$, positive when the pitch axis is located further downstream and negative when it is located further upstream. More explanations for the need of such parameter values are given in Appendix 4.B.

In order to validate that the guesses presented in Table 4.4 are correct and can result in a stable and

efficient response of the semi-passive turbine, numerical simulations solving the exact equation of motion in pitch (Eq. 4.14) are carried out. Although the high efficiencies and power coefficients obtained with the four reference fully-constrained turbine cases presented in Table 4.3 are obtained with different heave amplitudes depending on the pitch axis location, a heave amplitude of one chord length ($H_0/c = 1$) is chosen in order to remain consistent with Secs. 4.5.1 to 4.5.3, allowing a direct comparison of the results. For the same reason, the heave motion is prescribed at $f_h^* = 0.18$, even though the values of the structural parameters required for the different pitch axis locations have been estimated through the analysis of fully-constrained cases oscillating at a reduced frequency of 0.14 (see Table 4.4). The dimensionless moment of inertia is set to 2 for all the cases considered in this section, which is sufficiently large for the turbine performance to be almost insensitive to this parameter based on the results presented in Sec. 4.5.3, and an idealized frictionless turbine ($D_\theta^* = 0$) is considered. Regarding the dimensionless static moment, it is set to the values determined from the analysis of the reference fully-constrained turbine cases that are listed in Table 4.4. Finally, we only consider cases for which the frequency of the pitch motion synchronizes itself to the frequency of the prescribed heave motion, so that $f_\theta^* = f_h^* = 0.18$.

Fig. 4.13 shows the pitch amplitude, the phase lag between the heave and the pitch motions and the efficiency as functions of λ_θ^* for different positions of the pitch axis. Again, the error bars indicate the standard deviation of the corresponding metric and they are only shown when the standard deviation exceeds 0.01, for $\overline{\eta}$, and 1° for $\overline{\Theta_0}$ and $\overline{\phi}$.

These results confirm that an efficiency exceeding 40% can be achieved with all four pitch axis locations considered. The characteristics describing the optimal operating points obtained with each position of the pitch axis are given in Table 4.5. It is found that the estimated values of λ_θ^* required for each pitch axis location are valid since the actual values of λ_θ^* resulting in the best efficiencies are relatively close to the estimations listed in Table 4.4. The optimal value of λ_θ^* is below zero when $x_p/c = 0$, near but slightly below zero when $x_p/c = 0.25$ and above zero when $x_p/c = 0.50$ and $x_p/c = 0.75$. Interestingly, the pitch amplitude and the efficiency follow opposite trends when $x_p/c = 0$ or $x_p/c = 0.25$ compared to when $x_p/c = 0.50$ or $x_p/c = 0.75$.

As mentioned in Sec. 4.5.4, the key to reach a similar optimal performance with different positions of the pitch axis is to maintain similar motions of the foil surface since this is what governs the fluid dynamics. This is achieved when the pitch amplitude remains constant and when the phase lag between the heave and the pitch motions decreases as the position of the pitch axis is shifted toward the trailing edge, in a way similar to the trend shown in Fig. 4.11. Figs. 4.13a and 4.13b, along with Table 4.5, show that this is indeed what happens for the four optimal semi-passive cases. Consequently, the foil motions of the best efficiency points described in Table 4.5 are very similar, as confirmed in Fig. 4.14, which presents the time evolution of the dimensionless vorticity field over one turbine cycle.

However, the motions of the foil surface do not directly affect the dynamics of the elastically-supported

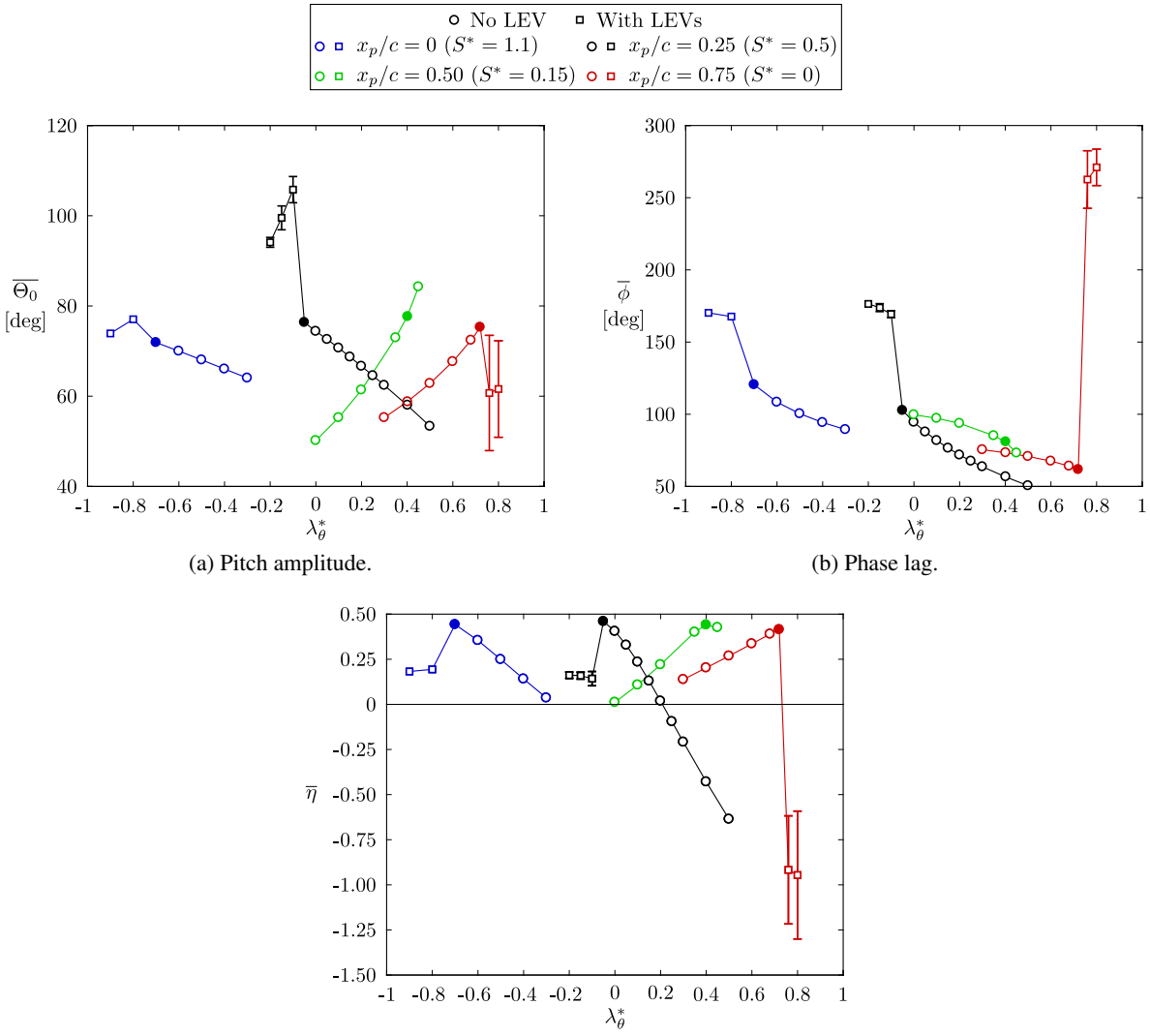

(a) Pitch amplitude.

(b) Phase lag.

(c) Efficiency.

Figure 4.13: Various metrics as functions of the parameter λ_θ^* for various positions of the pitch axis. Filled markers are used to identify the maximum efficiency cases.

foil in pitch. It is rather governed by the motion of the pitch axis along with the hydrodynamic moment about this point. The fact that the moment about the pitch axis varies with x_p/c explains why different values of λ_θ^* and S^* are required when considering different positions of the pitch axis.

Considering that $D_\theta^* = 0$ throughout the current study and that the motions leading to large values of $\overline{\eta}$ and $\overline{C_{P_{\text{gen}}}}$ are periodic, the power required by the foil to sustain its pitch motion on average during one cycle ($\langle C_{P_\theta} \rangle$) is necessarily compensated by the power transferred from the heave motion to the pitch motion via the inertial coupling terms ($\langle C_{P_{S,\theta}} \rangle$), according to Eq. 4.28. For example, Boudreau et al. (2019) demonstrated that a positive value of S^* is required to compensate for the negative value of $\overline{C_{P_\theta}}$ characterizing the optimal operating points with $x_p/c = 0.25$. The fact that the foil requires different amount of power, i.e., different values of $\langle C_{P_\theta} \rangle$, to undergo similar motions of the foil surface with

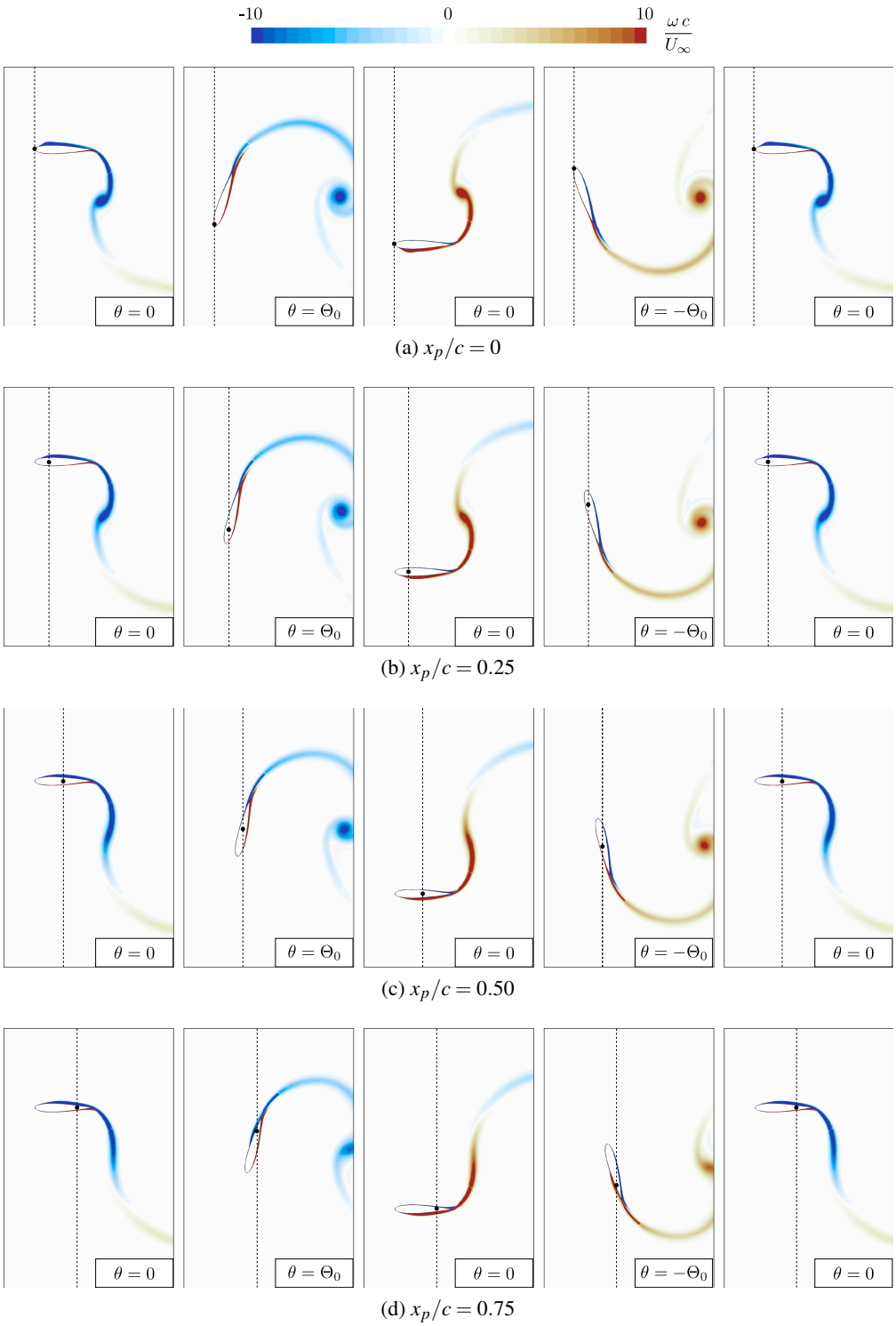

(a) $x_p/c = 0$

(b) $x_p/c = 0.25$

(c) $x_p/c = 0.50$

(d) $x_p/c = 0.75$

Figure 4.14: Time evolutions of the dimensionless vorticity field ($\omega c/U_\infty$) during one complete representative foil oscillation for the best efficiency points obtained with the four different pitch axis locations considered (see Table 4.5). Note that these cases are semi-passive cases with a prescribed heave amplitude of one chord length. The dashed lines indicate the streamwise position of the pitch axis, which is itself indicated with a black dot.

Table 4.5: Best efficiency points obtained for the semi-passive flapping-foil turbine with different pitch axis locations when varying λ_θ^* with constant S^* and I_θ^* values.

Parameters	**Values**			
Prescribed parameters				
x_p/c	0	0.25	0.50	0.75
H_0/c	1	1	1	1
$f_\theta^* = f_h^*$	0.18	0.18	0.18	0.18
S^*	1.10	0.5	0.15	0
I_θ^*	2	2	2	2
k_θ^*	1.86	2.51	2.96	3.28
D_θ^*	0	0	0	0
Results				
λ_θ^*	-0.70	-0.05	0.40	0.72
$\overline{\Theta_0}$	71.9°	76.4°	77.7°	75.3°
$\overline{\phi}$	120.5°	102.7°	81.0°	61.7°
$\overline{\eta}$	44.3%	46.0%	44.1%	41.5%
$\overline{C_{P_h}}$	2.32	1.84	1.33	0.97
$\overline{C_{P_\theta}}$	-1.38	-0.74	-0.23	0
$\overline{C_{P_{\text{gen}}}}$	0.94	1.10	1.10	0.97

different positions of the pitch axis (see Fig. 4.12b and Table 4.5) corroborates the fact that different values of S^* are required. High efficiencies are obtained when using a value of zero for S^* with $x_p/c = 0.75$, thereby implying that the foil does not provide or extract energy from the flow through its pitch motion on average ($\langle C_{P_\theta} \rangle = 0$) in this specific case, in agreement with the observation made in Fig. 4.12b regarding the fully-constrained turbine cases. However, this does not mean that the pitch motion is independent of the heave motion since the coupling between the heave motion and the moment generated by the fluid flow remains.

4.5.5 Varying the frequency of the prescribed heave motion

Considering that the passive pitch motions of optimal operating points are close to sinusoidal motions, the ratio between the amplitude of the pitch acceleration and the amplitude of the pitch motion is roughly proportional to the square of the frequency of the pitch motion (see Eqs. 4.45 and 4.46), f_θ^*

being synchronized with f_h^*. For constant values of I_θ^* and k_θ^*, this implies that the relative contribution of the term $I_\theta^* \ddot{\theta}^*$ in Eq. 4.14 becomes more important compared to that of the term $k_\theta^* \theta$ when the frequency is increased. Consequently, the value of k_θ^* leading to an optimal turbine performance varies with f_h^* when I_θ^* is kept constant. For example, the results obtained with $f_h^* = 0.18$ that are presented in Fig. 4.1c are compared to other results obtained with $f_h^* = 0.22$ in Fig. 4.15.

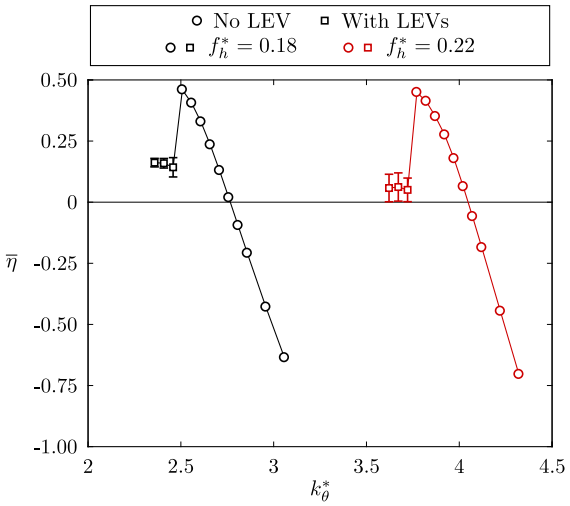

Figure 4.15: Efficiency as a function of k_θ^* for various values of f^* with $x_p/c = 0.25$. See Table 4.1 for the values of the other structural parameters.

The effective pitch stiffness takes this effect into account. However, a variation of f_h^*, and thus of f_θ^*, does not only affect the term $\lambda_\theta^* \theta$ in the approximated version of the dimensionless equation of motion in pitch (Eq. 4.50), but also the two other terms appearing in this equation, namely $C_M/2$ and $S^* \ddot{h}^* \cos(\theta)$. Indeed, the amplitude of the heave acceleration ($\ddot{h}^*$) is directly proportional to the square of f_h^* and the dependence of the fluid dynamics to the frequency of the foil motions affects the hydrodynamic moment coefficient. This therefore raises a question about the applicability of the parameter λ_θ^* when different prescribed frequencies are considered. To answer this question, simulations with different values of f_h^*, ranging from 0.1 to 0.3, have been carried out for the four positions of the pitch axis considered in the present study. This frequency range has been selected based on the parametric study conducted by Kinsey and Dumas (2014) on the fully-constrained flapping-foil turbine concept.

Contours of the efficiency are presented in Fig. 4.16. Each marker corresponds to a simulated operating point. The shape of the markers are used to indicate if leading-edge vortices (LEVs) are formed during the foil oscillations and their colors indicate the standard deviation of the efficiency. The operating points characterized by a standard deviation of the efficiency exceeding 5% are not considered when computing the contours, but they are still indicated in Fig. 4.16 with black markers. The corresponding areas are colored in gray. Part of the reason explaining the large fluctuations of the efficiency is that the frequency of the pitch motion is not synchronized with the frequency of the heave motion for some of these cases. The gray areas should not be confused with the white areas, which rather indicate a negative, but relatively constant, efficiency. Note also that the cases with $x_p/c = 0$, $f^* = 0.10$

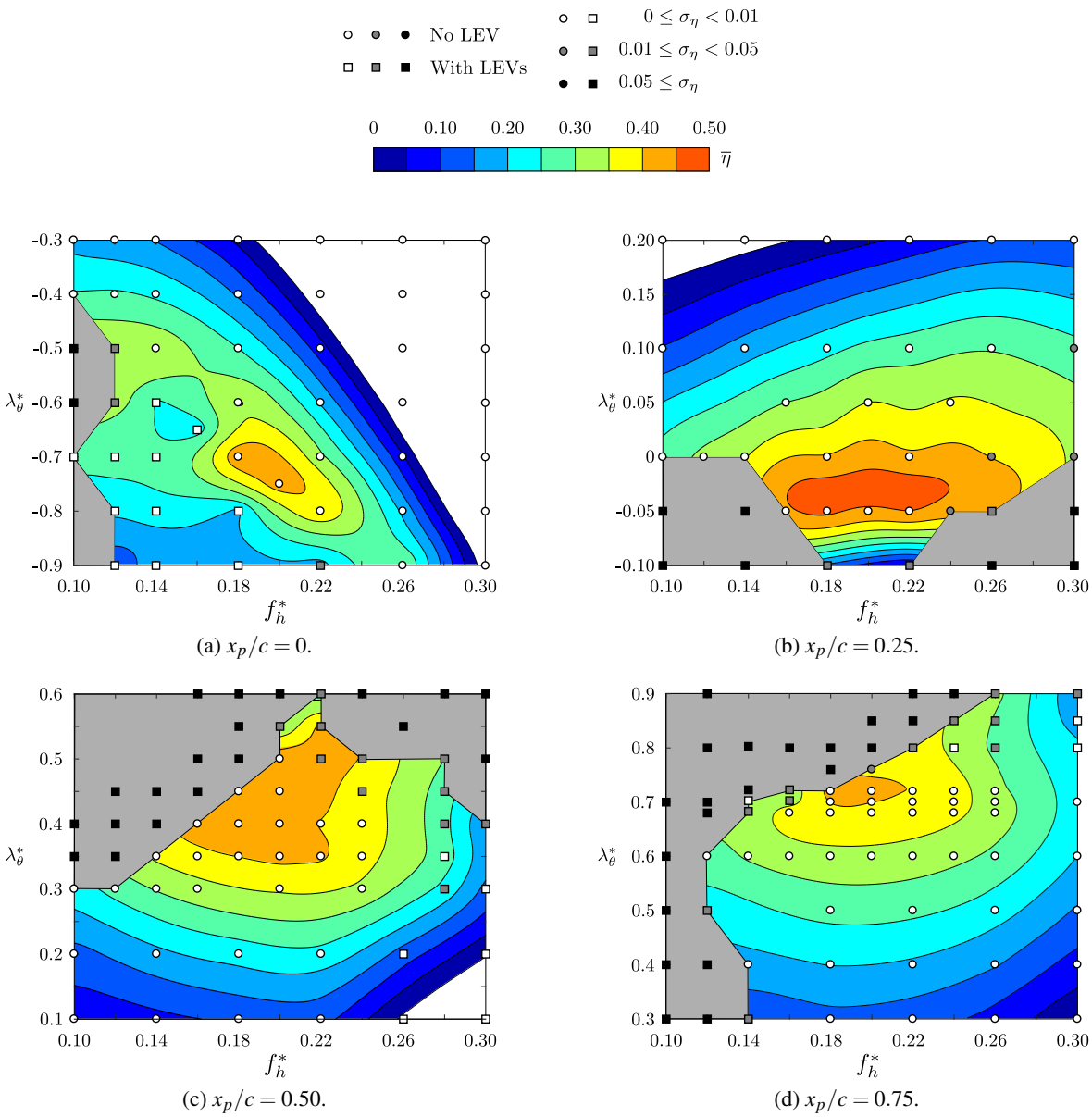

(a) $x_p/c = 0.$

(b) $x_p/c = 0.25.$

(c) $x_p/c = 0.50.$

(d) $x_p/c = 0.75.$

Figure 4.16: Efficiency contours obtained with different positions of the pitch axis. The white areas indicate negative efficiency values while the gray areas indicate zones where the data is not presented because of the large cycle-to-cycle variations ($\sigma_\eta \geq 0.05$). The values of S^* used with the different pitch axis locations are given in Table 4.4.

and $\lambda_\theta^* = -0.8$ and -0.9 have not been tested because they would require a negative pitch stiffness coefficient, which is impossible.

Fig. 4.16 reveals that the best efficiencies are always obtained with a reduced frequency around 0.2. This reduced frequency is the same in heave and in pitch since the frequencies are synchronized for these optimal cases. This observation justifies the choice of presenting the results for $f_h^* = 0.18$ in the rest of the current work.

It is also found that the value of λ_θ^* leading to the maximum efficiency, for a given frequency of the prescribed heave motion, does not vary much with f_h^*. In other words, the optimal values of λ_θ^* observed in Fig. 4.13c remain valid for other values of f_h^* around 0.18, namely from $f_h^* = 0.16$ to $f_h^* = 0.24$ approximately. Larger differences are observed when f_h^* departs from this range of frequencies because the influence of the frequency of the foil motions on the hydrodynamic moment coefficient and on the inertial coupling term eventually becomes too important.

4.5.6 Practical considerations

Considering a NACA0015 foil of constant density ρ_s and a span length (b) of one, the dimensionless moment of inertia about the quarter-chord point is approximately equal to $0.009\,\rho_s/\rho$, where ρ_s is the solid density and ρ is the fluid density. For a foil made of steel and operating in water, the density ratio is around 7.8 and the dimensionless moment of inertia of such a case is therefore roughly equal to 0.07. However, some other components undergoing the pitch motion would also be present on a real turbine setup, hence contributing to a larger I_θ^*. For example, the dimensionless moment of inertia of the steel blade used on the fully-passive turbine prototype tested by Boudreau et al. (2018) was around 0.1 because of the presence of some components undergoing the pitch motion that were located above water, such as the shaft holding the blade.

Based on the results of the present study with a pitch axis located at the quarter-chord point, I_θ^* should be larger than 0.5 in order to reach the large-inertia asymptote characterized with high efficiencies (see Fig. 4.8a). This suggests that a flywheel having a moment of inertia about four times that of the turbine blade would be required. Nevertheless, high efficiencies are still achieved with smaller values of I_θ^* and the specific threshold value of I_θ^* to reach a maximum efficiency is expected to depend on the specific sets of structural parameters selected. Note that a flapping-foil wind turbine would likely operate in the large-inertia asymptote without even needing the addition of a flywheel because of the smaller density of air compared to water.

Since the maximum efficiencies reached with the four different pitch axis locations are obtained with different values of λ_θ^*, but constant values of I_θ^* and f_θ^*, they are also obtained with different frequency ratios. This is shown in Fig. 4.17, which presents the data shown in Fig. 4.13, but plotted against r instead of λ_θ^*.

The optimal frequency ratio is around one (slightly above) when the pitch axis is located at the quarter-chord point, larger than one when the pitch axis is further upstream and smaller than one when it is further downstream. Thaweewat et al. (2018) observed the opposite behavior in the case of a similar semi-passive flapping foil with a passive pitch motion and $x_p/c = 0$, but in the context of propulsion instead of energy extraction. Their optimal performance was found with a phase lag around 70° and a frequency ratio of 0.5. The frequency ratio leading to the optimal propulsive efficiency obtained by Mackowski and Williamson (2017) for a flapping foil with a prescribed pitch motion and a passive heave motion also varies with the pitch axis location. However, it is worth recalling that optimal

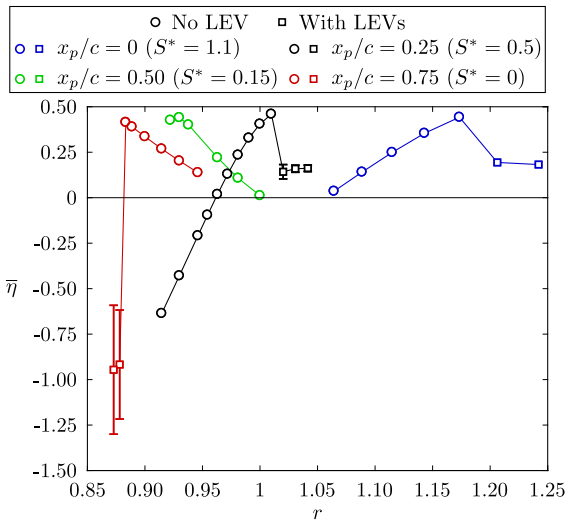

Figure 4.17: Efficiency as a function of the frequency ratio for various positions of the pitch axis. See Table 4.5 for the values of the other parameters.

frequency ratios vary with I^*_θ (see Fig. 4.4) since the dynamics of the passive pitch motion does not directly depend on r, but rather on λ^*_θ. Nevertheless, $\lambda^*_\theta < 0$ is always associated to $r > 1$, and vice versa.

Even though f^*_θ synchronizes itself to f^*_h in the range of λ^*_θ values resulting in high energy-extraction efficiencies, the frequency of the transient pitch response, that could result from a perturbation of the turbine structure or a perturbation occurring in the flow, would be different if $f^*_{n,\theta} \neq f^*_h$. This suggests that a pitch axis located at the quarter-chord point should be preferred since the best efficiencies are obtained when λ^*_θ is near zero in that case, hence corresponding to a frequency ratio close to unity and therefore avoiding the presence of two significantly different frequencies in the pitch motion in the event of a perturbation. This aspect also further supports the recommendation of having a large value of I^*_θ because f^*_θ approaches $f^*_{n,\theta}$ when I^*_θ increases for a given value of λ^*_θ.

Lastly, while variations of I^*_θ and k^*_θ essentially do not affect the permanent pitch response when they are sufficiently large and when λ^*_θ is kept constant, they do affect the transient period that would follow a perturbation in the flow. The larger I^*_θ is, the longer the transient period lasts. For example, a permanent response is typically reached after completing about ten cycles when $I^*_\theta = 2$, with the methodology described in Sec. 4.4, while more than 200 cycles can be required when $I^*_\theta = 100$.

4.6 Conclusion

The dynamics of a semi-passive flapping-foil, with a prescribed heave motion and a passive pitch motion, operating at a Reynolds number of 3.9×10^6 has been investigated. Two-dimensional numerical simulations of the incompressible Navier-Stokes equations with the Spalart-Allmaras turbulence model and an implicit fluid-structure coupling algorithm have been carried out. The results demon-

strate that an optimal power-generation performance can be maintained over large ranges of values of I_θ^*, k_θ^*, x_p/c and, to a lesser extent, f_h^*. This leaves a lot of flexibility regarding the design of such semi-passive flapping-foil turbines.

Using the fact that the passive pitch motions of the optimal operating points are almost sinusoidal and that their frequency synchronizes itself to the frequency of the prescribed heave motion, a simple effective parameter combining the moment of inertia and the pitch stiffness (λ_θ^*) has been proposed. We refer to it as the effective pitch stiffness. High efficiencies are maintained when I_θ^* and k_θ^* are properly scaled, that is, by keeping λ_θ^* constant. When I_θ^* and k_θ^* are scaled so that the pitch natural frequency remains constant instead of λ_θ^*, the efficiency quickly deteriorates as I_θ^* and k_θ^* are varied. In order to maximize the efficiency, threshold values of I_θ^* are k_θ^* must be exceeded. In practice, this suggests that the dimensionless moment of inertia should be about fives times larger than the dimensionless moment of inertia of a steel blade operating in water. Consequently, a flywheel is expected to be required in such conditions.

Four different pitch axis locations have been tested, namely the leading edge, the quarter-chord point, the mid-chord point and the three-quarter-chord point. Operating points characterized by periodic pitch motions of large amplitude and efficiency exceeding 40% have been obtained with all four positions of the pitch axis. In order to do so, the governing structural parameters have to be adjusted adequately because of the different phase lags between the heave and the pitch motions (ϕ) required to obtain similar motions of the foil surface with different positions of the pitch axis and the fact that the phase difference between the heave motion and the moment coefficient varies with x_p/c. One consequence of these variations of the structural parameters is that the ratio between the frequency of the pitch motion and the pitch natural frequency also changes with the pitch axis location. It is only around one when $x_p/c = 0.25$. It is larger than one when $x_p/c < 0.25$ and smaller than one when $x_p/c > 0.25$.

Lastly, the results of the current study prove that the semi-passive flapping-foil turbine with a prescribed heave motion and a passive pitch motion is a viable alternative to the more complex fully-constrained flapping-foil turbine since both have a similar potential in terms of energy extraction, with maximum efficiencies of the order of 45%.

Acknowledgments

Financial support from the Natural Sciences and Engineering Research Council of Canada (NSERC Discovery Grant/RGPIN/121819-2013 and CGS-D scholarship), the Tyler Lewis Clean Energy Research Foundation (2016 TLCERF grant) and the Leadership and Sustainable Development Scholarship Program of Université Laval is gratefully acknowledged by the authors. The computations presented in this work were carried out with the supercomputer Colosse at Université Laval, managed by Calcul Québec and Compute Canada.

Appendix

4.A Variations of $\overline{C_{P_h}}$ and $\overline{C_{P_\theta}}$ with x_p/c.

This appendix provides more information regarding the variations of $\overline{C_{P_h}}$ and $\overline{C_{P_\theta}}$ for the fully-constrained turbine cases with different positions of the pitch axis (see Fig. 4.12b).

Fig. 4.A.1 presents the time evolutions of the heave force and moment coefficients, the dimensionless heave and pitch velocities and the instantaneous heave and pitch power coefficients over one cycle for two different positions of the pitch axis, namely the leading edge and the three-quarter-chord point. Note that the heave and pitch power coefficients, defined by Eqs. 4.31 and 4.23, are also equal to the products of the corresponding force, or moment coefficient, with the corresponding dimensionless heave, or pitch, velocity:

$$\langle C_{P_h} \rangle = \frac{1}{T} \int_{t_i}^{t_i+T} \left(C_y \dot{h}^* \right) dt \ , \tag{4.58}$$

$$\langle C_{P_\theta} \rangle = \frac{1}{T} \int_{t_i}^{t_i+T} \left(C_M \dot{\theta}^* \right) dt \ , \tag{4.59}$$

where $T = 1/f$, f being the prescribed frequency of the heave and pitch motions of the fully-constrained turbine cases considered in this appendix. Since the instant $t/T = 0$ is defined as an instant at which $h = 0$ and $\dot{h} > 0$, the adjustment of the phase lag between the heave and the pitch motions with the position of the pitch axis (see Fig. 4.11) is not visible in Figs. 4.A.1a and 4.A.1b, but it can be seen in Figs. 4.A.1c and 4.A.1d. Also, the time evolutions of the heave velocity for the two considered pitch axis locations can be hardly distinguished from each other because the adjusted heave amplitude is very similar in both cases and the frequency is kept constant.

Figs. 4.A.1a and 4.A.1b show that the larger heave power coefficient observed when $x_p/c = 0$ (see Fig. 4.12b) is due to a larger amplitude of the heave force coefficient. Regarding the pitch power coefficient, Figs. 4.A.1c and 4.A.1d show that the phase difference between the heave motion and the moment coefficient is considerably altered when changing the position of the pitch axis. When $x_p/c = 0$, the moment coefficient and the pitch velocity are out of phase, that is, the moment coefficient is positive when the pitch velocity is negative, and vice versa. As a result, the instantaneous pitch power coefficient is almost always negative, which leads to a large negative cycle-averaged pitch power coefficient ($\langle C_{P_\theta} \rangle$). Conversely, the phase difference between the pitch velocity and the moment coefficient is around 90° when $x_p/c = 0.75$, which results in a cycle-averaged pitch power coefficient

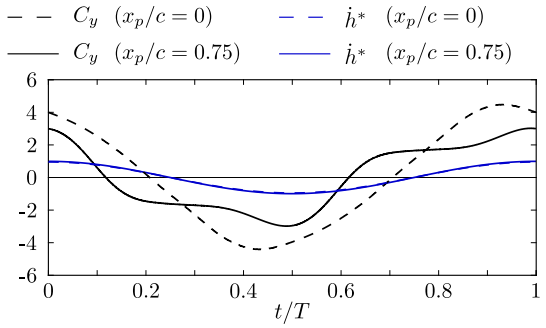

(a) Heave force coefficient and dimensionless heave velocity.

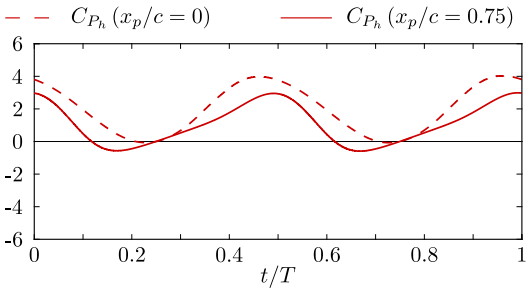

(b) Instantaneous heave power coefficient.

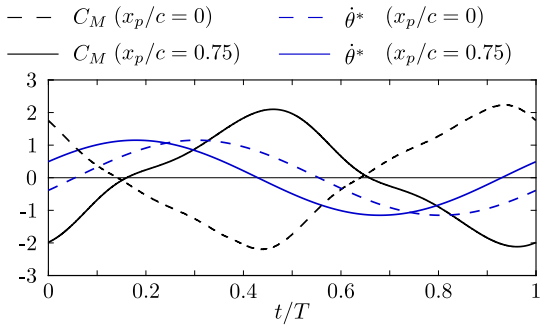

(c) Moment coefficient and dimensionless pitch velocity.

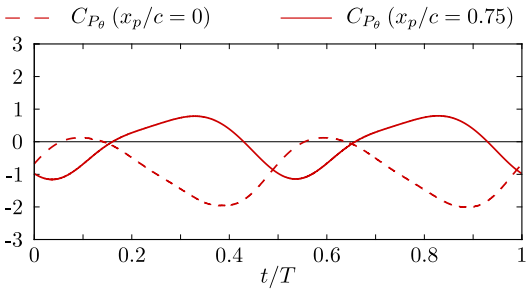

(d) Instantaneous pitch power coefficient.

Figure 4.A.1: Time evolutions of various metrics over one cycle for two different positions of the pitch axis. The instant $t/T = 0$ corresponds to an instant at which $h = 0$ and $\dot{h} > 0$.

close to zero. This result implies that a smaller amount of power is required to drive the pitch motion when $x_p/c = 0.75$ than with any other pitch axis location (see Fig. 4.12b), even though the amplitude of the moment coefficient reaches its minimum value when $x_p/c = 0.25$ since this point is close to the aerodynamic center.

4.B Explanations regarding the estimations of the structural parameter values listed in Table 4.4

The estimations of the structural parameter values required with different positions of the pitch axis presented in Table 4.4 have been determined from the reverse solver technique proposed by Veilleux and Dumas (2017). In order to further explain why such values are required, the time evolutions of the moment coefficient, the pitch angle (θ), the pitch velocity ($\dot{\theta}^*$) and the term $\ddot{h}^* \cos(\theta)$, obtained from the reference fully-constrained turbine cases, are presented over one cycle in Fig. 4.B.1.

Fig. 4.B.1b shows that the pitch velocity is in antiphase (phase difference of about 180°) with the moment coefficient term ($C_M/2$) when $x_p/c = 0.25$. This means that D^*_θ would need to have a negative value for the corresponding term to balance the moment coefficient term in Eq. 4.49, which is not possible because this implies that the pitch damper would need to act as an energy source instead of

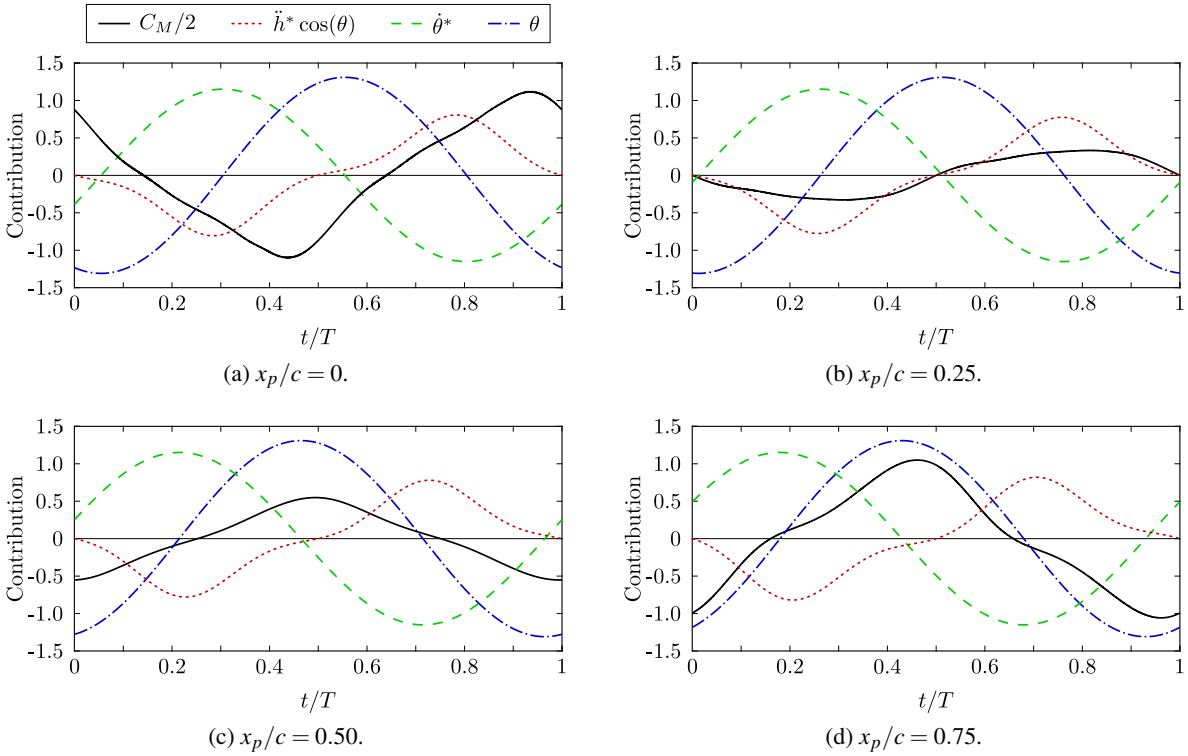

(a) $x_p/c = 0$. (b) $x_p/c = 0.25$.

(c) $x_p/c = 0.50$. (d) $x_p/c = 0.75$.

Figure 4.B.1: Time evolutions of the different contributions appearing in Eq. 4.49 obtained from the reference fully-constrained turbine cases presented in Table 4.3 over one cycle. θ is given in radians and the instant $t/T = 0$ corresponds to an instant at which $h = 0$ and $\dot{h} > 0$.

an energy sink. In other words, an actuator would be needed. This figure also shows that there is a phase difference of about 90° between θ and the moment coefficient term, hence making the term involving λ_θ^* not suitable to satisfy Eq. 4.49 with this pitch axis location. Lastly, the term $\ddot{h}^* \cos(\theta)$ is in phase with the moment coefficient term, thus allowing satisfying Eq. 4.49 with a positive static moment value, i.e. with a center of mass located downstream of the pitch axis.

When $x_p/c = 0.75$ (see Fig. 4.B.1d), the phase lag between the heave and the pitch motions (ϕ) is smaller than when $x_p/c = 0.25$ following the adjustment presented in Fig. 4.11. As a result, the curves corresponding to the pitch angle, the pitch velocity and the term $\ddot{h}^* \cos(\theta)$ shift to the left in Fig. 4.B.1d compared to the corresponding ones in Fig. 4.B.1b since the instant $t/T = 0$ corresponds to an instant at which $h = 0$ and $\dot{h} > 0$. The phase difference between the heave motion and the moment coefficient also decreases when passing from $x_p/c = 0.25$ to $x_p/c = 0.75$, and this decrease is more important than for the other terms involved in Eq. 4.49. Consequently, the term $\ddot{h}^* \cos(\theta)$ is no longer in phase with the moment coefficient term and thus cannot be used to satisfy the equation of motion in pitch. This means that a value of zero for the static moment is expected to be needed when the pitch axis is located at the three-quarter-chord point. In other words, this suggests that the center of mass should coincide with the pitch axis in that specific case. The damping term, which is proportional to the pitch velocity, is again not useful to balance the moment coefficient term, which

thus leaves the term proportional to λ_θ^* as the only one that can satisfies Eq. 4.49.

The opposite behavior is observed when the pitch axis is located at the leading edge, i.e., the phase lag between the heave and the pitch motions as well as the phase difference between the heave motion and the moment coefficient increase when switching from $x_p/c = 0.25$ to $x_p/c = 0$ instead of decreasing. Consequently, the term with λ_θ^* has to be negative instead of positive to balance the moment coefficient term. Finally, the case with $x_p/c = 0.50$ lies in between the cases with $x_p/c = 0.25$ and $x_p/c = 0.75$, both in terms of the value of S^* and the value of λ_θ^*.

Bibliography

Abiru, Hisanori and Yoshitake, Akira. Study on a Flapping Wing Hydroelectric Power Generation System. *Journal of Environment and Engineering*, 6(1):178–186, 2011.

Abiru, Hisanori and Yoshitake, Akira. Experimental Study on a Cascade Flapping Wing Hydroelectric Power Generator. *Journal of Energy and Power Engineering*, 6(9):1429–1436, 2012.

Boudreau, Matthieu, Dumas, Guy, Rahimpour, Mostafa, and Oshkai, Peter. Experimental investigation of the energy extraction by a fully-passive flapping-foil hydrokinetic turbine prototype. *Journal of Fluids and Structures*, 82:446 – 472, 2018.

Boudreau, Matthieu, Gunther, Kevin, and Dumas, Guy. Investigation of the energy-extraction regime of a novel semi-passive flapping-foil turbine concept with a prescribed heave motion and a passive pitch motion. *Journal of Fluids and Structures*, 84:368 – 390, 2019.

Chen, Yongliang, Nan, Jingwen, and Wu, Jie. Wake effect on a semi-active flapping foil based energy harvester by a rotating foil. *Computers & Fluids*, 160:51 – 63, 2018.

Dacles-Mariani, J., Zilliac, G. G., Chow, J. S., and Bradshaw, P. Numerical/Experimental Study of a Wingtip Vortex in the Near Field. *AIAA Journal*, 33(9):1561 – 1568, 1995.

Dacles-Mariani, J., Kwak, D., and Zilliac, G. On numerical errors and turbulence modeling in tip vortex flow prediction. *International Journal for Numerical Methods in Fluids*, 30(1):65 – 82, 1999.

Davids, S.T. A Computational and Experimental Investigation of a Flutter Generator. Master's thesis, Naval Postgraduate School, Monterey, CA, USA, 1999.

Deng, Jian, Teng, Lubao, Pan, Dingyi, and Shao, Xueming. Inertial effects of the semi-passive flapping foil on its energy extraction efficiency. *Physics of Fluids*, 27(5):053103 (17 pp.) –, 2015.

Derakhshandeh, J.F., Arjomandi, M., Dally, B., and Cazzolato, B. Flow-induced vibration of an elastically mounted airfoil under the influence of the wake of a circular cylinder. *Experimental Thermal and Fluid Science*, 74:58 – 72, 2016.

Ferziger, J.H. and Perić, M. *Computational Methods for Fluid Dynamics*. Springer, third edition, 2002.

Griffith, Martin D., Jacono, David Lo, Sheridan, John, and Leontini, Justin S. Passive heaving of elliptical cylinders with active pitching – from cylinders towards flapping foils. *Journal of Fluids and Structures*, 67:124 – 141, 2016.

Huxham, G. H., Cochard, S., and Patterson, J. Experimental Parametric Investigation of an Oscillating Hydrofoil Tidal Stream Energy Converter. In *Proceedings of the 18th Australasian Fluid Mechanics Conference*, Launceston, Australia, 2012.

Kim, Daegyoum, Strom, Benjamin, Mandre, Shreyas, and Breuer, Kenneth. Energy harvesting performance and flow structure of an oscillating hydrofoil with finite span. *Journal of Fluids and Structures*, 70:314 – 326, 2017.

Kinsey, Thomas and Dumas, Guy. Parametric Study of an Oscillating Airfoil in a Power-Extraction Regime. *AIAA Journal*, 46(6):1318–1330, 2008.

Kinsey, Thomas and Dumas, Guy. Three-dimensional effects on an oscillating-foil hydrokinetic turbine. *Journal of Fluids Engineering*, 134(7):071105 (11 pp.) –, 2012.

Kinsey, Thomas and Dumas, Guy. Optimal Operating Parameters for an Oscillating Foil Turbine at Reynolds Number 500,000. *AIAA Journal*, 52(9):1885–1895, 2014.

Kinsey, Thomas, Dumas, Guy, Lalande, G., Ruel, J., Mehut, A., Viarouge, P., Lemay, J., and Jean, Y. Prototype testing of a hydrokinetic turbine based on oscillating hydrofoils. *Renewable Energy*, 36 (6):1710 – 1718, 2011.

Mackowski, A. W. and Williamson, C. H. K. Effect of pivot location and passive heave on propulsion from a pitching airfoil. *Phys. Rev. Fluids*, 2:013101 (24pp.), 2017.

McKinney, William and DeLaurier, James. Wingmill: An Oscillating-Wing Windmill. *Journal of Energy*, 5(2):109–115, 1981.

Onoue, Kyohei, Song, Arnold, Strom, Benjamin, and Breuer, Kenneth S. Large amplitude flow-induced oscillations and energy harvesting using a cyber-physical pitching plate. *Journal of Fluids and Structures*, 55:262 – 275, 2015.

Panton, Ronald L. *Incompressible Flow*. John Wiley & Sons, Inc., Hoboken, NJ, USA, 4$^{\text{th}}$ edition, 2013.

Peng, Zhangli and Zhu, Qiang. Energy harvesting through flow-induced oscillations of a foil. *Physics of Fluids*, 21(12):174–191, 2009.

Shiels, D., Leonard, A., and Roshko, A. Flow-induced vibration of a circular cylinder at limiting structural parameters. *Journal of Fluids and Structures*, 15(1):3 – 21, 2001.

Shimizu, Eriko, Isogai, Koji, and Obayashi, Shigeru. Multiobjective Design Study of a Flapping Wing Power Generator. *Journal of Fluids Engineering*, 130(2):021104 (8 pp.) –, 2008.

Sitorus, Patar Ebenezer, Le, Tuyen Quang, Ko, Jin Hwan, Truong, Tri Quang, and Park, Hoon Cheol. Design, implementation, and power estimation of a lab-scale flapping-type turbine. *Journal of Marine Science and Technology*, 2015.

Spalart, P. R., Jou, W-H., Strelets, M., and Allmaras, S. R. Comments on the Feasibility of LES for Wings, and on a Hybrid RANS/LES Approach. In *Advances in DNS/LES, Proceedings of the First AFOSR International Conference on DNS/LES*, pages 137 – 147, Ruston, Louisiana, USA, 1997.

Spalart, Philippe. R. and Allmaras, Steven R. A One-Equation Turbulence Model for Aerodynamic Flows. *Recherche Aérospatiale*, (1):5–21, 1994.

Spalart, Philippe R. and Rumsey, Christopher L. Effective inflow conditions for turbulence models in aerodynamic calculations. *AIAA Journal*, 45(10):2544 – 2553, 2007.

Teng, Lubao, Deng, Jian, Pan, Dingyi, and Shao, Xueming. Effects of non-sinusoidal pitching motion on energy extraction performance of a semi-active flapping foil. *Renewable Energy*, 85:810 – 818, 2016.

Thaweewat, Nonthipat, Phoemsapthawee, Surasak, and Juntasaro, Varangrat. Semi-active flapping foil for marine propulsion. *Ocean Engineering*, 147:556 – 564, 2018.

Veilleux, Jean-Christophe. Optimization of a Fully-Passive Flapping-Airfoil Turbine. Master's thesis, Université Laval, Québec, Qc, Canada, 2014.

Veilleux, Jean-Christophe and Dumas, Guy. Numerical optimization of a fully-passive flapping-airfoil turbine. *Journal of Fluids and Structures*, 70:102 – 130, 2017.

Wang, Zhuo, Du, Lin, Zhao, Jisheng, and Sun, Xiaofeng. Structural response and energy extraction of a fully passive flapping foil. *Journal of Fluids and Structures*, 72:96 – 113, 2017.

Wu, J., Qiu, Y. L., Shu, C., and Zhao, N. Pitching-motion-activated flapping foil near solid walls for power extraction: A numerical investigation. *Physics of Fluids*, 26(8):083601, 2014.

Wu, J., Chen, Y. L., and Zhao, N. Role of induced vortex interaction in a semi-active flapping foil based energy harvester. *Physics of Fluids*, 27(9):093601, 2015.

Xiao, Qing and Zhu, Qiang. A review on flow energy harvesters based on flapping foils. *Journal of Fluids and Structures*, 46:174–191, 2014.

Xu, G.D., Xu, W.H., and Dai, J. Numerical and experimental study of a flapping foil generator. *Applied Ocean Research*, 63:242 – 250, 2017.

Young, John, Ashraf, Muhammad A., Lai, Joseph C. S., and Platzer, Max F. Numerical Simulation of Fully Passive Flapping Foil Power Generation. *AIAA Journal*, 51(11):2727–2739, 2013.

Young, John, Lai, Joseph C. S., and Platzer, Max F. A review of progress and challenges in flapping foil power generation. *Progress in Aerospace Sciences*, 67:2–28, 2014.

Zhan, Jiapu, Xu, Bing, Wu, Jie, and Wu, Jing. Power extraction performance of a semi-activated flapping foil in gusty flow. *Journal of Bionic Engineering*, 14(1):99 – 110, 2017.

Zhu, Qiang. Optimal frequency for flow energy harvesting of a flapping foil. *Journal of Fluid Mechanics*, 675:495–517, 5 2011.

Zhu, Qiang. Energy harvesting by a purely passive flapping foil from shear flows. *Journal of Fluids and Structures*, 34:157–169, 2012.

Zhu, Qiang and Peng, Zhangli. Mode coupling and flow energy harvesting by a flapping foil. *Physics of Fluids*, 21(3):033601 (10 pp.) –, 2009.

Zhu, Qiang, Haase, Max, and Wu, Chin H. Modeling the capacity of a novel flow-energy harvester. *Applied Mathematical Modelling*, 33(5):2207–2217, 2009.

Chapter 5

Paper IV:
A parametric study and optimization of the fully-passive flapping-foil turbine at high Reynolds number

5.1 Résumé

La dynamique d'une turbine à aile oscillante complètement passive, opérant à un nombre de Reynolds de 3.9×10^6, est étudiée à l'aide de simulations numériques bidimensionnelles résolvant l'interaction fluide-structure. Ce concept consiste en une aile attachée à la structure de la turbine seulement à l'aide de ressorts et d'amortisseurs. Ces supports élastiques permettent de remplacer les mécanismes plus complexes qui sont généralement utilisés pour contraindre l'aile à suivre des mouvements particuliers. La dynamique de l'aile dépend donc de son interaction avec ses supports élastiques et l'écoulement de fluide auquel elle fait face. Cette étude démontre que les performances optimales de la turbine à aile oscillante complètement contrainte peuvent être égalées avec ce concept plus simple de turbine complètement passive lorsque les paramètres structuraux sont ajustés adéquatement. En effet, une efficacité atteignant 53.8% a été obtenue. La présente étude révèle également que les effets liés à des variations de la masse et de la raideur en pilonnement peuvent être caractérisés par un seul paramètre qui n'est pas la fréquence naturelle en pilonnement. Par contre, la fréquence naturelle en tangage caractérise bien la dynamique du mouvement de tangage passif, ce qui implique du même coup que le moment d'inertie et la raideur en tangage peuvent aussi être combinés ensemble en un seul paramètre effectif. Une performance optimale en terme d'extraction d'énergie peut être conservée sur de larges plages de valeurs en ce qui concerne les propriétés inertielles et de raideur, autant en pilonnement qu'en tangage, lorsque les paramètres effectifs les combinant ensemble sont maintenus constants. Les résultats de cette étude montre aussi que la présence de frottement visqueux en tangage est nuisible

en ce qui concerne la performance de la turbine, mais son effet demeure faible pour un niveau de frottement réaliste.

5.2 Abstract

The dynamics of a fully-passive flapping-foil turbine, operating at a Reynolds number of 3.9×10^6, is studied via two-dimensional fluid-structure numerical simulations. This turbine concept consists in an oscillating foil that is constrained to move only in heave and in pitch. The foil is allowed to move freely in heave and in pitch by being simply attached to its structure by springs and dampers. These elastic supports eliminate the need for the more complex mechanisms that are traditionally used to prescribe specific foil motions. The consequence is that the foil dynamics depends entirely on its interaction with the elastic supports and the oncoming fluid flow. This study demonstrates that the optimal performance of fully-constrained flapping-foil turbines can be matched with a simpler fully-passive turbine when the structural parameters are adequately adjusted. Indeed, an efficiency reaching 53.8% has been achieved in the present work. The present study also shows that the effects of varying the heaving mass and the heave stiffness can be effectively characterized by a single parameter, which is not the heave natural frequency. On the other hand, the pitch dynamics is appropriately characterized by the pitch natural frequency, hence implying that the moment of inertia and the pitch stiffness can also be combined together into a single parameter. An optimal energy-extraction performance can be maintained over large variations of the inertial and stiffness properties, both in heave and in pitch, when the effective parameters that combine them together are kept constant. It is also found that the presence of viscous friction in pitch is detrimental to the turbine performance, but its effect remains small with a realistic level of friction.

5.3 Introduction

Fully-passive flapping-foil turbines are a viable and mechanically simpler alternative to their fully-constrained counterparts. Indeed, constraining the foil motions to follow specific functions of time, in heave and in pitch, requires intricate mechanisms that increase the risks of failure of the apparatus and may lead to important power losses (Kinsey et al., 2011). The fully-passive concept does not rely on such mechanisms because its foil is simply attached to the turbine structure with elastic supports, namely springs and dampers. It is therefore free to move in heave and in pitch. In fact, these two motions result from the interaction of the elastically-supported foil and the fluid flow, thereby leaving the designer of such a turbine with only an indirect control over the foil motions by adjusting the structural parameters that govern the foil dynamics.

A few research groups have already demonstrated the feasibility of the fully-passive flapping-foil turbine concept, both via numerical simulations (Peng and Zhu, 2009; Zhu, 2012; Veilleux and Dumas, 2017; Wang et al., 2017) and experiments (Boudreau et al., 2018; Iverson, 2018). They showed that different types of responses are obtained when varying the structural parameters, including pe-

riodic motions of large amplitudes leading to a net energy extraction from the flow. However, the increased simplicity provided by the use of elastic supports has come at the cost of a lower performance so far. Indeed, the maximum efficiencies reported for the fully-passive concept are of the order of 30% (Boudreau et al., 2018; Veilleux and Dumas, 2017; Wang et al., 2017) compared to 45% for its fully-constrained counterpart (Kinsey and Dumas, 2014; Xiao and Zhu, 2014; Young et al., 2014). All the optimal fully-passive cases reported in the literature have one thing in common: they rely on deep dynamic stall and the formation of leading-edge vortices (LEVs). In fact, Veilleux and Dumas (2017) and Boudreau et al. (2018) argued that, in their case, the foil's pitch motion is driven by a divergence instability (Dowell, 2004; Fung, 2008), which in turn drives the heave motion. As soon as the foil is released, the heave and pitch amplitudes are rapidly growing until they are limited by the unsteady separation of the flow, or, in other words, the occurrence of deep dynamic stall. Such a limitation of the amplitude following a divergence instability was also observed by Onoue et al. (2015) for an elastically-supported pitching plate.

The coupled-mode flutter instability can also generate passive heave and pitch motions of a foil. Although it has already been thoroughly studied, mainly with the purpose of determining the instability onset and ways to mitigate it in the field of aeronautics, few studies have analyzed the large-amplitude motions that can result from it (e.g., Amandolese et al. (2013); Pigolotti et al. (2017); Poirel and Mendes (2014)) and none obtained a level of power extraction near what can be achieved with a fully-constrained flapping-foil turbine.

Recently, Boudreau et al. (2019b) showed that efficiencies of the order of 45% could be reached with a semi-passive concept, i.e., when prescribing a sinusoidal heave motion while elastically-supporting the foil in pitch. This has been achieved with operating points for which no deep dynamic stall is observed. Under such conditions, the pitch motion requires energy on average rather than extracting energy from the flow (Boudreau et al., 2019b; Kinsey and Dumas, 2014). This energy must be transferred from the heave motion to the pitch motion. When no motor actuates the pitch motion and no rigid links couple the heave and pitch degrees of freedom, this transfer takes place via the inertial coupling that arises when the pitch axis and the foil's center of mass do not coincide. Considering a pitch axis located at the quarter-chord point, such an energy transfer is possible when the center of mass is positioned downstream of the pitch axis, i.e., when the static moment is positive.

In the case of the semi-passive flapping-foil turbine concept studied by Boudreau et al. (2019b), the foil responses are driven by the prescribed heave motion. In fact, the electric generator linked to the heave motion has to provide energy at some instants during the foil oscillations even when the cycle-averaged energy extraction is maximized. This cannot occur in the case of a fully-passive flapping-foil turbine for which both degrees of freedom are elastically supported.

The main objective of the present study is to determine if and how the best efficiencies reported for the fully-constrained and semi-passive flapping-foil turbine can be reached with a simpler fully-passive flapping-foil turbine. Moreover, we aim at determining if optimal fully-passive foil motions, in terms

of energy extraction, can be achieved without deep dynamic stall. Following the works of Boudreau et al. (2019a) on a semi-passive turbine, we also investigate how to properly scale the inertial and stiffness properties of the turbine in heave and in pitch in order to provide some flexibility to the designer of a fully-passive flapping-foil turbine prototype.

The fully-passive flapping-foil turbine concept, the metrics that characterize its performance and the numerical methodology are presented in Sec.5.4. A parametric study involving variations of the heave damping and stiffness coefficients is then presented in Sec. 5.5.1, followed by the analysis of effective parameters in Sec. 5.5.2 and the evaluation of the effect of nonzero viscous damping in pitch in Sec. 5.5.4.

5.4 Methodology

5.4.1 Dynamics

A rigid NACA0015 foil profile is considered and the turbine operates at a Reynolds number of 3.9×10^6 based on the freestream velocity and the chord length:

$$Re = \frac{U_\infty c}{\nu} = 3.9 \times 10^6 \, . \tag{5.1}$$

The foil of the fully-passive flapping-foil turbine considered here is only free to move in heave (y direction) and in pitch, as shown in Fig. 5.1. Since it is elastically supported in both these degrees of freedom, its dynamics is governed by the two following equations:

$$F_y = m_h \ddot{h} + S\left(\ddot{\theta}\cos\theta - \dot{\theta}^2 \sin\theta\right) + D_h \dot{h} + k_h h \, , \tag{5.2}$$

$$M = I_\theta \, \ddot{\theta} + S\ddot{h}\cos(\theta) + D_\theta \, \dot{\theta} + k_\theta \, \theta \, . \tag{5.3}$$

F_y and M are respectively the force component in the heave (y) direction and the moment coefficient about the pitch axis generated by the fluid flow. m_h is the heaving mass, i.e., the mass of all the components undergoing the heave motion. I_θ is the moment of inertia about the pitch axis. S is the static moment and it is equal to the product of the mass of the components undergoing the pitch motion (m_θ) with the distance between the center of mass (in pitch) and the pitch axis (x_θ):

$$S = m_\theta \, x_\theta \, . \tag{5.4}$$

A positive value of x_θ implies that the center of mass is located downstream of the pitch axis, as illustrated in Fig. 5.1. The pitch axis is positioned at the quarter-chord point throughout this study.

In Eq. 5.2, D_h is the heave damping coefficient and it represents the sum of two different contributions:

$$D_h = D_{h,\mathrm{e}} + D_{h,\mathrm{v}} \, , \tag{5.5}$$

where $D_{h,\mathrm{v}}$ accounts for the presence of undesired viscous friction in the setup and $D_{h,\mathrm{e}}$ models the presence of an electric generator, as was done in several previous works that considered a passive

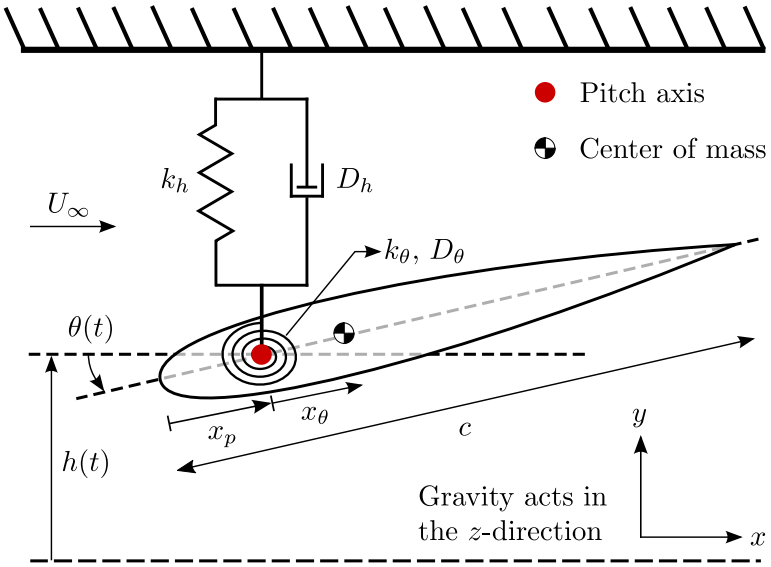

Figure 5.1: Schematic of the fully-passive flapping-foil turbine concept. In the present study, $x_p/c = 0.25$ and the foil is only free to move in heave (h) and in pitch (θ).

heave motion (Abiru and Yoshitake, 2011; Boudreau et al., 2018; Deng et al., 2015; Griffith et al., 2016; Iverson, 2018; Peng and Zhu, 2009; Teng et al., 2016; Veilleux and Dumas, 2017; Wang et al., 2017; Zhu, 2012). In other words, the energy that is dissipated in this damping contribution represents the energy that would be converted into electricity by an electric generator. D_θ is the pitch damping coefficient and it represents undesired viscous friction in pitch. All the energy dissipated in the pitch damper is therefore considered to be lost as heat. k_h and k_θ are respectively the heave and pitch stiffness coefficients. The superscript $(\cdot)$ denotes a time derivative. Lastly, let us recall that the foil's motions are restricted to the heave and pitch degrees of freedom, i.e., the foil does not move in any other direction, and the gravitational acceleration does not affect the turbine dynamics because it is assumed to act in the span or z direction.

Using an appropriate normalization (Veilleux and Dumas, 2017; Boudreau et al., 2018; Onoue et al., 2015), Eqs. 5.2 and 5.3 can be written in their dimensionless form:

$$C_{F_y}/2 \;=\; m_h^*\ddot{h}^* \;+\; S^*\left(\ddot{\theta}^*\cos\theta - \dot{\theta}^{*2}\sin\theta\right) + D_h^*\dot{h}^* \;+\; k_h^* h^* \;, \tag{5.6}$$

$$C_M/2 \;=\; I_\theta^*\,\ddot{\theta}^* \;+\; S^*\ddot{h}^*\cos\theta \;+\; D_\theta^*\,\dot{\theta}^* \;+\; k_\theta^*\,\theta \;, \tag{5.7}$$

where:

$$C_{F_y} = \frac{F_y}{0.5\,\rho\,U_\infty^2\,b\,c} \;,\quad C_M = \frac{M}{0.5\,\rho\,U_\infty^2\,b\,c^2} \;,\; m_h^* = \frac{m_h}{\rho\,b\,c^2} \;,\; I_\theta^* = \frac{I_\theta}{\rho\,b\,c^4} \;,\quad S^* = \frac{S}{\rho\,b\,c^3} \;,$$

$$D_h^* = \frac{D_h}{\rho\,U_\infty\,b\,c} \;,\; D_\theta^* = \frac{D_\theta}{\rho\,U_\infty\,b\,c^3} \;,\quad k_h^* = \frac{k_h}{\rho\,U_\infty^2\,b} \;,\quad k_\theta^* = \frac{k_\theta}{\rho\,U_\infty^2\,b\,c^2} \;,$$

$$h^* = \frac{h}{c} \ , \quad \dot{h}^* = \frac{\dot{h}}{U_\infty} \ , \quad \ddot{h}^* = \frac{\ddot{h}\,c}{U_\infty^2} \ , \quad \dot{\theta}^* = \frac{\dot{\theta}\,c}{U_\infty} \ , \quad \ddot{\theta}^* = \frac{\ddot{\theta}\,c^2}{U_\infty^2} \ ,$$

in which ρ is the fluid density, U_∞ is the freestream velocity, c is the foil's chord length and b is the foil's span length. Since the turbine dynamics is analyzed via two-dimensional (2D) numerical simulations, forces per unit span are obtained and the span length is therefore considered to be equal to one ($b = 1$).

5.4.2 Evaluating the energy extraction performance

Using a similar procedure than the one presented in our previous works on a semi-passive flapping-foil turbine with a passive pitch motion (Boudreau et al., 2019b), the equations of motion can be transformed into power balance equations. This is done by putting all the terms appearing in Eqs. 5.2 and 5.3 on the left hand side of their respective equations, except the heave damping contribution that models the electricity generation, and by multiplying each equation of motion by the corresponding heave or pitch velocity. The resulting equations are then normalized with $0.5\,\rho\,U_\infty^3\,b\,c$, the kinetic energy flux passing through a plane of one chord length by one span length. Moreover, we define the instant 0 in every turbine cycle as the instant at which $h = 0$ and $\dot{h} > 0$. By cycle-averaging the normalized equations obtained with the procedure described above, the following relations are obtained:

$$\langle C_{P_h} \rangle + \langle C_{P_{m_h}} \rangle + \langle C_{P_{S,h}} \rangle + \langle C_{P_{D_{h,\mathrm{v}}}} \rangle + \langle C_{P_{k_h}} \rangle = \langle C_{P_{D_{h,\mathrm{e}}}} \rangle \ , \tag{5.8}$$

$$\langle C_{P_\theta} \rangle + \langle C_{P_{I_\theta}} \rangle + \langle C_{P_{S,\theta}} \rangle + \langle C_{P_{D_\theta}} \rangle + \langle C_{P_{k_\theta}} \rangle = 0 \ , \tag{5.9}$$

where:

$$\langle C_{P_h} \rangle = \frac{1}{T} \int_{t_i}^{t_i+T} \left(C_{F_y}\, \dot{h}^* \right) dt \ , \tag{5.10}$$

$$\langle C_{P_{m_h}} \rangle = \frac{1}{T} \int_{t_i}^{t_i+T} \left(-2\, m_h^*\, \ddot{h}^*\, \dot{h}^* \right) dt \ , \tag{5.11}$$

$$\langle C_{P_{S,h}} \rangle = \frac{1}{T} \int_{t_i}^{t_i+T} \left(-2\, S^*\, \dot{h}^* \left(\ddot{\theta}^* \cos\theta - \dot{\theta}^{*2} \sin\theta \right) \right) dt \ , \tag{5.12}$$

$$\langle C_{P_{D_{h,\mathrm{v}}}} \rangle = \frac{1}{T} \int_{t_i}^{t_i+T} \left(-2\, D_{h,\mathrm{v}}^*\, \dot{h}^{*2} \right) dt \ , \tag{5.13}$$

$$\langle C_{P_{k_h}} \rangle = \frac{1}{T} \int_{t_i}^{t_i+T} \left(-2\, k_h^*\, h^*\, \dot{h}^* \right) dt \ , \tag{5.14}$$

$$\langle C_{P_{D_{h,\mathrm{e}}}} \rangle = \frac{1}{T} \int_{t_i}^{t_i+T} \left(-2\, D_{h,\mathrm{e}}^*\, \dot{h}^{*2} \right) dt \ , \tag{5.15}$$

$$\langle C_{P_\theta} \rangle = \frac{1}{T} \int_{t_i}^{t_i+T} \left(C_M \, \dot{\theta}^* \right) dt \ , \tag{5.16}$$

$$\langle C_{P_{I_\theta}} \rangle = \frac{1}{T} \int_{t_i}^{t_i+T} \left(-2 I_\theta^* \, \ddot{\theta}^* \, \dot{\theta}^* \right) dt \ , \tag{5.17}$$

$$\langle C_{P_{S,\theta}} \rangle = \frac{1}{T} \int_{t_i}^{t_i+T} \left(-2 S^* \, \ddot{h}^* \, \dot{\theta}^* \cos\theta \right) dt \ , \tag{5.18}$$

$$\langle C_{P_{D_\theta}} \rangle = \frac{1}{T} \int_{t_i}^{t_i+T} \left(-2 D_\theta^* \, \dot{\theta^*}^2 \right) dt \ , \tag{5.19}$$

$$\langle C_{P_{k_\theta}} \rangle = \frac{1}{T} \int_{t_i}^{t_i+T} \left(-2 k_\theta^* \, \theta \, \dot{\theta}^* \right) dt \ . \tag{5.20}$$

The angle brackets indicate that the corresponding values are cycle-averaged, t_i is the time at which a given cycle starts, again defined as an instant at which $h = 0$ and $\dot{h} > 0$, and T is the period of one cycle. Note that unless otherwise indicated, the term power coefficient refers to a cycle-averaged value in the rest of the paper.

As mentioned in the previous section, the heave damping contribution, $D_{h,\mathrm{e}}$, models the presence of an electric generator. The power coefficient $\langle C_{P_{D_{h,\mathrm{e}}}} \rangle$ therefore measures the power-generation performance of the turbine. It is equal to the sum of the different contributions appearing on the left hand side of Eq. 5.8. A positive value of $\langle C_{P_{D_{h,\mathrm{e}}}} \rangle$ implies that a net amount of power is available for electricity production. On the other hand, the undesired heave damping contribution, $\langle C_{P_{D_{h,\mathrm{v}}}} \rangle$, is always negative and thus acts as a sink of power. In practice, it stems from the presence of friction in the moving components forming the turbine assembly and the power dissipated by this friction is lost as heat.

$\langle C_{P_h} \rangle$ and $\langle C_{P_\theta} \rangle$ are the heave and pitch power coefficients. They measure the power transfers occurring between the foil and the flow via the hydrodynamic force and moment and the corresponding foil motion. A positive value for one of these power coefficients means that a net amount of power is transferred from the flow to the foil. Conversely, a negative value implies that some power is required to maintain the corresponding motion. Both are related to each other because of the hydrodynamic coupling between the forces and moment acting on the foil.

The power available for the electric generator, $\langle C_{P_{D_{h,\mathrm{e}}}} \rangle$, is also coupled to the power balance in pitch because of the inertial coupling between both degrees of freedom that arises when the position of the pitch axis does not coincide with the position of the center of mass ($S \neq 0$). A positive value of $\langle C_{P_{S,h}} \rangle$ represents a net power transfer from the pitch motion to the heave motion on average during one turbine cycle, and vice versa. The equivalent term in Eq. 5.9 is $\langle C_{P_{S,\theta}} \rangle$. It is positive when a net

amount of power is transferred from the heave motion to the pitch motion. When the foil motions are periodic, these two power coefficients are equal in absolute value but with opposite signs (Veilleux, 2014):

$$\langle C_{P_{S,h}} \rangle = -\langle C_{P_{S,\theta}} \rangle \, . \tag{5.21}$$

Furthermore, the power coefficients involving m_h^*, I_θ^*, k_h^* and k_θ^* are equal to zero under such periodic conditions because these terms are conservative (Veilleux, 2014). The power balance equations (Eqs. 5.8 and 5.9) therefore simplify to:

$$\langle C_{P_h} \rangle + \langle C_{P_\theta} \rangle + \langle C_{P_{D_{h,\mathrm{v}}}} \rangle + \langle C_{P_{D_\theta}} \rangle = \langle C_{P_{D_{h,\mathrm{e}}}} \rangle \, , \tag{5.22}$$

when the heave and pitch motions are periodic at the same frequency. This equation states that, in this context, the power available to the electric generator is equal to the sum of the power extracted from the flow through the heave and pitch degrees of freedom, which we refer to as the hydrodynamic power coefficient:

$$\langle C_{P_{\mathrm{hydro}}} \rangle = \langle C_{P_h} \rangle + \langle C_{P_\theta} \rangle \, , \tag{5.23}$$

minus the losses due to friction since $\langle C_{P_{D_{h,\mathrm{v}}}} \rangle$ and $\langle C_{P_{D_\theta}} \rangle$ are necessarily negative. Even though the motions of a fully-passive flapping foil can be periodic (Boudreau et al., 2018; Peng and Zhu, 2009; Veilleux and Dumas, 2017; Wang et al., 2017), other types of responses are also possible. Consequently, $\langle C_{P_{D_{h,\mathrm{e}}}} \rangle$ is computed using the more general Eq. 5.8 throughout this study.

The efficiency, which represents the fraction of the total hydrokinetic power available to the turbine which is actually provided to the electric generator, is defined as:

$$\eta = \frac{\left(\langle C_{P_{D_{h,\mathrm{e}}}} \rangle \right) c}{d} \, , \tag{5.24}$$

where d is the overall transverse extent of the foil motion, i.e., the distance between the maximum and minimum positions reached by any point on the foil surface in the heave direction during one foil oscillation. Note that this definition slightly differs from another definition that is often used in the literature, especially for fully-constrained turbines, that is based on the power extracted from the flow rather than the power available to the electric generator:

$$\eta_{\mathrm{hydro}} = \frac{\langle C_{P_{\mathrm{hydro}}} \rangle \, c}{d} \, . \tag{5.25}$$

We refer to this efficiency as the hydrodynamic efficiency. When the friction is neglected and the motions are periodic, Eqs. 5.24 and 5.25 are equivalent (see Eq. 5.22) and both efficiencies are the same.

In addition to the power coefficients and the efficiency, a few other metrics are also of interest to characterize the turbine performance for a specific turbine cycle, such as the heave and pitch amplitudes (H_0^* and Θ_0), the phase lag between the heave and the pitch motion (ϕ) and the reduced frequency (f^*). These metrics are defined as:

$$H_0^* = \frac{h_{\max} - h_{\min}}{2\,c} \, , \tag{5.26}$$

$$\Theta_0 = \frac{\theta_{\max} - \theta_{\min}}{2} \,, \tag{5.27}$$

$$\phi = \frac{360}{T} \left(t_{\theta_{\max}} - t_{h_{\max}} \right) \quad \text{[degrees]} \,, \tag{5.28}$$

$$f^* = \frac{f\,c}{U_\infty} \,, \tag{5.29}$$

where $h_{\max}$, $h_{\min}$, $\theta_{\max}$ and $\theta_{\min}$ are the maximum and minimum heave positions and pitch angles reached during one specific cycle, $t_{\theta_{\max}}$ and $t_{h_{\max}}$ are the instants at which the maximum pitch angle and heave position are reached and f is the frequency of the foil motions. Note that for all the operating points considered in this study, the foil oscillates at the same reduced frequency in heave and in pitch ($f_h^* = f_\theta^*$) and we use the variable f^* to denote this common reduced frequency.

Although it does not directly affect the turbine dynamics since the pitch axis is restricted to move only in the heave direction, the streamwise force coefficient (C_x) is another useful metric to characterize the turbine performance:

$$C_x = \frac{F_x}{0.5\,\rho\,U_\infty^2\,b\,c} \,, \tag{5.30}$$

where F_x is the streamwise component of the hydrodynamic force acting on the foil.

The time-averaged values presented in this work are computed by taking the average of cycle-averaged quantities over a sufficient number of complete turbine cycles to obtain converged values. Note that this averaging process only starts after a permanent response is reached following the initial transient period. For example, the time-averaged efficiency is computed as:

$$\overline{\eta} = \frac{1}{N_{\text{end}} - N_{\text{start}} + 1} \sum_{j=N_{\text{start}}}^{N_{\text{end}}} \eta_j \,, \tag{5.31}$$

where the subscript j stands for the j^{th} cycle, N_{start} is the cycle number at which the averaging process begins, N_{end} is the total number of completed cycles for a given simulation and η_j is the efficiency of the j^{th} cycle. The standard deviation is computed using the same procedure:

$$\sigma_\eta = \sqrt{\frac{1}{N_{\text{end}} - N_{\text{start}}} \sum_{j=N_{\text{start}}}^{N_{\text{end}}} (\eta_j - \overline{\eta})^2} \,. \tag{5.32}$$

When error bars are drawn in the figures of the present study, they indicate the standard deviation of a specific metric. For the sake of clarity, they are only shown when the standard deviation exceeds 0.01 for $\overline{\eta}$ and $\overline{\eta_{\text{hydro}}}$, 0.05 for $\overline{C_{P_{D_{h,\text{e}}}}}$ and $\overline{C_{P_{\text{hydro}}}}$, 0.02 for $\overline{H_0^*}$ and 1° for $\overline{\Theta_0}$ and $\overline{\phi}$. The same convention is used throughout this work.

5.4.3 Numerics

Fluid and solid solvers

The numerical methodology used to carry out the current study closely follows the approach used to perform our previous investigations of the semi-passive flapping-foil turbine (Boudreau et al.,

2019b,a). Siemens' STAR-CCM+® software is used as the fluid solver to conduct two-dimensional incompressible Unsteady Reynolds-Averaged Navier-Stokes (URANS) simulations with the Spalart-Allmaras one-equation turbulence model with rotation correction (Dacles-Mariani et al., 1995, 1999; Spalart and Allmaras, 1994). Second-order schemes are used and the SIMPLE algorithm handles the pressure-velocity coupling (Ferziger and Perić, 2002).

A solid solver is coupled to the fluid solver and solves the equations of motion that govern the turbine dynamics, namely Eqs. 5.2 and 5.3. This fluid-solid algorithm is actually a two-degree-of-freedom (2-DOF) version of the 1-DOF fluid-solid coupling algorithm presented by Boudreau et al. (2019b) and follows the work of Olivier and Paré-Lambert (2019). Eqs. 5.2 and 5.3 are discretized as:

$$R_y^n = m_h \ddot{h}^n + S\left(\ddot{\theta}^n \cos\theta^n - \dot{\theta}^{n^2} \sin\theta^n\right) + D_h \dot{h}^n + k_h h^n - F_y^n \,, \tag{5.33}$$

$$R_\theta^n = I_\theta \ddot{\theta}^n + S\ddot{h}^n \cos(\theta^n) + D_\theta \dot{\theta}^n + k_\theta \theta^n - M^n \,, \tag{5.34}$$

with:

$$\ddot{h}^n = c_1 \dot{h}^n + c_2 \dot{h}^{n-1} + c_3 \dot{h}^{n-2} \,, \tag{5.35}$$

$$\dot{h}^n = c_1 h^n + c_2 h^{n-1} + c_3 h^{n-2} \,, \tag{5.36}$$

$$\ddot{\theta}^n = c_1 \dot{\theta}^n + c_2 \dot{\theta}^{n-1} + c_3 \dot{\theta}^{n-2} \,, \tag{5.37}$$

$$\dot{\theta}^n = c_1 \theta^n + c_2 \theta^{n-1} + c_3 \theta^{n-2} \,. \tag{5.38}$$

R_y and R_θ are the residuals of the discretized versions of the equations of motion. The superscript n denotes the current time step being solved, and thus the superscripts $n-1$ and $n-2$ denote the two previous time steps. c_1, c_2 and c_3 are the constants of the numerical scheme used for the temporal discretization, namely a second-order backward difference scheme to match the numerical scheme used by the fluid solver. These constants are therefore equal to:

$$c_1 = \frac{3}{2\Delta t} \,, \qquad c_2 = \frac{-4}{2\Delta t} \,, \qquad c_3 = \frac{1}{2\Delta t} \,, \tag{5.39}$$

where Δt is the time step.

The position of the foil in heave along with its pitch angle for a given time step (h^n and θ^n) are determined by finding the roots of the functions on the right hand side of Eqs 5.33 and 5.34, with h^n and θ^n as the independent variables, in order to minimize the absolute values of the residuals R_y^n and R_θ^n. In the 2-DOF version of the fluid-solid coupling algorithm used to perform the present study, the Broyden's method achieves this task. The procedure is summarized in Appendix 5.A.

Since the formulation of the fluid-solid coupling algorithm is implicit, the residuals of the discretized equations of motion for the n^{th} time step (R_y^n and R_θ^n) depend on the heave position and the pitch angle at this same time step (h^n and θ^n). As a result, h^n and θ^n have to be updated a few times within a given time step in order to determine converged values for this specific time step. We refer to these iterations as outer loops in Appendix 5.A and they are indicated with subscripts. During each outer

loop, and thus for each intermediate values of h^n and θ^n, iterations of the fluid solver are carried out to determine converged values of F_y and M for a specific foil position. The values of F_y and M are considered to be converged when the differences, in absolute values, between the values of the transverse force coefficient (C_{F_y}) and the moment coefficient (C_M), obtained from two successive fluid iterations, both fall below 10^{-5}. Regarding the values of h^n and θ^n, they are considered to be converged when the differences between the values determined from the last two outer loops, in absolute values and normalized with the chord length for the heave position and $\pi/2$ for the pitch angle, fall below 10^{-8}. Four outer loops are typically required. Before incrementing the time step and starting the whole process over again, some additional fluid iterations are performed to ensure that the fluid residuals for the pressure, the streamwise and transverse momentums and the turbulent viscosity at least drop by a factor of 10^{-4}, for the first three residuals, and 5×10^{-4}, for the residual of the turbulent viscosity, within a given time step.

Both the 1-DOF and the 2-DOF versions of this fluid-solid coupling algorithm have been validated in the work of Boudreau et al. (2019b) by comparing the results obtained with the present methodology to benchmark cases available in the literature.

Computational domain, initial conditions and boundary conditions

The computational domain, the mesh and the boundary conditions used to perform the present work are the same as the one used by Boudreau et al. (2019b,a). More specifically, the computational domain consists in a square of 100 chord lengths by 100 chord lengths with the foil located at the center. The overset mesh technique is used to handle the foil motions so that two different meshes are used: one for the moving foil region and one for the background region. The mesh of the moving foil region consists in a structured mesh composed of rectangular cells while the background mesh is composed of hexagonal cells. The size of the first layer of cell at the foil surface results in a dimensionless normal wall distance (y^+) around unity and about 500 nodes around the foil. The growth factor in the normal direction near the foil surface is kept below 1.2. This leads to a mesh composed of 78 614 cells.

A uniform and constant velocity is set at the inlet boundary condition along with a modified turbulent viscosity ratio of three ($\tilde{\nu}/\nu = 3$), based on the recommendation of Spalart and Rumsey (2007) to ensure that the Spalart-Allmaras turbulence model functions in its fully-turbulent mode. An empirical relation relates the modified turbulent viscosity to the turbulent viscosity (Spalart et al., 1997). At the outlet boundary, a pressure of zero is imposed and symmetry conditions are used for the two remaining lateral boundaries. For the initial condition, the values of the velocity and the turbulent viscosity ratio at the inlet boundary and the value of the pressure at the outlet are used throughout the computational domain. Regarding the foil, it starts with nonzero heave velocity and pitch angle to reduce the duration of the transient period preceding the permanent response. More specifically, $h^* = 0$, $\dot{h}^* = -1.25$, $\theta = 1.5$ and $\dot{\theta}^* = 0$ at the start of the simulations. Some additional tests with different initial conditions have been carried out to make sure that the results are not influenced by the

choice of these initial conditions.

For all the simulations considered in the present study, the time step is set to 0.005 convective time units:

$$\frac{\Delta t\, U_\infty}{c} = 0.005\ , \tag{5.40}$$

which results in roughly 1 000 time steps per cycle since f^* remains close to 0.2 for the vast majority of the cases considered in this study. However, a larger time step corresponding to 0.03 convective time units is used during the initial transient period in order to reduce the computational costs of the simulations. The switch between the two time step sizes occurs after completing 150 convective time units, which corresponds to about 30 turbine cycles when $f^* = 0.2$. In order to deal with this variable time step size, the definitions of the constants c_1, c_2 and c_3 appearing in Eqs. 5.35 to 5.38 that have been implemented in the fluid-solid coupling algorithm slightly differ from the definitions presented in Eq. 5.39. Nevertheless, the definitions implemented in the fluid-solid coupling algorithm simplify to those presented in Eq. 5.39 when the time step remains constant, which is the case for the whole duration of the simulations except for the precise instant at which the time step size is changed. Note also that only the data obtained after completing a minimum of 200 convective time units is considered for the analysis of the results in order to avoid being affected by the larger time step used during the initial transient period.

Lastly, the independence of the results to the spatial and temporal resolutions levels used for the current work have already been verified in the study of Boudreau et al. (2019b).

5.5 Results and discussion

5.5.1 Parametric study

In this section, the effects of varying the heave damping and heave stiffness coefficients are investigated. The values of the structural parameters affecting the dynamics of the pitch motion are selected based on previous studies on a semi-passive flapping-foil turbine with a passive pitch motion (Boudreau et al., 2019b,a). More specifically, I^*_θ and k^*_θ are respectively set to 2 and 3.16. No viscous friction is considered in heave and in pitch so that $D_{h,\mathrm{v}} = 0$ and $D^*_\theta = 0$. The dimensionless heaving mass is set to the same value as the dimensionless moment of inertia, i.e., $m^*_h = 2$. Lastly, two different values of S^* are tested, namely 0.40 and 0.65.

The values of the heave damping and heave stiffness coefficients required to maximize the energy extraction from the flow are estimated by using the reverse solver technique presented by Veilleux and Dumas (2017) and used by Boudreau et al. (2019a). Based on the simulation results of optimal semi-passive flapping-foil turbine cases reported by Boudreau et al. (2019b), these structural parameters are initially set to $D^*_h = 0.5$ and $k^*_h = 1.75$, with $S^* = 0.40$, and to $D^*_h = 0.75$ and $k^*_h = 1.15$, with $S^* = 0.65$. D^*_h and k^*_h are then varied around these initial values.

The results are presented in Figs. 5.1 and 5.2. Note that the cases for which the standard deviation of the efficiency exceeds 5% are omitted when creating the contour plots. Such large variations of the efficiency prevent these cases from being potential turbine candidates. The corresponding areas in Fig. 5.2 are colored in gray and the markers denoting these cases are colored in black.

A maximum efficiency of 45.4% has been reported by Boudreau et al. (2019b) for a semi-passive flapping-foil turbine with a passive pitch motion characterized by $S^* = 0.65$ and the same values of I^*_θ, D^*_θ and k^*_θ as the ones used in the present section. The current results show that even higher efficiencies, up to 51.0%, are reached with the fully-passive concept. Such a good performance is achieved when the heave amplitude is of the order of one chord length, the pitch amplitude is approximately between 70° and 95°, the phase lag between the heave and the pitch motions ranges between 95° and 110° and the reduced frequency of the motions is around 0.2, in agreement with several previous studies on flapping-foil turbines (Boudreau et al., 2018, 2019b,a; Kinsey and Dumas, 2014; Young et al., 2014; Xiao and Zhu, 2014). The contours of the reduced frequency are not shown in Figs. 5.1 and 5.2 because it is essentially unaffected by the variations of D^*_h and k^*_h over the ranges of values tested. Indeed, f^* varies between 0.195 and 0.205, with $S^* = 0.40$, and between 0.200 and 0.205 with $S^* = 0.65$. In fact, the frequency of the heave and pitch motions closely follows the pitch natural frequency in vacuum:

$$f^*_{n,\theta} = \frac{1}{2\pi}\sqrt{\frac{k^*_\theta}{I^*_\theta}}\,, \tag{5.41}$$

which is equal to 0.2 for all the cases considered in this section. This aspect is further discussed in Sec. 5.5.2.

It is found that the heave and pitch amplitudes are mainly affected by D^*_h, while the phase lag between the heave and the pitch motions is more affected by k^*_h. The decrease of the heave and pitch amplitudes as D^*_h is increased is responsible for the greater sensitivity of $\overline{C_{P_{D_{h,\mathrm{e}}}}}$ to D^*_h than $\overline{\eta}$. The maximum values of $\overline{C_{P_{D_{h,\mathrm{e}}}}}$ are obtained with smaller values of D^*_h than the maximum values of $\overline{\eta}$. Similar observations were made by Boudreau et al. (2018) regarding their experiments on a fully-passive flapping-foil turbine prototype characterized by significantly different structural parameter values.

Even though the topologies are similar for both values of the static moment, some differences are observed between the cases with $S^* = 0.40$ and the ones with $S^* = 0.65$. For example, the maximum efficiency obtained with $S^* = 0.40$ ($\overline{\eta} = 44.6\%$) is smaller than the maximum efficiency obtained with $S^* = 0.65$ ($\overline{\eta} = 51.0\%$), in agreement with previous results obtained with a semi-passive flapping-foil turbine with a passive pitch motion (Boudreau et al., 2019b). Despite this fact, the maximum power coefficient available for an electric generator, $\overline{C_{P_{D_{h,\mathrm{e}}}}}$, is larger with $S^* = 0.40$ ($\overline{C_{P_{D_{h,\mathrm{e}}}}} = 1.97$) than with $S^* = 0.65$ ($\overline{C_{P_{D_{h,\mathrm{e}}}}} = 1.49$). This is because the heave amplitude reaches much larger values with $S^* = 0.40$, namely up to 2.22 chord lengths for the operating point with the maximum value of $\overline{C_{P_{D_{h,\mathrm{e}}}}}$, compared to a maximum of 1.23 chord lengths with $S^* = 0.65$. A compromise in terms of efficiency in favor of a larger power coefficient at the generator may be of practical interest in a context where the energy resource and the space available for the turbine are not limiting factors. The characteristics of

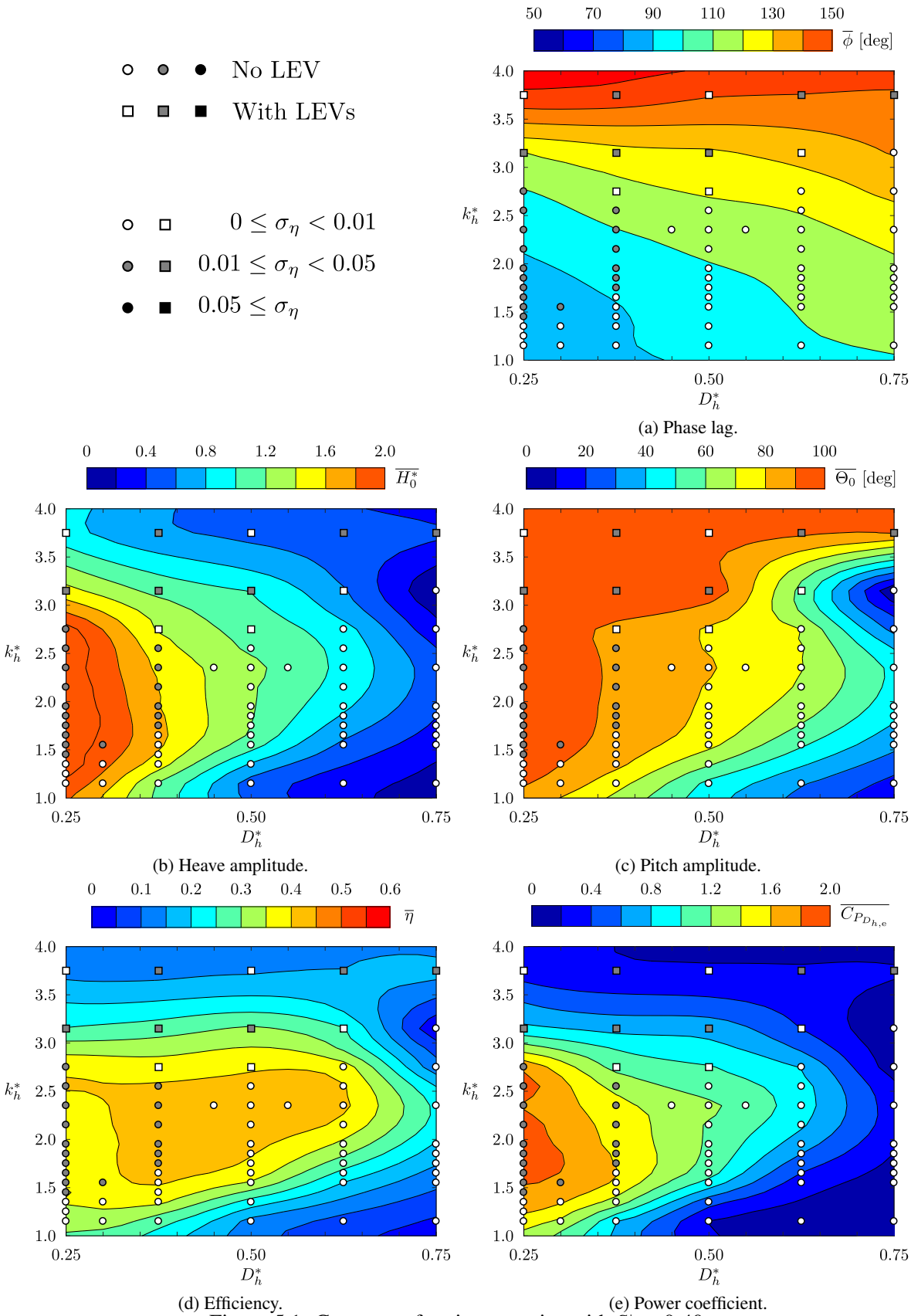

(a) Phase lag.

(b) Heave amplitude.

(c) Pitch amplitude.

(d) Efficiency.

(e) Power coefficient.

Figure 5.1: Contours of various metrics with $S^* = 0.40$.

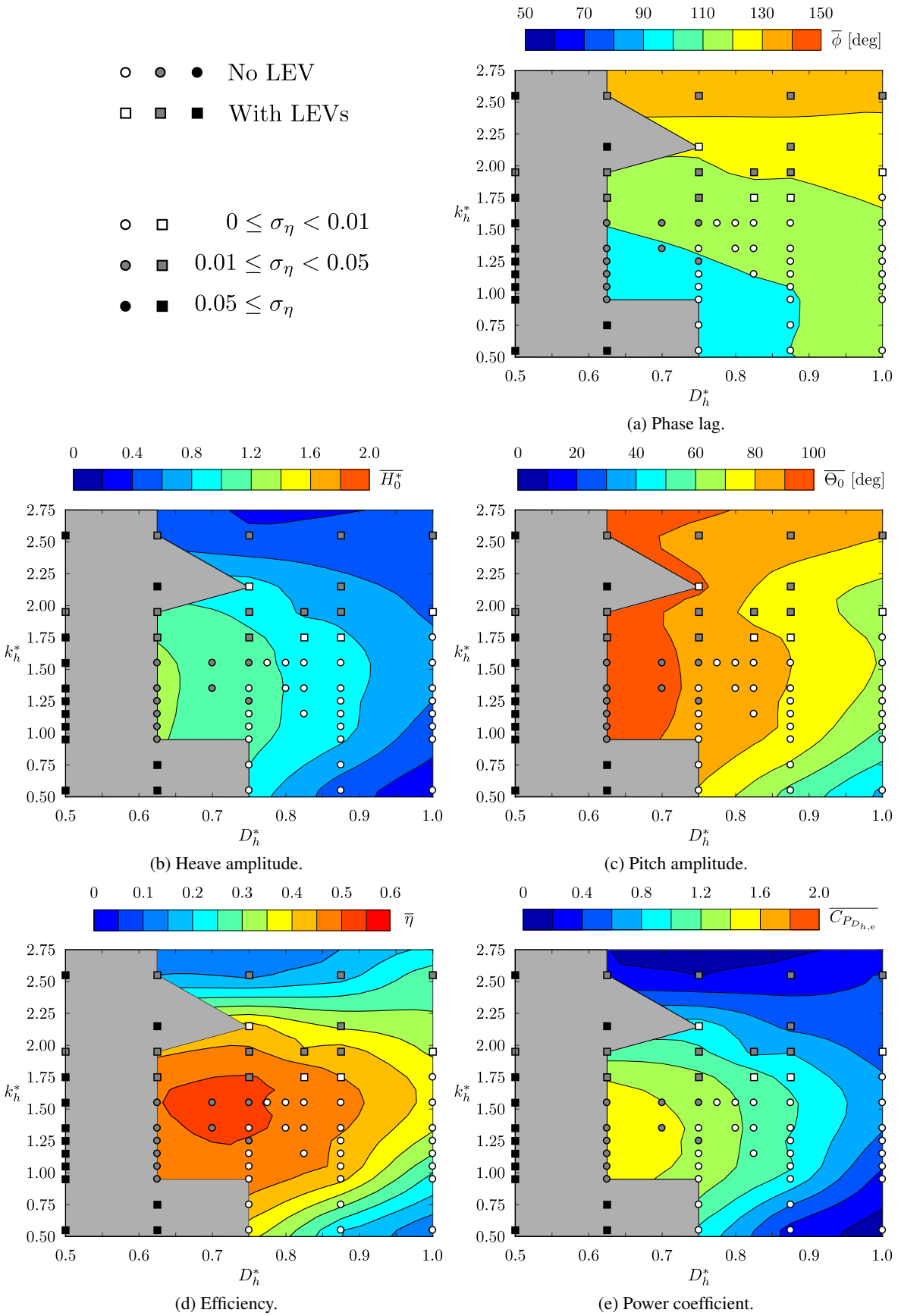

(a) Phase lag.

(b) Heave amplitude.

(c) Pitch amplitude.

(d) Efficiency.

(e) Power coefficient.

Figure 5.2: Contours of various metrics with $S^* = 0.65$. The gray areas indicate zones where the data is not presented because of the large variations occurring from cycle to cycle ($\sigma_\eta \geq 0.05$).

the cases achieving the maximum values of $\overline{\eta}$ and $\overline{C_{P_{D_{h,e}}}}$ in the present section are given in Tables 5.1 and 5.2, respectively, and the time evolutions of the dimensionless vorticity field for these two cases are shown in Fig. 5.3 over one turbine cycle.

Table 5.1: Characteristics of the cases achieving the best efficiency in Figs. 5.1 and 5.2.

Parameters	**Values**	**Parameters**	**Values**
Prescribed parameters		*Results*	
x_p/c	0.25	$\overline{H_0^*}$	1.14
m_h^*	2	$\overline{\Theta_0}$	91.3°
D_h^*	0.70	$\overline{\phi}$	101.7°
k_h^*	1.55	$\overline{\eta}$	51.0%
S^*	0.65	$\overline{C_{P_{D_{h,e}}}}$	1.41
I_θ^*	2	$\overline{C_x}$	3.69
D_θ^*	0	σ_η	0.015
k_θ^*	3.16		

Table 5.2: Characteristics of the cases achieving the best power coefficient at the generator in Figs. 5.1 and 5.2.

Parameters	**Values**	**Parameters**	**Values**
Prescribed parameters		*Results*	
x_p/c	0.25	$\overline{H_0^*}$	2.22
m_h^*	2	$\overline{\Theta_0}$	97.4°
D_h^*	0.25	$\overline{\phi}$	86.4°
k_h^*	1.85	$\overline{\eta}$	38.4%
S^*	0.40	$\overline{C_{P_{D_{h,e}}}}$	1.97
I_θ^*	2	$\overline{C_x}$	6.35
D_θ^*	0	σ_η	0.033
k_θ^*	3.16		

The vast majority of the semi-passive cases with high efficiencies reported by Boudreau et al. (2019b,a) are characterized by very regular and periodic motions from cycle to cycle, with a standard deviation of the efficiency below 1%. The motions of the most efficient fully-passive cases are also notably

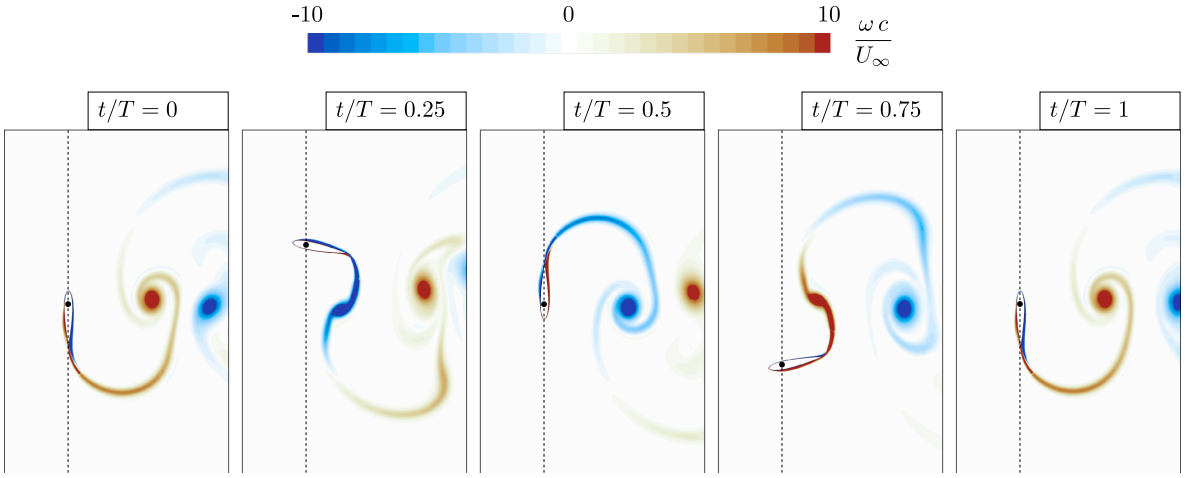

(a) Case with $\overline{\eta} = 51.0\%$.

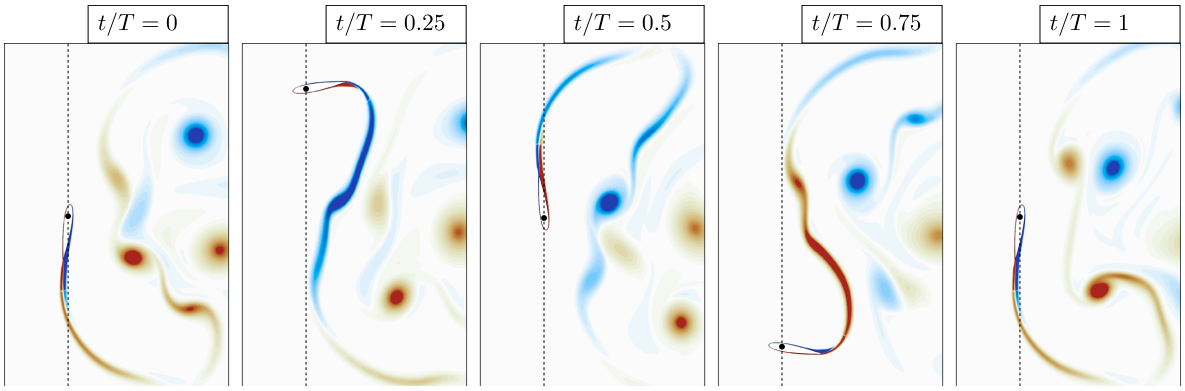

(b) Case with $\overline{C_{P_{h,e}}} = 1.97$.

Figure 5.3: Time evolution of the dimensionless vorticity field ($\omega c/U_\infty$) during one complete representative foil oscillation for the operating points achieving the best efficiency (a) and the best power coefficient at the generator (b) among the cases presented in Figs. 5.1 and 5.2. See Tables 5.1 and 5.2 for the values of the structural parameters characterizing these two cases. The dashed lines indicate the streamwise position of the pitch axis, which is itself indicated with a black dot. The instant $t/T = 0$ in these two figures corresponds to an instant at which $h = 0$ and $\dot{h} > 0$.

periodic, although the standard deviation of the efficiency is slightly higher, with values exceeding 1% for several cases (see the gray markers in Figs. 5.1 and 5.2). Nevertheless, the standard deviation of the efficiency remains below 2.5% for all the cases having an efficiency above 45%.

No leading-edge vortices (LEVs) are formed for the majority of the most efficient cases (see the circular markers in Figs. 5.1 and 5.2), unlike what was observed experimentally at a lower Reynolds number by Boudreau et al. (2018). In their case, the maximum efficiency was however much smaller ($\overline{\eta} \approx 30\%$). Even though high efficiencies have been achieved for cases with LEVs, they are generally associated to considerable variations of the motions from cycle to cycle (see the gray and black square markers in Figs. 5.1 and 5.2), as previously discussed by Boudreau et al. (2019b). Consequently, cases with LEVs are less suitable for a turbine application.

The formation and ejection of LEVs is not the sole mechanism that can cause significant cycle-to-cycle variations of the foil motions. Indeed, several cases without LEVs still have a standard deviation of the efficiency exceeding 1% (see the gray circular markers in Figs. 5.1 and 5.2). For such cases, the periodicity of the motions is impaired by the interaction of the foil with its own wake. The slower the wake is convected with respect to the foil motions, the stronger is the interaction between the forces acting on the foil and the wake flow field, and thus, the larger the cycle-to-cycle variations are expected to be. Since the frequency of the motion essentially remains the same for all the operating points considered in Figs. 5.1 and 5.2, the strength of the interaction between the foil and its wake depends on the wake velocity, which itself depends on the streamwise force component acting on the foil. The cycle-to-cycle variations are thus expected to be larger for cases with larger time-averaged streamwise force coefficients ($\overline{C_x}$). For example, the case achieving the largest value of $\overline{C_{P_{D_{h,e}}}}$ is characterized by $\overline{C_x} = 6.35$ and $\sigma_\eta = 0.033$ compared to $\overline{C_x} = 3.69$ and $\sigma_\eta = 0.015$ for the case achieving the largest value of $\overline{\eta}$. The wake patterns of these two cases can be observed in Fig. 5.3. One can notice that the negative vortex (blue vortex) generated around $t/T = 0.25$ has not traveled as far downstream at $t/T = 1$ in Fig. 5.3b than in Fig. 5.3a. Its influence on the hydrodynamic force and moment on the foil at $t/T = 1$ is therefore more important for the case achieving the largest value of $\overline{C_{P_{D_{h,e}}}}$, which is characterized by a larger standard deviation of the efficiency.

The correlation between the standard deviation of the efficiency (σ_η) and the time-averaged streamwise force coefficient ($\overline{C_x}$) of all the cases considered in Figs. 5.1 and 5.2 is shown in Fig. 5.4. For the cases without LEV (see the circular markers), σ_η is found to remain very close to zero when $\overline{C_x}$ is below a threshold value of approximately three, and it then increases with $\overline{C_x}$ as this threshold value is exceeded. The standard deviation of the efficiency of the cases with LEVs (see the square markers) is not correlated with the streamwise force coefficient because the fluctuations of the motions result from the interaction of the foil with the LEVs and not with its wake in these cases. Note that these two mechanisms affecting the periodicity of the forces acting on the foil also exist in the case of fully-constrained flapping-foil turbines, as discussed by Kinsey and Dumas (2014). However, the motions of a fully-constrained turbines are not affected by the hydrodynamic forces and moment because they are prescribed.

As discussed by Boudreau et al. (2019b), optimal pitch motions generally require a power input on average to be maintained. In other words, $\overline{C_{P_\theta}} < 0$ for these cases. This is especially true in the absence of LEVs (Kinsey and Dumas, 2014) since the suction at the foil surface associated with the presence of LEVs can positively contribute to $\overline{C_{P_\theta}}$ (Veilleux and Dumas, 2017; Zhu and Peng, 2009). In the present study, all the cases appearing in Figs. 5.1 and 5.2 are characterized by a negative value of $\overline{C_{P_\theta}}$ and a positive value of $\overline{C_{P_h}}$. Since no actuator in pitch nor mechanical links coupling both degrees of freedom together are present in a fully-passive flapping-foil turbine, the power required by the pitch motion must necessarily be transferred from the heave motion to the pitch motion via the inertial coupling terms, i.e., the terms involving the static moment in Eqs. 5.6 and 5.7. With the pitch axis located at the quarter-chord point ($x_p/c = 0.25$) and the types of motions characterizing the cases

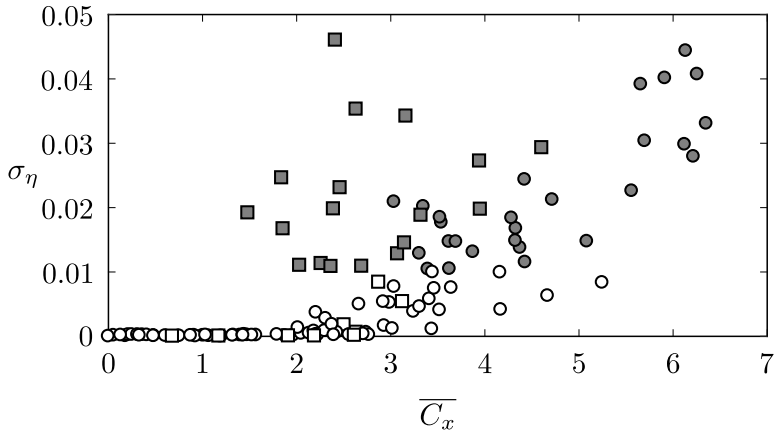

Figure 5.4: Correlation between the standard deviation of the efficiency and the time-averaged streamwise force coefficient. See Figs. 5.1 or 5.2 for the legend. The cases having a standard deviation of the efficiency exceeding 0.05 are not shown.

presented in Figs. 5.1 and 5.2, such a power transfer is only possible when $S^* > 0$. This implies that the center of mass has to be located downstream of the pitch axis.

Since the power transfer through the inertial coupling is proportional to the static moment (see Eqs. 5.12 and 5.18), a larger value of S^* allows for a more negative value of $\overline{C_{P_\theta}}$. It explains why the pitch amplitude is smaller for the optimal operating points with $S^* = 0.40$ than with $S^* = 0.65$. For example, $\overline{C_{P_\theta}} = -1.70$ and $\overline{\Theta_0} = 91.3°$, for the best efficiency point with $S^* = 0.65$, while $\overline{C_{P_\theta}} = -1.07$ and $\overline{\Theta_0} = 80.8°$, for the best efficiency point with $S^* = 0.40$.

5.5.2 Effective parameters

Heave dynamics

For all the cases considered in the previous section, m_h^* is kept constant and is equal to 2. The values of the heave stiffness coefficient (k_h^*) that result in an optimal performance in Fig. 5.2 ($k_h^* \approx 1.55$) are specific to this heaving mass value. Indeed, Fig. 5.5 shows that efficiencies comparable to the highest ones obtained with $m_h^* = 2$ can also be achieved with different values of m_h^*, but for significantly different values of k_h^*. Actually, the maximum efficiency obtained in the present study, namely 53.8%, is achieved when $m_h^* = 1$ and $k_h^* = 0$. The values of the other structural parameters characterizing all the cases analyzed in this section are presented in Table 5.3. The error bars indicate the standard deviation of the metric considered and they are only shown when the standard deviation exceeds the threshold values listed at the end of Sec. 5.4.2.

Changing the value of m_h^*, without adjusting any other parameter, results in a different equilibrium for the equation of motion in heave (Eq. 5.6), and thus a different turbine performance. However, a variation of m_h^* can be compensated by a variation of k_h^* when the heave motion is nearly sinusoidal.

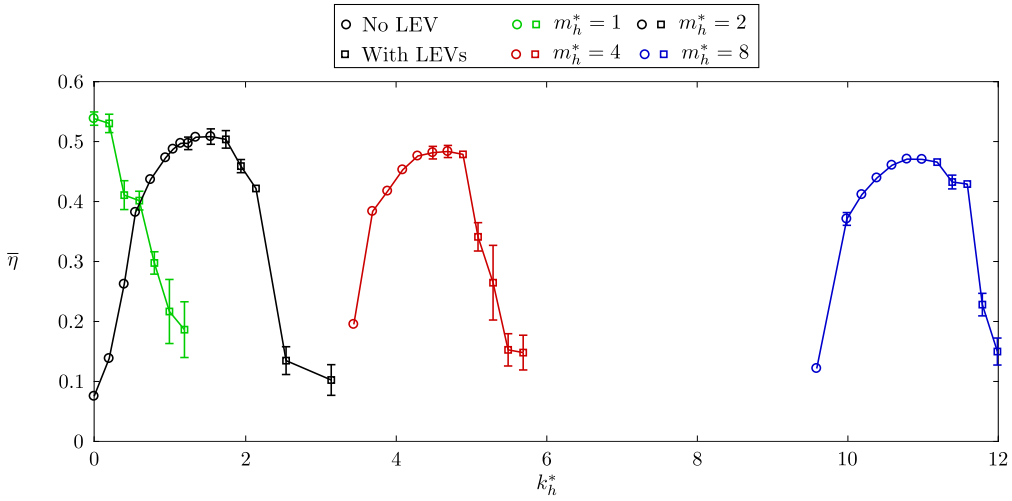

Figure 5.5: Efficiency as a function of the heave stiffness coefficient for various values of m_h^*.

Table 5.3: Values of the structural parameters that are kept constant to analyze the heave dynamics.

Parameters	**Values**
D_h^*	0.75
S^*	0.65
I_θ^*	2
D_θ^*	0
k_θ^*	3.16

Under such a condition, the heave position and acceleration can be roughly approximated as:

$$h(t) \approx H_0^* \sin(2\pi f^* t^*) \ , \tag{5.42}$$

$$\ddot{h}^*(t) \approx -(2\pi f^*)^2 H_0^* \sin(2\pi f^* t^*) \ , \tag{5.43}$$

where $t^* = t U_\infty / c$. Using these approximations, the inertial and stiffness terms appearing in Eq. 5.6 can be combined together into a single effective parameter:

$$m_h^* \ddot{h}^* + k_h^* h \approx \lambda_h^* h \ , \tag{5.44}$$

where:

$$\lambda_h^* = k_h^* - (2\pi f^*)^2 m_h^* \ . \tag{5.45}$$

We call λ_h^* the effective heave stiffness coefficient. This approach follows the ideas proposed by Shiels et al. (2001) and by Boudreau et al. (2019a) to analyze the dynamics of a cylinder undergoing vortex-induced vibrations (VIVs) and the pitch dynamics of a semi-passive flapping-foil turbine, respectively.

When plotting different metrics against the parameter λ_h^* introduced in Eq. 5.45, as is done in Fig. 5.6, instead of the parameter k_h^*, as is done in Fig. 5.5, one finds that the heave dynamics effectively depends on λ_h^*, the effective heave stiffness, rather than depending on two independent parameters, namely m_h^* and k_h^*. More specifically, the maximum amplitudes and efficiency are achieved around a specific value of $\lambda_h^* \approx -2$, regardless of the individual values of m_h^* and k_h^*. This implies that m_h^* and k_h^* can be scaled while preserving a similar dynamics, as long as λ_h^* and the other structural parameters listed in Table 5.3 are kept constant. This is demonstrated in Sec. 5.5.3.

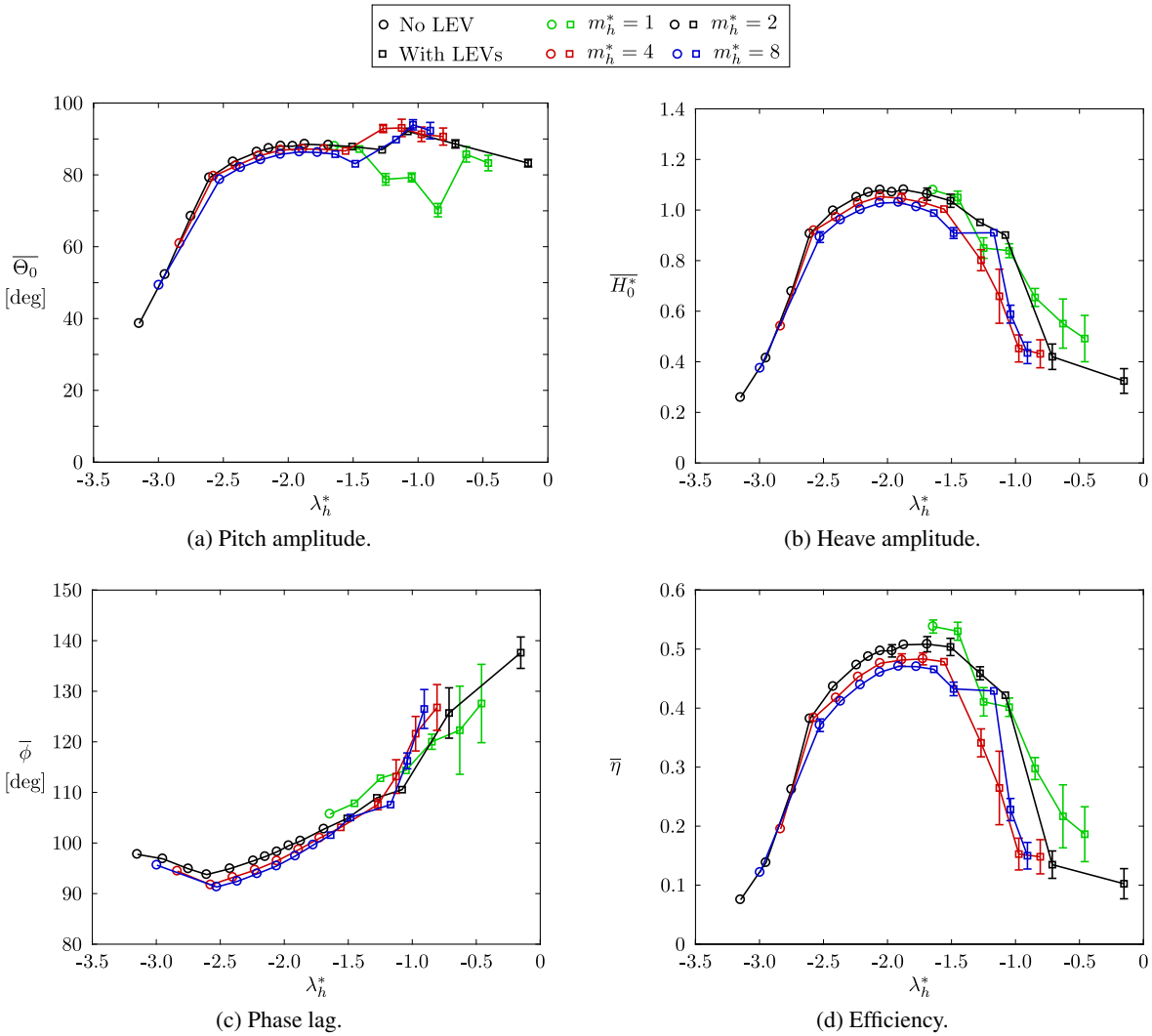

(a) Pitch amplitude.

(b) Heave amplitude.

(c) Phase lag.

(d) Efficiency.

Figure 5.6: Various metrics characterizing the foil dynamics as functions of λ_h^* for various values of m_h^*. See Table 5.3 for the values of the other structural parameters.

The data obtained with the different heaving mass values is more spread out when leading-edge vortices (LEVs) are formed and ejected from the foil surface. Nevertheless, we note that the irregularity of the foil motions and the smaller efficiency characterizing these cases make them less appropriate for a turbine application. For the cases without LEVs, the discrepancies between the results obtained with the different values of m_h are due to the fact that the heave motions are not pure sinusoidal mo-

tions. Therefore, the approximations given by Eqs. 5.42 and 5.43 are not exact. The less accurate these approximations are, the less the parameter λ_h^* is relevant and the more the inertial term and the stiffness term in Eq. 5.6 are independent from each other. Actually, the heave motion approaches a pure sinusoidal motion as m_h^* is increased, while it deviates from it as m_h^* approaches zero. Representative examples of the time evolutions of the heave position and acceleration over one complete foil oscillation are shown in Fig. 5.7. The heave acceleration is presented to emphasize the differences between the heave motions and a pure sinusoidal motion.

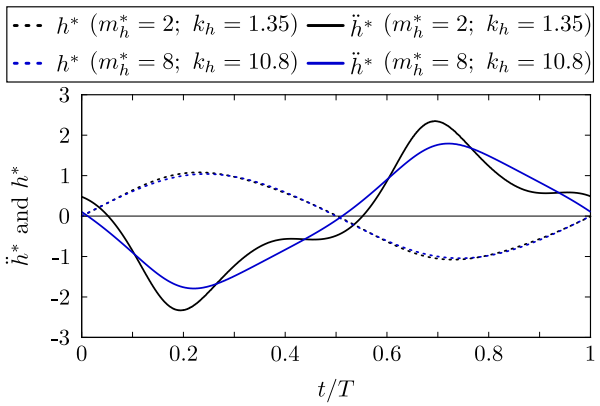

Figure 5.7: Time evolution of the dimensionless heave position (h^*) and acceleration ($\ddot{h}^*$) over one foil oscillation of period T for two different values of m_h^*.

As is the case in Sec. 5.5.1 when varying k_h^* and D_h^*, the frequency of the foil motions is essentially unaffected when the heaving mass is varied. It only differs from the pitch natural frequency, which is equal to 0.2, by less than 2.5% for all the cases presented in Fig. 5.6.

The fact that the heave and pitch amplitudes and the efficiency are maximized when λ_h^* is negative implies that the heave natural frequency in vacuum:

$$f_{n,h}^* = \frac{1}{2\pi}\sqrt{\frac{k_h^*}{m_h^*}}\,, \tag{5.46}$$

must be smaller than the frequency of the foil motion since Eq. 5.45 can also be written in the form:

$$\lambda_h^* = 4\,\pi^2\, m_h^* \left({f_{n,h}^*}^2 - {f^*}^2 \right)\,. \tag{5.47}$$

Based on this other form for the definition of λ_h^* and the fact that the heave dynamics essentially depends on this single effective parameter, it is not surprising to observe in Fig. 5.8 that the efficiency data do not collapse to a single curve when plotted against $f_{n,h}^*$ for different values of m_h^*. The same is true for the other characteristics of the foil motions, namely $\overline{H_0^*}$, $\overline{\Theta_0}$, $\overline{\phi}$. However, the next section demonstrates that this does not hold true regarding the pitch dynamics.

Pitch dynamics

In this section, I_θ^* and k_θ^* are varied while all the other structural parameters remain constant. The values of these fixed parameters are given in Table 5.4.

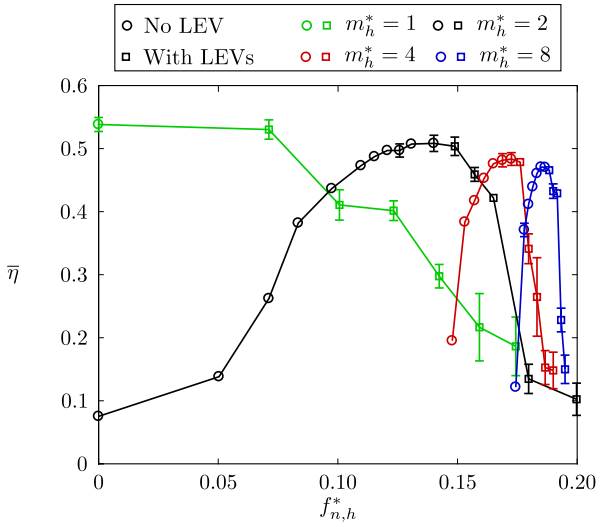

Figure 5.8: Efficiency as a function of the heave natural frequency for various values of m_h^*.

Table 5.4: Values of the structural parameters that are kept constant to analyze the pitch dynamics.

Parameters	**Values**
m_h^*	2
D_h^*	0.75
k_h^*	1.35
S^*	0.65
D_θ^*	0

The pitch motion is also similar to a sinusoidal motion and it approaches a pure sinusoid as I_θ^* increases, as shown in Fig. 5.9. The pitch angle and the pitch acceleration can therefore be approximated as:

$$\theta(t) \approx \Theta_0 \sin\left(2\pi f^* t^* - \phi\right) , \tag{5.48}$$

$$\ddot{\theta}^*(t) \approx -(2\pi f^*)^2 \Theta_0 \sin\left(2\pi f^* t^* - \phi\right) . \tag{5.49}$$

As a result, the inertial and stiffness terms appearing in Eq. 5.7 can be combined together into the following parameter:

$$I_\theta^* \ddot{\theta}^* + k_\theta^* \theta \approx \lambda_\theta^* \theta , \tag{5.50}$$

where:

$$\lambda_\theta^* = k_\theta^* - (2\pi f^*)^2 I_\theta^* , \tag{5.51}$$

which can also be written in the following form:

$$\lambda_\theta^* = 4\pi^2 I_\theta^* \left({f_{n,\theta}^*}^2 - f^{*2} \right) . \tag{5.52}$$

λ_θ^* actually corresponds to the effective pitch stiffness that was proposed by Boudreau et al. (2019a) in their study of a semi-passive flapping-foil turbine with a passive pitch motion and a prescribed heave motion.

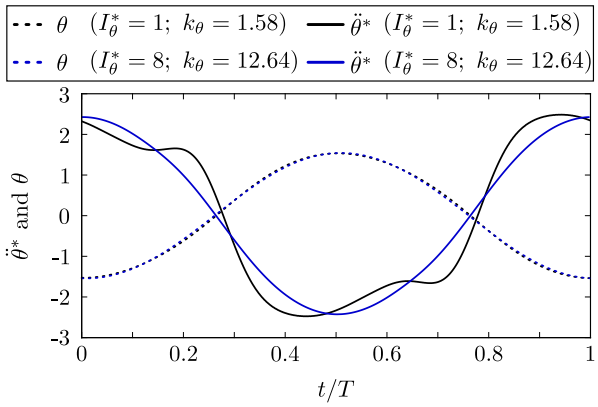

Figure 5.9: Time evolution of the pitch angle (θ) and the dimensionless pitch acceleration ($\ddot{\theta}^*$) over one foil oscillation of period T for two different values of I_θ^*. Note that θ is given in radians.

However, Fig. 5.10 shows that the frequency of the foil motions (f^*) is essentially dictated by the pitch natural frequency in vacuum ($f_{n,\theta}^*$), especially for the largest values of I_θ^*. f^* slightly deviates from $f_{n,\theta}^*$ as the moment of inertia decreases. This is because the surrounding fluid affects the pitch natural frequency, and its relative importance increases as I_θ^* and k_θ^* decrease. Nevertheless, f^* remains very close to $f_{n,\theta}^*$. Consequently, λ_θ^* approaches zero, no matter the values of I_θ^* and k_θ^*. The effective pitch stiffness (λ_θ^*) therefore becomes inappropriate to characterize the pitch dynamics.

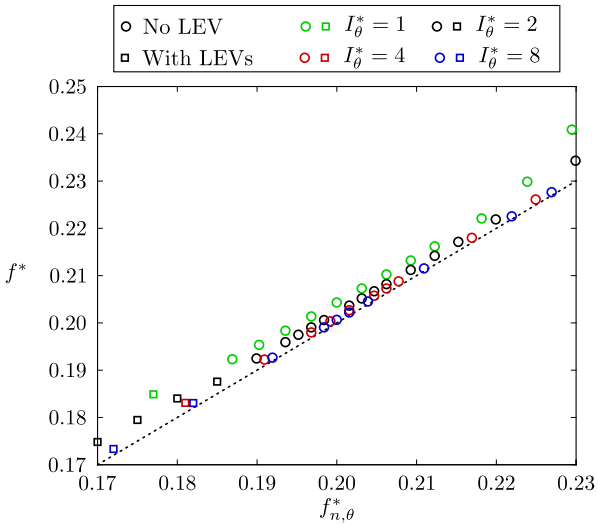

Figure 5.10: Frequency of the foil motions as a function of the pitch natural frequency for various values of I_θ^*. The dotted line corresponds to the value of the pitch natural frequency. See Table 5.4 for the values of the other structural parameters.

Besides, variations of I_θ^* and k_θ^* do not only affect the inertial and stiffness terms in the equation of

motion in pitch (Eq. 5.7), but also the moment coefficient and the inertial coupling term because of the resulting variations of the frequency of the foil motions. In other words, a specific balance between all the terms involved in the equation of motion in pitch is only expected to be maintained if the frequency of the foil motions remains the same. It therefore appears more logical to present the pitch dynamics as a function of the pitch natural frequency instead of λ_θ^*. This is shown in Fig. 5.11, which confirms that the pitch dynamics indeed depends on $f_{n,\theta}^*$ since the data essentially collapse to single functions of $f_{n,\theta}^*$ regardless of the value of I_θ^*.

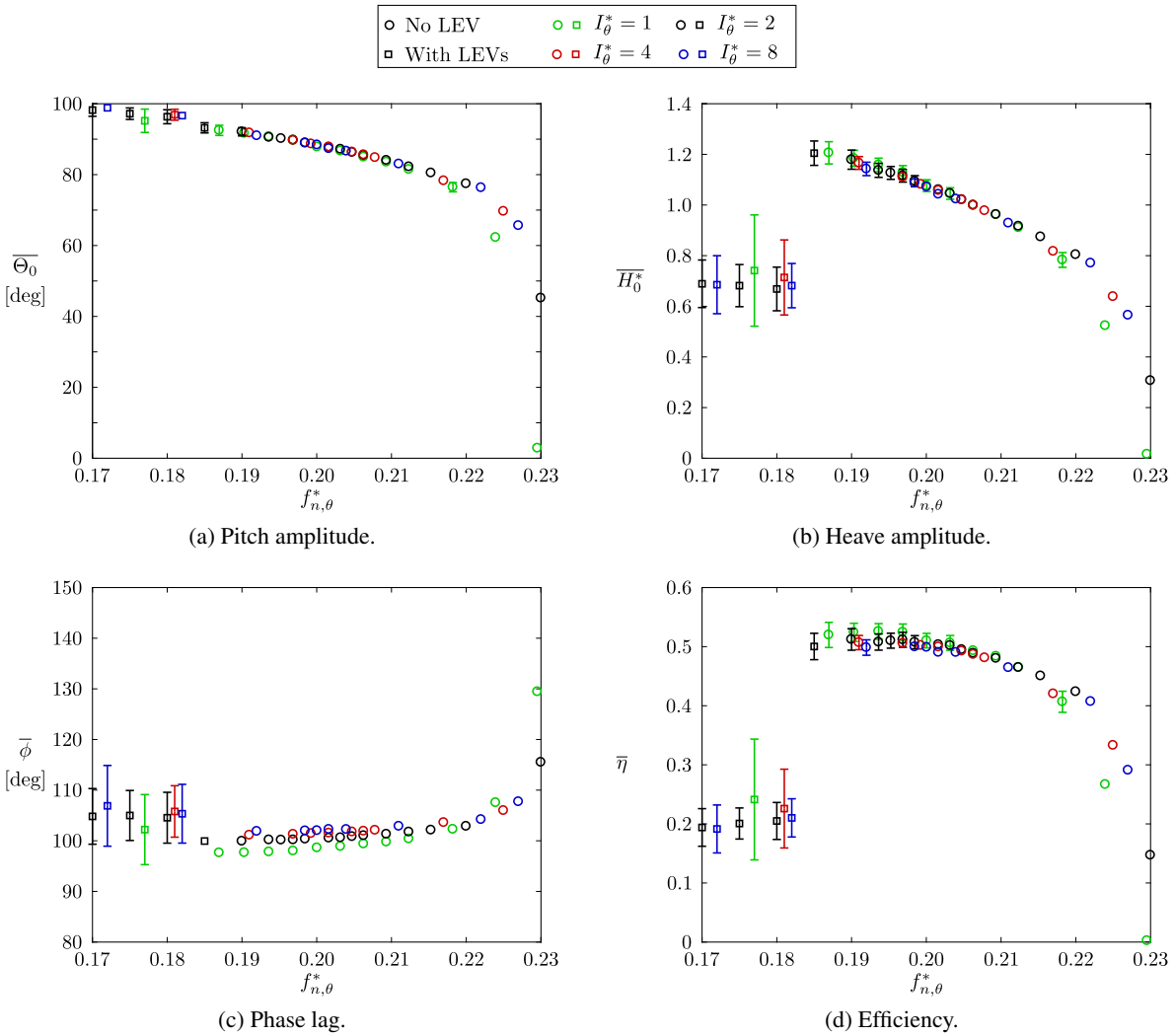

(a) Pitch amplitude.

(b) Heave amplitude.

(c) Phase lag.

(d) Efficiency.

Figure 5.11: Various metrics characterizing the foil dynamics as functions of the pitch natural frequency for various values of I_θ^*.

At first glance, this observation appears to contradict the conclusion drawn by Boudreau et al. (2019a) that the pitch dynamics depends on the effective pitch stiffnes coefficient (λ_θ^*) rather than $f_{n,\theta}^*$ for a semi-passive flapping-foil with a prescribed heave motion. The reason is that the frequency of the foil motions is dictated by the prescribed heave motion in the case of their semi-passive turbine, and is thus not influenced by I_θ^* and k_θ^*. This independence of the frequency to the inertial and stiffness

parameters is analogous to what is observed in heave in the present study.

5.5.3 Scaled inertial and stiffness properties

The designer of a real fully-passive flapping-foil turbine does not have a complete freedom regarding the values of m_h^* and I_θ^* due to several practical constraints, such as the obvious fact that the turbine structure must be able to withstand the forces at play. It is therefore valuable to have the possibility to properly scale the heave and pitch stiffness coefficients depending on the inertial properties of a specific turbine design. Since it is found that the frequency of the foil motions follows the pitch natural frequency, that it is not much influenced by m_h^* and k_h^* and that the heave dynamics is governed by the effective heave stiffness (λ_h^*), the values of k_h^* and k_θ^* required to maximize the turbine performance can be determined in advance for different sets of m_h^* and I_θ^* values.

Following this procedure, several simulations have been carried out by varying m_h^* from 1.018 to 50 and I_θ^* from 0.5 to 50. The analysis presented in the current section are conducted around a slightly different operating point than in the previous two sections. The static moment is still $S^* = 0.65$, but the heave damping coefficient is $D_h^* = 0.825$. Note that no LEVs are formed for any of the cases analyzed in the current section.

First, Fig. 5.12 shows the efficiency as a function of m_h^*. For each value of m_h^*, k_h^* is set so that $\lambda_h^* = -1.6$ by assuming a priori that the frequency of the foil motions will remain equal to the pitch natural frequency in vacuum, namely 0.2 for these cases. This procedure is similar to what a turbine designer would have to do in practice. All the other structural parameters are kept constant. Note that the smallest heaving mass considered ($m_h^* = 1.018$) corresponds to a case without heave spring ($k_h^* = 0$).

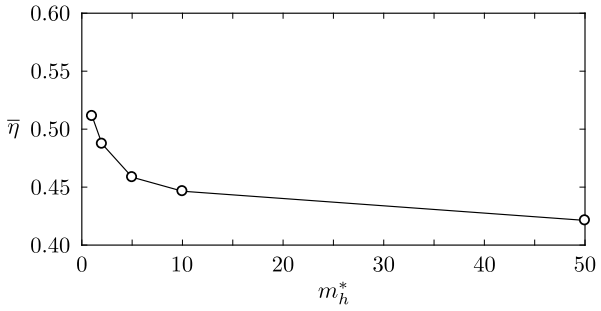

Figure 5.12: Efficiency as a function of the dimensionless heaving mass. The value of k_h^* is set to obtain $\lambda_h^* = -1.6$ by assuming that the frequency of the foil motions is equal to the pitch natural frequency ($f_{n,\theta}^* = 0.20$). The values of the other parameters are: $D_h^* = 0.825$; $S^* = 0.65$; $I_\theta^* = 2$; $D_\theta^* = 0$; $k_\theta^* = 3.16$.

It is found that the efficiency decreases as m_h^* is increased, in agreement with the results shown in Fig. 5.6d. Nevertheless, it still remains above 40% for all the values of m_h^* tested. As in Figs. 5.6a and 5.6b, the heave and pitch amplitudes also follow similar trends, i.e., they decrease with an increase of m_h^*. However, the frequency of the foil motions remains almost unchanged, as expected, with a

relative difference of only 2% between the case with the smallest heaving mass ($m_h^* = 1.018$) and the largest heaving mass ($m_h^* = 50$) tested.

The effect of varying I_θ^* and k_θ, while maintaining a pitch natural frequency of $f_{n,\theta}^* = 0.2$ and keeping all the other structural parameters constant, is shown in Fig. 5.13a for two different values of m_h^*. The variations of the efficiency are less pronounced when varying I_θ^* than when varying m_h^*, except when I_θ^* approaches zero. Indeed, the efficiency decreases by 7%, in relative difference, when I_θ^* is decreased from 1 to 0.5 with $m_h^* = 2$. This behavior is partly explained by the fact that the frequency deviates from the pitch natural frequency as I_θ^* approaches 0, as shown in Fig. 5.13b. As a result, the value of λ_h^* is not equal to -1.6, as desired, for such cases. For example, it is rather around -2 when $m_h^* = 2$ and $I_\theta = 0.5^*$. The increase of the frequency of the foil motions as I_θ^* is decreased is less pronounced when the heaving mass is larger, and thus the efficiency decrease is less important.

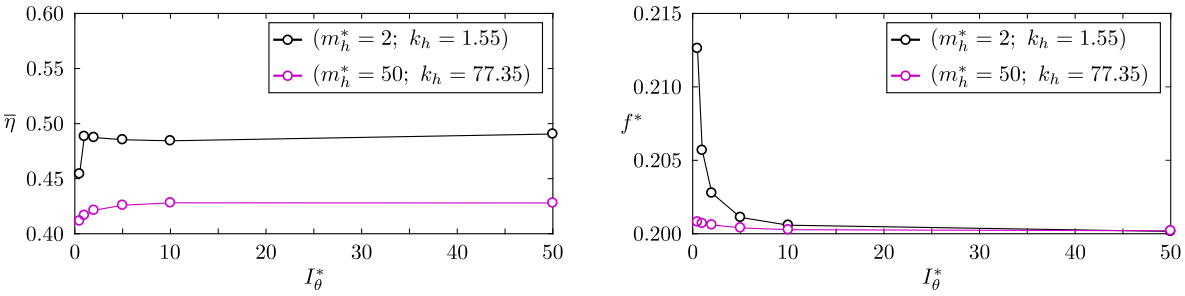

(a) Efficiency.

(b) Frequency of the foil motions.

Figure 5.13: Efficiency as a function of the dimensionless moment of inertia for two different values of m_h^* and k_h^*. The value of k_θ^* is set to obtain a pitch natural frequency of $f_{n,\theta}^* = 0.20$. The values of the other parameters are: $D_h^* = 0.825$; $S^* = 0.65$; $D_\theta^* = 0$.

Despite the different effects observed when varying m_h^* and I_θ^*, the current results still confirm that an optimal performance can be achieved over large ranges of m_h^* and I_θ^* values, provided that k_h^* and k_θ^* are adjusted adequately, thereby leaving a lot of flexibility to the designer of such devices.

The fully-passive flapping-foil turbine prototype designed and tested by Boudreau et al. (2018) consisted of a steel blade oscillating in water. It had a heaving mass of about $m_h^* = 3$ and a moment of inertia of about $I_\theta^* = 0.1$. The prototype was designed in order to minimize these values, while ensuring that it could withstand the forces generated by the fluid flow. It is therefore expected that smaller values of m_h^* and I_θ^* would be hard to reach in practice for a similar hydrokinetic turbine. In any case, the current results suggest that the dimensionless moment of inertia should exceed 0.5 to maximize the turbine performance, in agreement with the recommendation made by Boudreau et al. (2019a) for a semi-passive flapping-foil turbine with a passive pitch motion. The addition of a flywheel would therefore probably be required. Regarding the dimensionless heaving mass, the present work suggests that it should be kept to a minimum. The flywheel should therefore be designed to reach a sufficient value of I_θ^*, while also not resulting in a too large increase of m_h^*.

5.5.4 Impact of nonzero pitch damping

So far, an idealized frictionless turbine has been considered ($D^*_{h,\mathrm{v}} = 0$ and $D^*_\theta = 0$). Nevertheless, the effect of the heave damping coefficient has already been studied in Sec. 5.5.1. The presence of undesired viscous friction in heave ($D^*_{h,\mathrm{v}} \neq 0$) would not affect the foil dynamics if the total heave damping coefficient (D^*_h) remains constant. It would simply reduce the amount of power available for an electric generator since some power would be lost as heat. In this section, we investigate the effects of having a nonzero pitch damping coefficient. As discussed in Sec. 5.4.1, the energy dissipated in the pitch damper is considered to be unavailable for the electric generator and is therefore lost as heat. Note that no LEVs are formed for any of the cases analyzed in this section, no matter the value of D^*_θ. The large fluctuations occurring from cycle to cycle for some of the cases considered in this section rather stem from the interaction of the foil with its own wake, as discussed in Sec. 5.5.1.

One of the most efficient operating points presented in Fig. 5.2 with $S^* = 0.65$ is first selected to analyze the effects of D^*_θ, namely the case with $D^*_h = 0.75$ and $k^*_h = 1.35$. It is characterized by $\overline{\eta} = 50.7\%$ and $\overline{C_{P_{D_{h,\mathrm{e}}}}} = 1.36$ when $D^*_\theta = 0$. Fig. 5.14 shows that an increase of D^*_θ results in a linear decrease of the heave and pitch amplitudes up to $D^*_\theta = 0.04$. Beyond this critical pitch damping coefficient, the foil motions are completely damped even though large perturbations are used as the initial conditions, as mentioned in Sec. 5.4.3. Regarding the phase lag between the heave and the pitch motions ($\overline{\phi}$), it is not significantly affected by an increase of the pitch damping. It only increases by 2° when D^*_θ increases from 0 to 0.04.

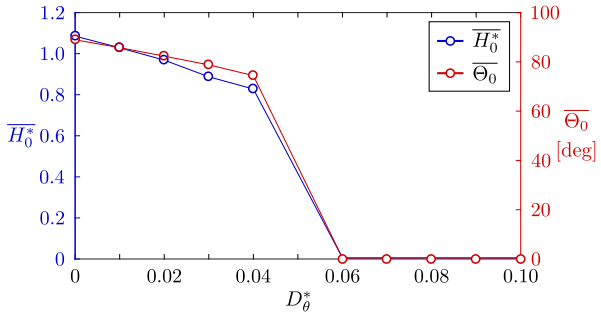

Figure 5.14: Heave and pitch amplitudes as functions of the dimensionless pitch damping coefficient. The values of the other parameters are: $m^*_h = 2$; $D^*_h = 0.75$; $k^*_h = 1.35$; $S^* = 0.65$; $I^*_\theta = 2$; $k^*_\theta = 3.16$.

The consequence of the heave and pitch amplitude decreases is that the hydrodynamic power coefficient ($\overline{C_{P_{\mathrm{hydro}}}}$) and the hydrodynamic efficiency ($\overline{\eta_{\mathrm{hydro}}}$), which measure the power extracted from the flow, decrease as D^*_θ increases. This is shown in Fig. 5.15. The fact that the differences between the values of $\overline{C_{P_{\mathrm{hydro}}}}$ and $\overline{C_{P_{D_{h,\mathrm{e}}}}}$ increase as D^*_θ increases implies that the amount of power lost as heat through the pitch damping increases linearly with D^*_θ, in spite of the reduction of the pitch amplitude. As a result, the power available for an electric generator ($\overline{C_{P_{D_{h,\mathrm{e}}}}}$) and the efficiency ($\overline{\eta}$) decrease more rapidly than the total power extracted from the flow ($\overline{C_{P_{\mathrm{hydro}}}}$) and the corresponding hydrodynamic efficiency ($\overline{\eta_{\mathrm{hydro}}}$). In the case of a fully-constrained turbine, only the power lost as heat due to the friction

in pitch would affect the power available for an electric generator since the same foil motions would be constrained to follow specific motions no matter the amount of friction in the setup. The fully-passive flapping-foil turbine concept is therefore more sensitive to friction than the fully-constrained concept.

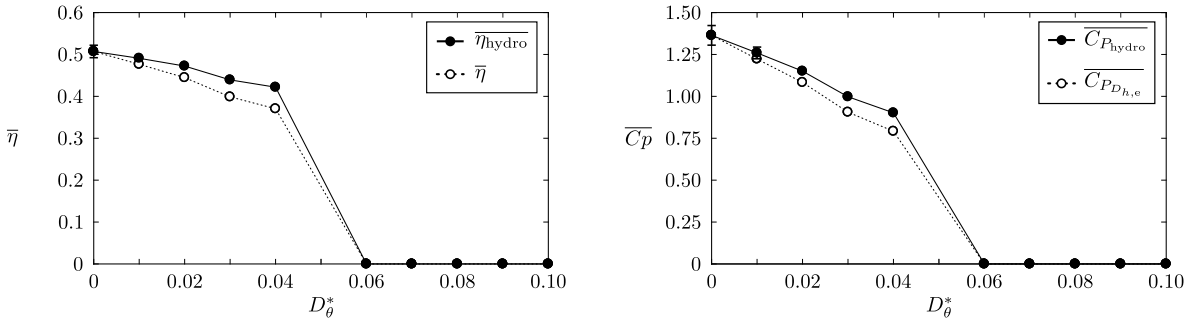

(a) Efficiencies (see Eqs. 5.24 and 5.25).

(b) Power coefficients (see Eqs. 5.8 and 5.23).

Figure 5.15: Comparison of the performance metrics based on the energy extracted from the flow and based on the energy available for the electric generator as functions of the dimensionless pitch damping coefficient.

The effect of the pitch damping is also analyzed for two additional sets of structural parameters taken from the parametric study with $S^* = 0.40$. Both sets of parameters are chosen for their larger heave and pitch amplitudes as well as their high value of $\overline{C_{P_{D_{h,e}}}}$, when $D^*_\theta = 0$. The heave and pitch amplitudes along with $\overline{\eta}$ and $\overline{C_{P_{D_{h,e}}}}$ obtained with different values of D^*_θ are shown in Fig. 5.16 for the three sets of structural parameters. The error bars indicate the standard deviation of the corresponding metric. Again, they are only shown when the standard deviation exceeds the threshold values listed at the end of Sec. 5.4.2 for the sake of clarity.

The amplitudes, the efficiency and the power coefficient also considerably decrease as D^*_θ increases for the two additional sets of structural parameters. Furthermore, the motions are again completely damped once critical values of D^*_θ are exceeded. However, these critical D^*_θ values are higher for the two additional sets of parameters characterized by larger amplitudes when $D^*_\theta = 0$. It is also found that the cases characterized with large amplitudes when $D^*_\theta = 0$ offer the possibility of maintaining large power coefficients for larger values of D^*_θ. Even though D^*_θ should be minimized, it is impossible to completely eliminate it on a real turbine. In the hypothetical case that the minimum value of D^*_θ would be 0.06, the set of parameters denoted with the red markers should obviously be preferred over the other two. Nevertheless, it is worth noting that D^*_θ was around 0.005 for the fully-passive flapping-foil turbine prototype tested by Boudreau et al. (2018). Based on this information, the presence of nonzero pitch damping is therefore not expected to be problematic in practice since the current results show that the effects of D^*_θ are minor with such a small amount of friction. It also suggests that parametric studies carried out with an idealized frictionless turbine are relevant.

Interestingly, the presence of pitch damping considerably reduces the level of fluctuations occurring from cycle to cycle. This is especially significant regarding the set of parameter denoted with red

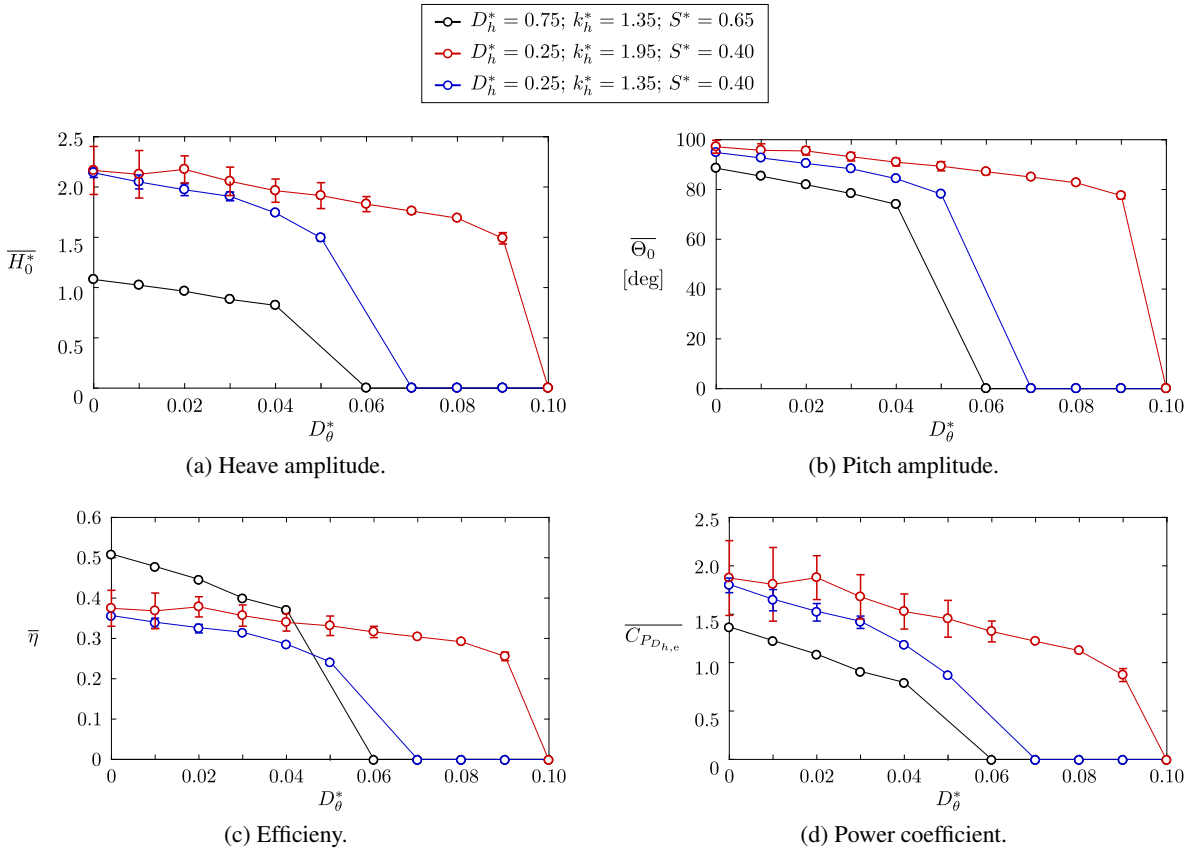

(a) Heave amplitude.

(b) Pitch amplitude.

(c) Efficieny.

(d) Power coefficient.

Figure 5.16: Variations of various metrics as D_θ^* is increased from 0 to 0.10 for three sets of structural parameters. Fixed parameters: $m_h^* = 2$; $I_\theta^* = 2$; $k_\theta^* = 3.16$.

markers in Fig. 5.16. This is due to a decrease of the maximum streamwise force coefficient as the heave and pitch amplitudes decrease, and thus to a weaker interaction of the foil with its own wake.

5.6 Conclusion

The fully-passive flapping-foil turbine concept, for which the foil is elastically supported both in heave and in pitch, has been investigated in this work through two-dimensional numerical simulations at a Reynolds number of 3.9×10^6. Based on the reverse solver technique proposed by Veilleux and Dumas (2017) and optimal semi-passive turbine cases reported by Boudreau et al. (2019b,a), initial sets of structural parameters have been determined around which a parametric study has been conducted. Cases characterized by self-sustained periodic motions without deep dynamic stall have been found, and efficiencies exceeding 50% have been achieved. This success demonstrates the great potential of the fully-passive concept since it matches the best performance reported for the fully-constrained flapping-foil turbine concept (Kinsey and Dumas, 2014; Young et al., 2014; Xiao and Zhu, 2014), but with a significant improvement in terms of the structural simplicity of the device.

This study shows that the heave damping coefficient (D_h^*), which models the effect of an electric gen-

erator, mainly affects the heave and pitch amplitudes. An increase of D_h^* is associated to a decrease of the amplitudes. Regarding the static moment (S^*), a decrease from $S^* = 0.65$ to $S^* = 0.40$ can result in a considerable increase of the heave amplitude and the power coefficient at the generator, with a maximum value reaching $\overline{C_{P_{D_{h,e}}}} = 1.97$ with $S^* = 0.40$ compared to 1.49 with $S^* = 0.65$. However, the maximum efficiency decreases from 51.0% to 44.6% as S^* is decreased from 0.65 to 0.40. Therefore, different sets of structural parameter values would be selected depending on the specific turbine deployment scenario, i.e., depending on which performance metric one seek to optimize.

Taking into consideration that the passive heave motion is similar to a sinusoidal motion, the heaving mass and the heave stiffness coefficient can be combined into a single parameter referred to as the effective heave stiffness (λ_h^*). The current results prove that the heave dynamics is essentially independent of variations of m_h^* and k_h^*, as long as λ_h^* is kept constant. Even though Boudreau et al. (2019a) successfully used an equivalent effective pitch stiffness to characterize the pitch dynamics of an elastically-supported foil with a prescribed sinusoidal heave motion, it is impractical with the present fully-passive flapping-foil turbine. This is because the frequency of the fully-passive flapping-foil motions closely follows the pitch natural frequency ($f_{n,\theta}^*$). Therefore, it is more convenient to characterize the pitch dynamics with $f_{n,\theta}^*$. Starting from an optimal operating point, a high performance can be maintained over large ranges of m_h^* and I_θ^* values if k_h^* and k_θ^* are scaled so that λ_h^* and $f_{n,\theta}^*$ are kept constant.

The presence of viscous friction in pitch ($D_\theta^* > 0$) can be highly detrimental to the turbine performance and even completely damp the foil motions if D_θ^* is large enough. Nevertheless, the effect remains small for a practicable level of friction (Boudreau et al., 2018). The decrease in efficiency and power coefficient as D_θ^* increases stems from two different effects: a fraction of the energy extracted from the flow being lost as heat instead of being available for the electric generator and an alteration of the foil motions, which directly affects the amount of energy extracted from the flow.

The frequency of the foil motions is dictated by the pitch dynamics for all the cases considered in this study. However, the heave dynamics can also govern the frequency of passive heave and pitch motions with different sets of structural parameters (e.g. Poirel and Mendes (2014)). It would be interesting to investigate what would be the consequences of such a change on the heave and pitch dynamics as well as on the energy-extraction performance of the device. Furthermore, the dynamics of fully-passive flapping-foils is expected to be affected by some practical aspects that have not been investigated so far, such as the effects of blockage and tip losses. These elements should be addressed in the future.

Acknowledgments

Financial support from the Natural Sciences and Engineering Research Council of Canada (NSERC Discovery Grant/RGPIN/121819-2013 and CGS-D scholarship), the Tyler Lewis Clean Energy Research Foundation (2016 TLCERF grant) and the Leadership and Sustainable Development Scholarship Program of Université Laval is gratefully acknowledged by the authors. The computations

presented in this work have been carried out on the supercomputer Colosse at Université Laval, managed by Calcul Québec and Compute Canada.

Appendix

5.A Fluid-solid coupling algorithm in pseudocode

For the sake of conciseness, the heave position and pitch angle as well as the residuals of the corresponding equations of motion are written in vector form:

$$p = \begin{bmatrix} h \\ \\ \theta \end{bmatrix} , \qquad R = \begin{bmatrix} R_y \\ \\ R_\theta \end{bmatrix} . \tag{5.53}$$

Beginning of the n^{th} time step

1. Execution of the solid solver for the i^{th} outer loop:

   IF $i = 1$ (first outer loop) **THEN**

   a. Initial guess for the position vector at the current time step (p^n) using the explicit second-order Adams-Bashforth scheme:

$$p_1^n = p^{n-1} + \frac{\Delta t}{2}\left(3\dot{p}^{n-1} - \dot{p}^{n-2}\right) ; \tag{5.54}$$

   ELSE IF $i = 2$ (second outer loop) **THEN**

   a. Initial guess for the 2×2 Jacobian matrix:

$$J_2^n = J_2^{n-1} ; \tag{5.55}$$

   b. Computation of the new position vector:

$$p_2^n = p_1^n - J_2^{n^{-1}} R_1^n , \tag{5.56}$$

   where $J_2^{n^{-1}}$ is the inverse of the Jacobian matrix J_2^n;

ELSE IF $i > 2$ (subsequent outer loops) **THEN**

a. Estimation of the new Jacobian matrix using Broyden's method:

$$J_i^n = J_{i-1}^n + \frac{\Delta R^n - J_{i-1}^n \Delta p^n}{\|\Delta p^n\|^2} \Delta p^{n^T} \ , \tag{5.57}$$

where:

$$\Delta p = p_{i-1}^n - p_{i-2}^n \ , \tag{5.58}$$

$$\Delta R = R_{i-1}^n - R_{i-2}^n \ , \tag{5.59}$$

Δp^{n^T} is the transpose of vector Δp^n and $\|\Delta p^n\|$ is the norm of vector Δp^n;

b. Computation of the new position vector:

$$p_i^n = p_{i-1}^n - J_i^{n^{-1}} R_{i-1}^n \ , \tag{5.60}$$

where $J_i^{n^{-1}}$ is the inverse of the Jacobian matrix J_i^n;

END IF

2. Foil displacement and rotation according to the updated position vector (p_i^n);

3. Check if the solid convergence criteria are met:

IF $\left(\frac{|h_i^n - h_{i-1}^n|}{c} < 10^{-8} \textbf{ AND } \frac{|\theta_i^n - \theta_{i-1}^n|}{\pi/2} < 10^{-8} \textbf{ AND } i > 2 \right)$ **THEN**

a. Execution of the fluid solver: perform fluid iterations until the fluid residuals convergence criteria are met;

b. Incrementation of the time step and return to step 1.

ELSE THEN

a. Execution of the fluid solver: perform fluid iterations until the values of the transverse force coefficient and the moment coefficient with the updated position vector are converged;

b. Computation of the velocity and acceleration vectors using the updated position vector and Eqs. 5.35 to 5.38;

c. Computation of the residuals:

$$R_{yi}^n = m_h \ddot{h}_i^n + S\left(\ddot{\theta}_i^n \cos\theta_i^n - \dot{\theta}_i^{n^2} \sin\theta_i^n\right) + D_h \dot{h}_i^n + k_h h_i^n - F_{yi}^n \ , \tag{5.61}$$

$$R_{\theta i}^n = I_\theta \ddot{\theta}_i^n + S\ddot{h}^n \cos(\theta_i^n) + D_\theta \dot{\theta}_i^n + k_\theta \theta_i^n - M_i^n \ ; \tag{5.62}$$

d. Incrementation of the outer loop and return to step 2.

END IF

Bibliography

Abiru, Hisanori and Yoshitake, Akira. Study on a Flapping Wing Hydroelectric Power Generation System. *Journal of Environment and Engineering*, 6(1):178–186, 2011.

Amandolese, X., Michelin, S., and Choquel, M. Low speed flutter and limit cycle oscillations of a two-degree-of-freedom flat plate in a wind tunnel. *Journal of Fluids and Structures*, 43:244–255, 2013.

Boudreau, M., Gunther, K., and Dumas, G. Free-pitching flapping-foil turbines with an imposed sinusoidal heave motion. 2019a. Submitted to Journal of Fluids and Structures.

Boudreau, Matthieu, Dumas, Guy, Rahimpour, Mostafa, and Oshkai, Peter. Experimental investigation of the energy extraction by a fully-passive flapping-foil hydrokinetic turbine prototype. *Journal of Fluids and Structures*, 82:446 – 472, 2018.

Boudreau, Matthieu, Gunther, Kevin, and Dumas, Guy. Investigation of the energy-extraction regime of a novel semi-passive flapping-foil turbine concept with a prescribed heave motion and a passive pitch motion. *Journal of Fluids and Structures*, 84:368 – 390, 2019b.

Dacles-Mariani, J., Zilliac, G. G., Chow, J. S., and Bradshaw, P. Numerical/Experimental Study of a Wingtip Vortex in the Near Field. *AIAA Journal*, 33(9):1561 – 1568, 1995.

Dacles-Mariani, J., Kwak, D., and Zilliac, G. On numerical errors and turbulence modeling in tip vortex flow prediction. *International Journal for Numerical Methods in Fluids*, 30(1):65 – 82, 1999.

Deng, Jian, Teng, Lubao, Pan, Dingyi, and Shao, Xueming. Inertial effects of the semi-passive flapping foil on its energy extraction efficiency. *Physics of Fluids*, 27(5):053103 (17 pp.) –, 2015.

Dowell, E. H. *A Modern Course in Aeroelasticity Fourh Revised and Enlarged Edition*. Kluwer Academic Publishers, Dordrecht, The Netherlands, 4th edition, 2004.

Ferziger, J.H. and Perić, M. *Computational Methods for Fluid Dynamics*. Springer, third edition, 2002.

Fung, Y.C. *An Introduction to the Theory of Aeroelasticity*. Dover Publications, Mineola, New York, USA, 2008.

Griffith, Martin D., Jacono, David Lo, Sheridan, John, and Leontini, Justin S. Passive heaving of elliptical cylinders with active pitching – from cylinders towards flapping foils. *Journal of Fluids and Structures*, 67:124 – 141, 2016.

Iverson, Dylan. Experimental Investigation of Oscillating-Foil Technologies. Master's thesis, University of Victoria, Victoria, BC, Canada, 2018.

Kinsey, Thomas and Dumas, Guy. Optimal Operating Parameters for an Oscillating Foil Turbine at Reynolds Number 500,000. *AIAA Journal*, 52(9):1885–1895, 2014.

Kinsey, Thomas, Dumas, Guy, Lalande, G., Ruel, J., Mehut, A., Viarouge, P., Lemay, J., and Jean, Y. Prototype testing of a hydrokinetic turbine based on oscillating hydrofoils. *Renewable Energy*, 36 (6):1710 – 1718, 2011.

Olivier, Mathieu and Paré-Lambert, Olivier. Strong fluid-solid interactions with segregated CFD solvers. *International Journal of Numerical Methods for Heat and Fluid Flow*, 2019. accepted.

Onoue, Kyohei, Song, Arnold, Strom, Benjamin, and Breuer, Kenneth S. Large amplitude flow-induced oscillations and energy harvesting using a cyber-physical pitching plate. *Journal of Fluids and Structures*, 55:262 – 275, 2015.

Peng, Zhangli and Zhu, Qiang. Energy harvesting through flow-induced oscillations of a foil. *Physics of Fluids*, 21(12):174–191, 2009.

Pigolotti, Luca, Mannini, Claudio, Bartoli, Gianni, and Thiele, Klaus. Critical and post-critical behaviour of two-degree-of-freedom flutter-based generators. *Journal of Sound and Vibration*, 404: 116 – 140, 2017.

Poirel, D. and Mendes, F. Experimental Small-Amplitude Self-Sustained Pitch–Heave Oscillations at Transitional Reynolds Numbers. *AIAA Journal*, 52(8):1581–1590, 2014.

Shiels, D., Leonard, A., and Roshko, A. Flow-induced vibration of a circular cylinder at limiting structural parameters. *Journal of Fluids and Structures*, 15(1):3 – 21, 2001.

Spalart, P. R., Jou, W-H., Strelets, M., and Allmaras, S. R. Comments on the Feasibility of LES for Wings, and on a Hybrid RANS/LES Approach. In *Advances in DNS/LES, Proceedings of the First AFOSR International Conference on DNS/LES*, pages 137 – 147, Ruston, Louisiana, USA, 1997.

Spalart, Philippe. R. and Allmaras, Steven R. A One-Equation Turbulence Model for Aerodynamic Flows. *Recherche Aérospatiale*, (1):5–21, 1994.

Spalart, Philippe R. and Rumsey, Christopher L. Effective inflow conditions for turbulence models in aerodynamic calculations. *AIAA Journal*, 45(10):2544 – 2553, 2007.

Teng, Lubao, Deng, Jian, Pan, Dingyi, and Shao, Xueming. Effects of non-sinusoidal pitching motion on energy extraction performance of a semi-active flapping foil. *Renewable Energy*, 85:810 – 818, 2016.

Veilleux, Jean-Christophe. Optimization of a Fully-Passive Flapping-Airfoil Turbine. Master's thesis, Université Laval, Québec, Qc, Canada, 2014.

Veilleux, Jean-Christophe and Dumas, Guy. Numerical optimization of a fully-passive flapping-airfoil turbine. *Journal of Fluids and Structures*, 70:102 – 130, 2017.

Wang, Zhuo, Du, Lin, Zhao, Jisheng, and Sun, Xiaofeng. Structural response and energy extraction of a fully passive flapping foil. *Journal of Fluids and Structures*, 72:96 – 113, 2017.

Xiao, Qing and Zhu, Qiang. A review on flow energy harvesters based on flapping foils. *Journal of Fluids and Structures*, 46:174–191, 2014.

Young, John, Lai, Joseph C. S., and Platzer, Max F. A review of progress and challenges in flapping foil power generation. *Progress in Aerospace Sciences*, 67:2–28, 2014.

Zhu, Qiang. Energy harvesting by a purely passive flapping foil from shear flows. *Journal of Fluids and Structures*, 34:157–169, 2012.

Zhu, Qiang and Peng, Zhangli. Mode coupling and flow energy harvesting by a flapping foil. *Physics of Fluids*, 21(3):033601 (10 pp.) –, 2009.

Conclusion

6.1 Retrospective

In addition to the conclusions presented at the end of each paper, a summary of the main conclusions of the four papers is also presented in Sec. 1.6. They are therefore not all repeated here. Instead, we take a look back at the objectives of the present work that are listed in Sec. 1.5, namely:

1. Proving the feasibility and testing the power-generation performance of the fully-passive concept experimentally;
2. Investigating the potential of the semi-passive turbine concept with a passive pitch motion;
3. Improving our understanding of the dynamics of passive pitch motions;
4. Using this new knowledge to optimize flapping-foil turbines relying on passive motions.

Each of these four objectives have been addressed by the different papers forming this thesis.

Paper I proves that it is possible to design a fully-passive flapping-foil turbine prototype achieving a significant efficiency. This has been accomplished despite the presence of several detrimental aspects that are generally ignored in the literature, such as the tip losses, the presence of viscous and Coulomb friction and the drag of the components holding the blade.

Paper II demonstrates that the performance of a semi-passive flapping-foil turbine with a passive pitch motion can match the best performance obtained with fully-constrained turbines. Moreover, it highlights the important role of the inertial coupling between the heave and pitch degrees of freedom, and thus of the static moment, that is responsible for providing the necessary power to maintain an optimal pitch motion.

Paper III extends our knowledge of the dynamics of passive pitch motions by showing that the moment of inertia and the pitch stiffness coefficient can be combined into a single parameter. Consequently, the turbine performance is essentially independent of the moment of inertia, provided that the pitch stiffness coefficient is properly scaled. Also, this paper highlights the fact that the fluid dynamics, and therefore the overall energy extraction from the flow by the turbine, is governed by the motion

of the foil surface, not the motion of the pitch axis. However, the motion of the pitch axis and the hydrodynamic force and moment acting at this point are important regarding the dynamics of the elastically-supported foil. As a result, a similar turbine performance can be achieved with different positions of the pitch axis ranging from the leading edge to the three-quarter-chord point as long as the structural parameters are adjusted so that a similar motion of the foil surface is maintained.

Using the knowledge gained from Papers II and III, Paper IV shows that efficiencies of the order of 50% can been achieved with a fully-passive flapping-foil turbine. This exceeds the best efficiency values previously reported in the literature for fully-constrained turbines.

The present thesis therefore fulfills its overall objective of determining the power-generation potential of flapping-foil turbines with passive motions as well as the conditions required to maximize the turbine performance.

6.2 Future works

Despite the great progresses that have been made with the present study, a lot of works remains to be done before bringing the fully-passive flapping-foil turbine to a commercial stage. This section briefly presents some of the challenges and possible research avenues.

Except for the experiments presented in Paper I, an idealized two-dimensional (2D) foil in an unconfined environment has been considered throughout the present study. However, it is well known that the forces and moment acting on a blade having a finite span length differ from those acting on a 2D foil (Anderson, 1991). For example, Kinsey and Dumas (2012b) showed that the efficiency decreases by almost 30% because of the tip losses for a fully-constrained flapping-foil turbine with a blade span length of five chord lengths ($b = 5c$) compared to a 2D foil. A flapping-foil turbine with passive motions is expected to be even more sensitive to these 3D effects since a change in the hydrodynamic forces and moment also gives rise to a change in the foil motions. This statement has been confirmed with some preliminary tests conducted with the fully-passive turbine prototype presented in Paper I and a few numerical simulations. In fact, the optimal set of structural parameter values is expected to depend on the blade aspect ratio. And even if the optimal foil motions determined in 2D could be reproduced with a finite span blade by adequately adjusting the structural parameters, the turbine performance will always remain smaller than its 2D counterpart. Consequently, the development of techniques aiming at minimizing the tip losses, such as the use of well-designed end plates, should be considered.

A similar comment can be made regarding the confinement, which can be non negligible in a real environment either because of the finite size of the river or the presence of neighbor turbines. The blockage effects also affect the forces and moment acting on a flapping-foil turbine (Gauthier et al., 2016), and thus can alter the passive foil motions if the structural parameters are kept constant. More specifically, the influence of blockage on the dynamic stall phenomenon should be investigated in

more details.

A certain level of robustness of the foil's passive motions is necessary for the semi-passive or fully-passive flapping-foil turbine concepts to become viable. Investigating the sensitivity of the foil's dynamics to different kinds of perturbations in the flow is therefore crucial. Such perturbations can be related to the turbulence level in the upstream flow (incoherent flow structures), the presence of another turbine upstream (coherent flow structures) or the presence of shear in the upstream flow, which could arise due to the marine boundary layer or the specific bathymetry of the site considered for example. Iverson (2018) studied some of these aspects using the same turbine prototype and experimental facilities as those presented in Paper I. He showed that the foil passive motions are not significantly affected when increasing the turbulence intensity of the freestream flow from about 2% to 20% and that the turbine performance is increasing with the turbulence intensity. However, the foil motions and the turbine performance are much more sensitive to coherent perturbations produced by placing a fully-constrained flapping-foil turbine 6.5 chord lengths[1] upstream of the fully-passive flapping-foil turbine. Still, more works are required in that regard. The results could have been different in a less confined environment or with a greater distance between the two turbines. Moreover, these tests have been conducted with only a few operating points, based on the baseline case presented in Paper I. It would be interesting to repeat these experiments with the optimal cases reported in Paper IV, which rely on a different physics. Indeed, the operating points presented in Paper IV are subject to a coupled-mode flutter instability instead of a divergence instability. Furthermore, no LEVs are formed for several of the optimal cases reported in Paper IV, unlike the baseline case presented in Paper I.

If the semi-passive and fully-passive turbine concepts considered in this thesis happen to be too sensitive to perturbations in the freestream flow, other flapping-foil turbine concepts with passive motions could be considered. One possibility would be to keep the mechanism coupling both degrees of freedom together in order to constrain the phase lag between the heave and the pitch motions, but to remove the crank mechanism and to use a simple uncontrolled linear electric generator. As a result, the shape and the frequency of the heave motion would be unconstrained while the characteristics of the pitch motion would be directly related to the heave motion. The increased complexity of such a device compared to the fully-passive concept could be justified if imposing a specific phase lag would allow the turbine to operate in a broader range of conditions and be less sensitive to perturbations.

The optimization of the turbine structural and electrical design is another critical aspect that has not been investigated in details so far. For example, a swing-arm design (e.g. Huxham et al. (2012); Sitorus and Ko (2019)) would require less bearings than a design relying on a heaving carriage (e.g., the prototype presented in Paper I), thereby reducing the number of moving components and the undesired friction in heave in addition to avoiding the challenge of precisely aligning both ends of the heaving carriage. Moreover, the actual dynamics of the electric generator connected to the turbine should be considered for the final design of a full-scale turbine instead of an idealized damping law.

[1] This distance is measured between the pitch axis of the two turbines.

The dynamics of the energy sink would also be different if the turbine would be used as a pump instead of being directly connected to an electric generator.

A turbine extracting the energy of tidal streams would need to operate with the flow coming from two directions. Consequently, the use of a symmetric foil profile with a pitch axis positioned at the mid-chord point appears as a logical choice in that situation. Some work would be required to optimize this specific configuration. For example, if a flat plate is chosen as the foil profile, some flexibility could be beneficial to improve the turbine performance, especially if it can delay stall.

Lastly and on a more fundamental perspective, a better understanding of dynamic stall, unsteady separation as well as the formation and ejection of leading-edge vortices would be very valuable since the best efficiencies of the semi-passive and fully-passive turbines concepts are often obtained when the foil is on the edge of stalling.

Bibliography

Abdelkefi, A. Aeroelastic energy harvesting: A review. *International Journal of Engineering Science*, 100:112 – 135, 2016.

Abiru, Hisanori and Yoshitake, Akira. Study on a Flapping Wing Hydroelectric Power Generation System. *Journal of Environment and Engineering*, 6(1):178–186, 2011.

Abiru, Hisanori and Yoshitake, Akira. Experimental Study on a Cascade Flapping Wing Hydroelectric Power Generator. *Journal of Energy and Power Engineering*, 6(9):1429–1436, 2012.

Amandolese, X., Michelin, S., and Choquel, M. Low speed flutter and limit cycle oscillations of a two-degree-of-freedom flat plate in a wind tunnel. *Journal of Fluids and Structures*, 43:244–255, 2013.

Anderson, John David. *Fundamentals of aerodynamics*. McGraw-Hill, New York, NY, USA, 2nd edition, 1991.

Barrero-Gil, Antonio, Pindado, Santiago, and Avila, Sergio. Extracting energy from vortex-induced vibrations: A parametric study. *Applied Mathematical Modelling*, 36(7):3153 – 3160, 2012.

Bernitsas, Michael M., Raghavan, Kamaldev, Ben-Simon, Y., and Garcia, E. M. VIVACE (Vortex Induced Vibration Aquatic Clean Energy): A New Concept in Generation of Clean and Renewable Energy From Fluid Flow. *Journal of Offshore Mechanics and Arctic Engineering*, 130(4):041101 (15 pp.) –, 2008.

Boudreau, M., Gunther, K., and Dumas, G. Free-pitching flapping-foil turbines with an imposed sinusoidal heave motion. 2019a. Submitted to Journal of Fluids and Structures.

Boudreau, Matthieu and Dumas, Guy. Comparison of the wake recovery of the axial-flow and cross-flow turbine concepts. *Journal of Wind Engineering and Industrial Aerodynamics*, 165:137 – 152, 2017a.

Boudreau, Matthieu and Dumas, Guy. Vortex Dynamics in the Wake of Three Generic Types of Freestream Turbines. *Journal of Fluids Engineering*, 140(2):021106 (9 pp.) –, 2017b.

Boudreau, Matthieu, Dumas, Guy, Rahimpour, Mostafa, and Oshkai, Peter. Experimental investigation of the energy extraction by a fully-passive flapping-foil hydrokinetic turbine prototype. *Journal of Fluids and Structures*, 82:446 – 472, 2018.

Boudreau, Matthieu, Gunther, Kevin, and Dumas, Guy. Investigation of the energy-extraction regime of a novel semi-passive flapping-foil turbine concept with a prescribed heave motion and a passive pitch motion. *Journal of Fluids and Structures*, 84:368 – 390, 2019b.

Campobasso, M. Sergio, Piskopakis, Andreas, Drofelnik, Jernej, and Jackson, Adrian. Turbulent navier–stokes analysis of an oscillating wing in a power-extraction regime using the shear stress transport turbulence model. *Computers & Fluids*, 88:136 – 155, 2013.

Cape Sharp Tidal Venture Ltd. http://capesharptidal.com/, 2018. Accessed: 2018-10-09.

Chen, Yongliang, Nan, Jingwen, and Wu, Jie. Wake effect on a semi-active flapping foil based energy harvester by a rotating foil. *Computers & Fluids*, 160:51 – 63, 2018.

Coleman, H. W. and Steele, W. G. *Experimentation, Validation, and Uncertainty Analysis for Engineers*. Cambridge monographs on mechanics. Wiley, 2009. ISBN 9780470168882.

Corke, Thomas C. and Thomas, Flint O. Dynamic stall in pitching airfoils: Aerodynamic damping and compressibility effects. *Annual Review of Fluid Mechanics*, 47(1):479–505, 2015.

Dacles-Mariani, J., Zilliac, G. G., Chow, J. S., and Bradshaw, P. Numerical/Experimental Study of a Wingtip Vortex in the Near Field. *AIAA Journal*, 33(9):1561 – 1568, 1995.

Dacles-Mariani, J., Kwak, D., and Zilliac, G. On numerical errors and turbulence modeling in tip vortex flow prediction. *International Journal for Numerical Methods in Fluids*, 30(1):65 – 82, 1999.

Davids, S.T. A Computational and Experimental Investigation of a Flutter Generator. Master's thesis, Naval Postgraduate School, Monterey, CA, USA, 1999.

Deng, Jian, Caulfield, C. P., and Shao, Xueming. Effect of aspect ratio on the energy extraction efficiency of three-dimensional flapping foils. *Physics of Fluids*, 26(4):1318–1330, 2014.

Deng, Jian, Teng, Lubao, Pan, Dingyi, and Shao, Xueming. Inertial effects of the semi-passive flapping foil on its energy extraction efficiency. *Physics of Fluids*, 27(5):053103 (17 pp.) –, 2015.

Derakhshandeh, J.F., Arjomandi, M., Dally, B., and Cazzolato, B. Flow-induced vibration of an elastically mounted airfoil under the influence of the wake of a circular cylinder. *Experimental Thermal and Fluid Science*, 74:58 – 72, 2016.

Dimitriadis, Grigorios and Li, Jing. Bifurcation Behavior of Airfoil Undergoing Stall Flutter Oscillations in Low-Speed Wind Tunnel. *AIAA Journal*, 47(11):2577–2596, 2009.

Dowell, E. H. *A Modern Course in Aeroelasticity Fourh Revised and Enlarged Edition*. Kluwer Academic Publishers, Dordrecht, The Netherlands, 4th edition, 2004.

Farthing, S. P. Binary flutter as an oscillating windmill — scaling & linear analysis. *Wind Engineering*, 37(5):483–499, 2013.

Feeny, B.F. and Liang, J.W. A decrement method for the simultaneous estimation of coulomb and viscous friction. *Journal of Sound and Vibration*, 195(1):149 – 154, 1996.

Ferziger, J.H. and Perić, M. *Computational Methods for Fluid Dynamics*. Springer, third edition, 2002.

Fung, Y.C. *An Introduction to the Theory of Aeroelasticity*. Dover Publications, Mineola, New York, USA, 2008.

Gauthier, Étienne, Kinsey, Thomas, and Dumas, Guy. Impact of Blockage on the Hydrodynamic Performance of Oscillating-Foils Hydrokinetic Turbines. *Journal of Fluids Engineering*, 138(9): 091103 (13 pp.) –, 2016.

Gosline, Andrew H., Campion, Gianni, and Hayward, Vincent. On the Use of Eddy Current Brakes as Tunable, Fast Turn-On Viscous Dampers For Haptic Rendering. In *Proc. Eurohaptics 2006*, pages 229–234, 2006.

Gosselin, R., Dumas, G., and Boudreau, M. Parametric study of H-Darrieus vertical-axis turbines using CFD simulations. *Journal of Renewable and Sustainable Energy*, 8(5):053301 (22 pp.), 2016.

Griffith, Martin D., Jacono, David Lo, Sheridan, John, and Leontini, Justin S. Passive heaving of elliptical cylinders with active pitching – from cylinders towards flapping foils. *Journal of Fluids and Structures*, 67:124 – 141, 2016.

Haynes, W.M. *CRC Handbook of Chemistry and Physics*. CRC Press, Boca Raton, FL, USA, 96$^{\text{th}}$ edition, 2015.

Huxham, G. H., Cochard, S., and Patterson, J. Experimental Parametric Investigation of an Oscillating Hydrofoil Tidal Stream Energy Converter. In *Proceedings of the 18th Australasian Fluid Mechanics Conference*, Launceston, Australia, 2012.

Iverson, Dylan. Experimental Investigation of Oscillating-Foil Technologies. Master's thesis, University of Victoria, Victoria, BC, Canada, 2018.

Kim, Daegyoum, Strom, Benjamin, Mandre, Shreyas, and Breuer, Kenneth. Energy harvesting performance and flow structure of an oscillating hydrofoil with finite span. *Journal of Fluids and Structures*, 70:314 – 326, 2017.

Kinsey, Thomas, 2015. Private communication.

Kinsey, Thomas and Dumas, Guy. Parametric Study of an Oscillating Airfoil in a Power-Extraction Regime. *AIAA Journal*, 46(6):1318–1330, 2008.

Kinsey, Thomas and Dumas, Guy. Optimal Tandem Configuration for Oscillating-Foils Hydrokinetic Turbine. *Journal of Fluids Engineering*, 134(3):031103 (11 pp.) –, 2012a.

Kinsey, Thomas and Dumas, Guy. Three-dimensional effects on an oscillating-foil hydrokinetic turbine. *Journal of Fluids Engineering*, 134(7):071105 (11 pp.) –, 2012b.

Kinsey, Thomas and Dumas, Guy. Computational Fluid Dynamics Analysis of a Hydrokinetic Turbine Based on Oscillating Hydrofoils. *Journal of Fluids Engineering*, 134(2):021104 (16 pp.) –, 2012c.

Kinsey, Thomas and Dumas, Guy. Optimal Operating Parameters for an Oscillating Foil Turbine at Reynolds Number 500,000. *AIAA Journal*, 52(9):1885–1895, 2014.

Kinsey, Thomas, Dumas, Guy, Lalande, G., Ruel, J., Mehut, A., Viarouge, P., Lemay, J., and Jean, Y. Prototype testing of a hydrokinetic turbine based on oscillating hydrofoils. *Renewable Energy*, 36 (6):1710 – 1718, 2011.

Lee, T. and Gerontakos, P. Investigation of flow over an oscillating airfoil. *Journal of Fluid Mechanics*, 512:313–341, 2004.

M. S. Güney and K. Kaygusuz. Hydrokinetic energy conversion systems: A technology status review. *Renewable and Sustainable Energy Reviews*, 14(9):2996 – 3004, 2010.

Mackowski, A. W. and Williamson, C. H. K. Effect of pivot location and passive heave on propulsion from a pitching airfoil. *Phys. Rev. Fluids*, 2:013101 (24pp.), 2017.

McCroskey, W. J. The phenomenon of dynamic stall. Technical report, National Aeronautics and Space Administration (NASA), Washington, DC, USA, 1981.

McCroskey, W. J. Unsteady airfoils. *Annual Review of Fluid Mechanics*, 14(1):285–311, 1982.

McKinney, William and DeLaurier, James. Wingmill: An Oscillating-Wing Windmill. *Journal of Energy*, 5(2):109–115, 1981.

Munson, Bruce Roy. *Fundamentals of fluid mechanics*. John Wiley & Sons, Hoboken, NJ, USA, 7th edition, 2013.

Oberg, Erik, Jones, Franklin D., Horton, Holbrook L., and Ryffel, Henry H. *Machinery's Handbook*. Machinery's Handbook. Industrial Press, New York, 29th edition, 2012.

Olivier, Mathieu and Paré-Lambert, Olivier. Strong fluid-solid interactions with segregated CFD solvers. *International Journal of Numerical Methods for Heat and Fluid Flow*, 2019. accepted.

Onoue, Kyohei, Song, Arnold, Strom, Benjamin, and Breuer, Kenneth S. Large amplitude flow-induced oscillations and energy harvesting using a cyber-physical pitching plate. *Journal of Fluids and Structures*, 55:262 – 275, 2015.

Panton, Ronald L. *Incompressible Flow*. John Wiley & Sons, Inc., Hoboken, NJ, USA, 4th edition, 2013.

Paraschivoiu, I. *Wind Turbine Design: With Emphasis on Darrieus Concept*. Polytechnic International Press, 2002.

Paré-Lambert, Olivier and Olivier, Mathieu. A parametric study of energy extraction from vortex-induced vibrations. *Transactions of the Canadian Society for Mechanical Engineering*, pages 1 – 11, 2018.

Peng, Zhangli and Zhu, Qiang. Energy harvesting through flow-induced oscillations of a foil. *Physics of Fluids*, 21(12):174–191, 2009.

Pigolotti, Luca, Mannini, Claudio, Bartoli, Gianni, and Thiele, Klaus. Critical and post-critical behaviour of two-degree-of-freedom flutter-based generators. *Journal of Sound and Vibration*, 404: 116 – 140, 2017.

Poirel, D. and Mendes, F. Experimental Small-Amplitude Self-Sustained Pitch–Heave Oscillations at Transitional Reynolds Numbers. *AIAA Journal*, 52(8):1581–1590, 2014.

Pyrhonen, Juha, Jokinen, Tapani, and Hrabovcová, Valeria. *Design of rotating electrical machines*. Wiley, Chichester, West Sussex, United Kingdom, 2nd edition, 2014.

Rao, S. S. *Mechanical vibrations*. Prentice Hall, Upper Saddle River, N.J, 5th edition, 2011.

Shiels, D., Leonard, A., and Roshko, A. Flow-induced vibration of a circular cylinder at limiting structural parameters. *Journal of Fluids and Structures*, 15(1):3 – 21, 2001.

Shimizu, Eriko, Isogai, Koji, and Obayashi, Shigeru. Multiobjective Design Study of a Flapping Wing Power Generator. *Journal of Fluids Engineering*, 130(2):021104 (8 pp.) –, 2008.

Sitorus, Patar Ebenezer and Ko, Jin Hwan. Power extraction performance of three types of flapping hydrofoils at a reynolds number of 1.7e6. *Renewable Energy*, 132:106 – 118, 2019.

Sitorus, Patar Ebenezer, Le, Tuyen Quang, Ko, Jin Hwan, Truong, Tri Quang, and Park, Hoon Cheol. Design, implementation, and power estimation of a lab-scale flapping-type turbine. *Journal of Marine Science and Technology*, 2015.

Spalart, P. R., Jou, W-H., Strelets, M., and Allmaras, S. R. Comments on the Feasibility of LES for Wings, and on a Hybrid RANS/LES Approach. In *Advances in DNS/LES, Proceedings of the First AFOSR International Conference on DNS/LES*, pages 137 – 147, Ruston, Louisiana, USA, 1997.

Spalart, Philippe. R. and Allmaras, Steven R. A One-Equation Turbulence Model for Aerodynamic Flows. *Recherche Aérospatiale*, (1):5–21, 1994.

Spalart, Philippe R. and Rumsey, Christopher L. Effective inflow conditions for turbulence models in aerodynamic calculations. *AIAA Journal*, 45(10):2544 – 2553, 2007.

Stingray. Research and Development of a 150kW Tidal Stream Generator. Technical report, The Engineering Business Limited, 2002.

Teng, Lubao, Deng, Jian, Pan, Dingyi, and Shao, Xueming. Effects of non-sinusoidal pitching motion on energy extraction performance of a semi-active flapping foil. *Renewable Energy*, 85:810 – 818, 2016.

Thaweewat, Nonthipat, Phoemsapthawee, Surasak, and Juntasaro, Varangrat. Semi-active flapping foil for marine propulsion. *Ocean Engineering*, 147:556 – 564, 2018.

Veilleux, Jean-Christophe. Optimization of a Fully-Passive Flapping-Airfoil Turbine. Master's thesis, Université Laval, Québec, Qc, Canada, 2014.

Veilleux, Jean-Christophe and Dumas, Guy. Numerical optimization of a fully-passive flapping-airfoil turbine. *Journal of Fluids and Structures*, 70:102 – 130, 2017.

Vortex Hydro Energy, Inc. https://www.vortexhydroenergy.com/technology/how-it-works/. Accessed: 2018-07-13.

Šidlof, Petr, Vlček, Václav, and Štěpán, Martin. Experimental investigation of flow-induced vibration of a pitch–plunge naca 0015 airfoil under deep dynamic stall. *Journal of Fluids and Structures*, 67: 48 – 59, 2016.

Wang, Zhuo, Du, Lin, Zhao, Jisheng, and Sun, Xiaofeng. Structural response and energy extraction of a fully passive flapping foil. *Journal of Fluids and Structures*, 72:96 – 113, 2017.

Wouterse, J.H. Critical torque and speed of eddy current brake with widely separated soft iron poles. *Electric Power Applications, IEE Proceedings B*, 138(4):153–158, 1991.

Wu, J., Qiu, Y. L., Shu, C., and Zhao, N. Pitching-motion-activated flapping foil near solid walls for power extraction: A numerical investigation. *Physics of Fluids*, 26(8):083601, 2014.

Wu, J., Chen, Y. L., and Zhao, N. Role of induced vortex interaction in a semi-active flapping foil based energy harvester. *Physics of Fluids*, 27(9):093601, 2015.

Xiao, Qing and Zhu, Qiang. A review on flow energy harvesters based on flapping foils. *Journal of Fluids and Structures*, 46:174–191, 2014.

Xu, G.D., Xu, W.H., and Dai, J. Numerical and experimental study of a flapping foil generator. *Applied Ocean Research*, 63:242 – 250, 2017.

Young, John, Ashraf, Muhammad A., Lai, Joseph C. S., and Platzer, Max F. Numerical Simulation of Fully Passive Flapping Foil Power Generation. *AIAA Journal*, 51(11):2727–2739, 2013.

Young, John, Lai, Joseph C. S., and Platzer, Max F. A review of progress and challenges in flapping foil power generation. *Progress in Aerospace Sciences*, 67:2–28, 2014.

Zhan, Jiapu, Xu, Bing, Wu, Jie, and Wu, Jing. Power extraction performance of a semi-activated flapping foil in gusty flow. *Journal of Bionic Engineering*, 14(1):99 – 110, 2017.

Zhu, Qiang. Optimal frequency for flow energy harvesting of a flapping foil. *Journal of Fluid Mechanics*, 675:495–517, 5 2011.

Zhu, Qiang. Energy harvesting by a purely passive flapping foil from shear flows. *Journal of Fluids and Structures*, 34:157–169, 2012.

Zhu, Qiang and Peng, Zhangli. Mode coupling and flow energy harvesting by a flapping foil. *Physics of Fluids*, 21(3):033601 (10 pp.) –, 2009.

Zhu, Qiang, Haase, Max, and Wu, Chin H. Modeling the capacity of a novel flow-energy harvester. *Applied Mathematical Modelling*, 33(5):2207–2217, 2009.

Appendix A

Additional considerations regarding the experiments presented in Paper I

A.1 End-effects of the eddy-current brake

By extrapolating the data obtained during the calibration of the eddy-current brake for larger values of l_m (see Fig. 2.B.2), it has been estimated that an asymptote would be reached when l_m reaches 35 mm. Based on this estimation, it is expected that the heave damping coefficient decreases when the amplitude in heave is such that the distance between the center of the magnets and the end of the sliding plate in the heave direction becomes smaller than 35 mm. This happens when the heave amplitude exceeds 90 mm. Nevertheless, the maximum heave amplitude that has been reached for all the cases considered in Paper I is 77.9 mm (1.536c). Consequently, these eddy-current brake "end effects" have not affected the experimental results.

A.2 Estimation of the uncertainties

This appendix complements the information presented in Sec. 2.B of Paper I. The reader is therefore invited to read Sec. 2.B again before proceeding with the following appendix.

A.2.1 Preliminary concepts

This first section summarizes some basic concepts about the estimation of the uncertainties that are discussed in the book of Coleman and Steele (2009). The interested reader is referred to this reference for more details.

The standard uncertainty of a given variable X, referred to as u_X, is defined as: "an estimate of the standard deviation of the parent population from which a particular elemental error originates" (Coleman and Steele, 2009). From a standard uncertainty (u_X), an expanded uncertainty (U_X) is estimated by considering a certain confidence level that allows one to stipulate that the true value of a variable

X falls within the interval:

$$X_{\text{best}} \pm U_X \ , \tag{A.1}$$

where the mean value of X is often taken as X_{best}. The relation between the standard uncertainty and the expanded uncertainty depends on the statistical distribution of the error. For example, if one considers an error source following a Student's t-distribution, the expanded uncertainty is given by:

$$U_X = t_{\nu,\%}\, u_x \ , \tag{A.2}$$

where the subscript % is the confidence level and the subscript ν is the number of degrees of freedom. Considering that N is the sample population, or the number of times the same measurement has been taken:

$$\nu = N - 1 \ . \tag{A.3}$$

For example, the expanded uncertainty of a variable X that has been measured 51 times with a confidence level of 95% is given by:

$$U_X = t_{50,95\%}\, u_x = 2.009\, u_x \ . \tag{A.4}$$

When a variable r is a function of J other variables:

$$r = r(X_1, X_2, \ldots, X_J) \ , \tag{A.5}$$

the uncertainty of r, U_r, is estimated by propagating the uncertainties of each variable on which r depends. One well known method is the Taylor Series Method for which the expanded uncertainty of the result (U_r) is given by:

$$U_r^2 = \sum_{i=1}^{J} \left(\frac{\partial r}{\partial X_i} \right)^2 U_{X_i}^2 \ , \tag{A.6}$$

where U_{X_i} is the expanded uncertainty of the i^{th} variable. This formulation of the Taylor Series Method propagation equation is obtained by making the assumption that all the errors are uncorrelated.

When one is interested in the mean value of a given variable ($\overline{X}$) obtained by conducting N independent measurements, the standard uncertainty of the mean value ($u_{\overline{X}}$) is given by:

$$u_{\overline{X}} = \frac{u_X}{\sqrt{N}} \ . \tag{A.7}$$

In some other situations, the variable of interest is obtained from a first-order linear regression using the least-square method in order to obtain a relation of the type $y = Ax + B$. In such instances, the expanded uncertainty of the slope (U_A) obtained from a set of N points (x_i, y_i) is given by:

$$\begin{aligned} U_A^2 = & \sum_{i=1}^{N} \left(\frac{\partial A}{\partial y_i} \right)^2 U_{y_i}^2 + \sum_{i=1}^{N} \left(\frac{\partial A}{\partial x_i} \right)^2 U_{x_i}^2 + 2 \sum_{i=1}^{N-1} \sum_{k=i+1}^{N} \left(\frac{\partial A}{\partial y_i} \right) \left(\frac{\partial A}{\partial y_k} \right) U_{y_i} U_{y_k} \\ & + 2 \sum_{i=1}^{N-1} \sum_{k=i+1}^{N} \left(\frac{\partial A}{\partial x_i} \right) \left(\frac{\partial A}{\partial x_k} \right) U_{x_i} U_{x_k} + 2 \sum_{i=1}^{N} \sum_{k=1}^{N} \left(\frac{\partial A}{\partial x_i} \right) \left(\frac{\partial A}{\partial y_k} \right) U_{x_i} U_{y_k} \ , \end{aligned} \tag{A.8}$$

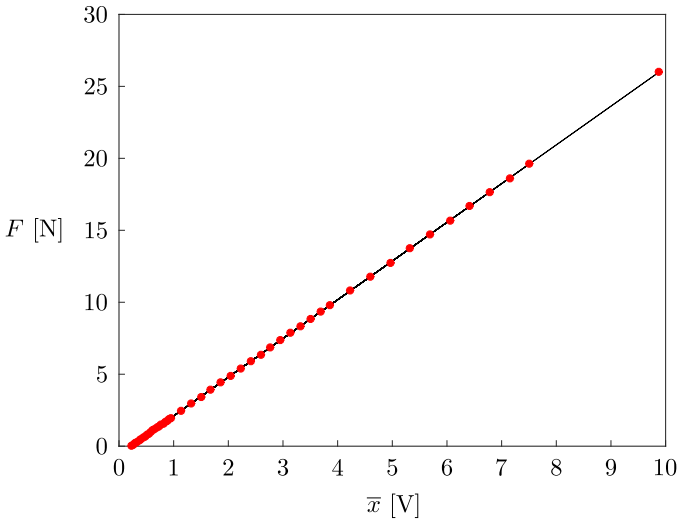

Figure A.1: Relation between the forces applied to the load (F) cell and the output voltage ($\overline{x}$) from the measurements (red dots) along with the linear regression curve (black).

and the expanded uncertainty of the intercept (U_B) is computed using the same equation by simply replacing A by B. Since it would be very challenging to evaluate the partial derivatives in Eq. A.8 analytically, they are estimated numerically. This is done by adding and subtracting a small perturbation to each data point one by one and by evaluating the modified values of the slope (A) and the intercept (B) with each new perturbed data point.

A.2.2 Load cell

An Omega LC703-25 load cell along with a EI1040 dual instrumentation amplifier set to a gain of 1000 were used to calibrate the springs and the heave damper. In order to calibrate the load cell, reference test weights with known masses (m) were suspended from it.

The mass of the test weights were measured with the Mettler PJ360 DeltaRange and the Mettler PM16 weighing scales depending on their mass. 100 000 samples of the output voltage were collected over 1 second and they were averaged for each mass value.

The relation giving the force in Newtons (F) versus the average output voltage of the load cell ($\overline{x}$) is of the form:

$$F = A\overline{x} + B\,, \tag{A.9}$$

where $F = m \cdot g$ and g is the gravitational acceleration. The collected data is plotted in Fig. A.1. The constants A and B appearing in Eq. A.9 are determined by performing a linear regression analysis:

$$A = 2.690 \qquad\qquad B = -0.586\,. \tag{A.10}$$

The expanded uncertainty of test weight masses used for the load cell calibration are estimated as half

of the smallest mass increment that can be read by the corresponding weighing scale:

$$U_m = \begin{cases} 0.0005g & \text{if } m < 50g \text{ ,} \\ 0.005g & \text{if } 50 <= m < 250g \text{ ,} \\ 0.05g & \text{if } m >= 250g \text{ .} \end{cases} \tag{A.11}$$

The expanded uncertainty of the instantaneous output voltage (U_x) is used to estimate the uncertainty of the average voltage ($U_{\bar{x}}$) as a conservative estimate. This uncertainty, with a 95% confidence level, is given by:

$$U_x = 1.96\, s_x \text{ ,} \tag{A.12}$$

where s_x is the standard deviation of a set of data corresponding to a given mass value. The factor 1.96, which corresponds to a normal distribution, can be used because of the very large number of samples. Note that since we directly estimate the standard uncertainty from the output voltage data, we do not have to consider the uncertainty related to the analog-to-digital converter resolution as it is included in the standard uncertainty estimated. The uncertainty stemming from the analog-to-digital converter resolution is one order of magnitude smaller than this standard uncertainty.

The uncertainties of the constants A and B in Eq. A.9 are then determined using Eq. A.8:

$$U_A = 0.003 \text{ N/V} \qquad\qquad U_B = 0.008 \text{ N .} \tag{A.13}$$

A.2.3 Positions and velocities

The uncertainty of the heave position is affected by the backlash between the timing belt undergoing the heave motion and the sprocket connected to the heave encoder's shaft (see Fig. 2.5). Indeed, one cannot know if the teeth of the timing belt and the sprocket are in contact on one of their side, on the other side or between these two contacts. However, we can assume that the teeth of the timing belt and the sprocket are always in contact when a local extremum is reached for the heave position, i.e., when the direction of the heave velocity changes. We can also assume that the heave encoder's shaft does not rotate further when the foil reaches a local extremum in heave. This is because of the presence of friction in the encoder and the fact that the inertia of the encoder's shaft and the sprocket are very small. Moreover, the contact side of the teeth is always the same for positive local extrema while negative local extrema are associated to the other contact side. Consequently, when one desires to compute the distance between a positive extremum and a negative extremum, the backlash can be added to the measured difference to obtain a more accurate value.

The backlash varies slightly with the heave position because the distance between the sprocket's axis of rotation and its contact point with the timing belt is not exactly uniform along the heave stroke. As a result, the uncertainty of the difference between the prescribed heave positions in Eq. 2.19 for a single test ($U_{(h_2-h_1)}$) is estimated as being equal to half the difference between the largest and the smallest backlash values measured at the different heave positions:

$$U_{(h_2-h_1)} \approx 1.4 \times 10^{-4} \text{ m .} \tag{A.14}$$

Note that the uncertainty stemming from the accuracy of the machining center is neglected as it is one order of magnitude smaller than this value.

The uncertainty of $(E_{h_2} - E_{h_1})$ is estimated with the standard deviation computed from the 100 measurements taken and by assuming a Student's t-distribution with a 95% confidence level:

$$U_{\left(E_{h_2}-E_{h_1}\right)} = t_{99,95\%}\, \sigma_{\left(E_{h_2}-E_{h_1}\right)} = 0.0024 \text{ V} , \tag{A.15}$$

where:

$$\sigma_{\left(E_{h_2}-E_{h_1}\right)} = 0.0012 \text{ V} , \tag{A.16}$$

and:

$$t_{99,95\%} = 1.984 . \tag{A.17}$$

Again, the resolution of the digital-to-analog converter is one order of magnitude smaller than this uncertainty value.

The uncertainty of the calibration constant A_h is then obtained by applying the Taylor Series Method to Eq. 2.19, which results in:

$$U_{A_h}^2 = \frac{U_{(h_2-h_1)}^2}{\left(\overline{E_{h_2} - E_{h_1}}\right)^2} + \frac{\left(\overline{h_2 - h_1}\right)^2}{\left(\overline{E_{h_2} - E_{h_1}}\right)^4} \cdot U_{\left(E_{h_2}-E_{h_1}\right)}^2 , \tag{A.18}$$

$$U_{A_h} = 5.7 \times 10^{-5} \text{ m/V} . \tag{A.19}$$

Having determined the value of U_{A_h}, the uncertainty of the heave position (h) is then estimated by applying the Taylor Series Method to Eq. 2.17:

$$\begin{aligned} U_h^2 &= A_h^2 \left(U_{E_h}^2 + U_{E_{h_0}}^2\right) + \left(E_h - E_{h_0}\right)^2 U_{A_h}^2 + U_{h_0}^2 , \\ &= A_h^2 \left(U_{E_h}^2 + U_{E_{h_0}}^2\right) + \left(\frac{h - h_0}{A_h}\right)^2 U_{A_h}^2 , \end{aligned} \tag{A.20}$$

since U_{h_0} is considered to be equal to 0. Indeed, we are not interested in knowing the heave position with respect to the exact position of the channel center, but rather with respect to a reference position, namely the initial position of the blade. Nevertheless, the initial position of the blade corresponds to the heave equilibrium position, which is set to be as close as possible to the center of the water channel.

The expanded uncertainty of the initial, or reference output voltage, of the heave encoder ($U_{E_{h_0}}$) is estimated by taking the standard deviation of this value ($\sigma_{E_{h_0}}$) from a signal having a duration of 3 minutes with the blade being held at its initial position and by assuming a Gaussian distribution:

$$U_{E_{h_0}} = 1.96\, \sigma_{E_{h_0}} = 9 \times 10^{-4} \text{ V} . \tag{A.21}$$

This uncertainty stems from the fact that the reference voltage varies very slightly over time and it includes the uncertainty due to the resolution of the digital-to-analog converter ($\approx 2 \times 10^{-4}$ V). This

signal has been recorded over a larger period of time than the duration of all the tests conducted during the experimental campaign (2 min signals). The standard deviation of the output voltage of the heave encoder therefore provides a representative estimation of its variation during a test. Lastly, the uncertainty of the instantaneous output voltage of the heave encoder (U_{E_h}) stems from the backlash of the timing belt and is estimated as being equal to half the maximum backlash value ($\approx$ 0.006 V or 0.3 mm). Note that this uncertainty is larger than the uncertainty of the reference output voltage given by Eq. A.21 and that the sum of the square of these two uncertainty values still results in 0.006 V. The uncertainty associated to the backlash can thus be considered as a good estimate of the total uncertainty of U_{E_h}.

From Eq. A.20, one finds that the uncertainty of the heave position is given by:

$$U_h \approx \sqrt{1.05 \times 10^{-7} + (1.12 \times 10^{-6})\, h^2}\,, \tag{A.22}$$

considering that $h_0 = 0$. One can notice that the uncertainty of the heave position depends on the heave position itself. It is maximum when the heave position reaches an extremum and minimum when the blade is at its heave equilibrium position ($h = h_0 = 0$). Considering the worst case scenario, namely a heave position of around 0.09 m, since it roughly corresponds to the position of the blockers and therefore to the maximum distance than the blade can reach, the expanded uncertainty of the heave position with a 95% confidence level is approximately 0.34 mm. It is about 0.32 mm when the blade is located at $h = 0$. An uncertainty of 0.3 mm is therefore a good estimate for any heave position.

The calibration constant A_θ has been estimated by holding the blade at two different pitch angles and measuring the corresponding output voltages of the pitch encoder (see Eq. 2.21). The blade was held in place with a dedicated pin inserted in two holes in the heaving carriage made for that purpose, as shown in Fig. A.2.

The uncertainty of θ at 0° and 30° with the pin in place is the sum of squares of the machining accuracy for the corresponding holes in the heaving carriage (0.06°) and the backlash between the pin and the holes (0.2°), thus resulting in an uncertainty of about 0.21°. The uncertainty $U_{(\theta_2-\theta_1)}$ is therefore estimated as 0.3°. The uncertainty of $(E_{\theta_2} - E_{\theta_1})$ is then given by:

$$U_{\left(E_{\theta_2}-E_{\theta_1}\right)} = t_{99,95\%}\, \sigma_{\left(E_{\theta_2}-E_{\theta_1}\right)} = 8.6 \times 10^{-4}\ \text{V}\,, \tag{A.23}$$

since:

$$\sigma_{\left(E_{\theta_2}-E_{\theta_1}\right)} = 4.3 \times 10^{-4}\,, \tag{A.24}$$

and $t_{99,95\%}$ is given by Eq A.17.

Using this information, the uncertainty of A_θ can be estimated as:

$$U_{A_\theta}^2 = \frac{U_{(\theta_2-\theta_1)}^2}{\left(\overline{E_{\theta_2} - E_{\theta_1}}\right)^2} + \frac{\left(\overline{\theta_2 - \theta_1}\right)^2}{\left(\overline{E_{\theta_2} - E_{\theta_1}}\right)^4} \cdot U_{\left(E_{\theta_2}-E_{\theta_1}\right)}^2\,, \tag{A.25}$$

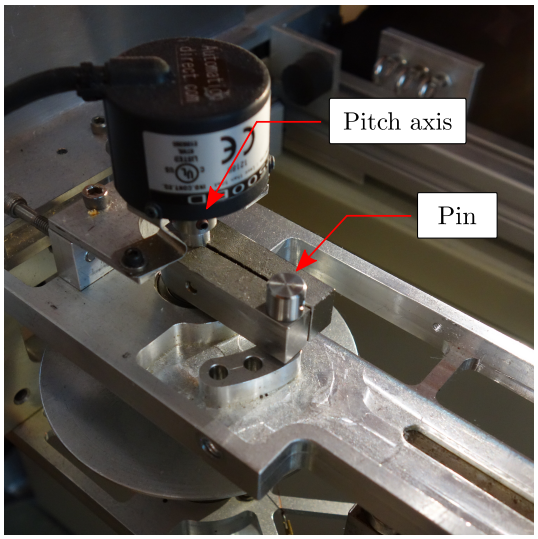

(a) $\theta = 0°$ (equilibrium position).

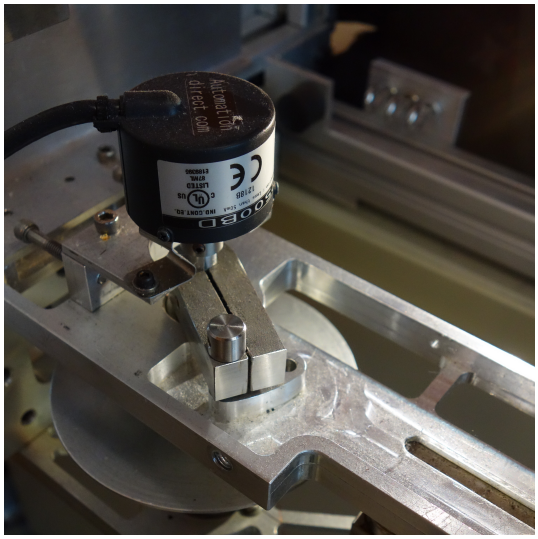

(b) $\theta = 30°$.

Figure A.2: Pitch holder with the blade positioned at 0° and 30°.

with $\left(\overline{\theta_2 - \theta_1}\right) = 30°$ and $\left(\overline{E_{\theta_2} - E_{\theta_1}}\right) = 0.2543$ V. The resulting uncertainty value of A_θ is therefore given by:

$$U_{A_\theta} = 1.2 \text{ degrees/V} \, . \tag{A.26}$$

Finally, the uncertainty of the pitch angle (θ) is obtained by applying the Taylor series method to Eq. 2.18, which gives:

$$\begin{aligned} U_\theta^2 &= A_\theta^2 \left(U_{E_\theta}^2 + U_{E_{\theta_0}}^2 \right) + \left(E_\theta - E_{\theta_0}\right)^2 U_{A_\theta}^2 + U_{\theta_0}^2 \, , \\ &= A_\theta^2 \left(U_{E_\theta}^2 + U_{E_{\theta_0}}^2 \right) + \left(\frac{\theta - \theta_0}{A_\theta} \right)^2 U_{A_\theta}^2 + U_{\theta_0}^2 \, , \end{aligned} \tag{A.27}$$

The uncertainty of the reference output voltage of the pitch encoder ($U_{E_{\theta_0}}$) is estimated as being equal to the uncertainty of the reference output voltage of the heave encoder ($U_{E_{h_0}}$), given by Eq. A.21. Since the pitch encoder is directly connected to the blade, the uncertainty of the instantaneous pitch output voltage (U_{E_θ}) is also estimated as being equal to $U_{E_{h_0}}$. In other words, there is no backlash between the blade motion and the encoder rotation.

Regarding the uncertainty of the initial pitch position (U_{θ_0}), it cannot be considered as being equal to zero as is done in heave because we are not only interested in the pitch angle with respect to the initial pitch angle, but rather to the pitch angle with respect to the oncoming flow. As a result, the accuracy of the assembly of the blade with the shaft contributes to this uncertainty.

When assembling the blade, the shaft was held in place with the pin placed as shown in Fig. A.2a while the blade was positioned so that its chord line was perpendicular to the direction of the heave motion ($\theta = 0°$). In order to position the blade, a height gauge was used to place the blade trailing

Figure A.3: Assembly of the blade with respect to the pitch holder in order to obtain a pitch angle of 0° when the pitch holder is used.

edge at the appropriate height. This is shown in Fig. A.3. This distance was measured a few times and its uncertainty is estimated as ± 0.1 mm, which is converted into a uncertainty in degrees of:

$$\text{atan}\left(\frac{0.1}{c-x_p}\right) \approx 0.17^\circ\,, \tag{A.28}$$

where c is the chord length and x_p corresponds to the distance between the leading edge and the pitch axis, so that $c - x_p = 33.3$ mm. In addition to this uncertainty contribution, the backlash in the pin holding the shaft in place also affects the uncertainty of the initial pitch position (U_{θ_0}). This backlash was measured on the turbine and the associated uncertainty is 8.5×10^{-4} V ($\approx 0.1^\circ$). The uncertainty of the initial pitch angle is thus estimated as:

$$\begin{aligned} U_{\theta_0} &= \sqrt{0.17^2 + 0.1^2}\,, \\ &\approx 0.2^\circ\,. \end{aligned} \tag{A.29}$$

From Eq. A.27, one finally finds that the uncertainty of the pitch angle is:

$$\begin{aligned} U_\theta &\approx \sqrt{0.02 + (1\times 10^{-4})\,\theta^2 + 0.04}\,, \\ &\approx \sqrt{0.06 + (1\times 10^{-4})\,\theta^2}\,, \end{aligned} \tag{A.30}$$

with θ given in degrees and considering that $\theta_0 = 0^\circ$. The uncertainty of the pitch position therefore ranges from about 0.2°, when the blade is at its pitch equilibrium position ($\theta = \theta_0 = 0^\circ$), to approximately 1° for the largest pitch angles reached during the tests ($\theta \approx 100^\circ$). Note that this is much larger than the resolution of the pitch encoder which is $360^\circ/10\,000$ pulses $= 0.036^\circ$/pulse.

Using Eq. 2.17 and considering that a second-order central-difference scheme is used to compute the heave velocity, one finds that:

$$\dot{h}(t) = \frac{A_h \left[E_h(t+\Delta t) - E_h(t-\Delta t)\right]}{2\,\Delta t} \,, \tag{A.31}$$

where Δ_t is the inverse of the sampling frequency ($1/f_{\text{sampling}}$). The uncertainty of Δ_t is neglected because it is much smaller than the other contributions. The uncertainty of the heave velocity ($U_{\dot{h}}$) is thus given by:

$$U_{\dot{h}}^2 = \frac{A_h^2}{2\,\Delta_t^2}\,U_{E_h}^2 + \frac{\dot{h}^2}{A_h^2}\,U_{A_h}^2 \,, \tag{A.32}$$

considering that:

$$U_{E_h}(t+\Delta t) \approx U_{E_h}(t-\Delta t) \approx U_{E_h}(t) \,. \tag{A.33}$$

For a sampling frequency of 83.333 Hz, the uncertainty of the heave velocity is:

$$U_{\dot{h}} = 0.02 \text{ m/s} \,. \tag{A.34}$$

It does not depend on the heave velocity because the term involving the heave velocity in Eq. A.32 is negligible compared to the other one that is mainly related to the backlash of the timing belt.

The pitch velocity is also obtained with a second-order central-difference scheme from Eq. 2.18:

$$\dot{\theta}(t) = \frac{A_\theta \left[E_\theta(t+\Delta t) - E_\theta(t-\Delta t)\right]}{2\,\Delta t} \,, \tag{A.35}$$

and its uncertainty is estimated as:

$$U_{\dot{\theta}}^2 = \frac{A_\theta^2}{2\,\Delta_t^2}\,U_{E_\theta}^2 + \frac{\dot{\theta}^2}{A_\theta^2}\,U_{A_\theta}^2 \,. \tag{A.36}$$

Again for a sampling frequency of 83.333 Hz, this results in:

$$U_{\dot{\theta}} = \sqrt{40 + (1\times10^{-4})\,\dot{\theta}^2} \,, \tag{A.37}$$

so that the uncertainty of the pitch velocity is around 6°/s when the velocity is close to zero and reaches 11°/s for the largest pitch velocities observed during the tests in the channel ($\dot{\theta} \approx 900$°/s).

A.2.4 Springs

The uncertainty of the spring stiffness coefficient (U_k) is obtained by considering the uncertainty propagation through a first-order least-square linear regression analysis (see Eq. A.8), and by estimating the expanded uncertainty of the spring elongation with a 95% confidence level (U_Δ) as 2.54×10^{-5} m (accuracy of the machining tool) and the expanded uncertainty of the tension force (U_F) from the results of the load cell calibration. Since we are only interested in the slope of the relation between the tension force in the spring and their elongation, the intercept of the load cell calibration (B in Eq. A.9)

is useless and the uncertainty of the constant B is not considered when estimating the uncertainty of the spring stiffness coefficients. U_F is therefore estimated as:

$$U_F^2 = A^2\, U_{\bar{x}}^2 + \bar{x}^2\, U_A^2 \,. \tag{A.38}$$

where A and U_A are respectively the slope of Eq. A.9 and its uncertainty, while $\bar{x}$ and $U_{\bar{x}}$ are the average output voltage of the load cell and its uncertainty. Note that the uncertainty U_Δ could be one order of magnitude larger without affecting the value of U_k since the uncertainty of the tension force (U_F) has a dominant contribution.

As more than one spring was used in heave for a given test, the uncertainty of the resultant heave stiffness coefficient is given by:

$$U_{k_h}^2 = \sum_{i=1}^{N} U_{k_i}^2 \,. \tag{A.39}$$

Regarding the uncertainty of the resultant pitch stiffness coefficient, it is estimated by applying the Taylor Series Method to Eq. 2.25, which results in:

$$U_{k_\theta}^2 = \frac{1}{16}\left[D^4\left(U_{k_1}^2 + U_{k_2}^2\right) + 4D^2\, U_D^2\left(k_1^2 + k_2^2\right)\right] \,. \tag{A.40}$$

A.2.5 Mass, moment of inertia and static moment

Again, the Taylor Series Method is used to estimate the uncertainty of the heaving mass (U_{m_h}) and the moment of inertia (U_{I_θ}). From Eq. 2.29, one finds that:

$$U_{I_\theta} = \frac{1}{16\,\pi^4}\left[T_\theta^4\left(1-\zeta_\theta^2\right)^2 U_{k_\theta}^2 + 4k_\theta^2\, T_\theta^2\left(1-\zeta_\theta^2\right)^2 U_{T_\theta}^2 + 4k_\theta^2\, T_\theta^4\, \zeta_\theta^2\, U_{\zeta_\theta}^2\right] \,, \tag{A.41}$$

where U_{k_θ} is given by Eq A.40, U_{T_θ} is the uncertainty of the pitch oscillation period length and U_{ζ_θ} is the uncertainty of the pitch damping ratio, which is derived in the next section (see Eq. A.50). The uncertainties of the period lengths have been estimated by considering their standard deviations and assuming a Student's t-distribution. An equation similar to Eq. A.41 is used to evaluate the fraction of the heaving mass involved in the free decays ($U_{m_{h\,\mathrm{free}}}$) by replacing the subscript θ with the subscript h. The uncertainty of the total heaving mass (U_{m_h}) is given by:

$$U_{m_h} = \sqrt{U_{m_{h\,\mathrm{free}}}^2 + \sum_{i=1}^{N_h}\left(U_{m_i}^2\right)} \,, \tag{A.42}$$

where N_h is the number of components involved in the heave motion that were not present during the free decay tests and U_{m_i} are the expanded uncertainties of the remaining component masses. These uncertainties are related to the accuracy of the weighing scale that has been used.

Using Eq. A.43, the uncertainty of the static moment (U_S) is found to be given by:

$$U_S^2 = \sum_{i=1}^{N_\theta}\left(m_i^2\, U_{x_{\theta,i}}^2 + x_{\theta,i}^2\, U_{m_i}^2\right) \,, \tag{A.43}$$

where U_{m_i} is the uncertainty of the mass of the i^{th} component, which again is simply related to the accuracy of the weighing scale, and $U_{x_{\theta,i}}$ is the uncertainty of the distance between the pitch axis and the center of mass. It would be very challenging to accurately estimate the uncertainty of x_θ following the procedure using the CAD that has been used to compute the static moment because it would imply considering the effects of varying every features of a component (such as the positions and the sizes of different holes in a given part) on the position of its center of mass. A much simpler and conservative approach consists in assuming that every component can be represented as a one-dimensional rod aligned with the blade chord and having a length corresponding to the length of the given component. In other words, we assume that the mass of every component is evenly distributed along the direction parallel to the blade chord. This would be an exact representation in the case of a rectangular plate. This gives more weight to the extremities of the parts because their actual mass distribution is more concentrated around the pitch axis than near their extremities. Therefore, it provides a conservative estimate of the uncertainty of the static moment.

The position of the center of mass of this simplified representation is easy to find as it is located at the geometric center of the rod idealizing a specific component. Using a coordinate system whose origin lies on the pitch axis (x_p), as shown in Fig. A.4, one finds that the distance between the pitch axis and the center of mass is given by:

$$x_\theta = \frac{x_1 + x_2}{2} \,, \tag{A.44}$$

where x_1 and x_2 respectively are the distances between the left end of the component and the pitch axis and between the right end of the component and the pitch axis. Note that x_1 is always negative or null if the pitch axis coincides with the left end of the component. The uncertainty of x_θ (U_{x_θ}) is thus given by the relation:

$$U_{x_\theta}^2 = \frac{1}{4}\left(U_{x_1}^2 + U_{x_2}^2\right) \,, \tag{A.45}$$

where U_{x_1} and U_{x_2} are the uncertainties of x_1 and x_2. These uncertainties are estimated considering a standard machining tolerance grade (IT 12) for a length of 50 mm (Oberg et al., 2012), which corresponds to the chord length. Again, this is a conservative estimate as the actual distances between the pitch axis and the extremities of every component are smaller or equal to 50 mm.

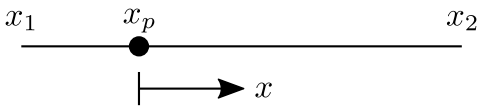

Figure A.4: Scheme of the simplified one-dimensional representation used to estimate the uncertainty of the static moment.

To sum up, the whole procedure consists of estimating the uncertainty of x_θ by simply considering the uncertainty of the distances between both ends of a component and the pitch axis. Since the uncertainty associated to the location and size of the different features of a given part is neglected, an evenly distributed mass distribution is assumed in order to give more weight to the sole uncertainty contribu-

tions considered. It is worth mentioning that all the parts involved in the pitch motion contribute to the uncertainty of the static moment, even those having a static moment of zero.

A.2.6 Linear and Coulomb damping

Regarding the uncertainties of the linear and Coulomb damping contributions, one first needs to find the uncertainty propagation in Eq. 2.33, which results in:

$$U_\beta^2 = \frac{1}{\pi^2 \left(X_{i+1} - X_{i-1}\right)} U_{(X_{i+1}-X_{i-1})}^2 + \frac{1}{\pi^2 \left(X_i - X_{i-2}\right)} U_{(X_i-X_{i-2})}^2 \,, \tag{A.46}$$

where U_β is the expanded uncertainty of β and $U_{(X_{i+1}-X_{i-1})}$ and $U_{(X_i-X_{i-2})}$ are the uncertainties of the difference between two successive positive or negative position extrema. As for the prescribed heave positions $(h_2 - h_1)$, the uncertainty of the difference between two heave position extrema ($U_{(h_{i+1}-h_{i-1})}$) is related to the difference between the largest and the smallest backlash values measured at the different heave positions, which is 1.4×10^{-4} m (see Eq. A.14). However, the uncertainty of the voltage measurement associated to these two positions, estimated as being equal to $U_{E_{h_0}}$ (9×10^{-4} V or 4.8×10^{-5} m), also adds up to the uncertainty of $(h_{i+1} - h_{i-1})$ so that:

$$\begin{aligned} U_{(h_{i+1}-h_{i-1})} &\approx \sqrt{\left(1.4 \times 10^{-4}\right)^2 + 2\left(4.8 \times 10^{-5}\right)^2} \,, \\ &\approx 1.6 \times 10^{-4} \text{ m} \,. \end{aligned} \tag{A.47}$$

Regarding the difference between two pitch angle extrema, one finds from Eq. 2.18 that:

$$\left(\theta_{i+1} - \theta_{i-1}\right) = A_\theta \left(E_{\theta_{i+1}} - E_{\theta_{i-1}}\right) \,, \tag{A.48}$$

so that:

$$U_{(\theta_{i+1}-\theta_{i-1})}^2 = 2A_\theta^2 U_{E_\theta}^2 + \left(E_{\theta_{i+1}} - E_{\theta_{i-1}}\right)^2 U_{A_\theta}^2 \,, \tag{A.49}$$

where U_{A_θ} is given in Eq. 2.21 and U_{E_θ} is given by Eq. A.21.

The uncertainty of the damping ratio can then be computed as:

$$U_\zeta^2 = \left(\frac{1}{\sqrt{1+\beta^2}} - \frac{\beta^2}{\left(1+\beta^2\right)^{3/2}} \right)^2 U_\beta^2 \,, \tag{A.50}$$

from Eq. 2.34. Using this result, the uncertainties of D_h and D_θ are evaluated with the relations:

$$U_{D_h}^2 = 4 k_h m_h U_{\zeta_h}^2 + \frac{\zeta_h^2 m_h}{k_h} U_{k_h}^2 + \frac{\zeta_h^2 k_h}{m_h} U_{m_h}^2 \,, \tag{A.51}$$

$$U_{D_\theta}^2 = 4 k_\theta I_\theta U_{\zeta_\theta}^2 + \frac{\zeta_\theta^2 I_\theta}{k_\theta} U_\theta^2 + \frac{\zeta_\theta^2 k_\theta}{I_\theta} U_{I_\theta}^2 \,, \tag{A.52}$$

stemming from Eqs. 2.35 and 2.36. Since the damping of the eddy-current brake is determined using Eq. 5.5, its uncertainty for each of the magnet positions tested during the calibration process ($U_{D_{h,\,\text{b,calib}}}$) is estimated as:

$$U_{D_{h,\,\text{b,calib}}}^2 = U_{D_h}^2 + U_{D_{h,\,\text{v}}}^2 \,. \tag{A.53}$$

As mentioned in Sec. 2.B.4, a linear interpolation has been performed to determine the heave damping for the exact position of the heave damper's magnets (l_m) during the tests in the water channel. This value of the heave damping coefficient is referred to as $D_{h,\text{e calib}}$ and it is determined using the following relation:

$$D_{h,\text{e calib}} = D_{h,\text{e calib},1} + (l_m - l_{m,1}) \left(\frac{D_{h,\text{e calib},2} - D_{h,\text{e calib},1}}{l_{m,2} - l_{m,1}} \right) , \tag{A.54}$$

where the variables without the subscripts 1 or 2 correspond to the values corresponding to a given test in the channel while the variables with the subscripts 1 and 2 correspond to the two magnet positions tested during the calibration process that are the closest to the position of the case considered. Because of these linear interpolations, an additional uncertainty contribution originates from the uncertainty of the positions of the magnets (U_{l_m}), which is related to the accuracy of the caliper used to measure this value. It has been estimated as 0.05 mm. From Eq.A.54, this additional uncertainty for a given value of l_m is estimated as:

$$U^2_{D_{h,\text{e calib}}} = (2A1 + 2A1A2)\, U^2_{l_m} + (1 + A2)\, U^2_{D_{h,\text{e calib},1}} + A2\, U^2_{D_{h,\text{e calib},2}} , \tag{A.55}$$

where:

$$A1 = \left(\frac{D_{h,\text{ b,calib},2} - D_{h,\text{ b,calib},1}}{l_{m,2} - l_{m,1}} \right)^2 , \tag{A.56}$$

$$A2 = \left(\frac{l_m - l_{m,1}}{l_{m,2} - l_{m,1}} \right)^2 . \tag{A.57}$$

Lastly, another uncertainty contribution stems from the temperature correction (see Eq. 2.38):

$$U_{D_{h,\text{e}}} = \frac{(1 + \alpha_{B_0} \Delta T)^4}{(1 + \alpha_{\rho_e} \Delta T)^2} U^2_{D_{h,\text{e calib}}} + D^2_{h,\text{e calib}} \left[\frac{2\, \alpha_{B_0}\, (1 + \alpha_{B_0} \Delta T)}{(1 + \alpha_{\rho_e} \Delta T)} - \frac{\alpha_{\rho_e}\, (1 + \alpha_{B_0} \Delta T)^2}{(1 + \alpha_{\rho_e} \Delta T)^2} \right]^2 U^2_{\Delta T} , \tag{A.58}$$

where $U^2_{\Delta T}$ is given as:

$$U^2_{\Delta T} = U^2_T + U^2_{T_{\text{calib}}} , \tag{A.59}$$

and:

$$U_T \approx U_{T_{\text{calib}}} \approx 0.1 \text{ °C} . \tag{A.60}$$

An uncertainty of 0.1°C has been estimated for the temperature during a given test to take into account the slight temperature variations occurring during a test. The same uncertainty has been considered for T_{calib}, even if this is larger than the thermometer accuracy, in order to obtain a conservative estimate and to take into account that no uncertainty has been considered for the two temperature coefficients (α_{B_0} and α_{ρ_e}) due to the lack of information on this aspect.

The Taylor series uncertainty propagation method has also been applied to Eqs. 2.42, 2.43 and 2.44 to obtain:

$$\begin{aligned} U^2_C = & \frac{1}{4\left(1 + e^{-\beta \pi}\right)^2} U^2_{(X_{i+1} - X_i)} + \frac{e^{-2\beta \pi}}{4\left(1 + e^{-\beta \pi}\right)^2} U^2_{(X_i - X_{i-1})} \\ & + \frac{4\pi^2 e^{-2\beta \pi}}{\left(1 + e^{-\beta \pi}\right)^2} \left(\frac{(X_{i+1} - X_i)}{1 + e^{-\beta \pi}} + (X_i - X_{i-1}) \left[\frac{e^{-\beta \pi}}{1 + e^{-\beta \pi}} - 1 \right] \right)^2 U^2_\beta , \end{aligned} \tag{A.61}$$

$$U_{f_c}^2 = k_h^2 U_{C_h}^2 + C_h^2 U_{k_h}^2 \,, \tag{A.62}$$

$$U_{m_c}^2 = k_\theta^2 U_{C_\theta}^2 + C_\theta^2 U_{k_\theta}^2 \,, \tag{A.63}$$

A.2.7 Hydrodynamic parameters

Since the resistive force in the direction of the flow associated to the presence of the blade is negligible compared to the other losses in the closed-loop system of the channel, its presence has a negligible effect on the water velocity. Nevertheless, PIV measurements have been carried out for a fixed blade with the chord line aligned with the flow ($\theta = 0°$), with the chord line perpendicular to the flow ($\theta = 90°$) and for a case with the baseline structural parameter values. The uncertainty of the mean velocity of the oncoming flow for a given pump rotational speed has been estimated as being equal to half the difference between the largest and the smallest velocities measured for the three cases tested, namely $\theta = 0°$, $\theta = 90°$ and the baseline case. In order to have a conservative estimate of this uncertainty, the largest uncertainty from the different flow velocities has been used as an estimate of the uncertainty for all the velocities, which is 2.2% of the mean velocity.

The boundary layer height at the channel's bottom surface, defined as the region for which the velocity is below 99% of the freestream velocity, has been measured to be around 9 mm at the PIV plane. Assuming that it behaves as a laminar boundary layer on a flat plate with zero pressure gradient, the estimated unperturbed (no blade in the channel) boundary layer height at the position of the blade pitch axis should be around 10.3 mm. The associated displacement thicknesses are 3 mm and 3.5 mm. If we consider that the displacement thicknesses are the same on the vertical side walls of the channel, the expected velocity increase due to the increasing blockage caused by the boundary layers growth is around 0.4%. This effect can therefore be neglected as it is smaller than the uncertainty of the velocity measurement.

The uncertainty of the water density and the dynamic viscosity, which are determined by interpolating the tabulated data available in the book of Munson (2013), have been estimated using an equation similar to Eq. A.55 and by considering the uncertainty of the ambient temperature measurement, which is estimated as 0.05°C.

A.2.8 Other uncertainties

The uncertainty of the chord length is $U_c = 0.05$ mm and is related to the accuracy of the caliper that has been used to measure this length. The uncertainty of the blade span length is estimated as $U_b = 0.05$ mm, when the blade is completely submerged, and $U_b = 1$ mm when it is only partially submerged since this uncertainty becomes dependent on the water depth, which has not been measured with the same accuracy.

Each period length (T) is evaluated by finding the time interval between two successive moments at

which the blade crosses its heave equilibrium position ($t_{h=0}$):

$$T = t_{h=0,\,i+1} - t_{h=0,\,i}\ , \tag{A.64}$$

where the subscript i denotes the i^{th} occurrence of $h = 0$. The uncertainty of the time at which one of this event occurs is estimated as $\Delta_t/2$ where Δ_t is the inverse of the sampling frequency ($1/f_{\text{sampling}}$). The uncertainty of the period length is therefore estimated as:

$$U_T = \sqrt{\left(\frac{\Delta_t}{2}\right)^2 + \left(\frac{\Delta_t}{2}\right)^2}\ . \tag{A.65}$$

The cycle-averaged power dissipated in the eddy-current brake, which models the energy extraction, is computed using Eq. 2.10 in Paper I. In practice, since the recorded signals are discrete, the integral is computed using the trapezoidal rule, which results in the following relation:

$$\overline{P_{h,\mathrm{e}\,j}} = \frac{D_{h,\mathrm{e}}}{T_j} \cdot \frac{\Delta_t}{2} \sum_{k=N_1+1}^{N_2} \left(\dot{h}_k^2 + \dot{h}_{k+1}^2\right)\ , \tag{A.66}$$

where:

$$N_1 = t/\Delta_t\ , \tag{A.67}$$

$$N_2 = (t+T_j)/\Delta_t\ . \tag{A.68}$$

The uncertainty of the cycle-averaged power dissipated in the heave damper is derived from Eq. A.66. After some manipulations, one obtains:

$$U^2_{\overline{P_{h,\mathrm{e}\,j}}} = \left(\frac{\overline{P_{h,\mathrm{e}\,j}} \cdot T_j}{D_{h,\mathrm{e}}}\right)^2 \cdot \left(\frac{1}{T_j^2} U^2_{D_{h,\mathrm{e}}} + \frac{D^2_{h,\mathrm{e}}}{T_j^4} U_T^2\right) + \left(\frac{D_{h,\mathrm{e}} \cdot \Delta_t}{T_j}\right)^2 \cdot \sum_{k=N_1+1}^{N_2} \left(\dot{h}_k^2 \cdot U^2_{\dot{h}_k} + \dot{h}_{k+1}^2 \cdot U^2_{\dot{h}_{k+1}}\right)\ . \tag{A.69}$$

In order to determine the uncertainty of the overall transverse extent of the blade motion (d), we assume that it can be estimated as:

$$\begin{aligned} d &\approx (h_{\max} + (c - x_p)\sin(\theta_{\max})) - (h_{\min} + (c - x_p)\sin(\theta_{\min}))\ , \\ &\approx (h_{\max} - h_{\min}) + (c - x_p)\left(\sin(\theta_{\max}) - \sin(\theta_{\min})\right)\ , \end{aligned} \tag{A.70}$$

where:

$$\sin(\theta_{\max}) - \sin(\theta_{\min}) \approx 2\sin(\theta_{\max})\ , \tag{A.71}$$

by assuming that the motions are symmetric about the pitch equilibrium position, so that:

$$d \approx (h_{\max} - h_{\min}) + 2(c - x_p)\sin(\theta_{\max})\ . \tag{A.72}$$

The uncertainty of d is therefore estimated as:

$$U_d = U^2_{h_{\max}-h_{\min}} + 4(c-x_p)^2\cos^2(\theta_{\max})U^2_{\theta_{\max}} + 4\sin^2(\theta_{\max})U^2_{c-x_p}\ , \tag{A.73}$$

where $U_{h_{\max}-h_{\min}}$ and $U_{\theta_{\max}}$ are determined using the information given in Sec. A.2.3 while U_{c-x_p} is estimated by considering a standard machining tolerance grade (IT 12), as has been done for U_{x_θ} in Eq. A.45.

Finally, all the uncertainties of the dimensionless quantities have been derived using the Taylor series propagation method and using the uncertainties presented in the previous subsections.

Bibliography

Coleman, H. W. and Steele, W. G. *Experimentation, Validation, and Uncertainty Analysis for Engineers*. Cambridge monographs on mechanics. Wiley, 2009. ISBN 9780470168882.

Dowell, E. H. *A Modern Course in Aeroelasticity Fourh Revised and Enlarged Edition*. Kluwer Academic Publishers, Dordrecht, The Netherlands, 4th edition, 2004.

Munson, Bruce Roy. *Fundamentals of fluid mechanics*. John Wiley & Sons, Hoboken, NJ, USA, 7th edition, 2013.

Oberg, Erik, Jones, Franklin D., Horton, Holbrook L., and Ryffel, Henry H. *Machinery's Handbook*. Machinery's Handbook. Industrial Press, New York, 29th edition, 2012.

Rao, S. S. *Mechanical vibrations*. Prentice Hall, Upper Saddle River, N.J, 5th edition, 2011.

Veilleux, Jean-Christophe and Dumas, Guy. Numerical optimization of a fully-passive flapping-airfoil turbine. *Journal of Fluids and Structures*, 70:102 – 130, 2017.

Appendix B

Additional results and discussion related to Paper III

B.1 Influence of the static moment with $x_p/c = 0.75$

A few additional simulations have been carried out for various values of S^* with $x_p/c = 0.75$. The corresponding contours of efficiency are shown in Fig. B.1. These results confirm that the static moment needs to be around zero when the pitch axis is positioned at the three-quarter-chord point in order to maximize the efficiency, which validates this choice in Paper III. It is also found that it is possible to achieve high efficiencies with the center of mass located upstream of the pitch axis under such conditions.

B.2 Driving mechanism of the semi-passive turbine

In paper I, we argue that a one-degree-of-freedom static instability, known as divergence (Dowell, 2004), is responsible for initiating the pitch motion of the fully-passive flapping-foil turbine prototype, and that this pitch motion is in turn driving the heave motion. The heave motion cannot be driven by the pitch motion in the case of the semi-passive turbine considered in Papers II and III study since it is prescribed. Nevertheless, it is still useful to analyze the driving mechanism responsible for the pitch motion of the foil.

Considering a foil that is elastically supported in pitch, but not allowed to move in heave and neglecting the friction in pitch, the pitch motion is governed by:

$$C_M/2 = I_\theta^* \, \ddot{\theta}^* + k_\theta^* \, \theta \; . \tag{B.1}$$

For small pitch angles around zero, the moment coefficient can be approximated as:

$$C_M = C_{M_{\theta=0}} + \frac{\partial C_M}{\partial \theta} \, \theta \; , \tag{B.2}$$

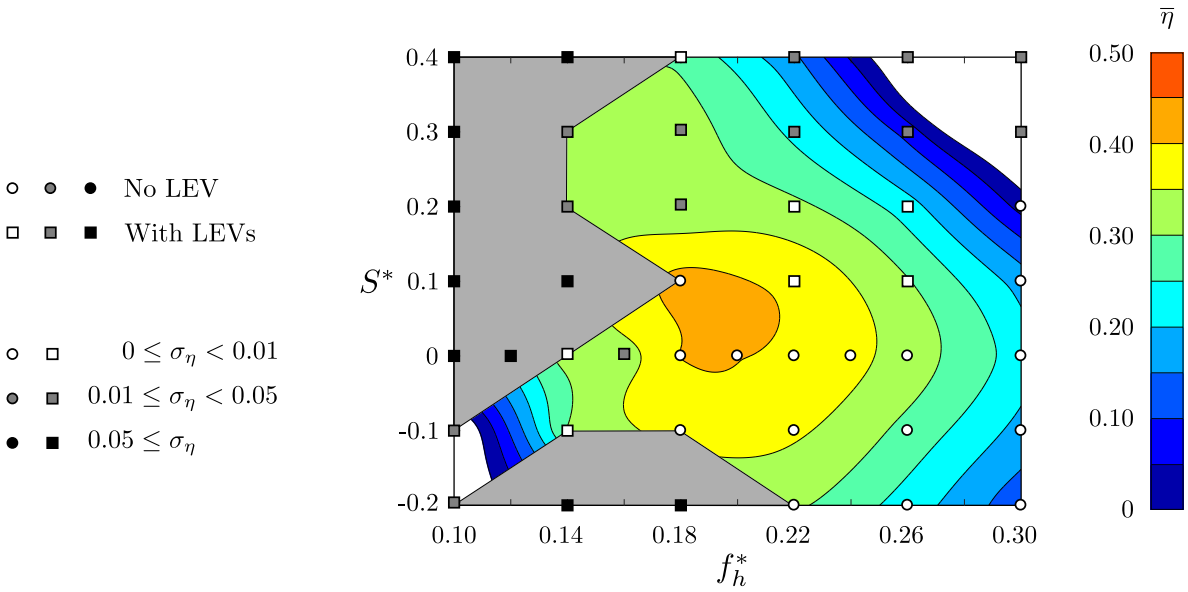

Figure B.1: Contours of the time-averaged efficiency ($\overline{\eta}$) for a pitch axis located at the three-quarter-chord point. The white areas indicate negative values while the gray areas indicate zones where the data is not presented because of the large variations ($\sigma_\eta \geq 0.05$). The values of the other parameters are: $\lambda_\theta^* = 0.7$; $I_\theta^* = 2$; $D_\theta^* = 0$.

where $C_{M_{\theta=0}}$ and $\partial C_M/\partial\theta$ are the moment coefficient and its slope at $\theta = 0$. In the case of symmetric foil profiles, $C_{M_{\theta=0}} = 0$. Eq. B.1 can therefore be written as:

$$I_\theta^* \ddot{\theta}^* + \left(k_\theta^* - \frac{1}{2}\frac{\partial C_M}{\partial \theta}\right)\theta = 0\,, \tag{B.3}$$

which shows that the slope of the moment coefficient acts as an added fluid-induced stiffness. The pitch motion is unstable when the effective stiffness is negative, i.e., when:

$$k_\theta^* - \frac{1}{2}\frac{\partial C_M}{\partial \theta} < 0\,. \tag{B.4}$$

The critical dimensionless pitch stiffness coefficient:

$$k_{\theta\,\mathrm{crit}}^* = \frac{1}{2}\frac{\partial C_M}{\partial \theta}\,, \tag{B.5}$$

below which the foil becomes unstable, can thus be found by determining the slope of the moment coefficient around $\theta = 0$. As for Veilleux and Dumas (2017), we used the thin airfoil theory in Paper I to achieve this task. In this appendix, the slope of the moment coefficient around $\theta = 0$ is rather determined by conducting a series of steady numerical simulations with the NACA0015 foil oriented at different pitch angles to obtain more accurate values for $k_{\theta\,\mathrm{crit}}^*$. The results are presented in Table B.1 for four different pitch axis locations. The foil cannot be unstable in divergence when $x_p/c = 0$ since a negative value of k_θ^* would be required for that to happen. This is because the point of application of the resultant hydrodynamic force on the foil is necessarily located downstream of the pitch axis in this specific case, hence having a stabilizing effect for the pitch motion.

Table B.1: Critical dimensionless pitch stiffness coefficient ($k^*_{\theta\ \mathrm{crit}}$) as a function of the pitch axis location.

Parameters	**Values**			
x_p/c	0	0.25	0.50	0.75
$k^*_{\theta\ \mathrm{crit}}$	-	0.007	0.802	1.597

Based on this analysis, some cases presented in Fig. 4.16d, with $x_p/c = 0.75$, are subject to the divergence instability. In order to visualize them, the contours presented in Fig. 4.16d are reproduced in Fig. B.1, but with the addition of the contours of the pitch stiffness coefficient. This allows delimiting the zone in which the operating points are subject to the divergence instability based the critical stiffness coefficient of 1.597.

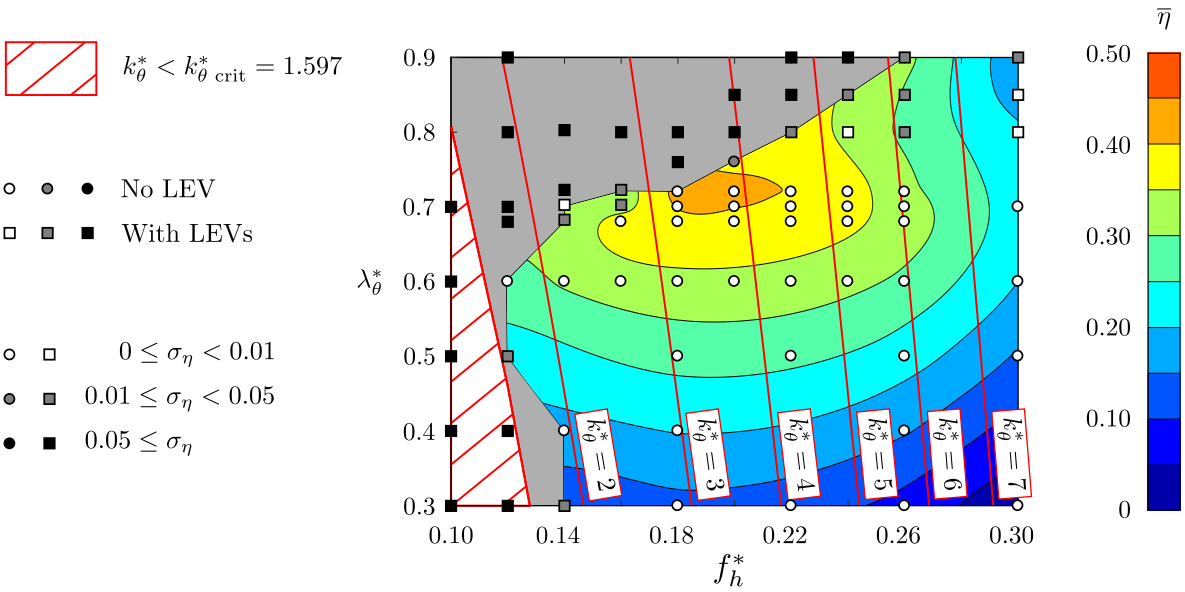

Figure B.1: Contours of the pitch stiffness coefficient (red lines) superimposed on the contours of the time-averaged efficiency with $x_p/c = 0.75$ and $S^* = 0$. The foil is subject to the divergence instability in the hatched area.

It is found that all the operating points that are unstable in divergence are characterized by very irregular motions, which make them inappropriate for turbine applications, unlike what is observed with a fully-passive turbine in Paper I and in the study of Veilleux and Dumas (2017). The reason is that the heave motion must drive the pitch motion for the semi-passive flapping-foil turbine considered in Papers II and III to work properly because the heave motion is not influenced by the pitch motion. Indeed, the heave motion is prescribed to a specific sinusoidal motion no matter what happens in pitch. When the foil is unstable in divergence, its pitch motion becomes self-driven while still being affected by the heave motion through the inertial coupling term. This results in erratic pitch motions.

B.3 Analogy with the linear vibration theory for the derivation of the parameter λ_θ^*

The results presented in Paper III demonstrate that the parameter λ_θ^* (see Eq. 4.48) effectively characterizes the dynamics of the optimal operating points achieved for a semi-passive flapping-foil turbine with a passive pitch motion. This implies that the dynamics of these operating points does not directly depends on the ratio between the frequency of the foil motion in pitch and the pitch natural frequency, referred to as the frequency ratio r (see Eq. 4.51). Some insights can be gained from the vibration theory of a one-degree-of-freedom linear mass-damper-spring system excited by a harmonic force (Rao, 2011). The equation of motion for such system undergoing a torsional motion is:

$$M_0 \cos(\omega t) = I_\theta \, \ddot{\theta} + D_\theta \, \dot{\theta} + k_\theta \, \theta \ , \tag{B.6}$$

where M_0 is the amplitude of the exciting moment and:

$$\omega = 2 \pi f \ , \tag{B.7}$$

f being the frequency of the torsional motion. Considering a general reference time scale (t_{ref}) and a general reference scale for the torsional motion (θ_{ref}), Eq. B.6 can be written in the following dimensionless form:

$$\cos\left(\omega \frac{t}{t_{\text{ref}}}\right) = \frac{I_\theta \, \theta_{\text{ref}}}{M_0 \, t_{\text{ref}}^2} \ddot{\theta}^* + \frac{D_\theta \, \theta_{\text{ref}}}{M_0 \, t_{\text{ref}}} \dot{\theta}^* + \frac{k_\theta \, \theta_{\text{ref}}}{M_0} \theta^* \ , \tag{B.8}$$

Using $1/\omega$ for t_{ref} and M_0/k_θ, the torsional deflection under a static moment M_0, for θ_{ref}, Eq. B.8 becomes:

$$\cos(t^*) = r^2 \ddot{\theta}^* + 2 \, \zeta \, r \, \dot{\theta}^* + \theta^* \ , \tag{B.9}$$

with:

$$t^* = \omega t \ , \ \theta^* = \frac{\theta \, k_\theta}{M_0} \ , \quad \dot{\theta}^* = \frac{\theta \, k_\theta}{\omega \, M_0} \ , \quad \ddot{\theta}^* = \frac{\theta \, k_\theta}{\omega^2 \, M_0} \ , \quad \zeta = \frac{D_\theta}{2\sqrt{k_\theta \, I_\theta}} \ .$$

Note that this normalization is different than the one used in the rest of this thesis. The analytical solution for this system is given by:

$$\theta^* = A_c \sin(t^* - \gamma_c) \ , \tag{B.10}$$

where A_c is the classical amplification factor (Rao, 2011):

$$A_c = \frac{1}{\sqrt{(1 - r^2)^2 + (2 \, \zeta \, r)^2}} \ , \tag{B.11}$$

and γ_c is the classical phase difference between the torsional motion and the exciting moment:

$$\gamma_c = \arctan\left(\frac{2 \, \zeta \, r}{1 - r^2}\right) \ . \tag{B.12}$$

This result implies that the dynamics of such a linear mass-damper-spring system in torsion only depends on two dimensionless parameters, namely the frequency ratio (r) and the damping ratio (ζ).

However, this development is based on the use of M_0/k_θ as a representative scale for the torsional motion. This reference scale is not relevant for the optimal semi-passive flapping-foil turbine cases presented in Paper III because the fluid-structure interaction characterizing these cases is strong enough for the pitch amplitude to be significantly influenced by the flow dynamics rather than being simply dependent on the solid dynamics, i.e., the dynamics of the elastically-supported foil in vacuum. The reference scale M_0/k_θ also becomes irrelevant when k_θ approaches zero.

Considering a reference scale of one for θ_{ref} and c/U_∞ for t_{ref}, which is consistent with the reference scales that have been selected to derive the dimensionless equation of motion in pitch (see Eqs. 4.8 used in the present thesis, Eq. B.8 becomes:

$$\cos(2\pi f^* t^*) = \frac{I_\theta U_\infty^2}{M_0 c^2}\ddot{\theta}^* + \frac{D_\theta U_\infty}{M_0 c}\dot{\theta}^* + \frac{k_\theta}{M_0}\theta \ , \tag{B.13}$$

and its analytical solution is:

$$\theta = A\sin\left(2\pi f^* t^* - \gamma\right) \ , \tag{B.14}$$

where:

$$A = \frac{1}{\sqrt{\left(\frac{k_\theta}{M_0} - \frac{I_\theta U_\infty^2}{M_0 c^2}\omega^2\right)^2 + \left(\frac{D_\theta U_\infty}{M_0 c}\omega\right)^2}} \ , \tag{B.15}$$

$$\gamma = \arctan\left(\frac{\frac{D_\theta U_\infty}{M_0 c}\omega}{\frac{k_\theta}{M_0} - \frac{I_\theta U_\infty^2}{M_0 c^2}\omega^2}\right) \ . \tag{B.16}$$

Eq. B.15 and Eq. B.16 again only depends on two dimensionless parameters, one appearing at the numerator in Eq. B.16 and another one at the denominator. It reduces to only one parameter when the damping is kept constant. If we further consider that the moment generated by the fluid flow is not constant and rather scales with $0.5\rho U_\infty^2 b c^2$ (see Eq. 4.13), the parameter appearing at the denominator of Eq. B.16 becomes equivalent to the parameter λ_θ^*. This analysis relying on the dynamics of a linear mass-damper-spring system therefore corroborates the idea of characterizing the strong fluid-structure interactions of the semi-passive flapping-foil turbine with λ_θ^* instead of the frequency ratio.